MOLECULAR MECHANICS OF GLASSY AND SEMICRYSTALLINE POLYMERS

A Dissertation

Presented to

The Graduate Faculty at The University of Akron

In Partial Fulfillment

of the Requirements for the Degree

Doctor of Philosophy

Masoud Razavi

August, 2020

MOLECULAR MECHANICS OF GLASSY AND SEMICRYSTALLINE POLYMERS

Masoud Razavi

Dissertation

Approved:

_____
Advisor
Dr. Shi-Qing Wang

_____
Committee Member
Dr. Toshikazu Miyoshi

_____
Committee Member
Dr. Mesfin Tsige

_____
Committee Member
Dr. James Eagan

_____
Committee Member
Dr. Ruel McKenzie

Accepted:

_____
Department Chair
Dr. Tianbo Liu

_____
Interim Dean of the College
Dr. Ali Dhinojwala

_____
Interim Director, Graduate School
Dr. Marnie Saunders

_____
Date

ABSTRACT

Polymers are a unique class of modern materials. Despite their light mass density, their mechanical properties are strong enough for a variety of applications either through crystallization or vitrification to achieve sufficient rigidity. However, high Young's modulus is not the only necessary characteristic. Desirably, polymeric materials should be ductile, for example, tolerating considerable bending. In this regard polymers (at room temperature) can be classified as brittle or ductile polymers. A ductile or brittle polymer structurally, can be either amorphous or semicrystalline. Moreover, a polymeric material (either glassy or semicrystalline) could remain ductile at temperatures much lower than its glass transition temperature (T_g). Ductile polymers include semicrystalline polymers such as polyethylene (PE) and polypropylene (PP) with low T_g, and polyamide with high T_g, as well as some amorphous glassy polymers such as bisphenol A polycarbonate (bpA-PC) and polyethylene terephthalate (PET). Examples of the brittle polymers under ambient conditions, are semicrystalline polymers with high T_g such as semicrystalline PET or Poly(lactic acid) (PLA), or glassy amorphous polymers such as polystyrene (PS) and poly(methyl methacrylate) (PMMA). For decades mechanical behavior of polymers is an important research topic in polymer science and despite the tremendous researches in this filed, there is no comprehensive molecular picture that can universally describe the mechanical behavior of polymeric materials at the molecular level. Consequently, previous

studies are not able to propose a method to efficiently improve the mechanical properties of polymers without additives, e.g. turning a brittle polymer to a ductile one.

This dissertation consists of two parts: PART A is about the molecular mechanics of glassy amorphous polymers, and PART B focuses on the molecular mechanics of semicrystalline polymers. In each part, we carried out three independent projects to address several important questions in the mechanics of polymer glasses and semicrystalline polymers. Influenced by our recent phenomenological molecular model, this work comprehensively emphasizes on the important role of the chain networking, arising from intra-chain connectivity and chain uncrossability, on affording ductility into the polymeric materials.

Chapter I is a general introduction into the PART A. In Chapter II we study several different polymer glasses in tensile, creep and stress relaxation mechanical experiments in order to understand the crazing behavior of polymer glasses. Based on our inclusive experiments and counterintuitive results, an alternative molecular mechanism and model is proposed to explain craze initiation in polymer glasses. This chapter also includes a refrainment to our recent phenomenological molecular model. Chapter III studies the two-phase rubber-toughened polymer glasses. It is indicated that the commercial rubber-toughened polymer glasses do not undergo molecular level yielding characterized by the increased segmental mobility, thus we title the strain softening point of these materials as apparent yield point. Methods to switch the mechanism of yielding from apparent to the real one is also proposed. A novel rubber-toughening mechanism that is operative in the

recently synthesized nano-rubber-toughened PMMA by Dow chemicals, is suggested. In Chapter IV, real-time birefringence measurements during different mechanical experiments of PMMA and PS is performed in order to achieve molecular level insights into the deformation of polymer glasses. For the first time, birefringence changes at the post-yield deformation of PS and PMMA are measured. Attempts are made to explain the molecular reasons of the birefringence changes and its correlation/decorrelation with stress, during different mechanical experiments including uniaxial tensile, creep and stress relaxation experiments.

By an analogy with PART A, PART B of dissertation, starts with a general introduction into the molecular mechanics of semicrystalline polymers in Chapter V. In Chapter VI, our general framework and universal molecular picture of the deformation of semicrystalline polymers are introduced. Chapter VII investigates the molecular mechanics of semicrystalline PLA which is an ideal model semicrystalline polymer, through a comparative study with the mechanics of its amorphous state. Reasons behind mechanical weakness of this polymer and in general any other semicrystalline polymer below T_g, and lower drawability above T_g, are explained in light of the results from time-resolved polarized optical microscope (POM) observations during large deformation of semicrystalline PLA. After identifying the origins of the brittle response of semicrystalline polymers, a universal strategy is proposed in Chapter VIII to turn brittle semicrystalline polymers to ductile. Finally, Chapter IX summarizes the overall body of the dissertation and offers main conclusions.

To those who are big-hearted and enjoy doing science

ACKNOWLEDGEMENTS

First and foremost, I would like to express my heartfelt gratitude to my advisor, Prof. Shi-Qing Wang for his continuous support of my doctoral research and insightful discussions during the past four years. I found his persistence, enthusiasm and devotedness to the science quite unique. I believe the most essential skill one can achieve during PhD studies is critical thinking and having an objective and thorough perspective to the problems, and I owe this accomplishment to Dr. Wang' mentorship. I learned plenty from him on the fundamental research of polymer physics, and I am grateful for the encouraged discretion to pursue various projects and new directions without objection. I will most certainly miss our fruitful Monday group meetings which served as a sharpening stone to our thinking skills.

I would like to thank my doctoral dissertation committee: Prof. Toshikazu Miyoshi, Prof. Mesfin Tsige, Prof. James Eagan and Prof. Ruel McKenzie for their insightful comments on my projects. I am especially grateful to Dr. Miyoshi for his scientific advice and helpful discussions throughout the course of my research. I truly appreciate his encouragement and support when I started to explore the new direction of the mechanics of semicrystalline polymers, and I will never forget our friendly discussions during lunch or dinner at Rob's Dining Hall or restaurants near campus. Special thanks to Dr. Tsige for his continual support and willingness to provide advice on both academic and personal matters which any student may face during his PhD studies. I will miss his unexampled

lectures, as they were the best class sessions I have ever attended in our department. I will forever behold all the good memories with Drs. Miyoshi and Tsige during my PhD studies.

I express my sincere gratitude to my former M.Sc. advisors Prof. Hossein Ali Khonakdar and Prof. Seyed Hassan Jafari, as I learned the fundamentals of academic research through working with them and I would not have made this far without the precious experiences I achieved during those productive years.

I would like to thank our collaborators Prof. Liangbin Li and his student Wenwen Zhang from University of Science and Technology of China (USTC) for providing real-time X-ray measurements of our semicrystalline samples. Special thanks to Mr. Ed Laughlin from the university machine shop for his exemplary skills and generous help on machine devices. I would like to thank the wonderful staff at the Department of Polymer Science, especially Ms. Melissa Bowman and Ms. Jacqueline Clark for always being helpful and friendly and for the quick processing of my administrative paperwork.

I thank all the current and past group members at Dr. Wang's group; Dr. Xiaoxiao Li, Ms. Mingyu Yuan, Mr. Ruchao Yuan, Mr. Yi Feng, Dr. Zhichen Zhao (who was a great roommate as well), Dr. Jianning Liu (who helped me a lot with the instrumental training during the first year of my doctoral research), and Mr. Yexin Zheng—extremely nice and helpful officemate, as I will never forget our scientific discussions in the lab that could take until midnight. Special thanks to Da Huang, a young passionate M.Sc. student, who helped me a lot with the experimental side of my projects, and I wish him all the best with his PhD studies that start soon in Germany. I also thank Dr. Shijun Wang, a very nice friend from

Dr. Miyoshi's group, who helped me with the WAXS training. I am honored and privileged to meet such wonderful people; we made many good memories together and we were always supportive of each other. I would also like to thank my Iranian friends here in Akron, without whom it would be much more challenging to complete a PhD degree in a small town away from my family and country.

Last but not least, I would like to thank my parents, my brother, Hamed, and my beloved grandparents, for their unconditional love and encouragement. I thank my uncle, Dr. Karim Razavi, who was the reason I decided to study Polymer Engineering for my B.Sc. degree, and I have always benefitted from his invaluable advice. I am thankful for my aunt, Dr. Zeynab Razavi, for her true love and support. I also thank my youngest uncle, Dr. Jalil Razavi, who helped me with physics and mathematics courses during high school. I have always considered him as a supportive brother and "cool" friend. Looking back at the past several years, I find life quite amazing just by having had all these people alongside me, and I am looking forward to the years ahead with this peace of mind.

TABLE OF CONTENCTS

LIST OF TABLES

Table Page

LIST OF FIGURES

Figure Page

CHAPTER I

INTRODCUTON TO PART A: MOLECULAR MECHANICS OF GLASSY POLYMERS

Polymer glasses are structurally disordered materials that due to vitrification below T_g own sufficient mechanical strength for certain applications. Unlike small-molecule glassy materials, polymer glasses because of intrachain connectivity indicate unique behaviors above and below T_g. Below T_g it turns out that they are able be ductile and tolerate substantial amount of deformation before failure. Many mechanical models have been proposed in the past to understand the mechanical behavior of polymer glasses and explain the ductile vs brittle response of these materials[1-9]. Following is a brief summary of the latest molecular model that has been proposed by our group in 2014[10].

1.1 Phenomenological Hybrid Molecular Model

In this molecular model a polymer glass with high molecular weight is treated as a hybrid structure of two networks: i) Primary network, which originates from short-range Van der Waals interactions between segments. This network exists in small molecule organic glasses as well, and ii) Chain network which exists due to the intrachain connectivity and interchain uncrossability. This network is the unique characteristics of polymer glasses. Figure 1.1 shows the structure of this hybrid network.

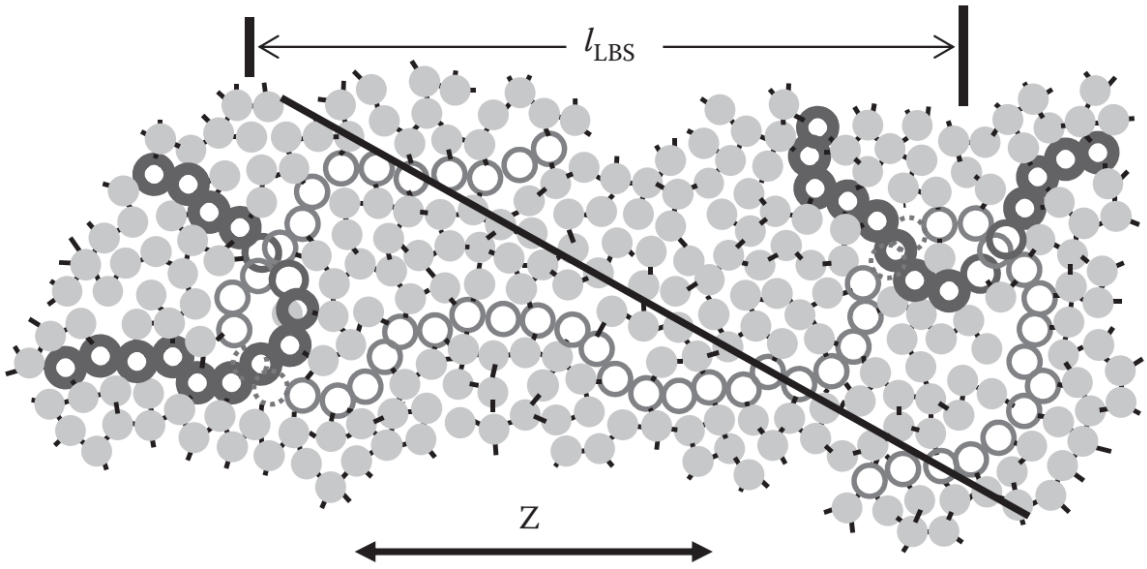

Figure 1.1 Hybrid structure made of primary network and chain network. Segments are shown by light grid dots and the Van der Waals interactions between them are represented by short bars. The chain network emerges as a result of entanglement between load bearing strand (thin rings) and two adjacent chains (thick rings). (replot of Figure 12.1 Roth, C. B., Polymer Glasses. CRC Press, Taylor & Francis, 2016, p395).

The chain network provides the global structural connectivity across the entire sample. During deformation the chain network by pushing its surrounding segments increases their mobility and activates them and drives the system toward yielding. If the global activity occurs in the system, the macroscopic behavior of the sample during large deformation will be ductile, otherwise high chain tension will be developed in the system and the brittle failure will take place through chain pull out at the network junctions, before chain network can produce enough segmental mobility[11].

Although the chain networking in the glassy state is inherited from entanglement network in the melt state, one should note that chain network at the glassy state is different than entanglement network in the melt state. In other words, not all the entanglements necessarily participate in the chain network upon deformation. This can be theoretically indicated by comparison between areal density of entanglement network and chain network. Areal density of entanglement network ψ_{ent} is proportional to $1/pl_{ent}$, where p is the packing length and l_{ent} is the length of entangled strand. Based on packing model length of entangled strand is proportional to the packing length. Therefore for a entanglement network we have $\psi_{ent} \sim 1/p^2$ 12. On the other hand, areal density of chain network ψ is proportional to $1/pl_{LBS}$, where p is the packing length and l_{LBS} is the length of load-bearing strand. The size of load-bearing strand scales with Kuhn length l_{k}. Therefore, for a chain network we have $\psi \sim 1/pl_k$ 10. Since Kuhn length is larger than packing length, therefore the areal density of chain network is smaller than areal density of entanglement network. This implies that not all the chain entanglements participate in the chain network.

1.2 Structure of Part A of Dissertation

Having this brief background, in Chapter II we are going to propose a refinement to this model and employ the updated model to understand the craze initiation in polymer glasses. Effects of different modification on the structure of the chain network and primary network on the craze initiation will be presented based on the update model, as well. Chapter III is the extension of this model for the two-phase rubber-toughened systems. By

studying three rubber-toughened polymer glasses we will propose new mechanism of rubber-toughening. In Chapter IV, by increasing the density of chain networking in the direction of stretching, for the first time, we will be able to measure the birefringence values during the post-yield deformation of PMMA and PS, and compare them with those of isotropic brittle PMMA and PS at the pre-yield region. This chapter is an attempt to correlate between birefringence and mechanical data in large deformation of polymer glasses and achieve a molecular-level understanding from the deformation of these materials.

CHAPTER II

CRAZING AND YIELDING IN GLASSY POLYMERS OF HIGH MOLECULAR WEIGHTH

2.1 Introduction

Polymers are a unique class of modern materials. Despite their light mass density, their mechanical properties are strong enough for a variety of applications either through crystallization or vitrification to achieve sufficient rigidity. However, high Young's modulus is not the only necessary characteristic. Desirably, polymeric materials should be ductile, for example, tolerating considerable bending. Ductile (at room temperature) polymers include several semicrystalline polymers with low glass transition temperatures, e.g., polyethylene (PE) and polypropylene (PP) as well as some amorphous glassy polymers such as bisphenol A polycarbonate (bpA-PC) and polyethylene terephthalate (PET). Other glassy polymers such as polystyrene (PS) and poly(methyl methacrylate) (PMMA) are brittle under ambient conditions. For decades mechanical behavior of polymers is an important research topic in polymer science. In the remaining of this Introduction, we survey the widely accepted ideas in the existing literature regarding ductility and crazing in glassy polymers.

2.1.1 Concerning Brittle-Ductile Transition in Glassy Polymers

The Ludwig[13]–Davidenkov[14]–Orowan[15] hypothesis has usually been regarded as the standard way [16] to rationalize the brittle-ductile transition (BDT) in uniaxial extension of glassy polymers. The popular application of the LDO hypothesis to explain the BDT is presumably rooted in the speculation that brittle fracture is caused by chain scission. Treating brittle fracture and yielding as two independent and competing processes, the logic of the LDO hypothesis is the following. Regarding the ductility observed above BDT, the argument of the LDO hypothesis is that if a polymer could not break (because it would involve a much higher stress) it would yield. This line of reasoning clearly did not address what causes yielding, nor did it explain why breaking could not happen above BDT. Upon some deliberation, it is not difficult to realize that the opposite logic can be more reasonable in absence of a molecular model: if a glassy polymer can yield it would do so, saving it from breaking. Thus, the important question to ask is when, how and why a given polymer can yield and undergo plastic deformation, i.e., being ductile. To properly answer this question, it is necessary to ask the opposite: when and why a polymer ceases to be ductile, i.e., losing its ability to yield and turning brittle at lower temperatures. The LDO hypothesis does not address these questions. Below the BDT temperature T_{BD}, the LDO hypothesis states that the yield stress would be higher than the breaking stress instead of addressing why yielding can no longer prevail. Based on finite-element calculations of a constitutive model the strain softening and hardening characteristics in uniaxial compression were proposed [17] to be the predictor of a polymer glass' ability to yield and avoid brittle fracture. This study interprets brittle fracture as due to unstable necking. Unfortunately, such a

correlation does not address molecular causation; any counter example would be sufficient to invalidate this approach. However, because of the extensive past research [16], [18-20], [10], it may now be less challenging to develop a chain-level phenomenological account.

According to the Eyring [21] type theory [22-23] for yielding of polymer glasses, the stress arising from the imposed deformation can lower the barrier height for activation and speed up the segmental relaxation dynamics until the alpha time matches the reciprocal deformation rate. Here, alpha time refers to the time scale in which the cooperative motions at the segmental level result in scape of the central segment from its cage formed by surrounding segments[19]. Unfortunately, the Eyring mechanism cannot inform us when a glassy polymer becomes incapable of yielding. In other words, the Eyring idea does not permit us to deal with the phenomenon of BDT. A different level of theory must be made to describe where the activating molecular force arises from, i.e., what structure is required to deliver the stress in the Eyring picture of activation. In a recent publication [10] we proposed a phenomenological model to supply such a missing description. It was asserted that the structure transmitting the molecular force to cause activation was chain networking due to the intermolecular uncrossability. This model depicts a plausible scenario to explain why a ductile glassy polymer turns brittle across a narrow temperature range. A glassy polymer can no longer yield below a critical temperature when the chain network can no longer remain structurally intact under large deformation including compression [24-25]. A glassy polymer does not prefer brittle fracture to yielding below the BDT. Conversely, the polymer yields above the BDT because it is possible to become activated: For example, bpA-PC is ductile and yields at room temperature because the external extension can cause

the system to become activated by the chain network. No first principles theory is available to predict that PS cannot be ductile at room temperature. In other words, it is so far unknown how the energy landscape [26-29] varies from one polymer to another, i.e., how it depends on the specific chemical structures of the monomers and on the intermolecular interactions. Until a theoretical description is developed to quantify the degree of vitrification in terms of the energy landscape or other pertinent variables, we simply cannot explain why at room temperature PMMA hardly shows any crazing on its path to brittle fracture, bpA-PC is free of crazing and ductile, and PS develops massive crazing before brittle fracture.

2.1.2 Previous Understanding on Crazing

Crazing is an important topic, closely related to the phenomena of brittle fracture and yielding and thus faces the same challenge that eluded many past attempts to explore the nature of the BDT. Typically, crazing refers to the emergence of openings (many microns in size) populating a glassy polymer under tensile extension [30]. Similar to the BDT, there is usually also a crazing-yielding transition (CYT) across a narrow range of temperature. The past efforts focus on how crazing occurs and attempts to explain why crazing is prevalent in glassy polymers such as PS but rarely observed in the bpA-PC at room temperature. The existing explanation on crazing also resorts to the logic of the LDO hypothesis [16]. The bpA-PC has higher chain entanglement density, with $\nu_e \sim 1/M_e \sim p^{-3}$, M_e and p being respectively the entanglement molecular weight and packing length. Thus, the crazing stress S via chain scission could be higher than the yield stress σ_y. Therefore,

the bpA-PC cannot craze and instead undergoes shear-yielding at room temperature [30]. Based on a comparison between *S* and σ_y, the same LDO type logic has been applied to explain why annealing that promotes physical aging and increases the yield stress can cause a ductile polymer such as bpA-PC to switch from shear yielding to crazing: "Armed with this reasoning, it also becomes clear why the appearance of shear deformation zones tends to be suppressed in favor of crazing if the polymer is annealed below its T_g. The annealing has no effect on the various crazing parameters, but it is well known for polymers such as PC that such a heat treatment increases the yield stress" [30].

In summary, past extensive studies, summarized in Ref. [30], aimed to relate certain crazing characteristics to different variables including entanglement density, molecular weight, temperature and rate of extension. The pioneering understanding achieved in Ref. [30] has remained as the available guideline. For example, the basic idea was later applied to crazing in semicrystalline polymers [31-34]. There have also been research activities on the craze initiation. According to Bucknall [35], crazing is frustrated failure initiated by the impurities. The standard evaluation of the stress condition for crazing needed to be revised to incorporate the effect of impurities that cause higher local stress. Argon emphasized the molecular structural flaws as the trigger for plastic and cavitation events [36].

2.1.3 Our Current View on Crazing

Yielding and subsequent significant drawability of glassy polymers are unique among the modern materials such as polymers, ceramics, and metals (metallic glasses). It occurs when the chain network can cause the vitreous state to activate so that polymer segments acquire sufficient mobility to match the external deformation rate. The chain network can

break down locally to result in crazing during extension before the polymer reaches the state of activation. The network failure leading to brittle fracture was argued [37] to involve chain pullout rather than chain scission, based on the experimental observations [38] that PS turns completely ductile at room temperature upon sufficient hydrostatic pressurization.

In the past, crazing is regarded as displaying internal necking [30]. Since crazing typically occurs prior to the yield point, such crazing clearly has nothing in common with the macroscopic necking that involves post-yield plastic deformation in an activated state. Crazing occurs not because chain scission can occur more readily, i.e., at a stress lower than the yield stress. Instead, it indicates that a glassy polymer cannot attain adequate activation to undergo global yielding; high chain tension builds up, resulting in chain pullout from the chain network [10]. The word "activation" here refers to the state of increased segmental mobility.

As we will demonstrate in Section 2.2, the chain network has the same structure and areal density among all linear flexible polymers. Therefore, the ability of the chain network to bring about activation depends on the energy landscape on which the glassy polymer situates. Apparently, room temperature is too low for PS to attain activation before the chain network fails through chain pullout. The crazing is the symptom of the localized failure of the chain network [37]. The bpA-PC does not undergo crazing while PS does because yielding can take place in bpA-PC at room temperature, not because crazing in bpA-PC would involve a higher stress than in PS. As indicated in the end of a preceding paragraph, we cannot explain why PS undergoes massive crazing and bpA-PC does not,

given the fact that their chain networks have comparable structures, as shown in Section 2.2.

It is reasonable to accept that presence of impurities or inherent structural heterogeneities can shift the CYT. However, Argon and Hannoosh [4] noted that crazing still occurred in PS at room temperature even when dusts and surfaces flaws were minimalized. This result indicates that crazing in PS may be due to inherent structural or/and dynamic heterogeneities. On the other hand, in absence of any impurities that can lead to premature failure of the chain network, both BDT and CYT would still be expected to take place albeit at lower temperatures.

2.1.4 Organization of This Chapter

The bulk of this chapter is devoted to describing how the various internal and external parameters promote or demote yielding to influence the crazing behavior. By various kinds of manipulations, a glassy polymer can either avoid localized network failure or develop greater propensity for crazing. Specifically, we will investigate the effects of melt stretching, physical aging, mechanical rejuvenation, solvent uptake on crazing at various temperatures, guided by the idea that the chain network can be affected to influence the ability for a glassy polymer to undergo yielding and plastic deformation. The molecular picture emergent from our observations and analyses may be used to anticipate in the future to explain when and why crazing takes place in various glassy polymers. This chapter is organized as follows. In Section 2.2, we contrast the conventional account of crazing with an alternative account. Here we propose a crucial revision of our previous model[10] regarding how to evaluate the structure of the chain network as the enabler for activation

and yielding in glassy polymers. According to the new analysis, we cannot predict that PS should undergo crazing and bpA-PC should be ductile and free of crazing at room temperature. Following a standard experimental section 2.3, various experiments motivated by the new understanding are presented in Section 2.4, along with further discussion Section 2.5 of the implications in relation to the past accounts of crazing. Section 2.6 contains a summary of this work that focuses on understanding why crazing takes place instead of how it occurs, which is a more complicated question and has been explored in numerous past studies as summarized in Ref. [30].

2.2 Theoretical Picture Concerning Molecular Mechanism of Crazing

2.2.1 Past Arguments

Entanglement is commonly used in the literature of crazing to correlate with the structure of the fibrils in crazes. Moreover, areal density of entanglement strands ψ_{ent} has been introduced to formulate the expression for the surface energy Γ associated with the crazing process. Such argument was motivated by the fact that the bpA-PC resists crazing at room temperature. Then the stress for crazing S is shown [30] to depend on Γ as $S \sim \Gamma^{½}$. For polymers of sufficiently high molecular weight, S is independent of molecular weight. Throughout this chapter, by "high molecular weight" we mean that chains are sufficiently long to form a robust chain network due to the interchain uncrossability. It is therefore asserted that crazes forms via chain scission [30] because crazing via chain pullout would be molecular weight dependent. According to Donald [30], Γ is linearly proportional to the areal density $\psi_{ent} \sim p^{-2}$ and is thus high for bpA-PC because bpA-PC has much smaller value for

p than that of PS. Thus, bpA-PC would not show crazing, unlike PS. In summary, by noting the difference in the entanglement density between different polymers, the past description of crazing concludes that the structure of the entanglement network would determine whether a glassy polymer would exhibit crazing or not. Since PS and PMMA have comparable ψ_{ent} and yet PMMA shows little crazing at room temperature, it has been challenging to rationalize the difference.

2.2.2 Revised Analysis – a Correction for Ref. [10]

Alternatively, the structural characteristic of the chain network may be defined in terms of the coil size l_{LBS} of load-bearing strands (LBSs) between adjacent network junctions. In our previous explanation [10] concerning why the chain network can fail, leading to crazing and brittle fracture, the pertinent structural quantity is the areal density ψ of LBSs, not volume density of any sort. The concept of the areal density is also necessary to account for the structural anisotropy produced by melt stretching. It is straightforward to show [10] that in the undeformed state ψ depends on l_{LBS} and p as

$$\psi = 1/pl_{LBS}. \quad (1)$$

where for simplicity we take the prefactor to be unity.

Treating the load-bearing strands to be the entanglement strands of coil size l_{ent}, the past analysis of crazing invoked $\psi_{ent} = 1/pl_{ent}$ to quantify the network structure [30]. Our previous description [10] asserted that l_{LBS} in Eq. (1) is proportional to the Kuhn length l_K instead of l_{ent}. In other words, instead of $\psi_{ent} \sim 1/p^2$, the chain network structure is characterized by $\psi = 1/pl_K \sim 1/p$. Unfortunately, the earlier discussion [10] erroneously argued that bpA-PC

was ductile and PS was brittle at room temperature because bpA-PC has a smaller value for p and thus larger ψ.

It is actually important to show that only a fraction of covalent bonds at any cross-section belong to load-bearing strands. To quantify, let us evaluate how close each chemical bond is next to its surrounding bonds in terms of its areal density ϕ. A Gaussian chain of n bonds of length l (with corresponding molecular weight M) has a physical volume v_M

$$v_M = (M/\rho N_a) = pR^2 = nv_1, \quad (2)$$

where ρ is mass density of the polymer, N_a is the Avogadro constant, R is the mean end-to-end distance, and v_1 denotes the physical volume of each bond, given by

$$v_1 = p(C_\infty l^2), \quad (3)$$

with C_∞ being the characteristic ratio. Treating the bond is a cylinder of length l and cross-section $s = (v_1/l)$, we can express ϕ as

$$\phi = 1/(v_1/l) = 1/pl_K, \quad (4)$$

where we have Kuhn length $l_K = C_\infty l$ as a good approximation for most linear flexible polymers. As shown in Figure 2.1(a), roughly each bond occupies as an area of $s = pl_K$. In contrast, as shown in Figure 2.1(b), the areal density ψ of LBSs (denoted by the solid circles) is smaller than ϕ by a factor of $1/\theta$

$$\theta = \frac{\psi}{\phi} = (l_K/l_{LBS}) < 1. \quad (5)$$

When evaluating the effectiveness of the chain network to cause yielding, it is more reasonable to describe its areal density ψ in reference to ϕ. In other words, the efficacy of

Gaussian chain networks to cause activation and plastic deformation should be quantified by θ of Eq. (5), not ψ of Eq. (1).

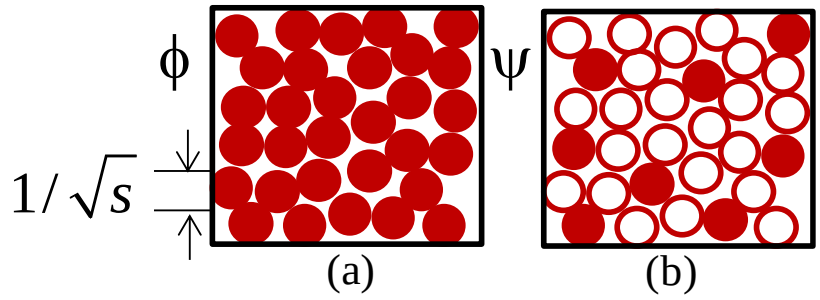

Figure 2.1 Schematic representations of the areal densities (a) ϕ and (b) ψ, depicting respectively the inherent bond density (determined by the cross-section of the molecular bonds) and that of a chain network.

To evaluate θ of Eq. (1), there are three scenarios to consider, regarding how l_{LBS} varies with different molecular parameters such as l_K and p. (A) If we envision the network formation to involve pairing of hairpins as shown Figure 2.2(a), then it followed [10] that the value of l_{LBS} merely depended on the chain flexibility, i.e., linearly proportional to l_K for all linear flexible polymers. In this case, the relative network density given by θ in Eq. (5) is a universal constant, hardly dependent on chemical structural differences among common glassy polymers such as bpA-PC, PMMA and PS. (B) Since the hairpin pairing involves multiple chains and the number of strands in the pervaded volume of a strand of size l_{LBS} is proportional to l_{LBS}/p, it is plausible that a polymer with larger p requires a longer l_{LBS}. In this case, θ would be a decreasing function of p. (C) If the structural characteristics of the network would be described in terms of the packing model [12, 39] so that $l_{LBS} \sim l_{ent} \sim p$, as illustrated in Figure 2.2(b) and θ would vary among different polymers

as $\theta \sim 1/p$. Polymers with smaller p (e.g., polyethylene and bpA-PC) would have denser networks. Available experimental data indicate [10] that the breaking stress σ_B at the BDT scales with p as $1/p$ instead of p^{-2}, i.e., $\sigma_B \sim \psi$, implying that l_{LBS} in Eq. (1) does not scale with p and $l_{LBS} \sim l_K$ gives the correct description of the network structure. Thus, it seems that scenarios B and C could be ruled out.

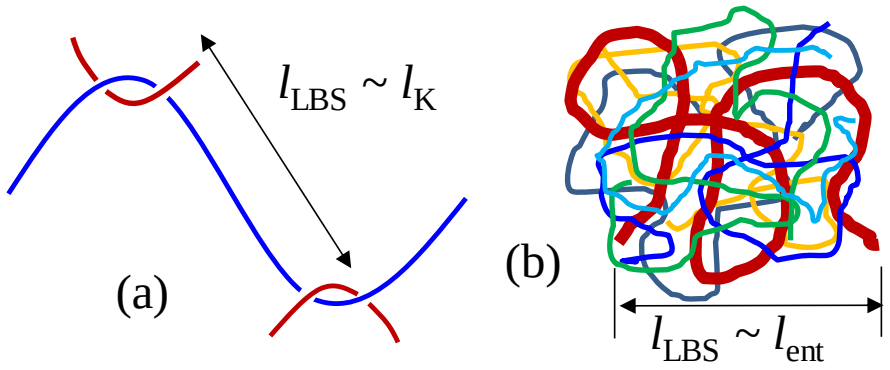

Figure 2.2 (a) Chain networking due to uncrossability, leading to formations of pairs of hairpins and (b) network according to the packing model that envisions a minimal chain length as the mesh size or entanglement strand with end-to-end distance l_{ent}.

One remark is in order here. In our analysis, the parameter θ of Eq. (5) quantifies the role of the chain networking among various polymers of linear chains. Since $l_{LBS} \sim l_K$ among various common linear flexible polymers we have θ = constant. In contrast, according to the past account [30], whether crazing occurs or not was argued to depend on the entanglement areal density ψ_{ent} that varies very strongly from one polymer to another since p can be rather different for different polymers. For example, p = 3.95 and 1.05 Å for PS and bpA-PC respectively, implying a difference of 14 in terms of ψ_{ent}. According to a previous report [40], relatively mild melt stretching can affect the ductility of PS and bpA-

PC in opposite directions at room temperature, e.g., making the brittle PS ductile and ductile PC brittle (when drawing respectively either parallel or perpendicular to the melt stretching direction). Thus, it appears implausible that ν_e is the pertaining parameter in the account for the molecular origin of polymer ductility in the glassy state.

To reiterate, the previous analysis of the model for yielding and BDT incorrectly concluded that because ψ is higher for bpA-PC than for PS, bpA-PC is more ductile [10]. In the present revised analysis, it is the fraction θ of Eq. (5) that characterizes the structure of the chain network. For glass polymers with comparable θ, their ductility rests squarely on where they situate in their energy landscapes. Apparently, the chain network can more readily bring bpA-PC out of its energy minimum at room temperature to attain activation whereas the same does not occur for PMMA and PS.

2.2.3 Crazing vs. Yielding

Thus, we cannot explain why the bpA-PC shows no crazing while PS does at room temperature until we have a better understanding of the nature of the glassy state. In the isotropic state, Gaussian chains in a glassy polymer are coiled up so that the network areal density ψ is significant smaller than ϕ. Consequently, the external drawing along z axis does not cause all segments to displace along z direction in an isotropic polymer glass. Failing to yield, crazing and brittle fracture are inevitable. In fact, the question of whether or when crazing or fracture would occur is the same as the question of whether the chain network would fail locally or macroscopically. Whether a chain network would fail or not depends on whether external extension would build up high chain tension to cause chain

pullout. Such pullout can induce localized failure of the chain network whose structure is characterized by Eq. (1). In absence of the chain network to mobilize the glassy state, the alpha relaxation would remain much slower than the rate of external deformation, and plastic deformation would not occur. Conversely, at a high enough temperature, the network can be robust enough to cause yielding through molecular activation of a majority of dormant segments. The mobilized state allows the imposed extension to conserve volume. In other words, upon activation, the system is able to undergo transverse contraction during uniaxial drawing.

In summary, in most cases, according to our account, crazing would not occur if the chain network is able to produce yielding via sufficient segmental activation. When the temperature is too low, yielding cannot occur because the polymer network is unable to bring about sufficient mobility before high chain tension arises. Chain pullout leads to local failures of the network, resulting in so called crazing. Thus, one strategy to suppress crazing is to make the chain network more effective in driving the system out of the glassy state. Since crazing plausibly involves chain pullout in glassy state, it is an activation process and thus requires a finite induction time t_{icraze}. When the induction time t_{icraze} for crazing is shorter than the deformation time required to arrive at the yield point, crazing can occur, as observed in drawing of the bpA-PC at elevated temperatures in Section 2.4.2. Shorter t_{icraze} can also plausibly be brought about by structural heterogeneities, either inherent or external (e.g., due to impurities), which can produce local stress concentration to induce a localized failure of the chain network.

2.3 Experimental

2.3.1 Materials and Methods

Five types of polymer glasses, poly(methyl methacrylate) (PMMA), polystyrene (PS), bisphenol A polycarbonate (bpA-PC), amorphous form of poly(L-lactic acid) (aPLLA) and high impact polystyrene (HIPS) are involved in this project. All the samples sources and characterizations are listed in Table 2.1.

Table 2.1 Sample sources and their structural characteristics

Polymer	Producer	M_w (kg/mol)	M_e (kg/mol)	PDI	T_g (°C)
PMMA	Arkema (ALTUGLAS®)	105	13	1.91	114
PS	Dow Chemical (Styron 663)	319	13	1.44	105
bpA-PC	SABIC (Lexan™ Resin)	63	1.33	1.58	145
PLLA	Nature works (3100HP)	115	3.24	1.63	60
HIPS	CHI MEI (PH-888G)	-	-	-	-

Effects of temperature, physical aging, mechanical rejuvenation, plasticizer, contamination, and melt/cold deformation on crazing characteristics are explored to study the consequences of changes in intermolecular packing that forms a primary structure and chain network.

2.3.1.1 Physical Aging

In order to achieve heavy physical aging, pre-melt-stretched amorphous PLLA was annealed at 40-45°C for 24 hrs. Physical aging of mechanically rejuvenated bpA-PC

samples by twisting and milling was performed by keeping the samples at 105 °C for 24 hr.

2.3.1.2 Solvent Effect

Sebum oil (the oil secreted by the human skin) and triphenyl phosphate (TPP) from TCI America (product code P0272) were used to study the effect of presence of small molecules on the craze formation. To smear the surface of polymer by sebum oil, the sample (bpA-PC) whipped out by oily hand. In another attempt TPP in 4 wt% was mixed into the bulk of PMMA using a Brabender Mixer (type 30 EHT). The detailed condition for mixing can be find in our previous paper [41].

2.3.1.3 Mechanical Rejuvenation

Two methods including twisting and milling are used to induce mechanical "rejuvenation". To have mechanical treatment of twisting, bpA-PC specimens are made of cylindrical filament from capillary extrusion at 216 ^{o}C under a constant stress of 5 psi. They have an effective length L of 10 mm and diameter, with two ends having a larger diameter to ensure proper gripping during twisting. For twisting, the cylindrical specimen was mounted onto a homemade rotational device, the setup holds one end of the sample fixed and turning the other by two full clockwise rotations (720 degree) at a rotational rate of 0.75 RPM before returning to the original position by two full counter clock-wise rotations. Such a twist involves a maximum shear deformation given by $\gamma_{max} = 2\pi D/(H)$, on the outer surface of the cylindrical sample. Given D = 2 mm, H = 10 mm, we have γ_{max} = 1.26. This is a moderate amount of mechanical "rejuvenation" that should not alter the

structure of the chain network and yet sufficient to elevate the energy landscape according to the computer simulation [42]. For preparing milling samples, large sheets of bpA-PC with dimensions of 100 mm x 100 mm x 2.0 mm (length by width by thickness) for milling were press-molded at 180 °C for one hour. After taking out from the press, they cool down naturally to room temperature before subjecting to milling. The milling process involves a thickness reduction of 0.1 mm each time by passing the samples through two counter-rotating cylinders of diameter of 15 cm. In this way, different milling degrees could be easily achieved. The final degree of milling is characterized by the elongation ratio $\lambda_{mill} = L/L_0$, where L_0 is the initial length of the sample, and the thickness shrinks by $1/\lambda_{mill}$. Before testing, these milled samples were cut into dog-bone shape by a dog-bone cutter (ASTM D-412D), which has a length of 39 mm in the middle section.

2.3.1.4 Melt Stretching

Small dog-bone shape PS and HIPS samples (10 mm × 3 mm × 1 mm, length × width × thickness) were press-molded using Carver™ Lab Press at 180 °C under a load of 9000 kg for 30 min to let polymer chains fully relax before unloading. Subsequently, samples undergone melt stretching at 120°C and Hencky rate of 0.113 s^{-1} to stretching ratios of $\lambda_{ms} = 3$ and $\lambda_{ms} = 4$, respectively for PS and HIPS, using the home-made environmental temperature control chamber and Instron 5969. Samples quenched using icy water to preserve melt-stretching effect. Same mold, i.e. dog-bone (middle dimension of 10mm × 3 mm × 1 mm) used to prepare aPLLA by quick molding at 200°C and fast quenching into the room temperature water to get fully amorphous material as confirmed by WAXS.

Subsequently, undergone melt-stretching at 70 °C and Hencky rate of 0.028 s^{-1} to $\lambda_{ms} = 3$ and then quenched by icy water to preserve effect of melt-stretching. Melt-stretched bpA-PC samples were prepared as follows: dog-bone shaped samples with the middle part of 60 mm × 35 mm × 0.50 mm and two end portions of 30 mm × 60 mm × 0.50 mm were prepared by molding the bpA-PC resin into a home-made mold. A vacuum molding press (TMP inc. Cleveland, OH) was used at 200 °C to make the specimens. The final applied load was 9000 kg. Such dog-bone shaped samples were subjected to melt-stretching at 155 °C and Hencky rate of 0.07 s^{-1} to the stretching ratio of $\lambda_{ms} = 2$. These melt-stretched bpA-PC specimens were cut into a dog-bone shape along the direction transverse to the melt stretching direction using a die cutter (ASTM D-638-V, Dewes Gumbs, Die, Co.), so that we can study the adverse effect of melt stretching on craze formation in perpendicular direction to the melt stretching direction. Melt stretching of PMMA dog-bone sample of 20 mm × 9 mm × 1.6 mm was done at 130 °C and Hencky rate of 0.05 s^{-1} to the stretching ratio of $\lambda_{ms} = 3$. Sample immediately quench into the glassy state to study the effect of melt deformation on the craze formation in the parallel direction with the melt-stretching direction. Figure 2.3 shows the engineering stress σ_{engr} vs stretching ratio λ for melt-stretched samples.

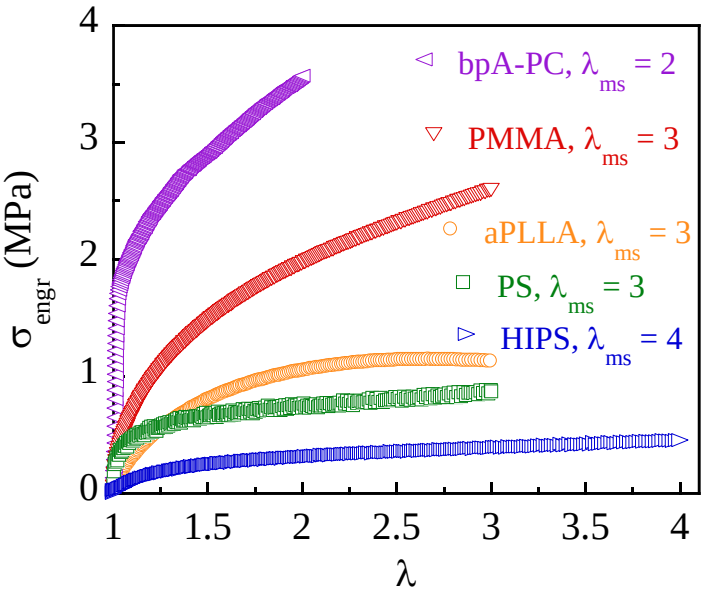

Figure 2.3 Engineering stress σ_{engr} vs stretching ratio λ from melt stretching of bpA-PC, PMMA, aPLLA, PS and HIPS. The detailed condition for melt stretching of each sample has been indicated in the section 2.3.4.

2.3.2 Apparatus

Tensile experiments of polymer glasses were done using Instron 5969 with a home-made environmental temperature control chamber. Creep tests were carried out by following a two-step procedure. In the first step, a constant rate was applied to first deform the sample to the prescribed stress level. In the second step, we switch the machine to the stress-control mode to hold the desired stress for at least one hour. After creeping, the samples were examined under optical microscope (Zeiss standard 25 Transmitted Light Microscope with and a Sony DFW-V500 digital color camera) to observe the generated crazes. For all the microscopic photos, the tensile direction is horizontal, unless specified otherwise. For some cases linearly-polarized plates were used in conjunction with

microscope to assess the amount of developed plastic deformation in the samples. Photos of crazing inserted in the various figures were obtained after tests, e.g., at the end of the creep experiments, presented in Figures 2.4, 2.5, 2.6, 2.15, 2.16(b), and 2.19, and at the end of displacement-controlled drawing, presented in Figures 2.11, 2.12, 2.17, 2.18 and 2.20. For in situ observation of craze formation during stress relaxation, a 2X objective lens is connected to a CCD camera (Everfocus-EQ120) through a tube-shaped adapter to achieve tele-microscopic video recording.

2.4 Results and Discussion

To make crazing appear or disappear, we will impose various conditions in order to explore the cause of crazing. These experiments are guided by the proposal that crazing is a result of localized failure in the chain network and occurs either when the glassy state is too vitreous to undergo yielding or defects of known or unknown origins create local stress concentrations to allow localized failures of the chain network. During extension of a glassy polymer, a load-bearing strand (LBS) can pull out from the chain network when chain tension exceeds a threshold determined by the intersegmental interactions at the network junction [10]. When many such pullout events take place, a structural breakdown can ensue. The buildup of chain tension depends on how dormant the glassy surroundings are. Over time, a certain level of chain tension can result in force imbalance to trigger chain pullout. It will take a longer time for crazes to form when chain tension is lower.

2.4.1 Crazing Over Time As an Activated Process

Crazing may not necessarily occur if fast tensile extension produces either yielding or brittle fracture in a glassy polymer on the time scale of either t_y or t_{bf} that is shorter than t_{icraze}. Here t_y is related to the yield strain ε_y as $t_y = \varepsilon_y / \dot{\varepsilon}$, thus dependent on the Hencky rate $\dot{\varepsilon}$. Alternatively, for a constant crosshead speed V and initial length L_0, $t_y = (L_0/V)[(L/L_0)_y - 1]$, where (L/L_0) is the draw ratio at the yield point. Ductile polymer typically undergoes yielding and plastic deformation without showing crazing, as is the case for the bpA-PC at room temperature. If yielding takes place before emergence of crazes, crazing would be absent. Conversely, crazing can occur even above the BDT, followed by yielding as demonstrated in 2.4.2.

It is also possible for brittle fracture to occur before crazing emerges, as is the case for PMMA at room temperature. In other words, PMMA typically does not exhibit noticeable crazing at room temperature presumably because $t_{icraze} > t_{bf}$. As activated events, delayed crazing, may also take place during the stress relaxation from stepwise extension that has not reached the point of brittle fracture. This behavior will be studied in subsequent 2.4.3.

Since the different reasons for bpA-PC and PMMA not to show crazing at room temperature in the strain-controlled mode are clear, due to the condition of $t_{icraze} > t_y$ and t_{bf} respectively, we can devise two protocols to investigate when these glassy polymers show crazing. This subsection presents the results that involve the two means to promote crazing. In the first case, the extension is imposed in the stress-controlled mode, i.e., creep mode that can avoid brittle fracture. Any observations of crazing during creep would suggest that crazing needs to be understood as an activated process [43] and can occur with little ongoing

deformation. In the second case, these two polymers are examined at elevated temperatures. Here the appearance of crazing would imply that t_{icraze} is sufficiently short in comparison to the elapsing time to reach the point of yielding, i.e., $t_{icraze} < t_y$.

2.4.1.1 Creep

Continuous straining in strain-controlled mode would surely either result in brittle failure or yielding because the overall external deformation would increase with time without bound. In contrast, when the applied stress is low enough in creep mode, the deformation may not proceed to the point of fracture over a long time, allowing crazes to form that would not be observable in the strain-controlled drawing.

Specifically, while PS readily shows crazing during strain-controlled drawing, PMMA rarely displays any observable crazing at room temperature until brittle fracture. The difference between PS and PMMA perhaps implies that localized chain pullout leading to crazing requires a longer t_{icraze} for PMMA. We subject PMMA to tensile extension in creep mode at appropriately chosen stresses to offer PMMA a sufficiently long induction time for crazing while avoiding macroscopic fracture. Crazing indeed emerges during creep as shown in Figure 2.4(a)-(b). Moreover, PMMA reaches considerably higher strain in creep before breaking at $L/L_0 = 1.13$. There is evidence from the non-vanishing residual birefringence that a certain level of irrecoverable deformation has occurred during the creep.

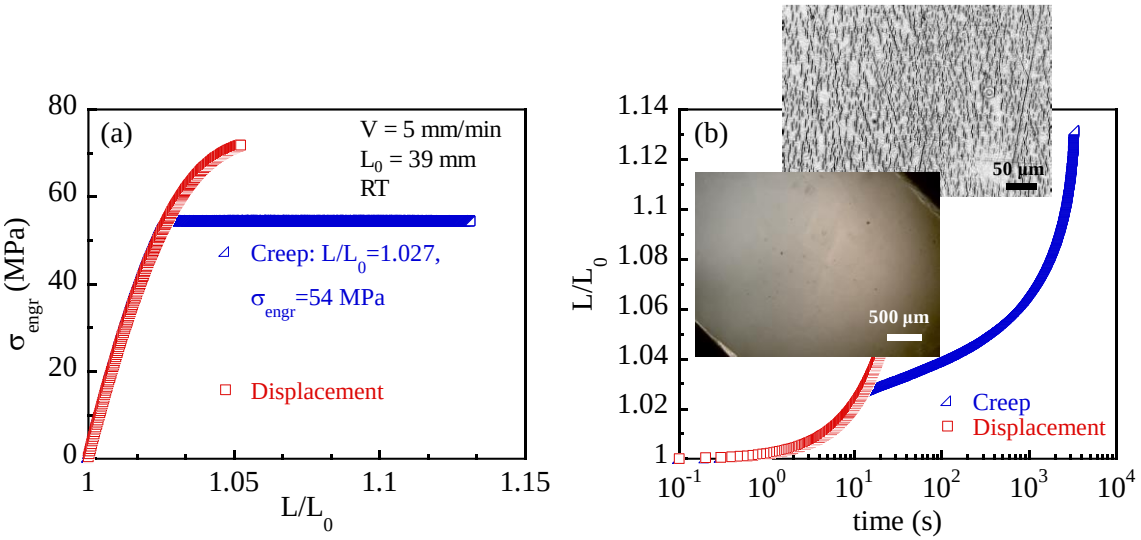

Figure 2.4 (a) Engineering stress σ_{engr} vs. draw ratio L/L_0 from extension of PMMA in the displacement (squares) and creep (triangles) modes at room temperature (RT), where creep is accomplished by switching from the displacement to creep mode after the displacement has resulted in σ_{engr} = 54 MPa at L/L_0 = 1.027. (b) Corresponding tensile creep in terms of L/L_0 as a function of time. Inset images respectively show the appearance of uniform crazes throughout the sample (the drawing direction being horizontal) and residual birefringence at the end of creep (appreciable light transmission for the sample sandwiched by two cross-polarizers) where the drawing direction for this photo is diagonal along the sample's length.

Unlike PMMA, the bpA-PC shows no crazing during creep at room temperature. However, when the test temperature rises significantly above room temperature, creep of the bpA-PC does result in crazing as shown in Figure 2.5(a)-(b). This suggests that t_{icraze} has become sufficiently shorter at the elevated temperature. When temperature is raised to shorten t_{icraze} the condition of $t_{icraze} > t_y$ can be reversed so that crazing could show up even in rate-controlled mode (photos omitted). Uniform crazes throughout the sample initially

appear during creep at 120 °C. At long times, shear yielding takes place, resulting in necking and rapid strain increase at around 600 s. This experiment shows that given a sufficient time macroscopic activation along with plastic deformation can take place at a significantly lower stress than the yield stress identified in the strain-controlled mode to be over 31 MPa as shown in by squares in Figure 2.5(a).

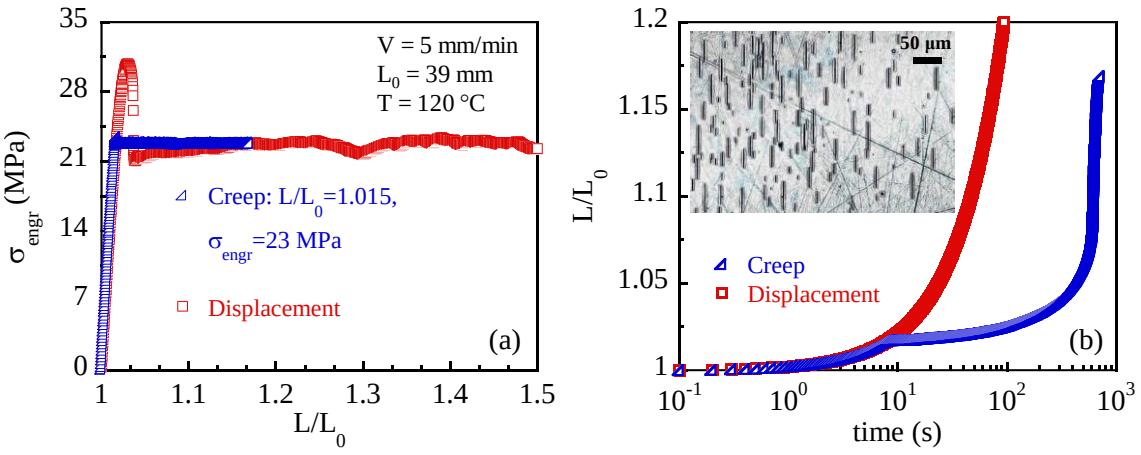

Figure 2.5 (a) Engineering stress σ_{engr} vs. draw ratio L/L_0 from extension of bpA-PC in displacement (squares) and creep (triangles) modes at 120 °C. (b) Corresponding tensile creep in terms of L/L_0 as a function of time, first drawn to $L/L_0 = 1.015$ in the displacement model to reach $\sigma_{engr} = 23$ MPa. The inset image shows the appearance of crazes in un-necked part of the sample at the end of the creep.

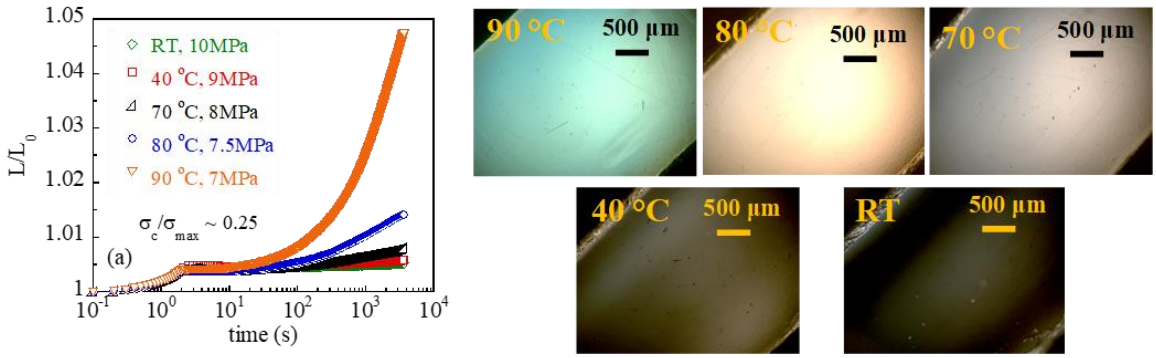

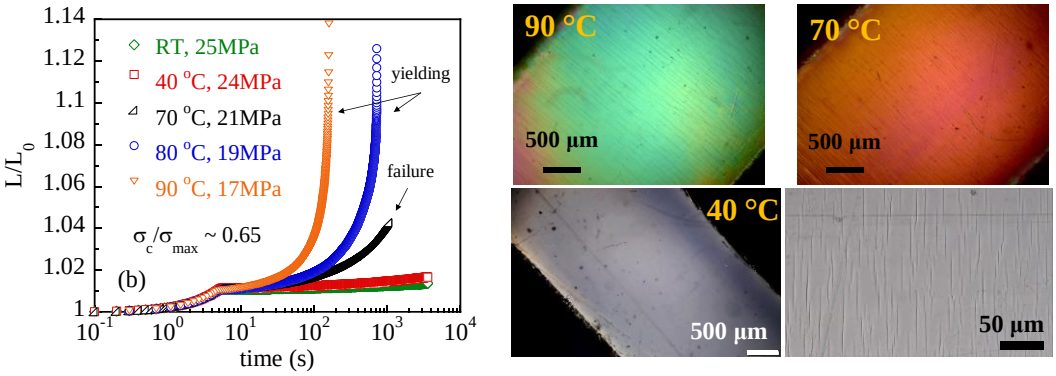

Figure 2.6 Creep behavior and resulting birefringence of PS at temperatures from ambient to 90 °C, where the applied engineering stress is (a) a quarter of and (b) two thirds of the engineering stress maximum $\sigma_{engr(max)}$ measured in displacement-controlled drawing. There are no crazes in (a) where the photos show increasing residual birefringence, measured ex situ at the end of creep. Under the condition of (b), crazing occurs at all the temperatures. At 80 and 90 °C, PS undergoes shear yielding and necking in the presence of crazes that form prior to yielding (corresponding to the rapid increase of the nominal strain). Inset photos show the increasing residual birefringence, including one from the unnecked region at 90 °C as well as two at 40 °C at different magnifications.

The observation in Figure 2.4(b) of non-vanishing birefringence during creep is not unique to PMMA. Figure 2.6(a) shows crazing-free creep of PS at a quarter of the breaking or yield stress (σ_{max}) at different temperatures, along with the residual birefringence that appears to increase with rising temperature. As shown in Figure 2.6(b), at a higher applied stress of $0.65\sigma_{max}$, crazing is evident, along with increasing birefringence (with temperature). PS can actually undergo shear yielding and necking after craze formation at

80 and 90 ^{o}C. Creep tests involving PMMA and bpA-PC reveal similar behavior (omitted here), i.e., irrecoverable birefringence accompanied by crazing and shear yielding at high ratios of σ^*/σ_{max}.

2.4.1.2 Competition Between Crazing and Yielding

The preceding subsections show that depending on the relative values of t_{icraze} to t_y and t_{bf}, crazing may or may not occur. It is instructive to mention a case of crazing different from those discussed above. In a recent study [44], it was demonstrated that PS was ductile at one drawing speed above its BDT temperature but turned brittle at some lower speeds that produced crazing. Specifically, a PS filament from capillary extrusion was ductile (evidenced by shear-yielding initiated necking) at 70 ^{o}C at $V/L_0 = 0.02$ min^{-1} and craze-free because of $t_{icraze} > t_y$. At lower $V/L_0 = 0.001$ min^{-1}, massive crazing occurred so that the tensile stress ceased to increase. In fact, PS turns from ductile (at 0.02 min^{-1}) to brittle (at 0.001 min^{-1}), resulting from the re-entrant crazing. Below we contrast such re-entrant crazing with the crazing in ductile polymers, such as bpA-PC or PMMA at temperatures above the BDT.

2.4.2 Crazing in Ductile Polymers (bpA-PC and PMMA) at Elevated Temperatures

Crazing usually occurs in brittle polymers. There is insufficient literature on crazing in ductile polymers. Both bpA-PC and PMMA, crazing free at room temperature at normal drawing speeds, exhibit crazing behavior at elevated temperatures as shown in Figure 2.7(a)-(b). But such crazing is not followed by brittle fracture. According to the preceding discussion, crazing as an activation process requires a finite t_{icraze}. At higher temperatures t_{icraze} can be expected to be shorter so that the condition of $t_{icraze} < t_y$ can be met. The fact

that crazing occurs has little to do with whether the glassy polymer must be brittle or not. In other words, the phenomenon of crazing above the BDT challenges the conventional explanation that crazing occurs because the polymer is unable to undergo yielding. Figure 2.7(a)-(b) show the cases based on bpA-PC and PMMA that crazing precedes yielding and does not prevent yielding. In passing, we note that crazing in pre-melt-stretched PS is another example of crazing in ductile glassy polymers, to be presented in Section 2.4.6.

At a sufficiently high drawing speed V, it can be expected that crazing has no time to form when $t_y = (L_0/V)[(L/L_0)_y - 1]$ is sufficiently decreased. It was indeed found that when the speed is increased by a factor of 10, i.e., when V = 10 mm/min is applied instead of 1 mm/min to draw PMMA at 80 °C, no crazing occurs because the condition of $t_{icraze} < t_y$(1 mm/min) is no longer met: t_y(10 mm/min) = 0.1t_y(1 mm/min). PMMA undergoes shear yielding and necking, and no crazing occurs in the plastically deforming part.

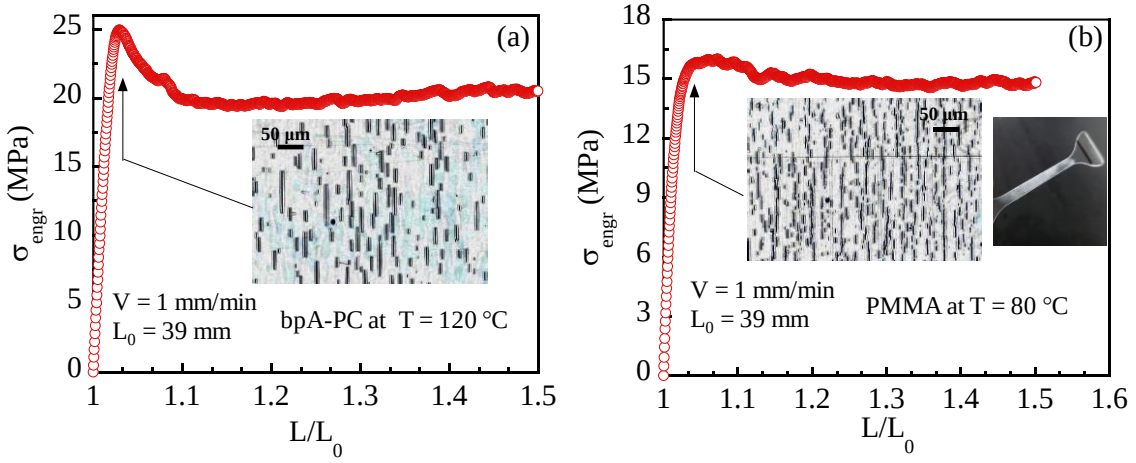

Figure 2.7 Engineering stress σ_{engr} vs draw ratio L/L_0 from extension of (a) bpA-PC at 120 °C and (b) PMMA at 80 °C. The microscopic photos, obtained from repeated runs of these two polymers, terminated at (a) L/L_0 = 1.03 and (b) L/L_0 = 1.04, show the emergence of

crazes in the displacement mode at these elevated temperatures. The other inset photo, taken at the end of the drawing, shows that the crazes survives during the subsequent ductile extension

2.4.3 Emergence of Crazes Without Ongoing Extension

Below the BDT, uniaxial extension can produce a large tensile stress before brittle fracture. We speculate that even if crazing does not emerge during the extension (because of $t_{icraze} > t_{bf}$) it may still show up after cessation of the applied strain. Using tele-microscopic video recording as described in Section 2.3, we can observe in real time the emergence of crazes during the stress relaxation, described in Figure 2.8. The recorded movie confirms that there are no visible crazes at the beginning of the stress relaxation. Over time, crazes appear in increasing numbers and grow in size. Such behavior cannot be explained in terms of the existing understanding that craze widening [30] can only occur during ongoing extension. Actually, this delayed crazing is an indication that crazing must be studied as an activation process, i.e., chain pullout can be activated to result in localized structural collapse in the form of crazes, per discussions presented in Section 2.2.

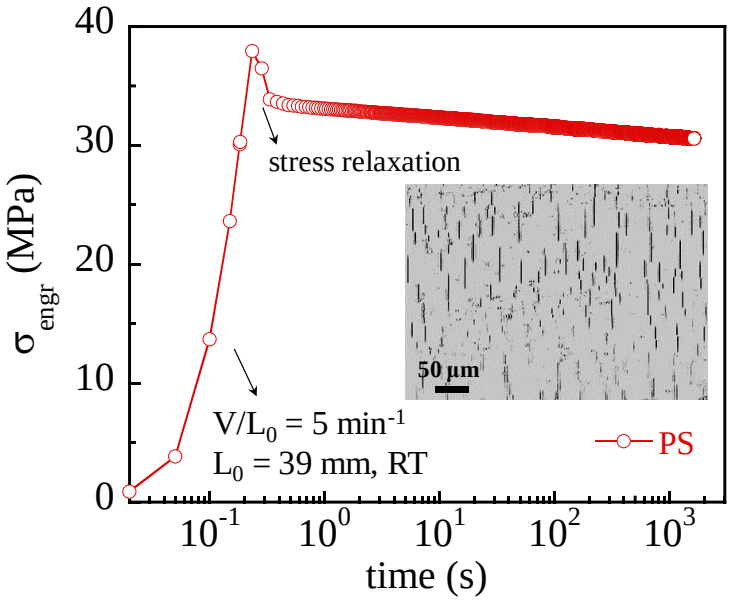

Figure 2.8 Stress growth and relaxation of PS in terms of engineering stress σ_{engr} as a function of time, where the photo in the inset shows the emergence of crazing at the end of the stress relaxation, i.e., 17 min after the cessation of the imposed stepwise extension at $L/L_0 = 1.02$.

2.4.4 Fracture in Absence of Ongoing Deformation

If crazing can emerge in absence of ongoing drawing, it is plausible that macroscopic fracture could also occur during the stress relaxation. Remarkably, this is indeed the case. While freshly prepared amorphous poly(L-lactic acid) (aPLLA) through rapid thermal quenching is ductile, it soon undergoes physical aging at room temperature, turns brittle [45] and displays considerable crazing during drawing (cf. Figure 2.17(a) below). Such a non-fresh sample is labeled as aaPLLA in this chapter. We show that this aaPLLA can undergo macroscopic fracture in absence of any ongoing deformation during stress relaxation. Specifically, we found that crazing emerges after the stress relaxation, during which the

crazes grow in number and broaden in size until the specimen breaks up. Figure 2.9 shows the stress growth associated with the stepwise extension and stress relaxation up to the point of breaking.

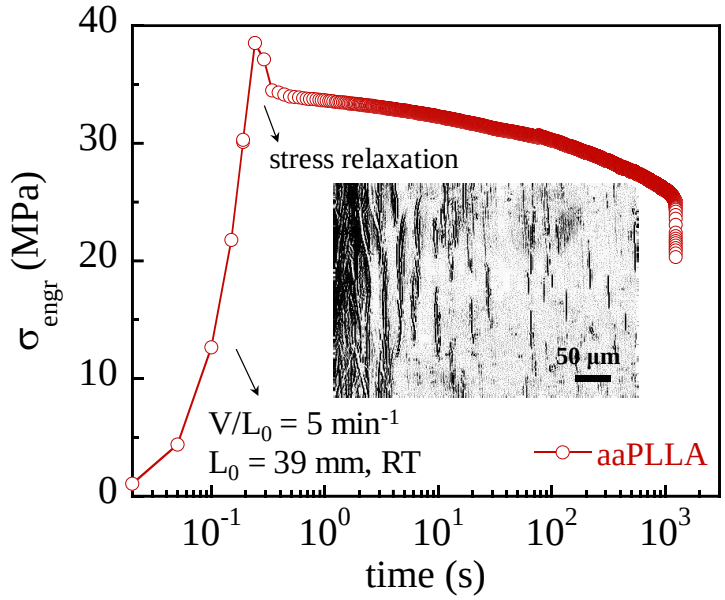

Figure 2.9 Stress growth and relaxation from stepwise extension of aaPLLA to $L/L_0 = 1.02$ in terms of engineering stress σ_{engr} as a function of time. The photo in the inset shows a gradient of increasing craze size as the breaking plane is approach at the left-hand side.

2.4.5 Crazing During Annealing of a Pre-drawn Glassy Polymer

As a further example of crazing in absence of any ongoing extension, we consider the scenario of annealing a pre-drawn polymer such as the bpA-PC. This example is also related to the case of 2.4.2 where crazing takes place in ductile polymers. Can annealing induce crazing in a pre-drawn glassy polymer? Crazing as a localized breakdown of the chain network is due to chain pullout upon the force imbalance. Thus, a sufficiently cold-

drawn polymer can show crazing at some elevated temperatures [46]. Let us consider large cold-drawing (along Z axis) of a glassy polymer such as bpA-PC, at a temperature T_{cd} above the BDT, e.g., T_{cd} being room temperature. We expect relatively high chain tension to be embedded in such a pre-drawn sample. Upon annealing of this pre-deformed polymer at (T_{cd} <) $T_a < T_g$ during which its dimension along the Z axis is held fixed, it is plausible that crazing can emerge over time because the pre-drawing produces significant chain tension, which remains balanced (before annealing) by the chain's glassy surroundings. Upon annealing at an elevated temperature above T_{cd}, force imbalance occurs at the network strand level [47-49]: The chain tension could be high enough to initiate pullout, leading to localized disintegration of the chain network in the form of crazing. As expected, annealing of pre-drawn bpA-PC (Figure 2.10(a)) at 120 °C generates a significant number of crazes all over the sample (Figure 2.10 (b)).

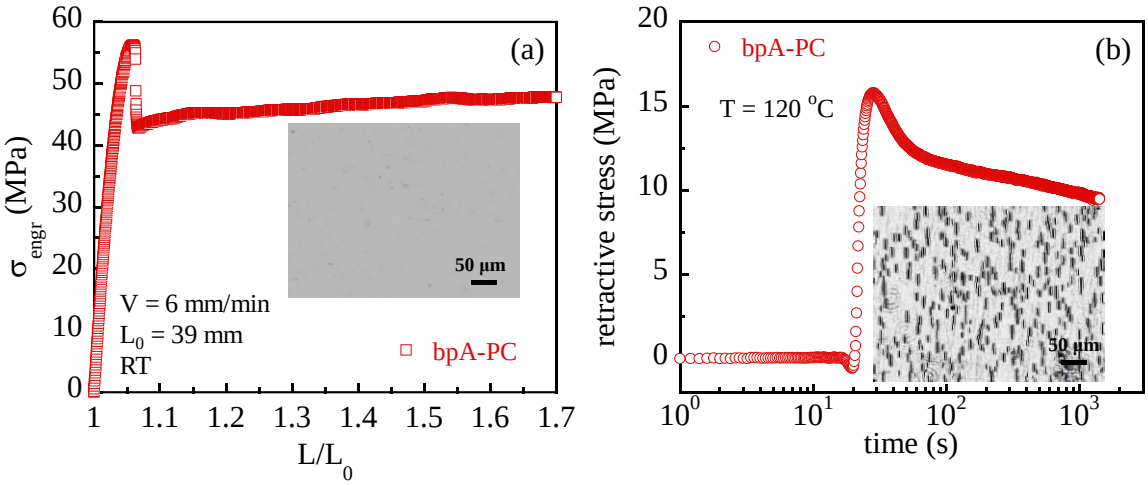

Figure 2.10 (a) Engineering stress σ_{engr} vs draw ratio L/L_0 from cold drawing of bpA-PC at room temperature. Inset photo shows absence of any craze after drawing. (b) Emergence

of retractive stress during annealing at 120 °C of the drawn bpA-PC described in (a). Inset photo shows the emergence of crazes after annealing.

2.4.6 Melt Stretching Effect

Melt stretching is known [40, 50-51] to make brittle polymers such as PS and PMMA behave in a ductile manner when drawn at room temperature parallel to the melt stretching direction. Conversely, when drawn in the direction perpendicular to the melt-stretching direction, a pre-melt-stretched ductile glassy polymer such as bpA-PC can even turn brittle [40]. The affine-like melt stretching alters the structure of the chain network in an anisotropic manner. Specifically, the effect of melt-stretching can be understood [10] as producing geometric condensation (parallel) and dilation (perpendicular) of the chain network.

Since melt stretching makes brittle glassy polymers ductile, can it eliminate crazing? According to 2.4.2, crazing can occur in a ductile polymer if it takes place before yielding. Can melt stretching also delay the craze formation so that yielding takes place first? The answer depends on whether t_{icraze} can be increased by melt stretching. The value of t_{icrase} or the onset of crazing in turn depends on how soon sufficient chain tension can build up to reach the threshold for chain pullout, initializing craze formation, relative to the state of no melt-stretching. Through the effect of geometric condensation that increases the ability of such a pre-treated glassy polymer to activate, it can be expected that the chain tension is lower in the pre-melt stretched state. Thus, we could expect t_{icraze} to increase in a pre-melt-stretched glassy polymer. At applied rate V/L_0 that determines the time to yield according to $t_y = (L_0/V)[(L/L_0)_y - 1]$, crazing would be suppressed if $t_{icraze} > t_y$.

2.4.6.1 Suppression of Crazing

The key to suppress crazing is to promote favorable conditions for yielding so that transverse contraction can readily take place. Our understanding of yielding and BDT in glassy polymers provides straightforward insights into how to turn a brittle polymer ductile. Since the activation is caused by the displacement of a robust chain network, we can bring about yielding by enhancing the chain network through adequate geometric condensation [40] of the load-bearing strands (LBSs). Uniaxial melt stretching, done in the approximate limit of affine extension to a stretching ratio of λ_{ms}, increases the areal density ψ in Eq. (1) of LSB in the XY plane by λ_{ms}. With the increased density $\psi_{xy} \sim \lambda_{ms}\psi$, the efficiency of the enhanced network to displace and mobilize segments multiplies. Melt stretching can suppress crazing because (a) yielding can arise before any craze formation and (b) the geometrically-condensed network delays the buildup of high chain tension required for pullout-led crazing. Consistent with this expectation, indeed, after melt stretching to $\lambda_{ms} = 3$, PS no longer shows crazing and becomes ductile when drawn at room temperature. Figure 2.11 shows the contrast.

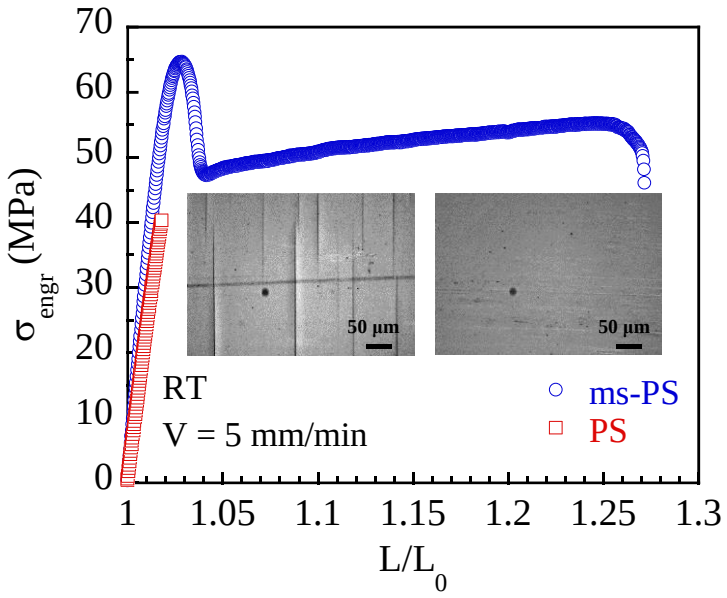

Figure 2.11 Engineering stress σ_{engr} vs draw ratio L/L_0 from extension of isotropic PS (L_0 = 39 mm) and melt-stretched PS (λ_{ms} = 3) with L_0 = 30 mm at room temperature, at V = 5 mm/min. Inset photos show the presence of crazes in isotopic PS (left photo) and its disappearance after melt-stretching (right photo).

Melt stretching also suppresses the type of crazing described in 2.4.2 where PMMA is found to show crazing at 80 ^{o}C although it does not do so at room temperature. Figure 2.12 shows the effect: the pre-melt-stretched PMMA is craze free at 80 °C.

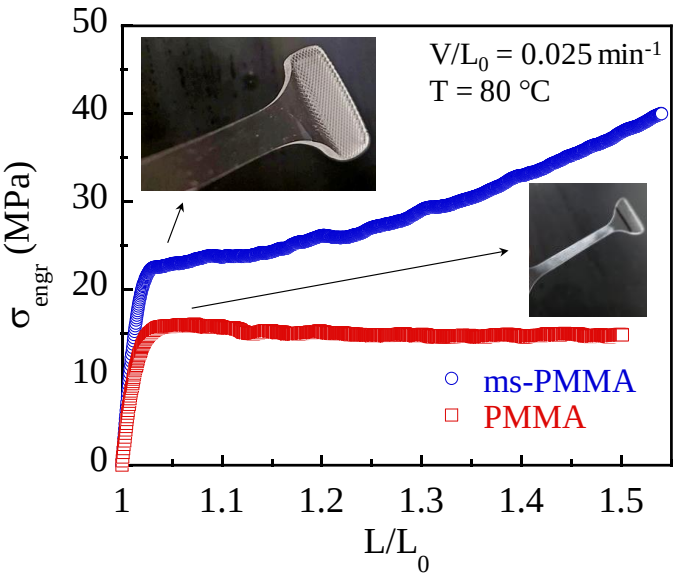

Figure 2.12 Engineering stress σ_{engr} vs draw ratio L/L_0 from extension of isotropic PMMA and pre-melt-stretched PMMA (λ_{ms} = 3) at 80 °C. Inset photos show presence of craze in isotopic sample and lack of crazing in the pre-melt-stretch PMMA.

Both Figures 2.11 and 2.12 show that over the same amount of time, crazes form in the untreated PS (at room temperature) and PMMA (at 80 °C) but do not form after the melt-stretching treatment. For the isotropic PS and PMMA, crazing takes place on the time scales shorter than $t_{bf} \approx \varepsilon_{bf}(L_0/V)$ = 9.4 s (PS) and $t_y \approx \varepsilon_y(L_0/V)$ = 11 s (PMMA) respectively, with ε_{bf} = 0.02 and ε_y = 0.03. This suggests that the induction times t_{icraze} for crazing in the pre-melt-stretched PS and PMMA have become sufficiently longer than 9.4 and 11 s respectively.

2.4.6.2 Delayed Crazing

Because crazing competes with yielding in a ductile polymer in the sense that its appearance requires $t_{icraze} < t_y$, the absence of crazing in pre-melt-stretched PS and PMMA

as demonstrated in the preceding 2.4.6.1 does not imply crazing cannot take place in such samples. Drawn at much lower speeds these samples take much longer times to yield, and at higher temperatures t_{icraze} becomes shorter. In either case we increase the chance for crazing to emerge before the point of yield. Figure 2.13 presents such a contrast to the result in Figure 2.11.

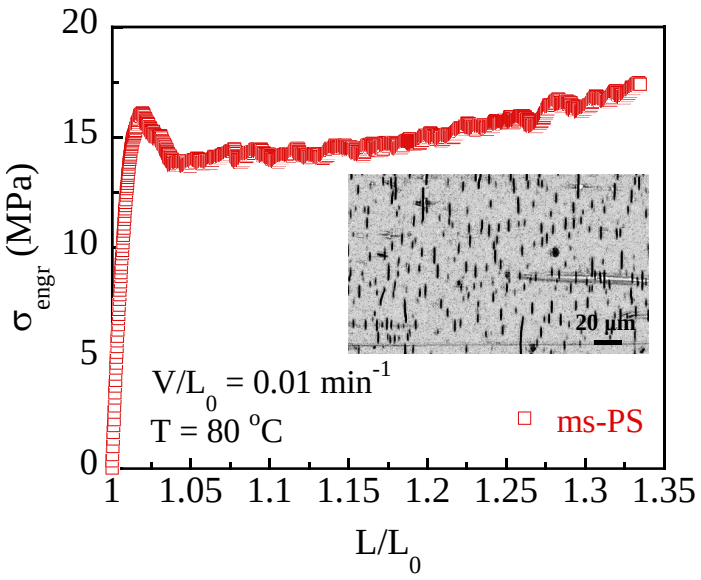

Figure 2.13 Engineering stress σ_{engr} vs draw ratio L/L_0 from extension of pre-melt-stretched PS ($\lambda_{ms} = 3$) at 80 °C and $V/L_0 = 0.01$ min^{-1} with $L_0 = 25$ mm. Inset photos show crazes that emerge at $L/L_0 = 1.02$ prior to yielding and necking.

2.4.6.3 Promotion of Crazing

If yielding cannot occur, then transverse contraction cannot accompany the extension and brittle fracture is inevitable. Uniaxial melt stretching along the Z axis condenses the chain network in the transverse dimensions so that the network strands are denser in the XY plane, i.e., $\psi_{xy} > \psi$. Conversely, in the orthogonal direction, e.g., in the XZ plane, the areal density $\psi_{xz} < \psi$, i.e., lower than that of the isotropic sample. When a pre-melt-

stretched bpA-PC is subjected to extension along Y axis, it can turn brittle [40]. Thus, uniaxial melt stretching has indeed produced two populations of strands, parallel strands (to Z axis), condensed on the XY plane, and perpendicular strands (to Z axis), dilated in the XZ plane. When drawn along Z axis, the parallel strands are more effective than those in the isotropic sample to activate the glassy state. When drawn along Y axis, because there are fewer perpendicular strands per unit cross-sectional area, yielding may not take place. Thus, it is plausible that crazing could emerge during perpendicular drawing, which is the case. Figure 2.14 summarizes the two different effects of pre-melt stretching in terms of the three stress vs. strain curves.

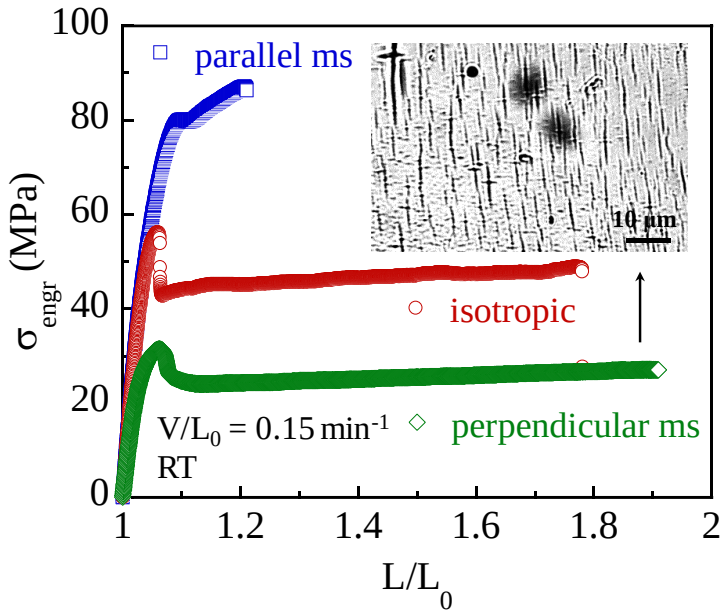

Figure 2.14 Engineering stress σ_{engr} vs draw ratio L/L_0 in extension of isotropic and pre-melt-stretched (λ_{ms} = 2) bpA-PC at room temperature in two directions; perpendicular and parallel to the melt stretching direction, all at V/L_0 = 0.15 min^{-1} but different L_0 = 15 mm (diamonds and squares) and 39 mm (circles). Inset photo shows the emergence of crazes

when the pre-melt stretched bpA-PC is extended to L/L_0 = 1.06 in the direction perpendicular to the melt-stretch direction (diamonds), while drawing of isotropic and parallel-melt-stretched samples does not result in any crazing.

2.4.7 Mechanical Rejuvenation and Physical Aging

As emphasized in both Sections 2.1 and 2.2, whether crazing occurs or not could depend on whether the glassy polymer can undergo yielding, which is not something determined by the chain network alone. For the same polymer, yielding is more likely at a higher temperature, because the segmental mobilization can occur more readily during deformation. Conversely, as the temperature decreases, the same chain network eventually becomes unable to bring about yielding because the reduced segmental mobility permits more efficient buildup of chain tension. Physical aging also makes it harder to mobilize and easier to increase chain tension. The buildup of high chain tension can lead to chain pullout and destruction of the chain network, leading to crazing.

2.4.7.1 Mechanical Rejuvenation

Based on the available understanding [10], we can anticipate that after adequate mechanical rejuvenation, which is an effective protocol that convert a brittle glassy polymer into a ductile polymer, crazing would cease to take place during drawing. When the mechanical rejuvenation brings a glassy polymer to a higher energy state in a new energy landscape, high chain tension may not emerge to reach force imbalance because yielding readily occurs in the mechanically-rejuvenated polymer.

Through either milling or twisting, we subject surface-contaminated bpA-PC (cf. the following 2.4.8.2) to mechanical rejuvenation, crazing no longer takes place presumably for the reason presented in the preceding paragraph. Figure 2.15(a)-(b) respectively show the effect of rejuvenation by twisting on the removal of craze formation in such bpA-PC in both displacement-controlled drawing and tensile creep.

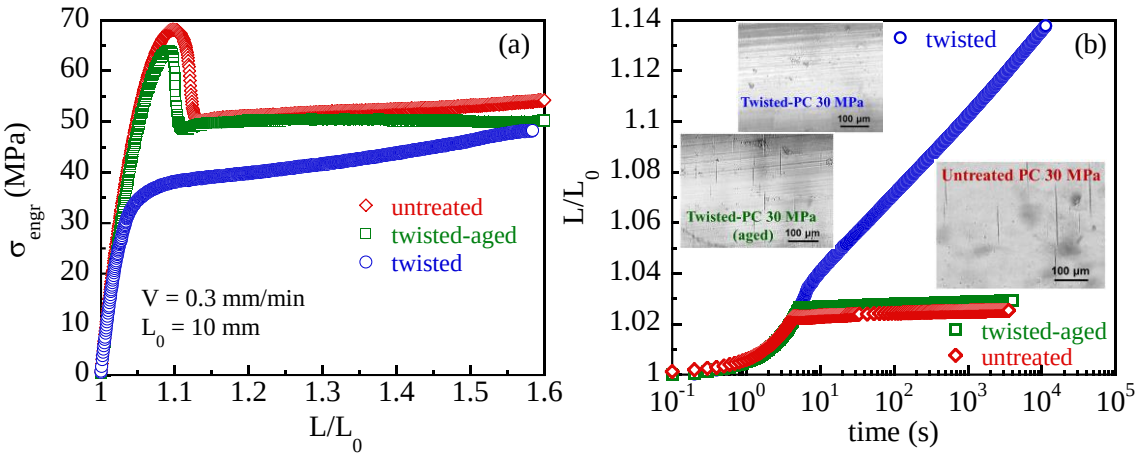

Figure 2.15 (a) Engineering stress σ_{engr} vs draw ratio L/L_0 from extension at room temperature of un-treated bpA-PC, rejuvenated bpA-PC by twisting and twisted bpA-PC after aging. (b) creep behavior of the same samples in terms of draw ratio L/L_0 vs time at σ_{engr} = 30 MPa. Surface crazes of untreated surface-contaminated bpA-PC disappear as a result of mechanical rejuvenation by twisting and subsequently "recovered" after sufficient aging of twisted bpA-PC.

2.4.7.2 Physical Aging

Conversely, a ductile polymer glass can turn brittle and shows crazing after annealing that permits the system to situate to a deeper minimum in its energy landscape. In such an aged glassy polymer, because of the reduced molecular mobility as depicted by the darker

dots in the cartoon of Figure 2.16(a), the task is harder for the chain network to activate the system out of its glassy state. Due to the physical aging, external deformation can produce higher chain tension so that pullout can take place to result in a structural collapse of the chain network, leading to crazing. Aging promotes crazing not because it raises the yield stress above the crazing stress [30] but because the lack of yielding permits buildup of higher chain tension until the point of imbalance between the intrachain tension and interchain forces. As indicated in Figure 2.16(b), moderate aging can remove the effects of mechanical rejuvenation, restores the stronger mechanical response and results in craze formation during creep of the surface-contaminated bpA-PC.

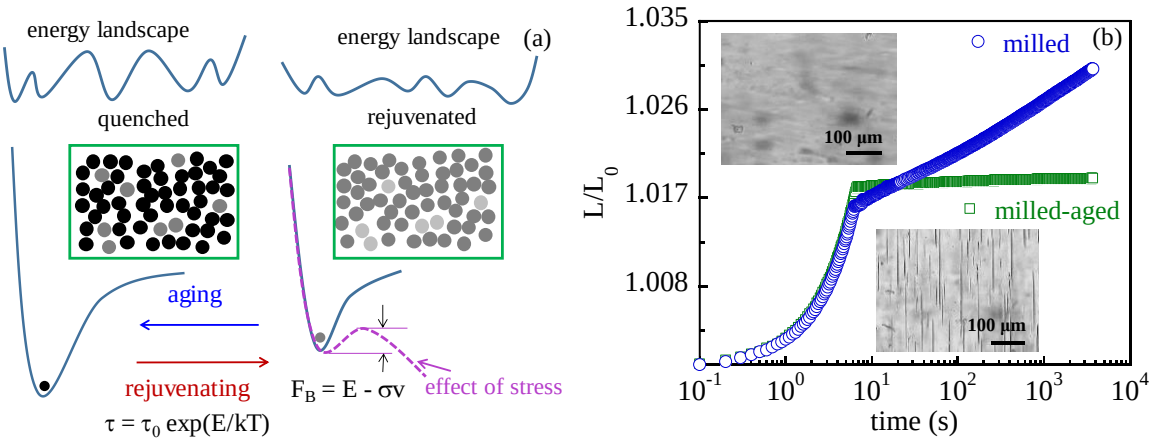

Figure 2.16 (a) Schemes depicting the effects of aging and mechanical rejuvenation on the energy landscape and state of glass, showing that applying mechanical force can decrease the energy barrier for a segment to hop out of the energy well. (b) Creep of milled and aged milled bpA-PC (surface-contaminated) in terms of draw ratio L/L_0 vs time at a constant stress of 30 MPa. The inset images show the absence of crazes in the milled sample and crazes in the aged milled bpA-PC.

In a second case, it is shown in Figure 2.17(a) that physical aging can make a craze-free ductile aPLLA undergo crazing and brittle fracture. It is necessary to note that the cusp, also observed in PS [38] is not an indication of molecular yielding, but rather associated with excessive crazing that delays the brittle fracture.

It is also interesting to evaluate the combined effect of melt-stretching and physical aging on crazing and ductility. As a continuation of the topic of 2.4.6 and expansion of the present topic of physical aging, we might broadly claim that after considerable pre-melt-stretching glassy polymers of sufficiently high molecular weight can be expected to stay ductile even after appreciable physical aging. Significant melt-stretching may assure that the amorphous PLLA (labeled as a-ms-aPLLA) remains ductile over time and even nearly craze-free, as shown in Figure 2.17(b).

However, upon heavy aging of ms-aPLLA as described in Section 2.3.1, the sample, labeled as hpa-ms-aPLLA to indicate heavy-physical aging of pre-melt-stretched aPLLA, whitens past the yield point, as shown in Figure 2.17(b) (upper left photo). The whitening only occurs in the necked region: The specimen remains transparent in the un-necked regions. WAXS measurements confirm that the whitening is not an indication of cold crystallization, which aPLLA is capable of (but not during room-temperature drawing, well below T_g = 60 ^oC). Thus, such whitening is rather unusual, because (a) it occurs during the transition at the neck front, (b) it does not occur in the same sample that has not undergone heavy aging, and (c) it does not occur in the un-necked parts of the sample. The whitening reveals a different appearance from that of normal crazing, as shown by the microscopic photo in the right-hand side inset of Figure 2.17(b). The crazes are much larger and denser.

There are crazes aligned in the drawing direction (in contrast to the common crazes that are perpendicular to the drawing direction. A dominant number of crazes form at an angle to the drawing direction. After melt-stretching the chain network becomes highly anisotropic, effective to activate the glassy state when drawn along the pre-melt-stretching direction, but also risking shear failure as well as splitting due to the maximal dilation of the chain network in the XZ and YZ planes. Such failures appear as the dark lines running parallel to the drawing direction. The complicated strain field at the neck front apparently could cause the localized failures to orient in a direction at an angle with the drawing direction, as shown in the microscopic photo.

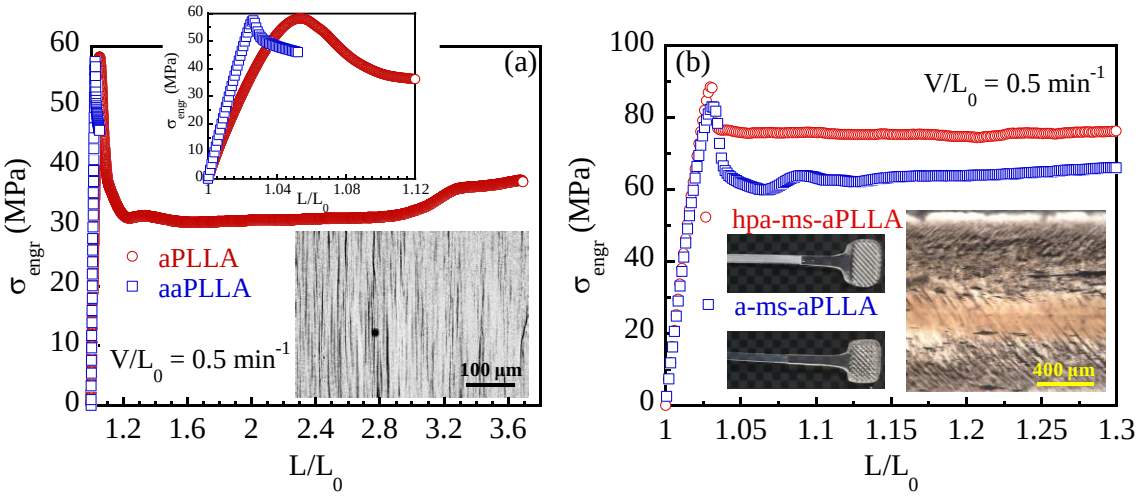

Figure 2.17 (a) Engineering stress σ_{engr} vs draw ratio L/L_0 from the room-temperature extension of aaPLLA (brittle after hours of storage under ambient condition) and freshly thermal-quenched aPLLA, (ductile and craze-free in the first half an hour), with L_0 = 39 mm, where the inset photo shows the massive crazing and the cusp (squares) in the inset figure reveals the pseudo-yield feature in aaPLLA, reminiscent of PS behavior [38]. (b) Engineering stress σ_{engr} vs draw ratio L/L_0 from the room-temperature extension of aPLLA

and heavily aged aPLLA, both of which had already undergone melt stretching to $\lambda_{ms} = 3$, as described in Figure 2.3. Inset photos with dark background on the left show whitening in the heavily aged pre-melt-stretched aPLLA (hpa-ms-aPLLA) and non-whitening craze-free a-ms-aPLLA. The other inset photo shows the microscopic view of the crazes in the necked hpa-ms-aPLLA, where the height of the image represents nearly the whole width of the drawn sample.

Craze formation in oriented samples has been previously studied: When drawn in a direction different from the pre-extension direction, crazes during pre-yield were found to orient at an angle to the drawing direction [52-53]. Post-yield drawing can also produce crazes at an angle [53], similar to the photo in Figure 2.17(b). In all cases, the crazing results from the localized breakdown of the chain network. The crazing "morphology" is straightforward when a glassy polymer is isotropic because the drawing direction uniquely determines the morphology. Our anisotropic a-ms-aPLLA can avoid pre-yield crazing and is also craze-free during necking. However, after heavy-aging, the anisotropic structural weakness produced by melt-stretching in the hpa-ms-aPLLA cannot prevent localized failures upon shear yielding and necking. Here the inhomogeneous strain field at the neck front complicates the craze morphology.

2.4.8 Effect of Small Molecules

The propensity for solvent-contaminated glassy polymers to undergo crazing is well known [54-56]. For example, the bpA-PC is particularly susceptible to solvent crazing, as we will confirm in a subsequent subsection. Although it is difficult to predict whether incorporation

of a given small-molecule liquid into a glassy polymer always promotes craze, it is straightforward to indicate what it implies when the solvent incorporation does bring about crazing.

2.4.8.1 Crazing at Room Temperature in Plasticized PMMA

As indicated in 2.4.1, PMMA hardly shows any crazing at room temperature although it is brittle. However, it is plausible that small-molecules in PMMA could act as lubricant to reduce the threshold chain tension for pullout so that t_{icraze} for crazing is shortened. We examine a system of PMMA containing 4% of TPP. The effect of TPP is to plasticize PMMA, for example, reducing the yield stress at 60 ^{o}C as shown in Figure 2.18. It has also caused crazing to occur under the same creep condition where the TPP-free PMMA does not show crazing.

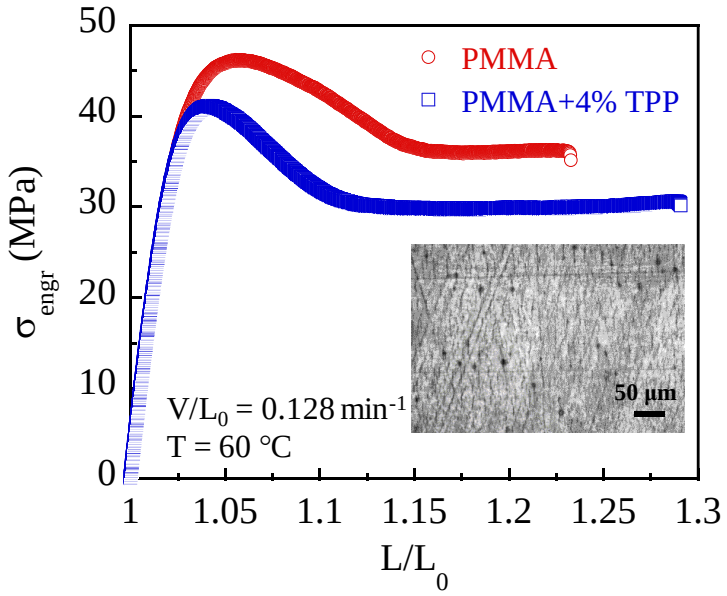

Figure 2.18 Engineering stress σ_{engr} vs draw ratio L/L_0 from room-temperature extension of the TPP-containing PMMA, showing craze formation in the inset image.

2.4.8.2 Surface Contamination in bpA-PC

Small-molecule contamination can cause crazing in bpA-PC. When bpA-PC is handled with bare hands, as shown by the photo in Figure 2.19, crazing tends to occur, given enough induction time. In passing, it is worth mentioning, consistent with the observations presented in 2.4.6.1, that adequate pre-melt-stretching [57] has the effect of suppressing the crazing during creep of the surface-contaminated bpA-PC. In this previous study, crazing was observed during creep because of the surface contamination. When the specimens were handled using rubber gloves no craze formation was observed.

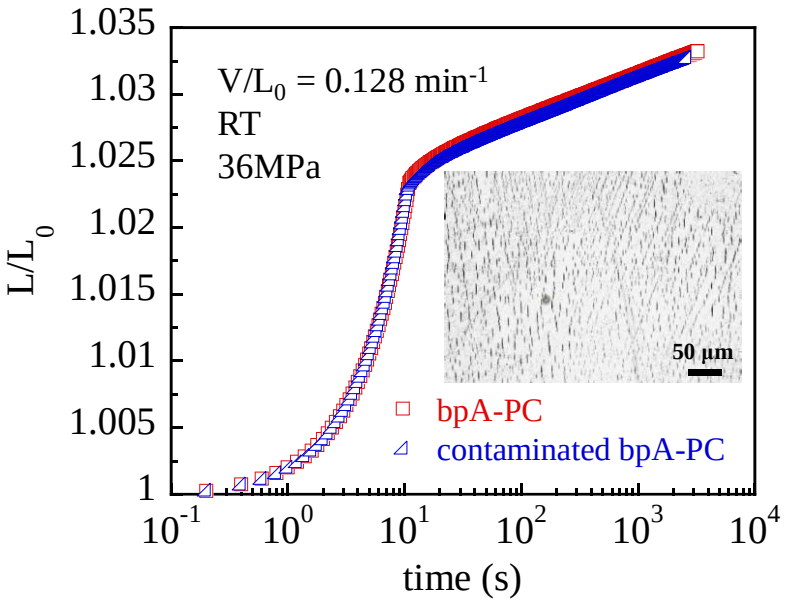

Figure 2.19 Tensile creep in terms of draw ratio L/L_0 vs. time involving an initial displacement at $V/_0 = 0.128$ min^{-1} ($L_0 = 30$ mm) to ca. $L/L_0 \sim 1.022$ and subsequent creep at $\sigma_{engr} = 36$ MPa. Inset photo shows the emergence of surface crazes in the hand-oil-contaminated sample, while the non-contaminated bpA-PC is craze free under the same condition.

2.4.9 Crazing in High-Impact Polystyrene (HIPS)

In rubber-toughened PS, known as high-impact polystyrene (HIPS), brittle fracture is delayed rather than suppressed [58]. In other words, the rubber phase merely takes up the imposed extension but does not activate the glassy PS matrix. Specifically, crazing prevails rather than being suppressed during cold drawing (e.g., at room temperature), initiating the "stress whitening" [59], i.e., cavitation in the rubber phase. The final fracture is a result of brittle failure of the PS matrix. This updated view of the rubber-toughening mechanism can be found in Ref. [58]. Upon pre-melt-stretching, the response of HIPS can change. For example, after melt stretching of HIPS depicted in Figure 2.3, as shown in Figure 2.20, the pre-melt-stretched HIPS exhibits much stronger mechanical responses (circles and squares) relative to the untreated HIPS. At the low drawing speed (squares) of $V/L_0 = 0.1$ min^{-1}, the pre-melt-stretched HIPS still suffers from crazing and subsequent whitening before undergoing shear yielding and subsequent necking at the second stress maximum. The second yielding at such a large nominal strain of ca. 30-40% can be understood in terms of the crazing and accompanied cavitation that "absorbs" the imposed strain and prevents the PS matrix from reaching the strain required to undergo yielding. This pre-melt-stretched HIPS provides a remarkable case analogous to the scenario of crazing in ductile glassy polymers as demonstrated in 2.4.2 for bpA-PC and PMMA at elevated temperatures.

Moreover, the effect of melt stretching on HIPS is analogous to that in the case of crazing in pre-melt-stretched PS under slow extension shown in Figure 2.13. In such ductile polymers, crazing does not terminate the extension. Instead, yielding subsequently takes

place, as shown in 2.4.2. Measurement of the transverse dimensions of the HIPS during drawing provides a powerful way to differentiate between crazing/whitening and shear yielding/necking. At the lower-rate, i.e., 0.1 min^{-1}, during drawing of the pre-melt-stretched HIPS the transverse dimensions of sample are unchanged until the second maximum in the stress, indicating that the mechanism of deformation is excessive craze and cavitation instead of yielding until the second peak. The second peak takes place because of the shear yielding of the glassy PS matrix leading to necking.

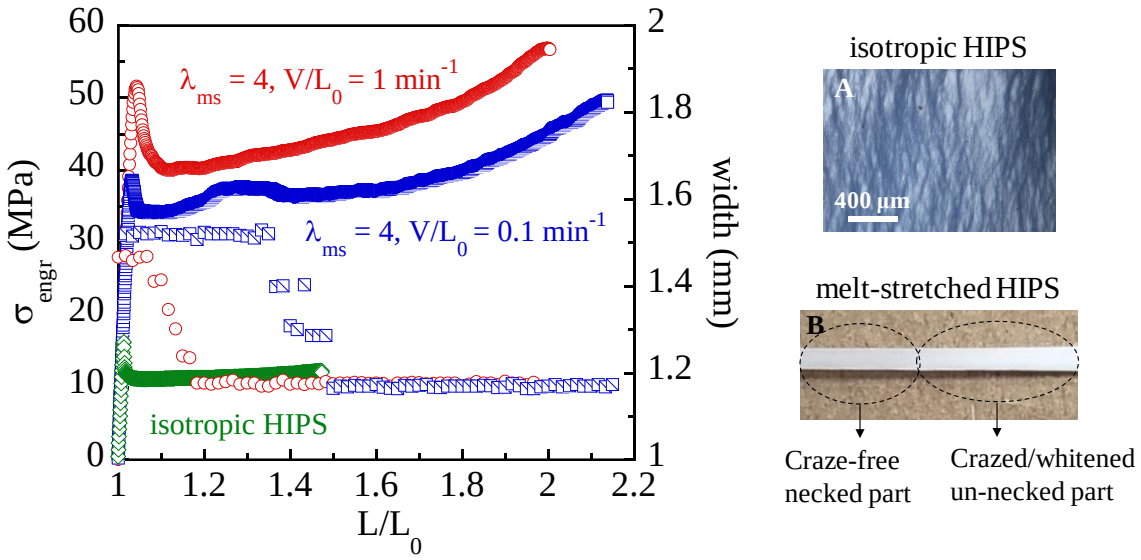

Figure 2.20 Engineering stress σ_{engr} vs draw ratio L/L_0 from extension of one isotropic (0.1 min^{-1}) and two pre-melt-stretched HIPS samples (0.1 and 1 min^{-1} respectively) along with the variation of the width during drawing at room temperature. Photo A shows the crazes in isotropic HIPS. Photo B (1 min^{-1}) is that of the necked segment, showing both the crazing/whitening free portion on the left and the whitened portion that is produced by the neck propagating from the right to the left, invading into the un-necked part that eventually developed whitening by the time the neck front passes through.

When the applied rate is increased to 1 min^{-1}, the pre-melt-stretched HIPS undergoes shear yielding that initiates craze-free necking. The neck front propagates by invading into the un-necked portion of the specimen that is only initially craze-free and whitening-free. Subsequently, over time, because the elapsed time has exceeded t_{icraze}, crazing appears in the un-necked portion and starts to induce whitening. Later on, when the necked front invades the un-necked whitened part it can propagate through and leaves a whitened neck behind. The photo in Figure 2.20 captures this "transition", showing both the whitening-free neck and whitened neck. Thus, even in a more complex, composite system of pre-melt-stretched HIPS, the same trend is uncovered: Yielding can prevail over crazing at higher rates when t_{icraze} is longer than t_y.

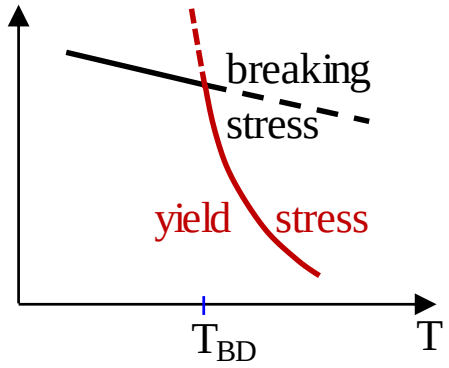

Figure 2.21 Illustration of the LDO hypothesis, showing the temperature dependences of the yield stress and breaking stress. The two curves meet at the point of the brittle-ductile transition temperature T_{BD}.

2.4.10 Contrasting Previous and Present Views

While crazing involves localized activation, i.e., pullout, yielding involves macroscopic mobilization of the dormant segments. The two processes can compete and

coexist when a glassy polymer is ductile. A glassy polymer is ductile when its chain network is sufficiently robust to fulfill the task of activating the glassy state without undergoing catastrophic structural failure.

We have previously noted [37] that an Eyring-like molecular picture for yielding of glassy polymers is insufficient until another theory is developed to explain what can deliver the barrier-lowering stress. We concluded [10] that this entity is the chain network arising from the intermolecular chain uncrossability. The challenge to identify the molecular picture of crazing is as great as that to explain the nature of the BDT. Similar to the BDT, crazing-prone glassy polymers such as PS exhibit a crazing-yielding transition (CYT) [38] as the temperature is elevated across the transition temperature T_{BD} for the BDT. Thus, a successful molecular-level account of the BDT may contain valuable insights regarding the molecular origin of crazing.

Until recently, the only widely accepted account of the BDT is the LDO hypothesis as summarized in Ref. [16]. According to the LDO hypothesis, brittle fracture and plastic flow are independent processes, concurrently operative, as illustrated by the two separate curves in Figure 2.21. It argues that the process involving the lower stress prevails. Perhaps the LDO hypothesis has tried to explain the BDT as follows. Above the BDT, the glassy polymer yields because it does not break; below the BDT, it cannot yield because it breaks. Unfortunately, such statements speak of little insights about the molecular nature of the BDT. Such a logic appears to implicitly predicate that brittle fracture originates from chain scission. For those who claim to understand the mechanism for yielding, a different logic makes more sense: Above the BDT, the glassy polymer does not break because it can yield;

below the BDT, it breaks because it cannot yield. According to our molecular picture [10], a glassy polymer can yield instead of breaking when it is not overly hard for its chain network to bring about activation. The chain networking is unable to cause activation when the polymer is either at a temperature too low or has undergone considerable physical aging. In passing, we note that Argon also recommended the LDO hypothesis as a way to understand the nature of the BDT and stated on p. 418 of his book [20] that "increasing strain rate that evokes an increase in plastic resistance will result in an increase in T_{BD}." We have previously reported a counter-example [44], showing that PS and PMMA can be totally ductile at one strain rate and turns brittle at a lower strain rate. While such an extraordinary "re-entry" case cannot be explained based on the Eyring type idea of activation and Argon's characterization, our model [10] can encompass a mechanism by which such re-entrant ductile-to-brittle transition occurs with lowering the rate of deformation.

Up to the present, the LDO hypothesis appears to have affected the way by which crazing behavior is understood. Here we show how the explanation on crazing has often resorted to the essence of the LDO hypothesis. According to Ref. [30], the effect of aging is explained by saying that annealing to induce physical aging increases the yield stress above the crazing stress. Hence shear no longer occurs at the lower stress and crazing starts to appear" [18] and "…annealing in this way is known to increase the yield stress σ_y" [18].

According to Ref. [30], both scission and disentanglement can be the cause for crazing. "Which process actually takes place, or whether the stress required for both is too high so that yield, and hence shear, takes place in preference, determines the response of the glassy polymer to an external stress" [60]. In explaining why bpA-PC does not show crazing, it is

argued [18] that bpA-PC has higher entanglement volume density ν_e and crazing due to chain scission would require a higher stress than the shear yielding stress. In other words, bpA-PC does not undergo crazing because it would involve a much higher stress than observed for PS. In contrast, we have just shown in Section 2.2 that bpA-PC and PS have comparable chain network structures, sharing a common value of θ (cf. Eq. (5)). Thus, the difference between bpA-PC and PS has little to do with their difference in terms of ν_e or ψ_{ent}.

The fact that bpA-PC shows crazing at elevated temperatures and the logic of LDO hypothesis led to the conclusion that such crazing does not involve chain scission: "If scission crazing is ruled out on the grounds that the stress required lies above the shear yield stress, can we understand high temperature crazing in highly entangled polymers by considering the alternative crazing mechanism of disentanglement?" [18] The LDO logic also appears in the discussion of the competition between shear (yielding) and crazing: "This means that disentanglement will also be hard to achieve, and so the stress for crazing via either mechanism will be high. It is for this reason that we associate shear with the highly entangled polymers" [18].

Several observations affirm the claim that there are different levels of dynamic and structural heterogeneities among the different glassy polymers in the present study. First, craze formation prior to yielding does not result in brittle fracture. In other words, crazing does not prevent bpA-PC and PMMA from undergoing yielding and plastic extension. This implies that the crazing is actually induced by heterogeneity – the chain network is otherwise robust, able to accomplish the task of activation in locations away from the crazes. Second, the crazing-plagued PMMA can achieve considerable strain during creep,

indicating that crazes in PMMA also arise from some unknown heterogeneities. Third, physical aging permits development of additional heterogeneity. Pre-melt stretched aPLLA (a-ms-aPLLA) is ductile and hardly shows any crazing during room temperature drawing. However, upon heavy aging, the same ms-aPLLA whitens during the necking formation, as shown in Figure 2.17(b), labelled as hpa-ms-aPLLA. Thus, among the robust chain network there are locations where crazing takes place, plausibly initiated by stronger heterogeneity.

In short, we are inclined to agree that the crazing phenomenon is an explicit manifestation of heterogeneity [61] in glassy polymers. Conversely, in absence of high heterogeneity, brittle fracture would involve little crazing, which is the case for PMMA drawn at relatively high rates at room temperature. Since PMMA does show crazing under creep at room temperature and in rate-controlled drawing at elevated temperatures, even PMMA presumably contains heterogeneity. The concept of heterogeneity in glassy polymers [62] is well known although much more work is required to quantify the heterogeneity as a function of numerous variables including the thermal history involved in preparing the glassy state. Finally, it is necessary to indicate that a sufficient robust chain network, e.g., achieved through pre-melt stretching, can usually overcome the adversity associated with the heterogeneity and ensure ductility even in presence of crazing.

2.5 Summary

Using different glassy polymers, we have collected a significant amount of phenomenology to draw a coherent molecular picture of crazing. Specifically, in the nine sections from 2.4.1 to 2.4.9, we have discussed the various conditions for craze formation.

These observations consistently support our understanding on the molecular mechanism for crazing. Crazing is an activated process, as elucidated in 2.4.1, plausibly involving localized chain pullout leading to spatially isolated structural failures of the chain network, likely initialized by certain unspecified heterogeneities. Thus, it can compete with the yielding process in a ductile polymer and prevails, typically at sufficiently low drawing speed or during creep, when it takes shorter times to incubate the crazes than the time taken to achieve macroscopic yielding, as shown in 2.4.2. Being an Eyring like process, crazing and even macroscopic breaking, can occur without ongoing extension in the various examples presented in 2.4.3 to 2.4.5. Melt stretching not only can turn brittle glassy polymers including PS ductile at room temperature but also makes them craze-free under the normal circumstance. However, like crazing in ductile polymers, melt stretching does not necessarily suppress crazing as shown 2.4.6.2. Pre-melt stretching not only turns brittle polymers ductile but also guards them against the adverse effect of physical aging. However, in the extreme case of heavily aged amorphous poly(L-lactic acid), as shown in 2.4.7.2, the pre-melt stretched aPLLA undergoes a severe form of localized failure during ductile drawing to suggest that physical aging may have promoted additional heterogeneities. The effect of small-molecule inclusion can be understood to have the effect of promoting localized chain pullout, making it easier (taking a shorter induction time) for crazing to develop as shown in 2.4.8. In the present study, we have also shown in 2.4.9 how crazing and whitening can be controlled by pre-melt-stretching in rubber-toughened high-impact polystyrene.

Crazing represents a major aspect of the mechanical behavior of glassy polymers. Consequently, for decades it has been a significant undertaking to develop a reliable molecular-level account. The available phenomenology discussed in the present work has finally allowed us to achieve a satisfactory chain-level qualitative understanding of the crazing phenomena in glassy polymers in terms of the molecular mechanisms that focuses on why crazing can take place and how to avoid it.

CHAPTER III

EXPLORING A NEW MOLECULAR MECHANISM TO TOUGHEN GLASSY POLYMERS

3.1 Introduction

In polymer science and engineering, improvement of mechanical properties remains a key challenge. To meet this challenge, we must develop a molecular level understanding of mechanics of solid polymers. In the case of amorphous polymers, the leading questions are (a) why glassy polymeric materials can be so tough, (b) what physical means can turn brittle polymers ductile. For non-crystalline polymers such as polystyrene (PS) and poly(methyl methacrylate) (PMMA), the desired rigidity in solid state stems from their vitrification. While low molar mass glassy polymers are mechanically fragile like any other organic glasses, sufficiently high molecular weight may or may not guarantee ductility. For example, even high-molecular weight PS and PMMA are still brittle at room temperature. But glassy polymers are considered to be "capable of dissipating large amounts of energy per unit volume through viscoelastic-plastic flow, and strategies for toughening are therefore directed towards maximizing the volume of material participating in this type of deformation".[63] Thus, a popular approach to improve the impact resistance of PS-based materials is to incorporate a rubbery phase into the glassy PS matrix, commonly known as

rubber-toughening. In such high-impact polystyrene (HIPS) as well as acrylonitrile-butadiene-styrene (ABS), the rubber phase is chemically linked to styrene or styrene-acrylonitrile to ensure chain connectivity and networking arising from the interchain uncrossability.

The conventional description[63] of the rubber-toughening mechanism as applied to HIPS and ABS is that the rubbery particles not only store elastic energy during impact but also stop the crack propagation by cavitation of the rubbery domains.[64] At a continuum level, the second (rubbery) phase was viewed to modify the strain field, e.g., introducing triaxial straining during uniaxial drawing.[65] The rubbery particles are also thought to induce shear banding in the matrix.[66] Rubbery particles in PS were believed to reduce post-yield strain softening; the removal of strain softening in compression was taken as the reason for the observed toughness enhancement in HIPS[67]. Time-resolved small-angle X-ray scattering (SAXS) has been applied[68] to show that rubber cavitation occurs along with craze formation during tensile drawing of HIPS and ABS. At a continuum level, these rubber-toughened polymer glasses were often regarded to have undergone apparent yielding.[65]

For molecular design of future glassy polymeric materials, for example, to have transparent (i.e., optically clear) and tough plastics, the conventional rubber-toughening method would not work when the rubbery phase is either not refractive index matched with the glassy matrix or not small enough to avoid light scattering. In order to explore alternative ways to toughen glassy polymers it is desirable to gain more understanding of the conventional rubber-toughening mechanism. We can regard the multicomponent HIPS and ABS as a composite system made of a chain network in presence of rubbery fillers.

During drawing, failures take place locally in the glassy matrix in the form of crazing and in the rubber phase in the form of cavitation. The presence of crazing indicates the failure of the design to achieve plastic deformation in the systems. The rubbery cavitation that occurs subsequent to crazing takes up the increasing strain imposed on the composite. In other words, global extension proceeds as long as the overall networking (through chain uncrossability and crosslinking among rubbery chains) has not undergone macroscopic breakdown. The multiphase morphology makes it possible for the nominal strain to reach 50%. To elucidate nature of the final fracture, it would be necessary to answer the question of whether yielding has actually taken place at the molecular level during drawing of HIPS and ABS.

In the conventional rubber-toughened glassy polymers, the inter-rubber particle distances are too large for the rubber phases to induce sufficient molecular mobility in the glassy matrix. Thus, no new physics is required to understand the acquired "ductility" in HIPS and ABS, as will be explained in this project. Conversely, if the rubber phase can be nanoscopic in size and uniform in its spatial distribution, then sufficient loading of the rubber phase along with chemical bonding between the rubber phase and the glassy matrix might produce a glassy composite that can more readily undergo true yielding than the glassy matrix in absence of the rubber phase. At Dow Chemical, through its R&D efforts a new chemical route to achieve such molecular rubber-toughening has recently been invented for poly(methyl methacrylate).[69-70] The rubber-toughened PMMA is a mechanically-inverted nanocomposite, made of nanoparticles with core-shell structure: crosslinked rubbery cores and glassy shells of PMMA chains that are in part chemically

linked to the rubbery chains. The mechanical behavior of the new PMMA rubber-toughened nanocomposites (PMMA-rt/nc) indirectly confirms a well-known effect in the literature of polymer thin films[71-74] that the glass transition temperature can be considerably lowered on nanoscopic scales for a glassy polymer in contact with a rubbery substrate.[75-79]

In this project, we demonstrate how the acquired rubber-toughening in HIPS and ABS can be understood in terms of the recent molecular picture[10] to provide a background against which the PMMA-rt/nc can be evaluated in terms of a molecular rubber-toughening mechanism. Through the experiments and corresponding analysis, we can assert that only the PMMA-rt/nc achieves molecular yielding during cold drawing at room temperature and the apparent yielding-like stress responses of HIPS and ABS as well as the corresponding apparent ductility actually involve no activation of the glassy matrices.

3.2 Experimental

3.2.1 Apparatus and Procedures

All the melt-stretching and mechanical tests in the present study were done using Instron (model 5969). For melt stretching (i.e., extension above T_g), a temperature-controlled chamber is employed with the Instron programmed to apply a constant Hencky rate. While, for drawing of samples in the glassy state, a constant clamp speed is imposed.

ARES G2 (TA Instruments) was used to obtain the small amplitude oscillatory shear (SAOS) data in the frequency sweep mode of the samples at various temperatures ($T_g < T < T_g+100$ °C). Disk-shape samples with 8mm in diameter and thickness of 1-2 mm were used to do such SAOS tests.

Dynamic Mechanical Analyzer (DMA Q800, TA Instruments) was employed to collect the viscoelastic data and observe dynamic relaxation of different components for HIPS, ABS and PMMA-rt/nc50. The DMA tests were based on the temperature sweep mode at oscillation frequency of 1 Hz, the rate of temperature change of at 10 °C/min, and the strain amplitude of 0.01%. A typical sample for DMA had a dimension of 12 mm by 7 mm by 0.5 mm (length, width and thickness).

Dog-bone shape samples were prepared for tensile experiments by press-molding using Carver™ Lab Press at 180 °C under a load of 9000 kg for 30 min to permit diffusion and relaxation of polymer chains before unloading and subsequent quenching. The dog-bone has its middle thin section equal to 39 mm in length, 3.3 mm in width and 0.6 mm in thickness. Cylindrical samples for compression experiments are also prepared using a mold to produce dimensions of 6 × 6 (diameter × height) mm^2. To achieve uniaxial compression with Instron, silicon oil was applied to both ends of the cylindrical samples as lubricant.

3.2.2 Materials and their Characterization

The present study is based on two types of conventional rubber-toughened polymer glasses including high-impact polystyrene (HIPS, PH-888G from CHI MEI Co., Taiwan) and acrylonitrile-butadiene-styrene (ABS, MG94 from SABIC) along with a series of PMMA-based rubber-toughened nanocomposite (PMMA-rt/ncx) where x denotes the percentage of rubber phase.

PMMA-rt/ncx is synthesized by emulsion polymerization and represents a new generation of rubber-toughened materials, based on a new mechanism. Using atomic force microscope (AFM, Bruker Dimension Icon) in the tapping mode and scanning electron

microscope (FEI-Philips Model Tecnai T12T/STEM), the morphology of PMMA-rt/nc50 is described as shown in Figure 3.1(a)-(b), whereas the morphology of the PMMA-rt/nc70, which is similar to the PMMA-rt/nc50, has been published before.[80] The rubber particles are found to be uniform in size (<100 nm) and evenly distributed in presence of free PMMA chains. The system may be schematically illustrated as shown in Figure 3.1(c). Unlike the uniform and well-controlled nanoscopic morphology of PMMA-rt/nc, the conventional rubber-toughened systems such as HIPS and ABS typically have[81] relatively wide or bimodal distributions of particles sizes ranging from fractions of micrometer to many micrometers.

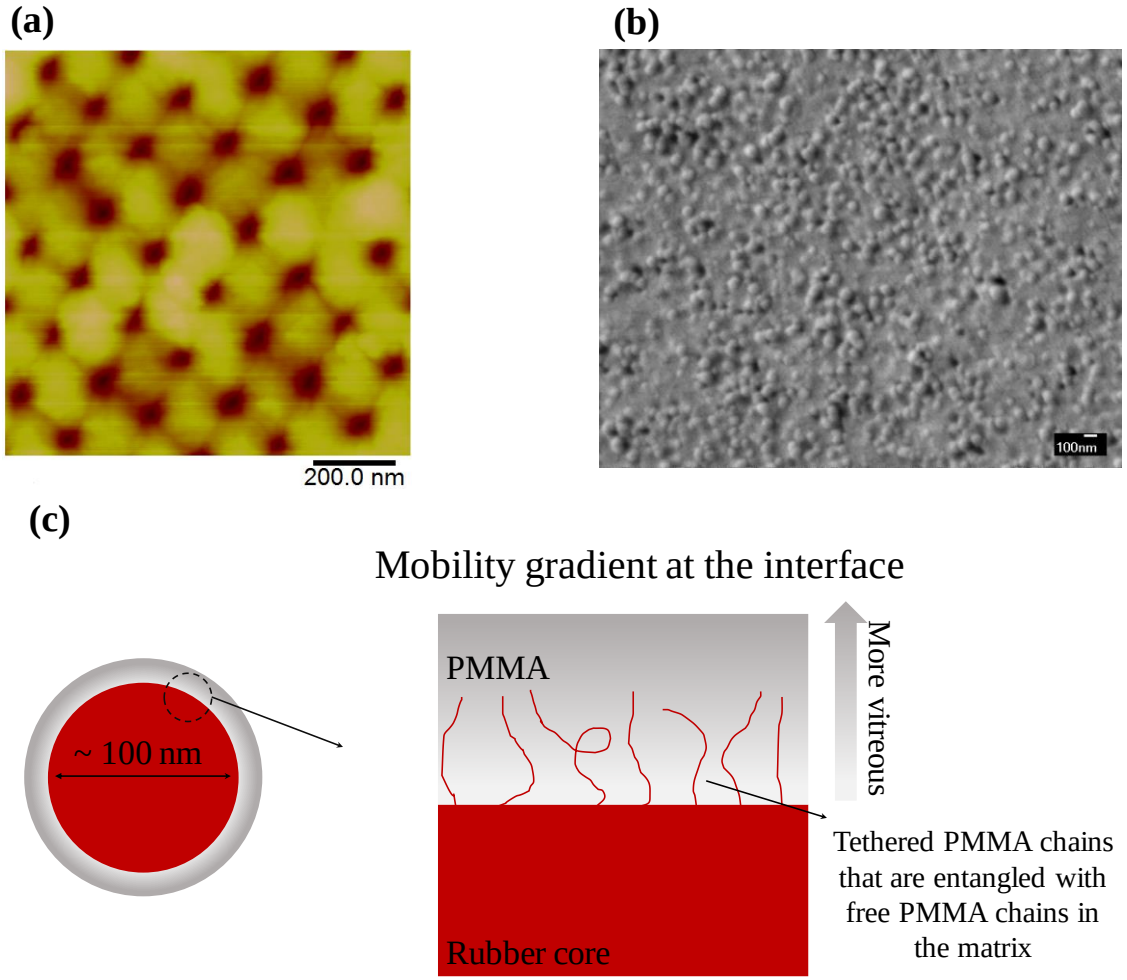

Figure 3.1 (a) AFM phase image of PMMA-rt/nc50 showing uniformly distributed nano-sized (<100 nm in diameter) particles. (b) SEM image of PMMA-rt/nc50. (c) Schematic depiction of the structure of PMMA-rt/nc50, which is a rubbery core closed by a glassy PMMA where PMMA and rubbery chains are chemically linked.

3.2.2.1 Small Amplitude Oscillatory Shear

SAOS measurements were carried out to show storage G' and loss G" moduli over a wide range of frequencies, as shown in Figure 3.2. HIPS and ABS show characteristics that resemble those of typical linear entangled polymer melts, with a crossover in the

terminal region, plateau at intermediate frequencies and segmental transitional region at higher frequencies. The plateau modulus of the HIPS and ABS can be read to be G_{pl} = 0.2 MPa and 0.45 MPa. Expectedly, these numbers are equal to the plateau modulus G_{pl} of atactic polystyrene (a-PS) and styrene acrylonitrile copolymer (SAN) that respectively form the matrix for HIPS and ABS. In the case of PMMA-rt/nc50 the magnitude of the plateau modulus is the same as that of a pure entangled PMMA melt, equal to 0.3 MPa. However, G' and G" do not cross in PMMA-rt/nc50. This feature can be expected of a dense colloidal system and thus confirms the structure of PMMA-rt/nc50 being made of nanoparticles. The second plateau in G' at the lowest frequencies reveal the close packing of the nanoparticles to result in jamming and inhabitation of "terminal flow". Such behavior is extensively observed for filled systems[82-84] and microphase-separated block copolymers[85-89].

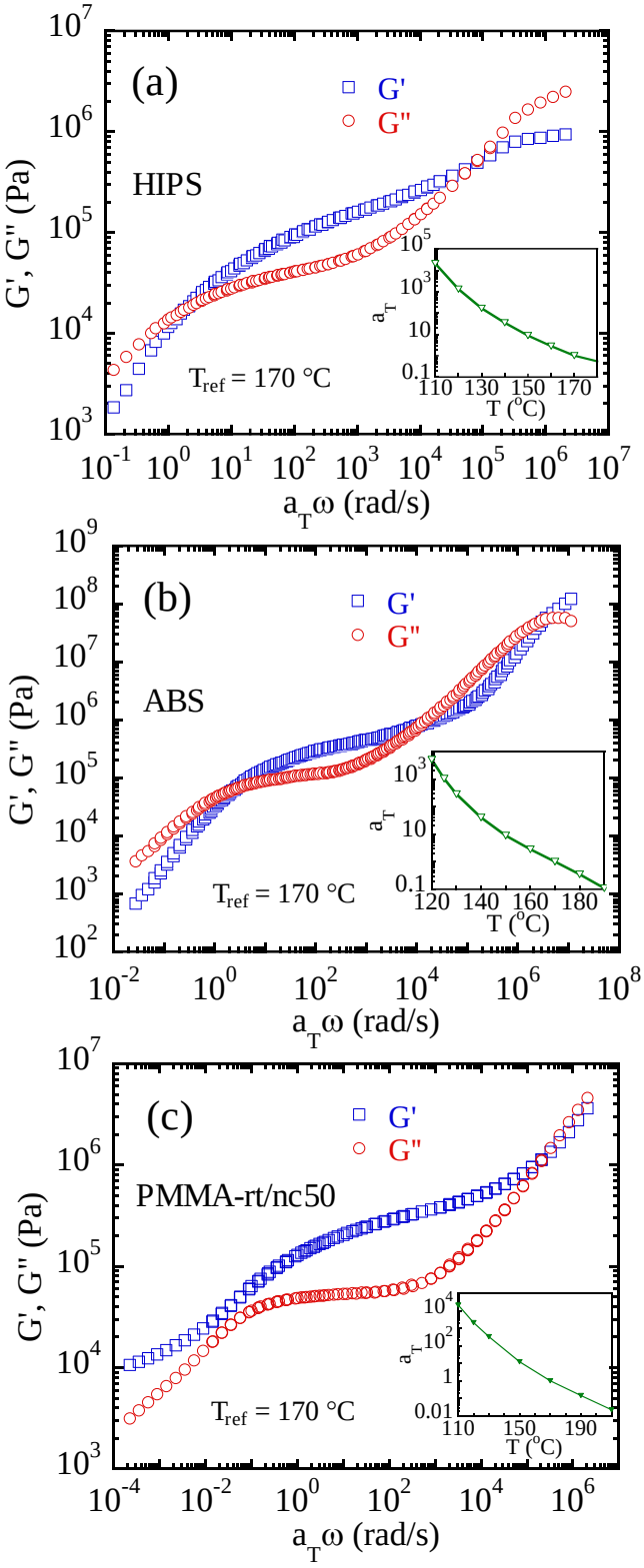
(a)
G'
G"
HIPS
T_ref = 170 °C
G', G" (Pa)
a_T ω (rad/s)
a_T
T (°C)
(b)
G'
G"
ABS
T_ref = 170 °C
G', G" (Pa)
a_T ω (rad/s)
a_T
T (°C)
(c)
G'
G"
PMMA-rt/nc50
T_ref = 170 °C
G', G" (Pa)
a_T ω (rad/s)
a_T
T (°C)

Figure 3.2 Master curves of storage and loss moduli G′ and G″ from SAOS measurements of (a) HIPS, (b) ABS and (C) PMMA-rt/nc50 at various temperatures. The reference temperature is 170 °C for all the curves and the inset figures show the corresponding William-Landel-Ferry shift factors for each polymer.

3.2.2.2 Melt Stretching

To alter the chain network characteristics of the glassy matrix, HIPS, ABS and PMMA-rt/nc50 were subjected to melt-stretching ($T > T_g$) under different conditions in terms of Hencky rate, stretching ratio and temperature. Figure 3.3 shows the engineering stress σ_{engr} vs stretching ratio λ for these samples. To evaluate the melt stretching condition, a rubber elasticity curve, $\sigma_{engr} = G_p(\lambda - 1/\lambda^2)$, is included to benchmark the stress responses. Specifically, Figure 3.3(c) shows that PMMA-rt/nc50 can also be regarded as an entangled melt: The melt rupture shown by the down-pointing triangles in Figure 3.3(c) indicates presence of an entanglement network capable of avoiding full disentanglement and permitting the residual entanglement to lock up until chain scission unleashes a catastrophic breakdown of the entanglement network.

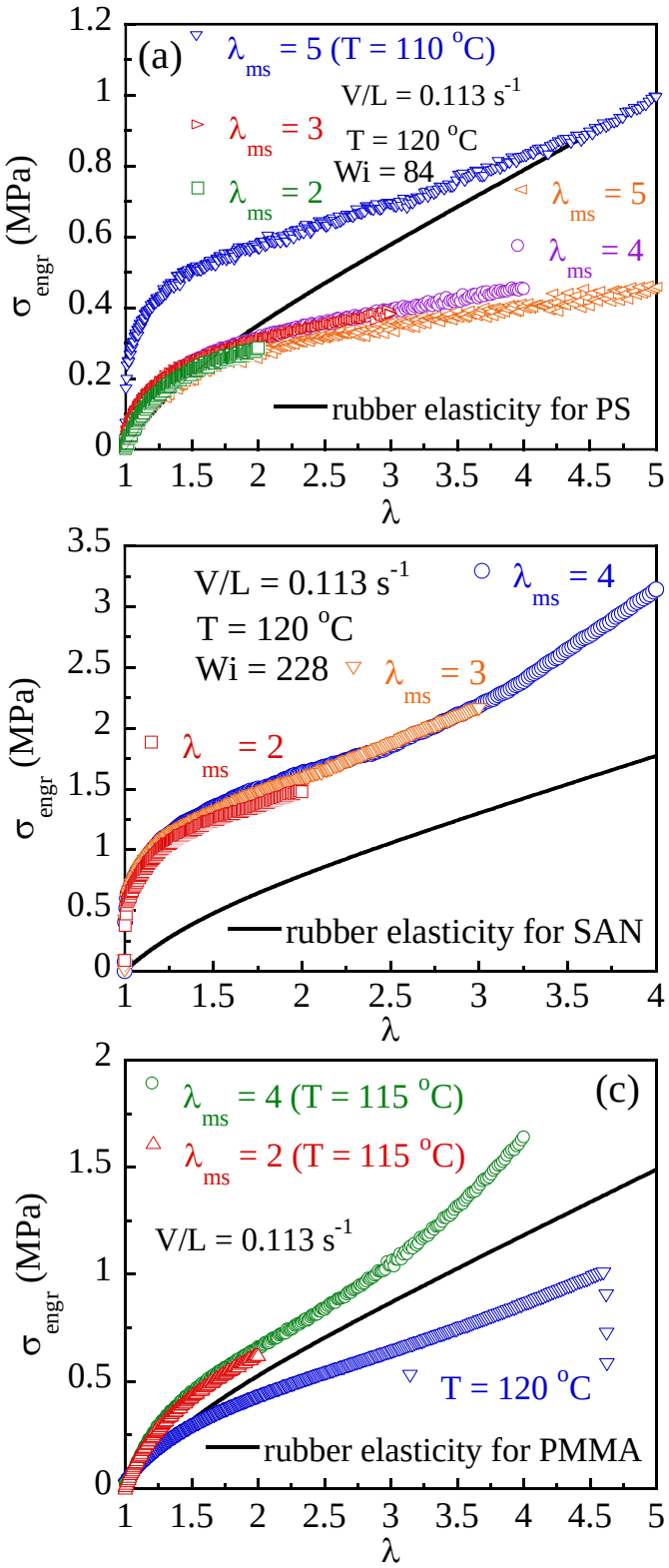
(a)
λ ms = 5 (T = 110 °C)
V/L = 0.113 s-1
λ ms = 3
T = 120 °C
Wi = 84
λ ms = 2
λ ms = 5
λ ms = 4
rubber elasticity for PS
σ engr (MPa)
λ
V/L = 0.113 s-1
λ ms = 4
T = 120 °C
Wi = 228
λ ms = 3
λ ms = 2
rubber elasticity for SAN
σ engr (MPa)
λ
(c)
λ ms = 4 (T = 115 °C)
λ ms = 2 (T = 115 °C)
V/L = 0.113 s-1
T = 120 °C
rubber elasticity for PMMA
σ engr (MPa)
λ

Figure 3.3 Engineering stress σ_{engr} vs. stretching ratio λ curves from melt stretching of (a) HIPS, (b) ABS and (c) PMMA-rt/nc50 at various temperatures. Hencky rate was 0.113 s^{-1} for all the tests. The effective length of the dog-bone shaped samples was L_0 = 10 mm at λ= 1. A rubber elasticity curve according $\sigma_{engr} = G_{pl}(\lambda - 1/\lambda^2)$ is included to benchmark the melt-stretching condition.

3.2.2.3 Dynamic Mechanical Analysis

For further characterization, DMA tests were carried out for three samples as shown in Figure 3.4(a)-(c). HIPS and ABS show two distinct and well-separated transition, one at lower temperature range between -100 °C to -50 °C related to the segmental relaxation of the rubber particles and the glass transition, signified by the peak of the loss modulus E" and indicated by the arrow above 100 °C, which corresponds to the glass transition of the matrix. In contrast, transitions of the rubbery and glass phases in the PMMA-rt/nc50 are not isolated. Segmental relaxation of the rubber phase takes place in the temperature range of -50 °C to 0 °C. At higher temperatures, we observe a gradual change in the storage modulus E' as indicated by the dashed oval in the Figure 3.4(c). Disappearance of the plateau and gradual decrease in E' are indicative of the fact that there is a spectrum of segmental relaxation times for the PMMA chains in PMMA-rt/nc50. This wide distribution of segmental dynamics originates from the unique structure of PMMA-rt/nc. Apparently, the rubbery cores are rather effective in causing the PMMA "matrix" to plasticize readily, thanks to the small inter-particle distances and covalent-bonding between the rubbery cores and glassy PMMA matrix. In other words, it is conceivable that segmental dynamics of

PMMA chains are appreciably faster in presence of the rubbery cores than those in a pure PMMA.

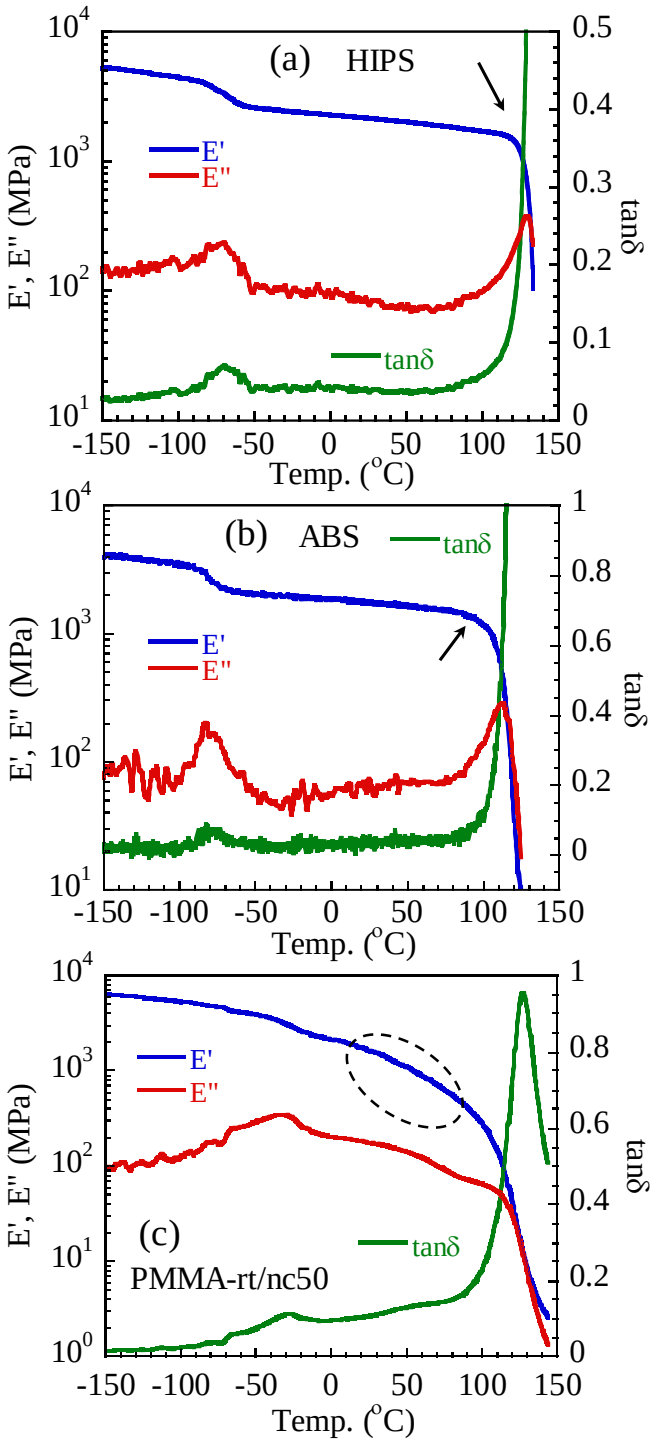

Figure 3.4 DMA measurements of storage E' and loss E'' moduli along with the damping factor tanδ = E''/E' of (a) HIPS, (b) ABS and (c) PMMA-rt/nc50 at the constant frequency of 1 Hz. The arrows in HIPS and ABS denote the onset of segmental relaxation which takes place in a narrow temperature range. In the case of PMMA-rt/nc50 the changes are gradual, indicative of a broad spectrum of segmental relaxation times. Moreover, there is no peak in E'', which is rather uncharacteristic of glassy polymers.

3.3 Results and Discussion

3.3.1 Apparent Yielding of HIPS and ABS

HIPS and ABS commonly show ductile-like responses to uniaxial extension. In this work we investigate the true nature of mechanical characteristics of these conventional materials. Specifically, Figure 3.5 compares the tensile extension behavior of HIPS and ABS with their counterparts, i.e., the pure PS and styrene-acrylonitrile (SAN), respectively. PS shows brittle fracture at the strain of 2% at a stress level of ca. 40 MPa. HIPS exhibits ductile-like response with a "yield" stress of ca 16 MPa and "yield" strain of ca. 1.3%. The pair of ABS and SAN behave similarly, except showing higher stress levels. With the "yielding" stress for SAN reaching 75 MPa at 3.5%, and 42 MPa at 2.7% for ABS. It is well documented[65] that the "yielding" in HIPS and SAN is accompanied by massive whitening as a result of cavitation in the rubbery phase.[59, 90-94] Subsequently, strain softening ensues, and the tensile stress ceases to increase plausibly because the increasing nominal strain is accommodated by the increasing cavitation as well as crazing, as shown by the inset photo in Figure 3.5.

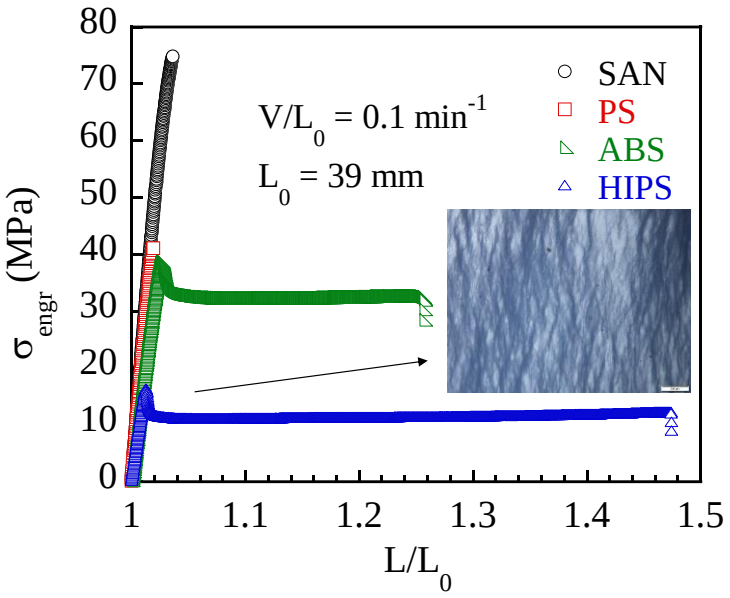

Figure 3.5 Engineering stress σ_{engr} vs. draw ratio L/L_0 curves, obtained from drawing at room temperature of PS and SAN, and the conventionally rubber-toughened pairs, HIPS and SAN, respectively. The constant speed drawing involves an initial (effective) dog-bone-shaped sample length L_0 equal to 39 mm.

There is at least one example in the literature[44] that to our knowledge indicates yield-like response in uniaxial extension of PS, i.e., tensile stress switching from monotonic increasing to leveling off, without actually undergoing real yielding. Therefore, the stress leveling off is not sufficient information to infer that the glassy state has undergone macroscopic activation. Actually, it remains to demonstrate whether HIPS and ABS is truly ductile, i.e., the stress peak signals the onset of plastic deformation or something else. Since all glassy polymers including the pure PS and SAN turn ductile above a certain temperature, i.e., the temperature T_{BD} for the brittle-ductile transition (BDT), it is instructive to examine the characteristics of HIPS and ABS such as the peak stress as a function of temperature

up to their glass transition temperatures above 100 ˚C (as indicated by the DMA data in Figures 3.4(a) and 3.4(b).

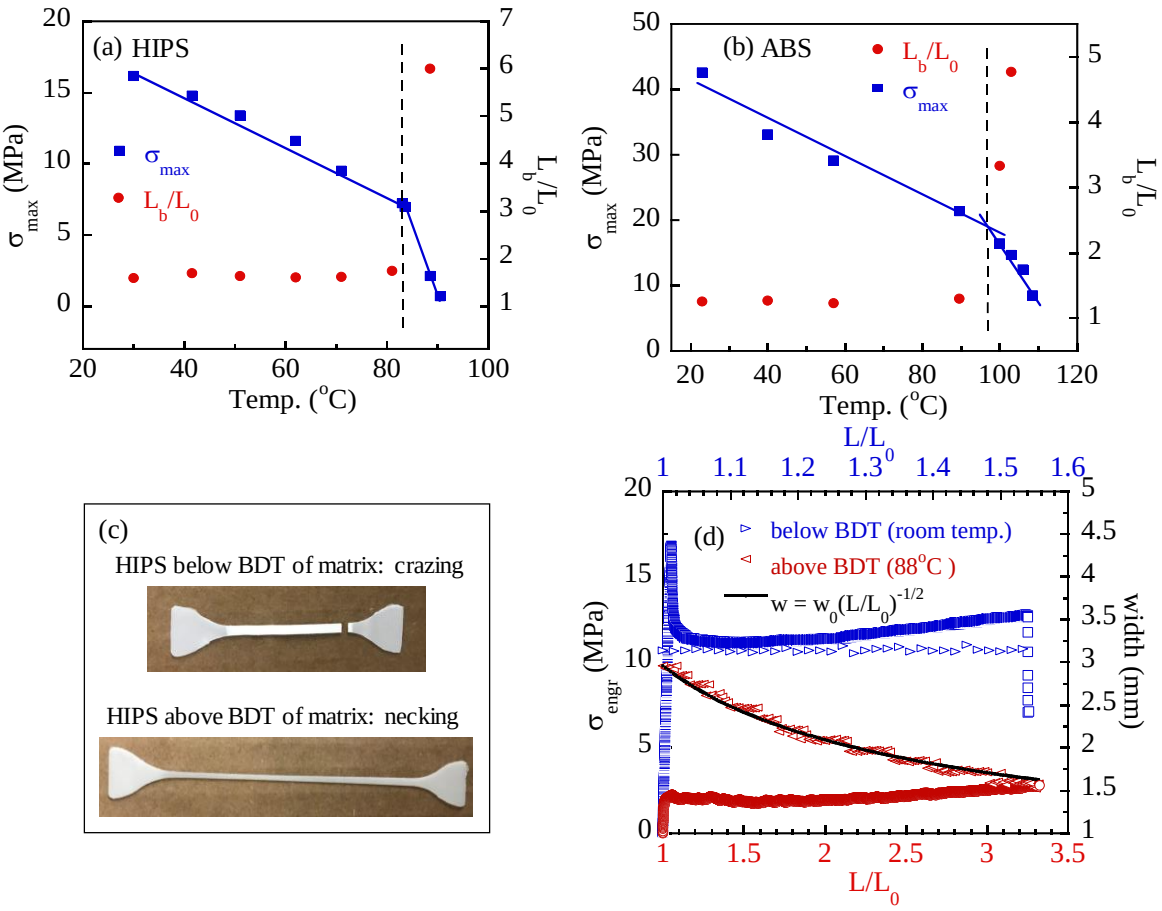

Figure 3.6 Engineering stress maximum σ_{max} as a function of temperature for (a) HIPS and (b) ABS. Also plotted is the draw ratio at breaking, L_b/L_0. The location of the kinks, denoted by the vertical dashed lines, is an indication of a transition. Typical appearances of HIPS below (RT) and above (88 °C) this transition are shown by the photos in (c). During drawing, the width of the HIPS is measured as shown in (d), at either room temperature (right-pointing triangles) or 88 °C (left-pointing triangles), along with their corresponding stress-strain data.

Figures 3.6(a) and 3.6(b) show that the stress maximum vs. temperature curves have kinks just above 80 ^{o}C and near 100 ^{o}C for HIPS and ABS respectively. Such kinks typically appear at T_{BD} (brittle-ductile transition temperature) for pure glassy polymers. By analogy, we infer that these kinks in Figures 3.6(a) and 3.6(b) also indicate the BDT for HIPS and ABS. In the example of HIPS, the temperature dependence of the response is also partially captured by the photo in Figure 3.6(c). First, it is necessary to mention that at room temperature where the drawing produced massive whitening, the crazing first took place, followed by whitening just beyond the stress maximum. Second, the drawing above BDT at T = 88 °C was homogeneous, the sample did not undergo whitening; and no crazing was present.

Finally, it is remarkable to observe that the drawing below BDT did not result in transverse contraction. By video-recording the drawing tests and performing evaluation of the specimen's width from the movies, we found, as shown in Figure 3.6(d), that in contrast the specimen width shrank during drawing at 88 ^{o} C. This is an indication that the plastic deformation has occurred. Specifically, Figure 6d shows that below BDT, e.g., at room temperature the width of HIPS specimen remains fixed during the uniaxial extension up to a draw ratio $L/L_0 = 1.55$; whereas for the HISP above BDT the ductile drawing is uniform, with the width varying with the draw ratio L/L_0 as $(L/L_0)^{-1/2}$, i.e., approximately following the trend of volume-conserving uniaxial extension. Also plotted in Figure 3.6(d) are the corresponding stress vs. strain curves.

The preceding results suggest that conventional rubber-toughening approach hardly shifts the BDT. The apparent ductility at room temperature of HIPS and ABS through

crazing and subsequent rubbery cavitation until the delayed brittle fracture do not involve any molecular level activation of the glassy state. In principle, plasticization by incorporation of a low-T_g component could push the BDT to a lower temperature by depressing T_g. However, conventional solvent-plasticization can have adverse effects on ductility, as shown in a recent study,[41] because the solvent could lower the intermolecular friction and reduce the threshold force for chain pullout, leading to a catastrophic failure of the chain network. Clearly, the objective of "plasticization" to gain ductility can only be achieved by preserving the cohesive strength of the chain network.

3.3.2 True Yielding of PMMA-rt/nc

PMMA-rt/nc explores a new strategy to toughen glassy polymers, specifically, PMMA that is typically brittle at room temperature. Figure 3.7(a) indicates the ductile responses of PMMA-rt/nc50 and PMMA-rt/nc70 in uniaxial extension. The stress levels correlate strongly with the rubber phase content, with Young's modulus decreasing from 825 MPa to 147MPa and yield stress dropping from ca. 22 to 5 MPa. Both samples can double its initial length without fracture. Because of the nano-size of the rubber particles, the samples are transparent and remain so during and after the drawing. The inset image in the Figure 3.7(a) shows the PMMA-rt/nc50 taken between the two crossed polarizers during drawing. The birefringence, absence of whitening and crazing as well as high drawability (L_b/L_0) contrast sharply with the characteristics of HIPS and ABS. Our measurements revealed that the stress-optical coefficient ($C=\Delta n/\sigma$) of PMMA-rt/nc50 at room temperature is around -1.765×10^{-11} Pa^{-1} which is considerably larger than its value for pure glassy PMMA[95] of -0.45×10^{-11} Pa^{-1}. Figure 3.7(b) further indicates in the case of PMMA-rt/nc50

that the temperature dependence of σ_{max} shows no kinks and the draw ratio to break increases gradually with temperature. Figure 3.7(a) also includes the stress-strain curve for PMMA-rt/nc70-10K that is made with lower molecular weight for PMMA. Because of the molecular weight dependence of the glass transition, this sample is hardly glassy at room temperature and thus also able to draw despite of the low molecular weight.

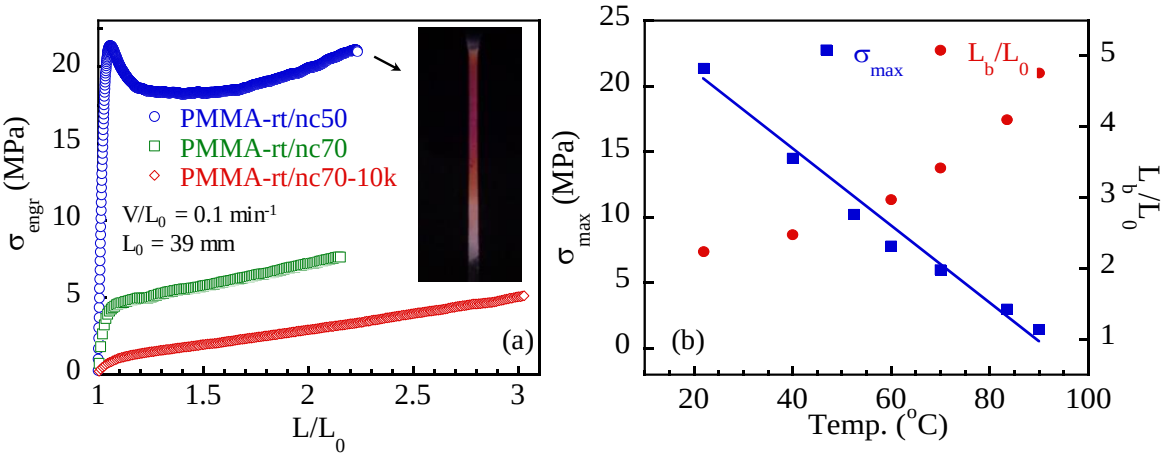

Figure 3.7 (a) Engineering stress σ_{engr} vs. draw ratio L/L_0 from room temperature drawing of PMMA-rt/nc50. Inset image shows the emergent birefringence in the sample during deformation, which is indicative of molecular yielding. (b) Engineering stress maximum σ_{max} and draw ratio at break L_b/L_0 at different temperatures and $V/L_0 = 0.1$ min^{-1} with $L_0 =$ 39 mm, showing absence of kink.

3.3.3 Yielding in Compression

Uniaxial compression of PS and SAN of sufficiently high molecular weight is ductile even at room temperature. The same can be expected of HIPS and ABS. Thus, the response to compression can provide a valuable reference for Figures 3.6(a) and 3.6(b). Figure 3.8(a) shows the compressive stress as a function of compression ratio for the three samples.

Carrying out such tests at different temperatures and taking the stress maximum as σ_y, we plot in Figure 3.8(b) the variation and show that there are no kinks, as expected. In other words, since the response to compression is ductile the peak stress is yield stress and not expected to show any kink over the same temperature range where extension produces kinks for HIPS and ABS in Figures 3.6(a) and 3.6(b). The contrast supports the idea that the presence of the kink is indicative of a transition, i.e., BDT. In other words, HIPS and ABS do not achieve yielding during uniaxial extension at room temperature, as is often mischaracterized in the literature,[63, 65] such as in a statement of "yielding occurred by multiple crazing in the PS matrix, accompanied by stretching of the rubber particles".

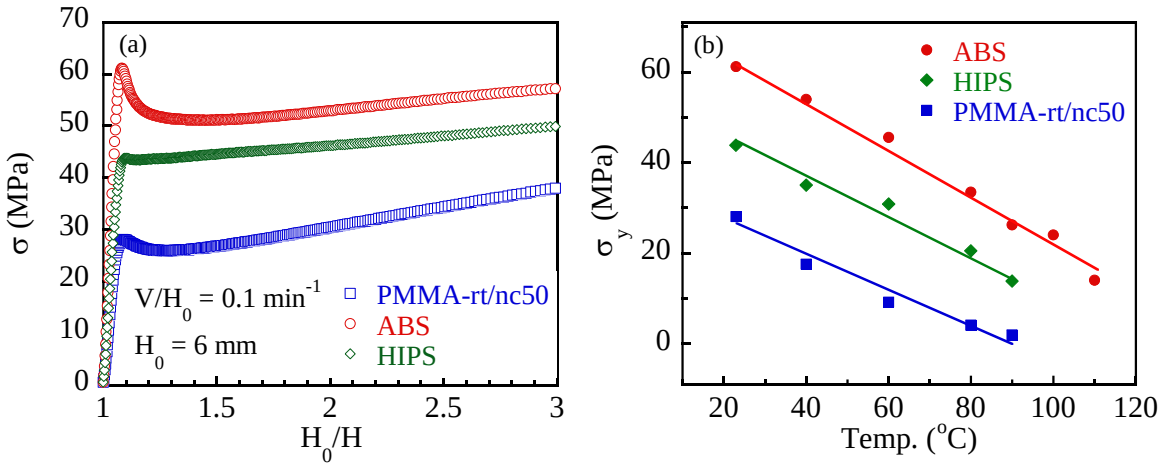

Figure 3.8 (a) Compressive stress σ vs. compression ratio H_0/H at room temperature for HIPS, ABS and PMMA-rt/nc50. (b) Compressive stress maximum, i.e., yield stress σ_y, vs. temperature, indicating absence of any brittle-ductile transition in uniaxial compression of all three samples. Cylindrical samples of 6 mm × 6 mm (diameter × height) were compressed with an initial rate of $V/H_0 = 0.1\ min^{-1}$.

3.3.4 Effects of Melt Stretching on HIPS and ABS: Switching from Brittle to Ductile Responses

Brittle polymer glasses such as PS, PMMA and SAN, after melt-stretching along Z axis, can become ductile at room temperature when drawn in the Z direction.[40, 51, 96-97] This phenomenon can be explained by recognizing the geometric condensation effect[10-11, 98] due to affine-like stretching of the entanglement network. According to our picture,[10] pre-melt-stretched glassy polymers can yield because the chain network is more effective in mobilizing the dormant segments. After melt stretching the network strands are no longer coiled, thus, they are now effectively closer to one another in the XY plane. It is instructive to explore the effect of melt stretching on HIPS and ABS.

As shown by the stress vs. strain curves in Figure 3.3, HIPS, ABS and PMMA-rt/nc50 can be successfully melt-stretched. To preserve the melt-stretching effect, the samples are immediately quenched to room temperature with spray of icy water. For HIPS most of the melt-stretching took place at 120 $^{\circ}$C except for one case (circles) where the melt-stretching took place at 110 $^{\circ}$C to achieve stronger melt stretching effect. Figure 3.9(a) shows the stress vs. strain curves obtained from room-temperature drawing of these HIPS samples involving two drawing speeds. With increasing level of melt stretching, HIPS become stronger, i.e., resisting the imposed drawing at increasingly higher stress levels. Pure PS shows similar characteristics.[40] The stronger stress responses suggest that the chain network directly contributes to the measured stress.

Several specific comments are in order on Figure 3.9(a). At $\lambda = 2$, the effect of melt stretching merely strengthens the PS matrix along the direction of melt stretching by

causing geometric condensation of the chain network. This level of melt stretching is apparently insufficient to turn the sample ductile at room temperature. Consequently, as shown by the up-pointing triangles in Figure 3.9(b), the width of the specimen remains unchanged when the length has doubled. However, at $\lambda = 4$, the pre-melt-stretched HIPS can yield at $L/L_0 = 1.3$, after an initial period of crazing and whitening, as indicated by the second peak in the stress vs. strain curve (squares). Specifically, the specimen width did not change until shear yielding initiated necking at ca. $L/L_0 = 1.3$ that causes the width to decrease to reach a natural draw ratio, as shown by down-pointing triangles.

More remarkably, when the same pre-melt-stretched ($\lambda = 4$) HIPS is drawn at higher rate of $V/L_0 = 1\ min^{-1}$, as shown by the diamonds in Figure 3.9(b), the sample behaves like a ductile polymer, free of crazing and whitening, with shear yielding and onset of necking taking place at a typical few percent of strain. In other words, at a higher rate of extension, our sample is more ductile, contrary to the common trend that a glassy polymer should be less ductile at higher rates of deformation. Thus, this striking feature is reminiscent of a recent report in the literature[44] where PS was shown to exhibit re-entry behavior, i.e., PS was found to be ductile at one drawing speed and but undergo brittle-like fracture during drawing a lower speed because of the emergence of massive crazing. The present pre-melt-stretched HIPS demonstrates a similar characteristic: yielding without crazing at $V/L_0 = 1\ min^{-1}$ but crazing and whitening at $V/L_0 = 0.1\ min^{-1}$. However, unlike pure PS, this system is capable of displaying delayed yielding as described above. It is the crazing and whitening that delayed the yielding. In other words, although the nominal strain L/L_0 is high but still

lower than 1.3, the craze-free parts of the PS matrix have hardly experienced sufficient strain to reach the condition for yielding until L/L_0 exceeds 1.3.

For $\lambda = 5$, the pre-melt-stretched HIPS yielded at tensile stress maximum within a small strain of 5%, characteristic of a typical ductile glassy polymer. However, the specimen still whitened after the yield point. In spite of whitening, the sample did undergo plastic deformation as a result of shear-yielding induced necking and stable neck front propagation. In all cases except for the circles in Figure 3.9(a), the samples whiten at the first peak in the engineering stress because the melt-stretching is still not sufficiently effective to promote yielding and prevent crazing. The right photo in Figure 3.9(c) shows the whitened sample at the end of the drawing according to the left-pointing triangles in Figure 3.9(a).

In contrast, when stronger melt-stretching (at 110 ^{o}C) is applied to HIPS as indicated in the stress vs. strain curve (down-pointing triangles) in Figure 3.3, we can draw HIPS free of whitening, corresponding to the circles in Figure 3.9(a), as shown by the left photo in Figure 3.9(c), in contrast to the other photo. The phenomenon suggests that (a) due to the geometric condensation the PS matrix can reach the point of yielding during drawing to avoid crazing; (b) conversely because of yielding the chain tension in this modified HIPS is insufficiently high to cause rubbery cavitation. It is remarkable nevertheless that there is no whitening even at the end of the drawing. In fact, the absence of whitening calls into question what detailed molecular processes take place to cause the rubbery cavitation. It is beyond the scope of the present study to clarify the molecular mechanism for the rubbery cavitation. However, it is reasonable to assert that the rubbery cavitation is initiated by

crazing in the PS matrix. When crazing is absent due to the melt stretching, the corresponding strain localization is no longer present to cause cavitation in the rubber phase.

It is useful to capture the rather unusual sequence of events observed in Figure 3.9(b) by presenting a schematic illustration as shown in Figure 3.9(d). HIPS contains rubbery phase as shown by the circles in (i) at $L/L_0 = 1$. Upon drawing, crazes emerge as shown in (ii). Rubbery phases adjacent to crazing would undergo large localized tensile straining until cavitation takes place in the rubbery particles as shown in (iii). As along as the rubbery phases and the PS matrix do not completely fail, the melt-stretching-enhanced PS matrix has a chance to experience sufficient strains and reach the state of activation. Yielding occurs because the PS matrix awoke from its dormant state as shown in (iv) in terms of it is turning light from its initial glassy state denoted by the darker background.

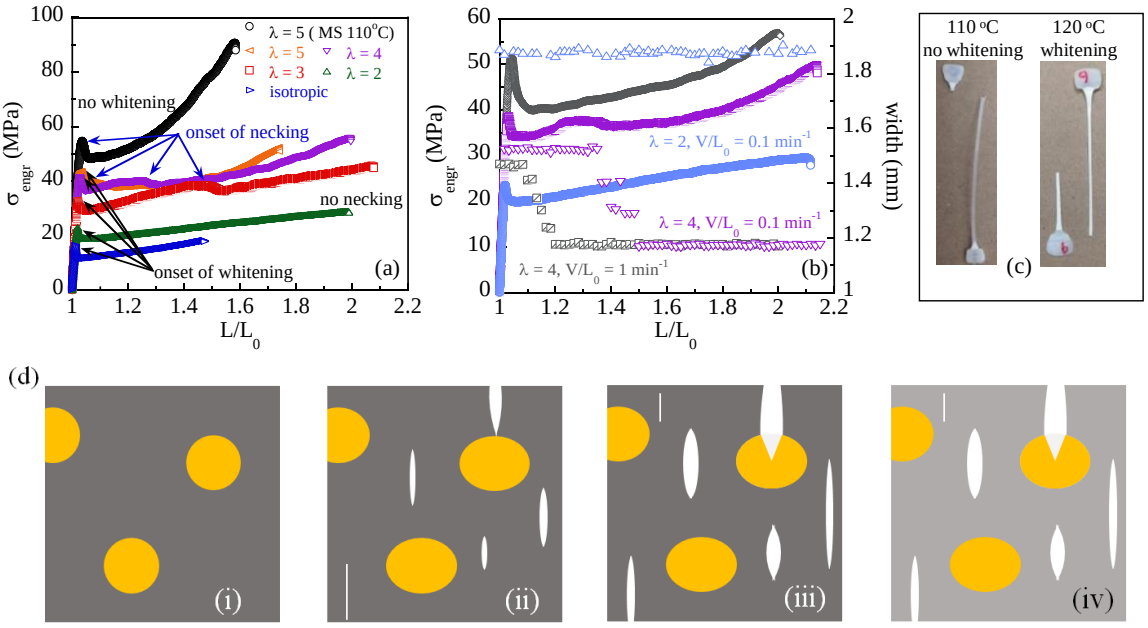

Figure 3.9 Engineering stress σ_{engr} vs. draw ratio L/L_0 at room temperature for (a) isotropic and five pre-melt-stretched HIPS (four melt-stretched at 120 °C and one at 110 °C). (b)

Variation of the width of three pre-melt-treated HIPS samples during drawing at room temperature along with their corresponding stress-strain data. All the measurements were carried out at $V/L_0 = 0.1\ min^{-1}$. For the isotropic sample, $L_0 = 39$ mm. In all other cases, $L_0 = 10$ mm, obtained by cutting from the middle of the melt-stretched samples. Photo in (c) contrasts the whitening-free sample after drawing of HIPS corresponding to circles in (a) with the whitened HIPS after drawing according to the left-pointing triangles. The case of delayed yielding represented by the squares in (b) may be depicted by the sketch given in (d).

For a second example, ABS specimens are subjected to stronger melt-stretching conditions evidenced by the larger positive deviation from the rubber elasticity line shown in the Figure 3.3(b). As shown in Figure 3.10, melt-stretching not only elevated the stress responses but also allowed the ABS to undergo shear yielding and necking. These three melt-stretched samples did not show whitening during the drawing. The higher attainable stress before the yield point at higher λ is an indication that the chain network contributes to the stress buildup even in the pre-yield regime. Specifically, the condition of $\lambda = 2$ is sufficient to turn ABS ductile, as confirmed by the appearance of necking upon reaching the stress maximum. The sufficient melt-stretching promotes yielding of the glassy matrix and prevents crazing. As consequence and similar to the case of strong melt-stretching of PS, whitening can be expected to be absent. Thus, for both HIPS and ABS we are able to apply melt stretching to convert these rubber-toughened glassy polymers into much stronger whitening-free materials.

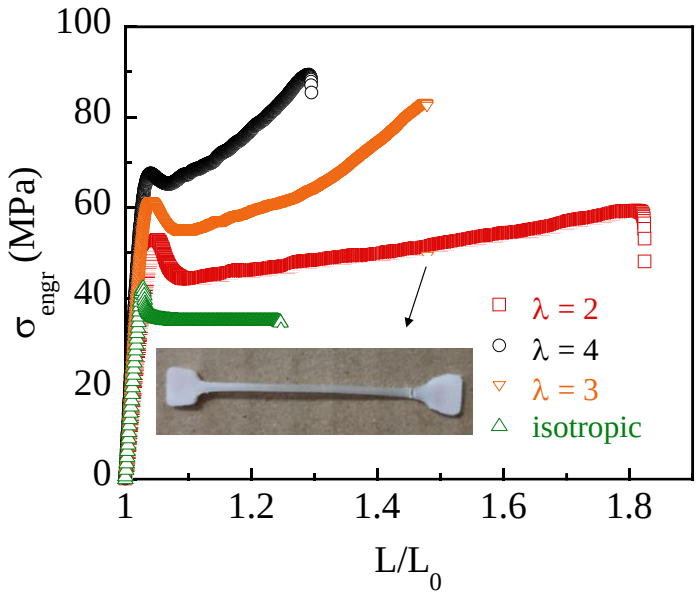

Figure 3.10 Engineering stress σ_{engr} vs. draw ratio L/L_0 for isotropic and three pre-melt-stretched ABS samples at $V/L_0 = 0.1\ min^{-1}$. For the isotropic sample, $L_0 = 39$ mm. In all other cases, $L_0 = 10$ mm, obtained by cutting from the middle of the melt-stretched samples. The inset photo shows the disappearance of crazing and whitening for the melt stretched sample ($\lambda = 2$).

3.3.5 Surprising Ductile Tenacity of PMMA-rt/nc

The effect of melt stretching is unsurprising on PMMA-rt/nc50 when examined in a subsequent drawing at room temperature along the same direction as that of the melt stretching, as shown in Figure 3.11. Because of the accumulated straining, the pre-melt-stretched specimens are less drawable, as expected, similar to the previous observations[40] of the melt-stretching effect on PS and PMMA.

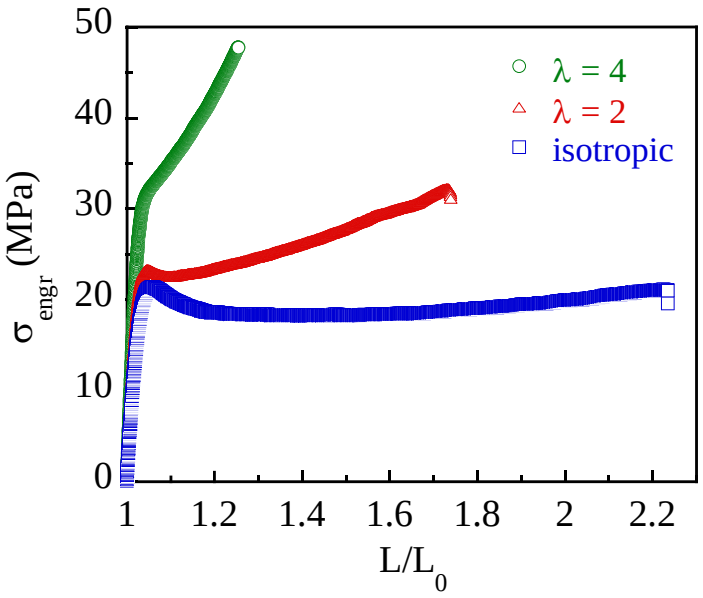

Figure 3.11 Engineering stress σ_{engr} vs. draw ratio L/L_0 for isotropic and two pre-melt-stretched PMMA-NC50. For all the measurements V/L_0 = 0.1 min^{-1}. For the isotropic sample L_0 = 39 mm. In all other cases, L_0 = 10 mm, obtained by cutting from the middle of the melt-stretched samples.

On the other hands, surprise awaits us when the pre-melt-stretched PMMA-rt/nc50 is examined by uniaxial drawing in the direction perpendicular to the melt-stretching direction. According to our recent understanding,[10] the chain network undergoes dilation upon affine-like melt stretching with respect to the direction perpendicular to the melt stretching direction. Consequently, melt-stretching would have adverse effect on the ductility of melt-stretched glassy polymers that are subjected to drawing perpendicular to the melt stretching direction. For example, it has been shown[40] that the extremely ductile bisphenol-A polycarbonate (bp-A PC) turns brittle during room-temperature drawing perpendicular to the melt stretching direction. We first subjected PMMA-rt/nc50 to melt-

stretching at T = 115 °C to a stretching ratio of λ = 3. Then this pre-melt stretched sample was further drawn at room temperature to a draw ratio of 1.47, as shown in Figure 3.12(a). Subsequently, the pre-elongated sample was cut into stripes to be drawn at three speeds in the direction perpendicular to that of the melt stretching. As shown in Figure 3.12(b), the effect to pre-stretching is rather strong, evidenced by the sharply reduced Young's modulus shown in the inset, which is an indication that the intrachain bonding makes a sizable contribution to the Young's modulus. Remarkably, these perpendicularly elongated PMMA-rt/nc50 are still able to yield and draw, displaying lower yield stress (relative to that of the isotropic sample) as expected, except for the data acquired with the highest stretching rate of 100 min^{-1}. Since all known ductile polymer glasses (including bp-A PC) turn brittle during extension in the direction perpendicular to the pre-melt-stretching direction, PMMA-rt/nc50 is truly exceptional and reveals its innate ability to allow activation of the PMMA matrix due to the presence of 50% nano-rubbery particles.

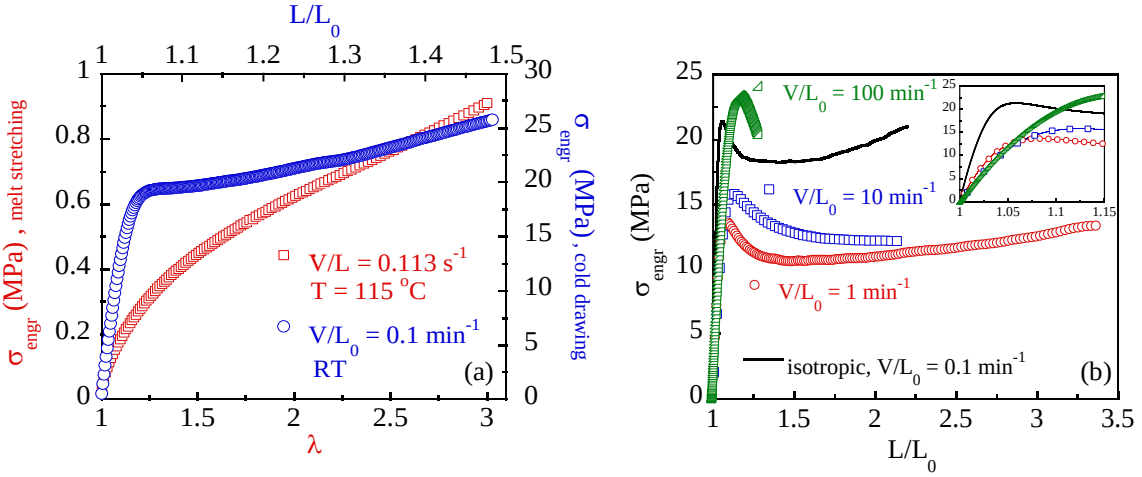

Figure 3.12 (a) Engineering stress σ_{engr} vs. stretching ratio λ and draw ratio L/L_0, involving melt stretching of PMMA-rt/nc50 at T = 115 °C (red squares) and subsequent cold drawing

(blue circles) at room temperature along the melt stretching direction. (b) Engineering stress σ_{engr} vs. draw ratio L/L_0 for cold-drawing of pre-melt-stretched PMMA-rt/nc50 along a direction perpendicular to the pre-melt-stretching direction.

3.3.6 Further Discussion

The preceding section has presented pertinent experimental data to illuminate the conventional rubber toughening mechanism and examine a new class of rubber-toughened PMMA that follows a strategy to directly "plasticize" the glassy matrix without losing the chain network and desirable rigidity. The contrast between HIPS and PMMA-rt/nc highlights how the new mechanism successfully tackled the challenge to promote ductility by direct influence of the rubbery inclusions on the glassy matrix while maintaining structural connectivity through chemical linkages between the PMMA chain network and rubbery domains. Given the length scales associated with the average size of the rubbery particles and distance between them, being on the order of tens of nanometers, the new mechanism exploited the well-known effects from the literature of polymer thin films[75-79] that a glassy polymer can experience depression of its glass transition temperature in contact with a rubbery phase. The DMA data in Figure 3.4(c) indicated the absence of a sharp glass transition and uncharacteristically showed that the loss modulus has no peak at the location where pure PMMA makes a glass transition, in contrast to the DMA data of HIPS and ABS in Figures 3.4(b) and 3.4(c). The effect of the rubbery phase on the glassy PMMA matrix is so strong that even pre-melt-stretched sample can yield when drawn in the perpendicular direction. In fact, the behavior presented in Figure 3.12(b) suggests that the glassy PMMA matrix stands ready (due to the influence of the rubbery phase) to

undergo plastic deformation at room temperature even when the chain network is dilated, i.e., made less effective by melt stretching.

In the conventional rubber-toughened glassy polymers, the role of the rubbery inclusion is not to directly cause depression of the glass transition temperature for the glassy matrix. Consequently, no true macroscopic yielding through molecular activation of the matrix ever takes place during room temperature drawing of HIPS and ABS. The incorporation of the rubber phase stops crazing from resulting in immediate catastrophic cracks by self-sacrifice, i.e., cavitation. The strategy delays the ultimate failure and dissipates the imposed mechanical energy. The stress vs. strain curve shows the deceiving apparent yield-like response with the stress leveling off although no yielding occurs in the sense of Eyring's activation. Actually, the stress stops increasing precisely when whitening starts to be observable. The subsequent drawing is possible as more rubbery cavitation events occurs to accommodate the increasing overall degree of extension. No plastic deformation of the glassy matrix takes place because the specimen remains incapable of responding to the extension by contraction of its transverse dimensions. The effects of melt-stretching on HIPS and ABS are revealing. The melt stretching can not only make them ductile through the same mechanism of geometric condensation that also applies to pure PS and SAN but also allow us to conclude that crazing is the precursor to rubbery cavitation. During drawing of untreated HIPS and ABS at room temperature, crazing occurs in the glassy matrix since it cannot be effectively "plasticized" by the rubbery phase. Crazing induces the rubber cavitation. Conversely, rubber cavitation prevents the crazes from reaching the unstable state to become runaway macroscopic cracks. In absence of

crazing, which is realizable in HIPS and ABS through melt-stretching that promotes activation of the glassy matrix, the rubbery phase is actually sufficiently strong, allowing the glassy matrix to undergo yielding and plastic deformation without developing cavitation.

3.4 Summary

Using HIPS, ABS and a new PMMA-based nanocomposite, we have elucidated the two different rubber-toughening mechanisms. The conventional mechanism involves copolymerization and phase separation to incorporate micron-sized rubbery phase into the glassy matrix. Instead of a few percent of extension before brittle fracture, as the unmodified glassy PS and SAN do, the HIPS and ABS can undergo as much as 50% extension before failure. The present study clarifies that such conventional rubber-toughened polymers accommodate the imposed extension by cavitation of the rubbery phase without any plastic deformation of the glassy matrix. In other words, at room temperature no yielding takes place during the drawing of HIPS and ABS unless they have undergone adequate melt stretching. Specifically, we demonstrate the brittle-ductile transition (BDT) for HIPS and ABS is rather close to their glass transition temperature. For example, at room temperature the lack of evidence for plastic deformation beyond the apparent yield point (when the tensile stress decreases to increase) is the observation that the specimen width stays constant instead of adjusting or shrinking during the extension. In contrast, above the BDT, the plastic deformation occurs, characterized by the contraction of the transverse dimension, e.g., the width going with the draw ratio L/L_0 as $(L/L_0)^{-1/2}$.

By examining the effect of pre-melt-stretching, we uncovered the causal relationship between crazing and whitening. At least for the HIPS and ABS under present study, it is found that adequate pre-melt stretching can prevent HIPS and ABS from developing crazing during the pre-yield drawing. In absence of crazing, HIPS and ABS no longer show whitening, which is widely known to originate from cavitation of the rubber phase. While HIPS and ABS with sufficient pre-melt-stretching can undergo at room temperature true yielding and plastic deformation by necking without whitening, the modestly melt-stretched samples show delayed yielding, i.e., a combination of initial crazing and whitening and subsequent shear-yielding-induced necking along with plastic deformation. When yielding is possible due to the melt stretching effect that produces the geometric condensation effect, the pre-existing whitening does not appear to result in premature failure, further suggesting that the brittle fracture of HIPS and ABS is a result of the failure of the glassy matrix whose molecular origin is the same as that for pure PS and SAN, as discussed[10] in detail before. In short, the brittle fracture occurs when sufficient chain tension builds up to cause imbalance between the intrachain force and the available intersegmental force that arises from the intermolecular uncrossability.

The new rubber-toughened PMMA (PMMA-rt/nc) is a nanocomposite that accomplishes the objective of direct activation of the PMMA matrix with nano-size rubber particles. Here the nanoparticles have crosslinked rubbery cores and PMMA shells that are covalently-bonded to the core. Our experiments on this new class of rubber-toughened PMMA confirms its extreme ductility in the sense that even perpendicular drawing (to the direction of melt stretching) of a pre-melt-stretched PMMA-rt/nc still results in ductile

response and plastic deformation. This new material represents a novel approach to the concept of polymer nanocomposites where the "fillers" are typically the more rigid component relative to the matrix. Here the novelty is not just in the inversion of the polymer nanocomposite concept but rather in how it exploits nanoscale "plasticization" or the well-known T_g depression effect from the polymer thin-film literature to achieve mechanical ductility by easing the task to activate the glassy matrix. In PMMA-rt/nc the PMMA chains stand ready to be activated at room temperature thanks to the fact that they exist in nanoscopic-sized spaces between rubbery domains.

CHAPTER IV

MOLECULAR INSIGHTS INTO THE DEFORMATION OF POLYMER GLASSES REVEALED BY REAL-TIME BIREFRINGENCE MEASUREMENTS

4.1 Introduction

Molecular designing of polymeric materials, especially polymer glasses, with advanced mechanical properties, is impossible in absence of a deep understanding of the ongoing molecular events during large deformation of these materials. Besides molecular dynamic (MD) simulation[99-102], there is no direct experimental technique to study the structural changes at the molecular level that contribute to emergence of stress during macroscopic mechanical experiment. Unlike stress, which is an implicit resultant of deformation, birefringence is an explicit consequence of deformation and it is easier to establish a relation between structural changes and birefringence development during deformation. Therefore, simultaneous measurement of birefringence and stress and finding correlation between them could be a conceivable approach to reach a molecular-level understanding of the mechanics of polymer glasses.

Deformation of polymers can lead to polarizability anisotropy at different length scales[103-104]. For the specific case of amorphous polymers; polymer melts above T_g and polymer glasses below T_g, the polarizability anisotropy may stem from the conformational

changes at the chain level, or orientation of side groups or repeat unit (in absence of side group). Considering the uniaxial deformation, one can define ordinary and extraordinary axes. The ordinary axis is defined along the direction of the applied force/displacement and the direction perpendicular to it, is the direction of extraordinary axis. The refractive index difference between these two directions, which basically arises due to the polarizability anisotropy between the corresponding directions, is called birefringence Δn and defined as $\Delta n = n_o - n_e$, where the n is the refractive index and the indexes of o and e refers to the ordinary and extraordinary axes[105].

4.1.1 Correlating Stress and Birefringence

At the melt state and conventional deformation rates, where we do not have any elastic contribution from the intersegmental interactions[106-107], polarizability anisotropy of the repeating unit as a whole is determining factor of birefringence. In this regime stress σ and birefringence Δn are correlated through the so-called stress-optical coefficient C, defined as $C = \Delta n / \sigma$[108]. By increasing the deformation rate which is feasible at sufficiently low temperatures, e.g. close to T_g, other sources start to contribute into the both stress[107, 109] and birefringence, therefore the relationship between stress and birefringence is no longer as straight forward as what was previously represented by stress-optical rule ($\Delta n = C\sigma$)[110].

Unlike the melt state, where the contribution into the birefringence is mainly from conformational changes at the chain level, at sufficiently cold temperatures below T_g, especially at small strains, it is the polarizability anisotropy of the side group[111-112] that mainly controls the birefringence. Because of the practical importance of birefringence measurements at these temperatures in designing optical devices, and desire to make simple

estimation of the birefringence from stress data or vice versa, analogous to the melt state, the stress-optical coefficient for the glassy state C_g has been introduced in the engineering literature[113-114] to related stress and birefringence in the polymer glasses $\Delta n = C_g \sigma$.

Similar to the birefringence that can have two sources, i.e. conformational change and side group orientation, our molecular dynamic simulations indicate that macroscopic stress that shows up during large deformation of polymer chains may have two components. In the melt state and the conventional deformation rates it is the intra chain component which results in the entropic stress. On the other hand, in the glassy state both inter and intra segmental components are dictating the overall stress value[99]. While, the inter-segmental component of the stress highly depends on the deformation rate, birefringence may not have the same dependency on deformation rate. Therefore, relating birefringence and stress at the glassy state through stress-optical rule, where the stress and birefringence may not necessarily have the same time-dependency, could be an erroneous deduction. In other words, the stress-optical coefficient of the glassy state should not essentially be a constant value and it can depend on the deformation-rate. In short, the dependency of birefringence and stress to the deformation rate in the melt state is same, while for the glassy state the dependency of the stress and birefringence to the deformation rate is not necessarily the same. Replacing the stress-optical coefficient with the strain-optical coefficient may initially seem as a better solution to resolve the problematic effect of rate-dependency of the stress-optical coefficient, however since the birefringence in the glassy state that arises from deformation of the side groups, itself is rate-dependent, therefore we will face the similar problem, i.e. strain-optical coefficient will depend on the deformation rate.

4.1.2 Objective and Structure of this Chapter

Having the preceding long introduction about the origins of birefringence and stress in the deformation of amorphous polymers, in this chapter, after experimental section, we will initially present the birefringence development during uniaxial extension of the two most common polymer glasses; PS and PMMA, and provide explanation regarding the origin of the developed birefringence in each case. Then, for the first time, change of birefringence in the post-yield deformation of these two polymer glasses is measured and contrasted with its values in pre-yield and also melt state. In continue, the birefringence chanes during stress relaxation of PS and PMMA from pre and post-yield, and also creep experiment are compared with respect to molecular structure of these polymers and origins of stress. Attempts are made to explain the reasons behind correlation or decorrelation between birefringence and stress data.

4.2 Experimental

4.2.1 Materials

Two types of polymer glasses including Poly (methyl methacrylate) (PMMA, Arkema, Altuglas) and polystyrene (PS, Dow Chemical, Styron 663) with the molecular weight Mw, poly dispersity index PDI of 105 kg/mol, 1.91 and 319 kg/mol, 1.44 were used in this study. The glass transition temperature T_g of PMMA and PS is respectively equal to 114 ˚C and 109 ˚C.

4.2.2 Sample Preparation

Standard dog-bone shape samples with the dimension of 30 mm by 10 mm by 2 mm (length, width, and thickness) were prepared for tensile deformation, creep and stress

relaxation at room temperature and melt stretching above T_g, by press-molding of resins using Carver™ Lab Press at 200 °C under a load of 9000 kg for 30 min to let polymer chains fully relax before unloading and subsequent quenching.

4.2.3 Melt Stretching

To alter the chain network density of PS and PMMA, they were subjected to melt stretching above T_g under different conditions in terms of the Hencky rate, stretching ratio, and temperature. Stretching was performed using Instron tester (model 5969) equipped with a home-made environmental temperature control chamber. Figure 1 shows the engineering stress σ_{engr} vs stretching ratio λ for these samples. After melt-stretching, samples were immediately quenched below T_g in order to preserve the effect of stretching. It was indicated before that such melt-stretched samples turn ductile when they are further drawing along the stretching direction at room temperature RT[115].

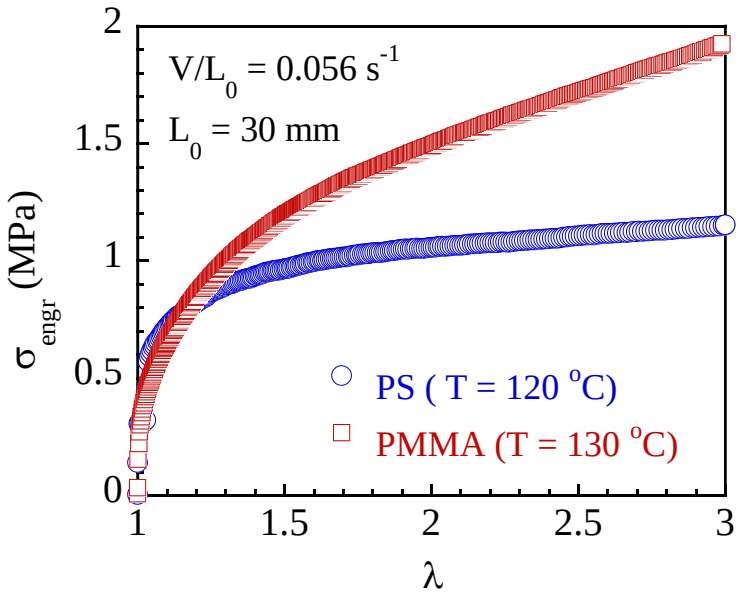

Figure 4.1 Engineering stress σ_{engr} vs stretching ratio λ during melt-stretching of PS and PMMA respectively, at 120 ˚C and 130 ˚C with the Hencky rate V/L_0 of 0.056 s^{-1}.

4.2.4 Real-time Birefringence Measurements

To measure birefringence of polymer glasses (PS and PMMA) during mechanical experiment, two setups were developed. Figure 4.2 is a schematic representation of those setups. The first setup Figure 4.2(a) uses a green laser light source with the wavelength of λ = 532 nm. Sample is clamped between two grips of an Instron tester and located vertically between two linearly-polarized plates which their polarization directions are perpendicular to each other and make 45 degrees with sample. The light that becomes polarized after passing the first polarizer, by transmitting through the sample and hitting the beam splitter, splits into two, one of them is reference light and its intensity is measured using a photodiode in terms of voltage V_2, the other light directly travels and after passing the second polarizer (analyzer) its intensity is measured by another photodiode as V_1. It can be indicated that $V_1/V_2 = A\sin^2(\varphi/2)$ [116], where V_1 and V_2 are voltages recorded from photodiode detectors, A is the calibration factor which is calibrated before each experiment by changing the orientation of the analyzer, i.e. A is equal to V_1/V_2 when the polarizer is located parallel to analyzer, and φ is the phase difference of ordinary and extraordinary light after passing through the sample. The phase difference is related to the absolute value of birefringence using a simple relation $|\Delta n| = \lambda\varphi/2\pi t$, where t is the thickness of the sample and λ is the wavelength of the light source e.g. 532 nm. It worth nothing that here in the description of the birefringence setup, λ denotes the wavelength of the light source, while everywhere else in the text it refers to the stretching ratio during melt stretching. This

setup can measure the absolute value of birefringence. However, it is not possible to measure the sign of birefringence using this setup. In order to measure the directionality of the birefringence we use the second setup shown in Figure 4.2(b). In this setup laser light is replaced by white light source and instead of splitting the light into two parts we record the developed interference colors in the sample, using a CCD camera which is located at the opposite side of the light source. The recorded colors later are converted to the retardation δ using the Michel-Lévy interreference color chart[117]. Normalizing the retardation δ respect to the thickness of sample t gives the absolute value of birefringence; $|\Delta n| = \delta/t$. The directionality of birefringence is determined using an additional element with known birefringence sign forming the background color in the recorded videos. If the change of interreference color recorded by CCD camera which is combination of retardation in sample and background color is in an accumulative order in Michel-Lévy chart (constructing combination), therefore the sign of birefringence in the sample is the same as the birefringent plate (retardation plate), otherwise, i.e. if the colors are going toward left side of Michel-Lévy chart (destructing combination), then the sing of Δn is opposite of the retardation plate.

Real-time birefringence data were collected during three different modes of mechanical experiments: i) uniaxial displacement deformation with a fixed extension rate V/L_0, L_0 is the initial length of sample, until the sample fails in a brittle (for isotropic glasses) or ductile (pre-melt stretched samples) manner. ii) stress relaxation in which the sample initially is deformed with a preset rate V/L_0 until a defined strain L/L_0 and then deformation is stopped at the defined strain L/L_0 while Instron records the stress data and

iii) uniaxial creep experiment where at a specific strain L/L_0, the displacement model deformation stops and the Instron using a feedback loop holds the stress level at a constant value and allows the sample to undergo creep under the constant stress.

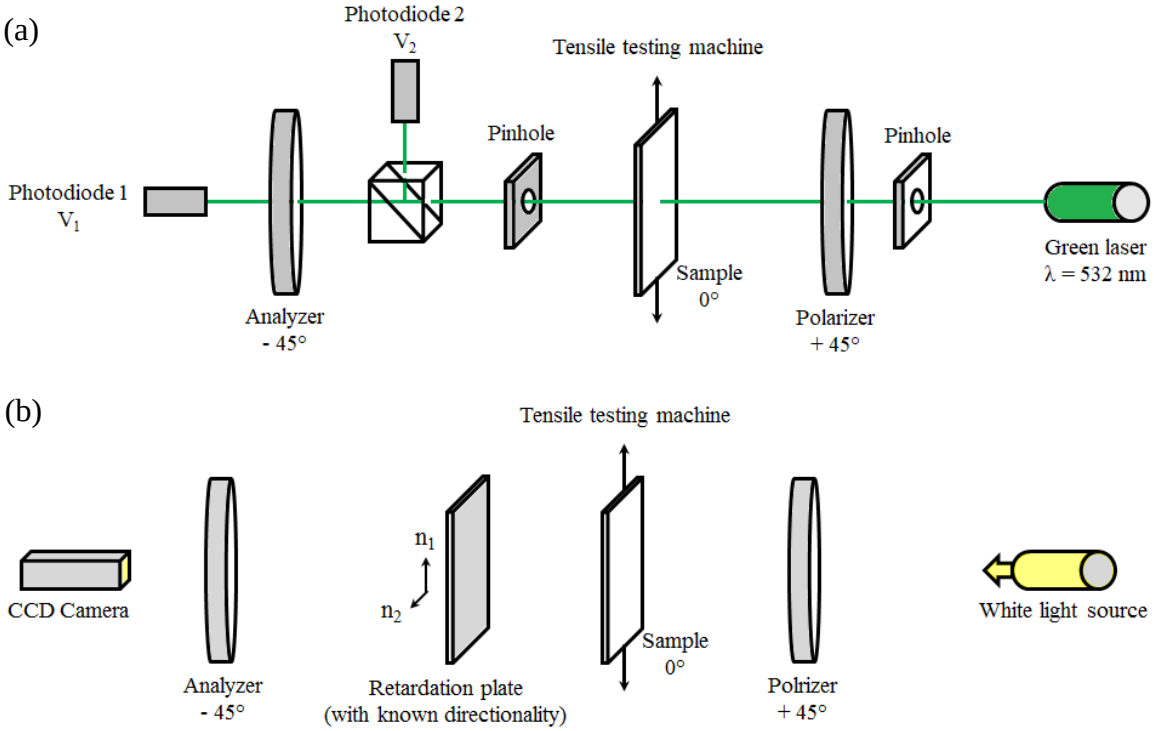

Figure 4.2 Two different optical setups to measure birefringence values during mechanical experiment

4.3 Results and Discussion

4.3.1 Uniaxial Tensile Deformation

4.3.1.1 Pre-Yield Region (Isotopic PS and PMMA)

Figures 4.3 and 4.4 show the real-time birefringence measurements during tensile deformation of isotropic PS and PMMA. These two polymers are brittle at room temperature and fail within few percentages of deformation, so in neither of these two

polymers, the developed birefringence (read from left-hand side of Figures 4.3(a) and 4.4(a)) regardless of its sign, does involve any significant conformational change at the chain level. The polymer chains remain in their coiled conformation, and the sign and magnitude of birefringence is mainly controlled by the side group orientation and/or rotation. In the case of PS, the sign of birefringence is positive, while for PMMA is it negative. Polarizability of phenyl group in PS is uniform in the plane of phenyl ring and non-uniform in the plane perpendicular to the phenyl ring, as shown with the arrows in the bottom cartoon of Figure 4.3. Phenyl group is free to rotate around the bond that connects it to the backbone[118]. We can consider phenyl rings as the randomly dispersed disks in a uniform media, during defamation these disks prefer to align in the extension direction and since the polarizability is larger in the plane of disks compared to polarizability in the direction perpendicular to the plane of disks, so the developed birefringence has positive value.

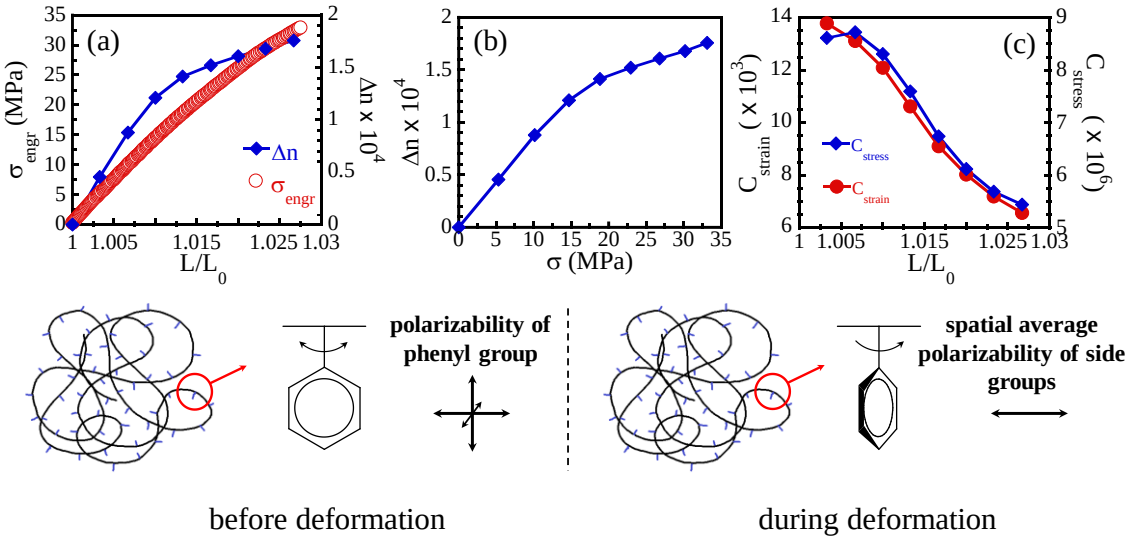

Figure 4.3 Real-time measurement of birefringence during tensile deformation of PS with extension rate of $V/L_0 = 0.1\ min^{-1}$. (a) simultaneous recording of engineering stress σ_{engr} and birefringence Δn vs draw ratio L/L_0. (b) birefringence Δn vs stress σ. (c) strain-optical coefficient C_{strain} and stress-optical coefficient C_{stress} vs draw ratio L/L_0. Lower set of images schematically indicate the sources of polarizability and the reason behind development of positive birefringence during room temperature deformation of PS (drawing direction is horizontal).

The situation in PMMA is a little bit more complex. In PMMA, the ester side group as a whole, can rotate around C-C bond connected to the main chain, meanwhile OCH3 can rotate around C-O bond. Also, C=O and COCH3 are the main chemical constitute that control the polarizability of side group[112]. Depending on the rotation of these two rotating bonds it is possible that the average polarizability gets aligned in the direction of deformation or lateral to it. In our experiment it turns out that for the both melt and glassy states the average polarizability of this group it perpendicular to the orientation direction and therefore the sign of birefringence is negative. Negative birefringence for both melt and glassy states has been recently reported by other groups as well[119-120]. However, there are old reports on the negative birefringence for the glassy state and positive one for the melt state[112, 121].

For the both PS and PMMA at first, birefringence proportionally increases by increasing draw ratio L/L_0 (Figures 4.3(a) and 4.4(a)). After 1% deformation in PS and 3% deformation in PMMA, the slope of birefringence vs. L/L_0 curves decreases. The reduction in slope of Δn vs. L/L_0 could have different reasons: It can be due to creation of crazes that

does not let to develop higher chain tension in the non-crazed parts of samples. It may be because of partial yielding of samples through yielding of primary network or it could be related to the saturation of orientation and/or rotation of side group by increasing strain. The first scenario is more likely to occur for PS which is more prone to crazing[122]. While, in the case of PMMA that does not craze at room temperature[122], the second scenario is more possible to happen, i.e. getting partially yielded and losing ability to develop higher birefringence. In engineering literature, it is common to plot birefringence vs. stress. This representation has been indicated in Figures 4.3(b) and 4.4(b) respectively, for PS and PMMA. This type of representation may be informative form some aspects such as design and stress-field measurement of optical devices, however, scientifically it is not a perceptive depiction. Because for a specific extension rate, birefringence and stress both are the effects of deformation and they may differently depend on time (deformation rate). Similarly, strain-optical coefficient C_{strain} and stress-optical coefficient C_{stress} are the parameters that due to the reasons mentioned in section 4.1.1 are not necessarily constant for glassy polymers, as shown in Figures 4.3(c) and 4.4(c). Indeed, instant slope of Δn vs. L/L_0 and Δn vs. σ could be more informative than C_{strain} and C_{stress}, because they are indicative of how the birefringence instantly response to defamation and stress.

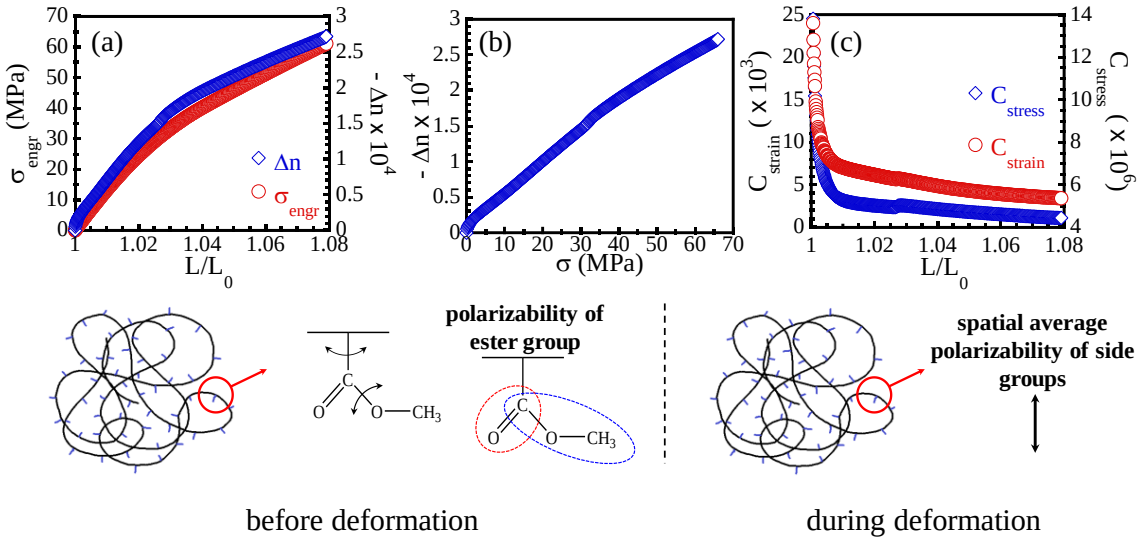

Figure 4.4 Real-time measurement of birefringence during tensile deformation of PMMA with extension rate of $V/L_0 = 0.1\ min^{-1}$. (a) simultaneous recording of engineering stress σ_{engr} and birefringence Δn vs draw ratio L/L_0. (b) birefringence Δn vs stress σ. (c) strain-optical coefficient C_{strain} and stress-optical coefficient C_{stress} vs draw ratio L/L_0. Lower set of images schematically indicate the sources of polarizability and the reason behind development of negative birefringence during room temperature deformation of PMMA (drawing direction is horizontal).

4.3.1.2 Post-Yield Region (Melt-Stretched PS and PMMA)

It has been found that melt-stretching of brittle polymer glasses above T_g makes them ductile when they are further subjected to uniaxial stretching at room temperature along the orientation direction[40]. We implemented this technique to make PS and PMMA ductile at room temperature and trace the birefringence changes in a wider range of deformation including both pre and post-yield regions. Melt-stretching of PS was performed at T = 130 ˚C using the Hencky rate of $\dot{\varepsilon} = 0.056\ s^{-1}$ to the stretching ratio of $\lambda = L/L_0 = 3$. After melt

stretching, sample was immediately quenched below T_g to preserve the stretching effect. Figure 4.5(a) compares the engineering stress σ_{engr} vs draw ratio L/L_0 between isotropic PS which is brittle and pre-melt-stretched ms-PS which is ductile, at room temperature. Comparison of the birefringence of these two samples is made in Figure 4.5 (b). It has to be pointed out that after melt treatment, ms-PS has an initial frozen in birefringence equal to -1.69×10^{-2} and Figure 4.5(b) indicates the additional change in birefringence during cold drawing at room temperature. In other words, the initial birefringence of ms-PS was set to zero and we only measure further changes in birefringence during room temperature drawing. Deformation of PS in the melt state results in negative birefringence[123]. This is due to the fact that phenyl groups are perpendicularly located toward the orientation direction so the polarizability in the lateral direction of phenyl groups averages out to zero while in the direction perpendicular to the main chain it results in large polarizability anisotropy. Figure 4.5(c) is the zoomed in representation of Figure 4.5(b) in the lower deformation range (< 4%). It shows that the birefringence values of PS and ms-PS are initially (< 1.5%) positive and have almost same magnitude, with slightly higher values in the case of ms-PS. The higher value of birefringence in ms-PS could be due to the more effective rotation of pre-aligned phenyl groups during deformation. Around 1.5% deformation, the birefringence of ms-PS starts to decay toward zero while that of PS keeps increasing until failure. Reduction in birefringence of ms-PS can have two sources: relaxation of phenyl rings toward equilibrium conformation and/or conformational change at the chain level where similar to the melt state the polarizability anisotropy of repeat unit is perpendicular to the deformation direction and results in negative birefringence. By

increasing deformation in ms-PS segmental mobility starts to increase. The increase in the mobility at the segmental level is found to be in a way that segmental relaxation rate (τ_α) at yield and post-yield regions, becomes fast enough to accompany with the deformation rate ($\dot{\varepsilon}$), i.e. $Wi_\alpha = \dot{\varepsilon} \times \tau_\alpha \sim 1$[124-125]. However, since the dynamic of side group is faster than segmental dynamic, therefore it is reasonable that mobility increase at sub-segmental level starts to show up at smaller draw ratios (~ 1% for ms-PS) prior to the yield point. Such acceleration in dynamic of side groups is not observed for isotropic PS, because the chain network in PS, unlike ms-PS is not dense enough to easily activate the system. It is worth mentioning that at these small deformations, the negative contribution from conformational change at the chain level cannot considerably influence the total birefringence. Therefore, it is the relaxation of side group that mainly results in decay of birefringence toward zero rather than conformational change of polymer chains. Further deformation of ms-PS results in emergence of negative birefringence after 4% deformation along with strain localization and necking in sample. The birefringence values at the nominal deformation L/L_0 around 1.15 and 1.25 are similar and order of magnitude larger than their values at small strain regions. At these nominal strains, the local draw ratio, calculated from the change in cross-sectional area in the necked part, i.e. $L/L_{0\text{-local}} \sim A_0/A$, is equal to 1.8. The birefringence at post-yield of ms-PS is -5.46×10^{-2}. The negative sign of Δn is because of the uncoiled conformation of polymer chains and perpendicular situation of phenyl rings respect to the chain backbone. The total birefringence in this sample is accumulation of melt and glassy birefringence. Stretching ratio for melt deformation was $L_0/L_i = 3$, L_i is the initial length of sample before melt stretching and L_0 is the length after melt stretching which itself is the

initial length of sample before cold drawing. The draw ratio in the glassy state L/L_0 is 1.8, therefore the total stretching ratio of chains is $L/L_i = L_0/L_i \times L/L_0 = 3 \times 1.8 = 5.4$. This sample has a total birefringence around $(-1.69 \times 10^{-2})_{melt} + (-5.46 \times 10^{-2})_{glass} = -7.15 \times 10^{-2}$. While, if a PS melt is stretched to $\lambda_{ms} = 5.4$ only in the melt state, such sample would have $\Delta n = C_{melt} \times \lambda_{ms} \times \sigma_{engr} = (-4700 \times 10^{-6}) \times 5.4 \times 1.37 = -3.48 \times 10^{-2}$. This comparison shows that deformation in the glassy state results in development of higher birefringence. This could be due to the effective deformation of the chains in the glassy state in comparison to the melt state. Theoretical maximum of chain extension ratio λ_{max} between entanglements calculated as $\lambda_{max} = l_{ent}/l_k = \sqrt{N_e}$ for PS with $N_e \approx 16$[126] is equal to 4. This indicate that after λ_{ms} of 4, defamation may not be affine or there could be slippage in the junctions. This can result in lower value of birefringence in the sample that directly stretched to the λ_{ms} of 5.4 in the melt state, in comparison to the sample which undergone two stage drawing firstly in melt state to $\lambda_{ms} = 3$ and then in the glassy state to $L/L_0 = 1.8$.

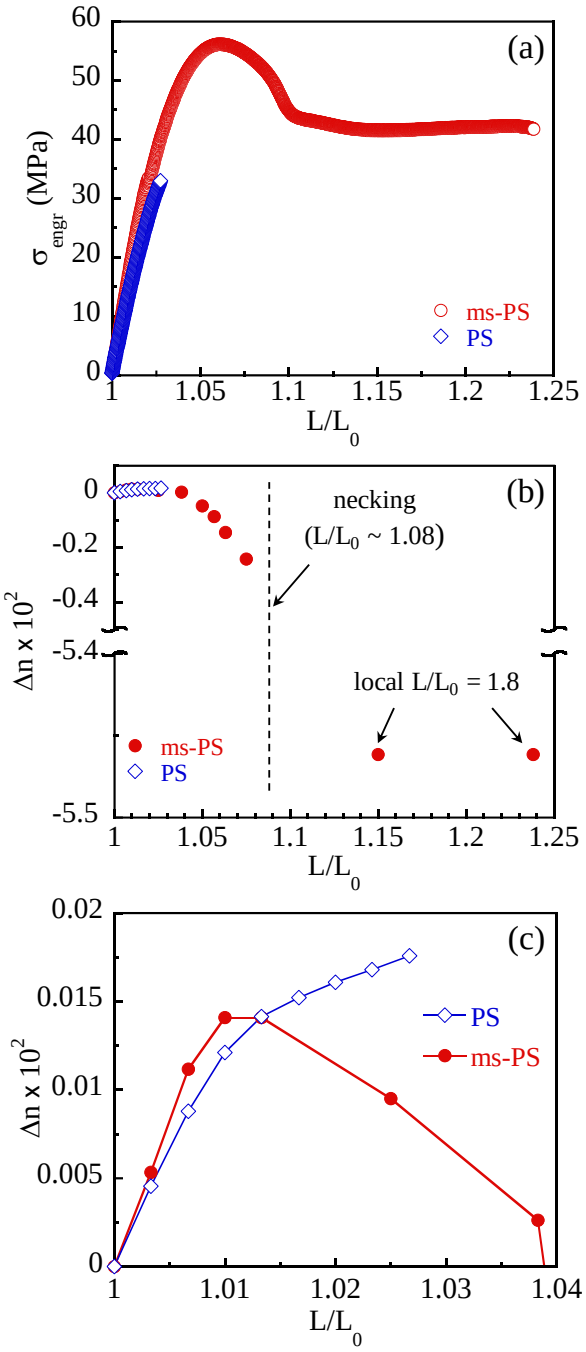

Figure 4.5 Real-time measurement of birefringence during tensile deformation of pre-melt-stretched PS, ms-PS and isotropic PS with extension rate of V/L_0 = 0.1 min^{-1}. (a)

engineering stress σ_{engr} vs draw ratio L/L_0. (b) birefringence Δn vs draw ratio L/L_0. (c) birefringence Δn vs draw ratio L/L_0 for the lower range of draw ratios.

Similar to PS, PMMA was subjected to the melt stretching to the stretching ratio of $\lambda_{ms} = 3$ using the Hencky rate $\dot{\varepsilon}$ of 0.056 s^{-1} at T = 130 ˚C, in order to make it ductile when it is deformed at room temperature in the same direction along the stretching direction. After this melt-treatment sample was immediately quenched below T_g to preserve the orientation in PMMA. The frozen in birefringence in ms-PMMA is equal to -7.7×10^{-4}. Figure 4.6(a) compares the σ_{engr} vs L/L_0 during tensile deformation of ductile ms-PMMA with the brittle isotropic PMMA at room temperature. Unlike ms-PS, ms-PMMA at post-yield uniformly deforms and does not show any strain localization in terms of necking. Development of birefringence during deformation of these samples are compared in Figure 4.6(b). Several points are in order here. First, birefringence sign of both PMMA and ms-PMMA in the glassy state are negative, similar to the melt state. Initially the magnitude of birefringence change, for PMMA and ms-PMMA is almost same. Divergence between magnitude of Δn of these two samples appears around 5% deformation and slope of Δn vs L/L_0 curve decreases for PMMA. While, Δn of ms-PMMA steadily keeps increasing in magnitude by passing the yield point and finally around the onset of strain hardening (15% of deformation) starts to level off and then decrease. Before melt stretching there was better correlation between stress and birefringence while after melt stretching, that correlation is lost, e.g. at 5% deformation the stress reaches the yield point while the birefringence keeps increasing until the onset of strain hardening. Our previous experiments and molecular dynamic simulations indicate that melt-stretching increases the contribution of intra-

segmental component, in deformation and determining the stress value. Therefore, losing the correlation between Δn and stress around yield point in melt-stretched sample, can imply that increase in the intra-segmental contribution into the deformation does not affect the birefringence and the origin of birefringence probably is more controlled by the inter-segmental interactions affecting orientation side groups. Unlike PS case where the orientation and relaxation of side group is highly coupled with backbone though a C-C bond, in the case of PMMA due to the freedom of side group through an additional rotation around the C-O bond, the side group's dynamic may not strictly controlled by the backbone which is intra-segmental in nature. This can explain the reason behind decorrelation of the stress and birefringence around yield point of ms-PMMA. The decrease in the birefringence values at larger strains in the strain hardening region could be because of the further increase in the segmental mobility at the hardening region and stronger effect of higher mobility of backbone on the side group orientation. There are two opposite views about the segmental mobility at the strain hardening region during deformation of polymer glasses; based on the theoretical work of Chen and Schweizer[127] the segmental mobility decreases at the hardening region, while simulation results by Rottler indicate the opposite[128]. Thus, decrease of birefringence in the hardening region in our study could be an experimental support to the second view.

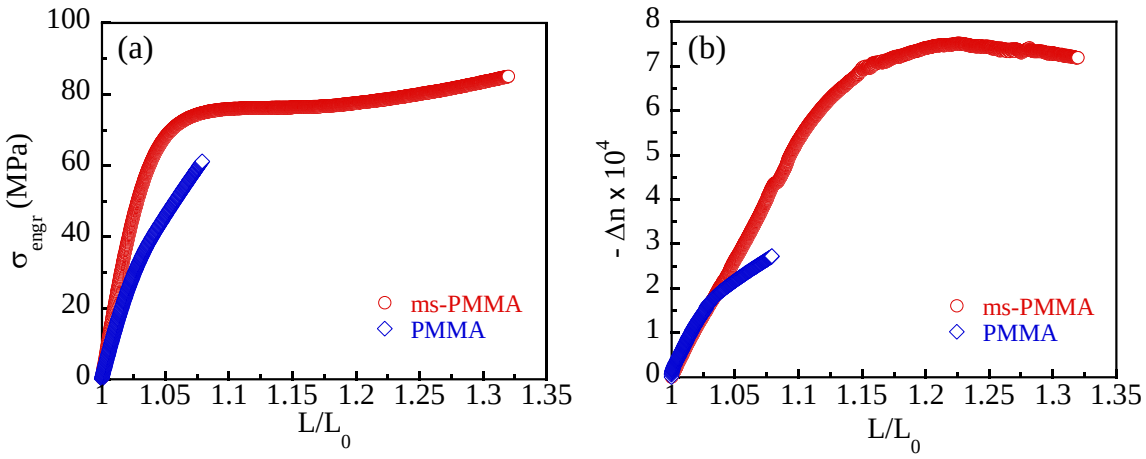

Figure 4.6 Real-time measurement of birefringence during tensile deformation of pre-melt-stretched PMMA, ms-PMMA and isotropic PMMA with extension rate of $V/L_0 = 0.1\ min^{-1}$. (a) engineering stress σ_{engr} vs draw ratio L/L_0. (b) birefringence Δn vs draw ratio L/L_0.

4.3.2 Stress Relaxation

Preceding we are going to compare the stress relaxation of the different samples in pre and post yield regions in order to acquire more insights about the origins of stress and birefringence in deformation of polymer glasses.

Stress relaxation of PS and PMMA were performed in the pre-yield region by stopping the deformation at the strain of $L/L_0 = 1.02$ where the stress is around 25 MPa for both polymers. The initial values of birefringence at the beginning of stress relaxation were equal to 1.6×10^{-4} and -1.4×10^{-4} respectively for PS and PMMA. To establish a fair comparison between the stress relaxation and birefringence relaxation behavior of PS and PMMA, stress and birefringence values during stress relaxation were normalized by their initial values at the beginning of stress relaxation. Figure 4.7 shows the normalized stress σ_{engr}/σ_0 (on the left-hand side) and birefringence $\Delta n/\Delta n_0$ (on the right-hand side) of PS and

PMMA during stress relaxation. For easier comparison between stress and birefringence, same limits are chosen for the ranges of Y axes on left and right sides. It is well known that the stress relaxation in the pre-yield region is controlled by the α process through segmental relaxation[129]. The stress relaxation rate, controlled by segmental relaxation, is faster in the case of PMMA in comparison to the PS. By comparing the birefringence relaxation with the stress relaxation, it turns out that there is no correlation between the relaxation of stress and relaxation of birefringence. The rate of stress relaxation and birefringence relaxation is not the same for an individual sample. This primarily indicates that the birefringence relaxation in not merely controlled by the segmental dynamics. In addition, the absence of correlation between two relaxations is also an indicative of breakdown of stress-optical rule. Moreover, the rate of birefringence relaxation could be either faster or slower than the rate of stress relaxation. It is seen that birefringence drop is faster than stress relaxation for the PS, while the opposite is observed for PMMA. In other words, for PS, relaxation of birefringence is happening faster than the segmental relaxation, whereas in the case of PMMA birefringence relaxation is taking place slower than segmental relaxation (stress relaxation). This is because of the different structures of the side group in these two polymers. In PS the phenyl ring is a planar structure that is free to rotate around the C-C bond that connects it to the backbone, therefore relaxation of phenyl group which results in relaxation of birefringence is a pre-requisite to the relaxation of stress through the segmental relaxation. On the other hand, in PMMA relaxation of side group can involve two types of rotation, rotation around the C-C bond connected to the backbone (similar to the PS) and an additional rotation of CH_3 group around the C-O bond. This additional

rotational freedom, in side-group of PMMA, may generate a situation in which the relaxation of birefringence is not strictly coupled to the relaxation of backbone, therefore, the birefringence in PMMA can relax with slower rate than segmental relaxation, unlike PS where two relaxations are highly coupled.

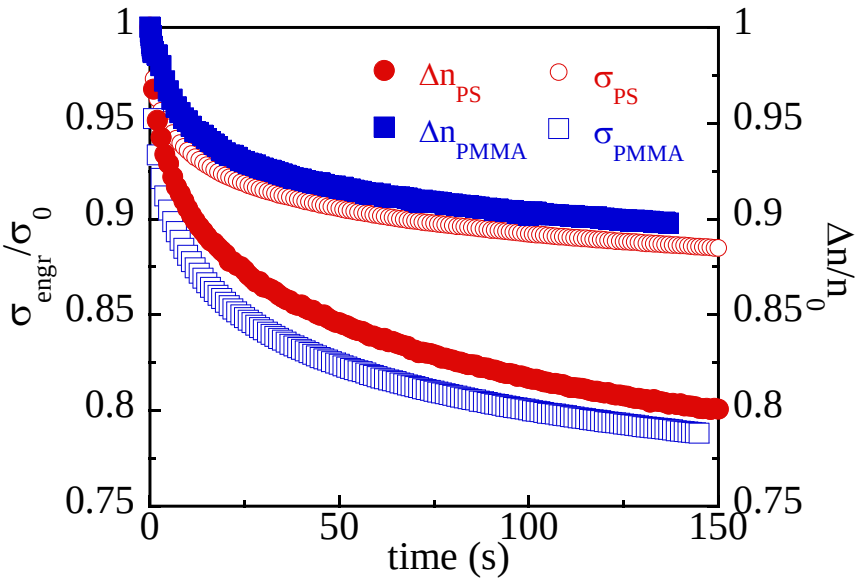

Figure 4.7 Normalized stress σ_{engr}/σ_0 and birefringence $\Delta n/\Delta n_0$ during pre-yield (L/L_0 = 1.02) stress relaxation of PS and PMMA. The t = 0 s is the onset of stress relaxation.

Similar comparison of pre-yield stress and birefringence relaxations was made between PMMA and ms-PMMA at the strain of L/L_0 = 1.02. As it is seen in Figure 4.8(a), at the onset of relaxation (draw ratio of L/L_0 = 1.02), the stress values of PMMA and ms-PMMA are respectively equal to 25 MPa and 38 MPa, while relatively similar values of birefringence were developed due to the deformation to the same strain in these two samples. It has been indicated that pre-melt stretching of a polymer glass increases the contribution of intra-segmental component into the deformation and stress. This is the

reason of higher modulus of ms-PMMA in comparison to isotropic PMMA. The normalized values of stress and birefringence during stress-relaxation are indicated in the Figure 4.8(b). The stress relaxation rate of ms-PMMA is considerably slower than that of isotropic PMMA. As previously mentioned, it is well accepted that the deformation of polymer glasses increases the segmental relaxation during deformation, however to the best of our knowledge there is no report on the effect of pre-melt stretching on the rate of α process. It can be speculated that the reason of slower stress relaxation in ms-PMMA is due to the increased contribution of intra-segmental component of stress after melt-stretching. Our previous studies indicated the persistence of intra-segmental part of stress during post-yield stress relaxation of polymer glasses[99] and here it seems that a similar effect is valid during the pre-yield stress relaxation. The slower relaxation of birefringence in the ms-PMMA where the intra part of stress does not decay may imply that the birefringence relaxation hardly takes place in presence of large amount of intra-segmental stress, while in the PMMA that the larger portion of stress is inter-segmental, the birefringence relaxes with higher rate.

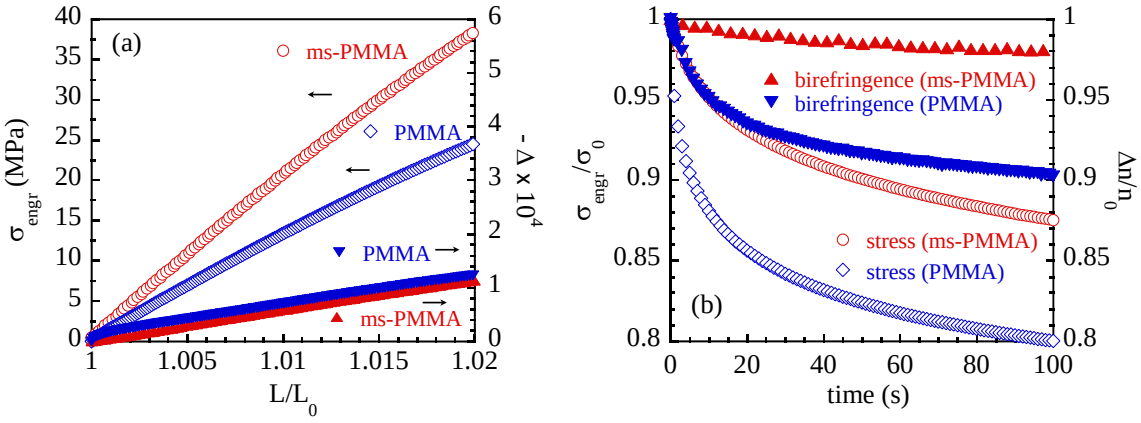

Figure 4.8 (a) stress and birefringence changes during uniaxial deformation of PMMA and ms-PMMA to the strain of L/L0 = 1.02 (b) normalized stress σ_{engr}/σ_0 and birefringence $\Delta n/\Delta n_0$ during pre-yield (L/L_0 = 1.02) stress relaxation of PMMA and ms-PMMA. The t = 0 s is the onset of stress relaxation.

Comparison is also made between the pre- and post-yield stress relaxation of ms-PMMA (Figure 4.9). The rate of stress relaxation is much higher in the post-yield compared to the pre-yield. This is primarily due to the increased segmental mobility in the post-yield region. On the other hand, the birefringence relaxation rate from post-yield is slower than pre-yield. This can again be associated to the increased contrition from intra-segmental component of stress in the post-yield region and more importantly, inability of the relaxation of the birefringence that is developed as a result of conformational change at the chain level at the post-yield, unlike the birefringence at pre-yield which only involves the side group orientation.

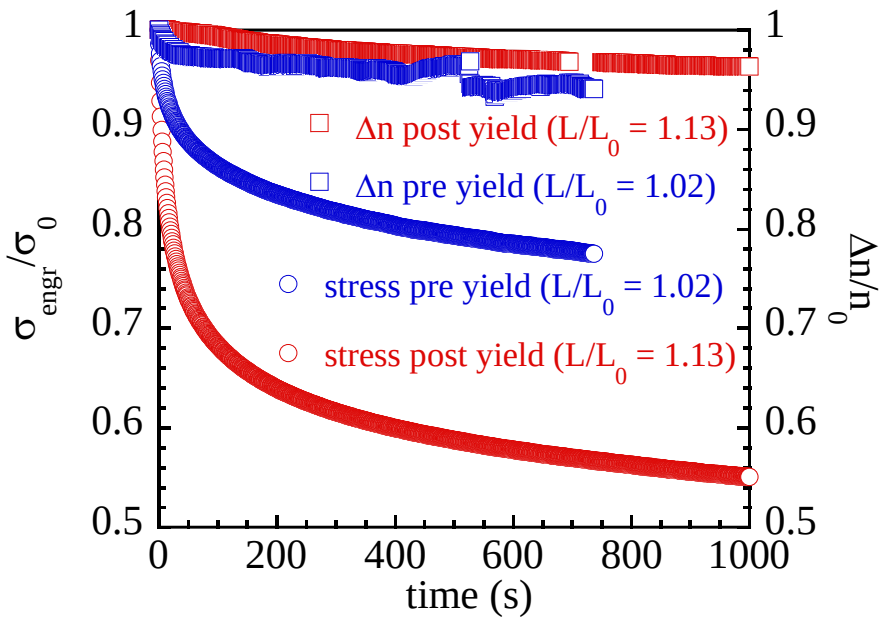

Figure 4.9 Normalized stress σ_{engr}/σ_0 and birefringence $\Delta n/\Delta n_0$ during pre-yield (L/L_0 = 1.02) nad post-yield (L/L_0 = 1.13) stress relaxation of ms- PMMA. The t = 0 s is the onset of stress relaxation.

4.3.3 Creep

Interesting contrasts are observed when we compare the birefringence development during uniaxial creep of PS and PMMA by stopping the uniaxial deformation at L/L_0 = 1.02 and fixing the stress at the corresponding stress value and giving the samples enough time to undergo creep under a fixed stress. Figures 4.10(a) and 4.10(b) show the changes in the strain and absolute values of birefringence during such experiment. PS and PMMA undergo uniaxial creep in absence of any crazes at L/L_0 = 1.02. The creep rate for PMMA is faster than PS which could be due to the faster α process in this polymer, as it was discussed in the results of stress relaxation at pre-yield in Figure 4.7. However, the observed trend in the birefringence data is quite different than the creep data. It is seen that

during creep the birefringence of PMMA keeps increasing, whereas it is decreasing for PS. In the stress relaxation experiment the strain was constant, and birefringence was changing, while in the creep experiment stress is constant and birefringence is changing. These two experiments indicate the failure of respectively strain-optical and stress-optical rules in describing the birefringence in the glassy state. Although the trend of birefringence data in creep experiment looks surprising, the physical interoperation is same as the conclusion drawn in the discussions of Figure 4.7. Creep experiment is in fact a complementary experiment to the stress relaxation form pre-yield of PS and PMMA (Figure 4.7) to show the rate of birefringence relaxation for the PS is much faster than that for PMMA and faster than stress relaxation, as well. In Figure 4.7 we observed that the birefringence relaxation compared to stress relaxation is faster and slower respectively in the case of PS and PMMA. Therefore, in creep experiment, by keeping the stress constant for both polymers, since in the PS, birefringence relaxes faster than stress therefore the constant stress cannot result in increase of birefringence, thus it keeps decreasing. On the other hand, in the case of PMMA where the birefringence relaxation is slower than stress relaxation, by keeping the stress constant birefringence can increase during creep experiment.

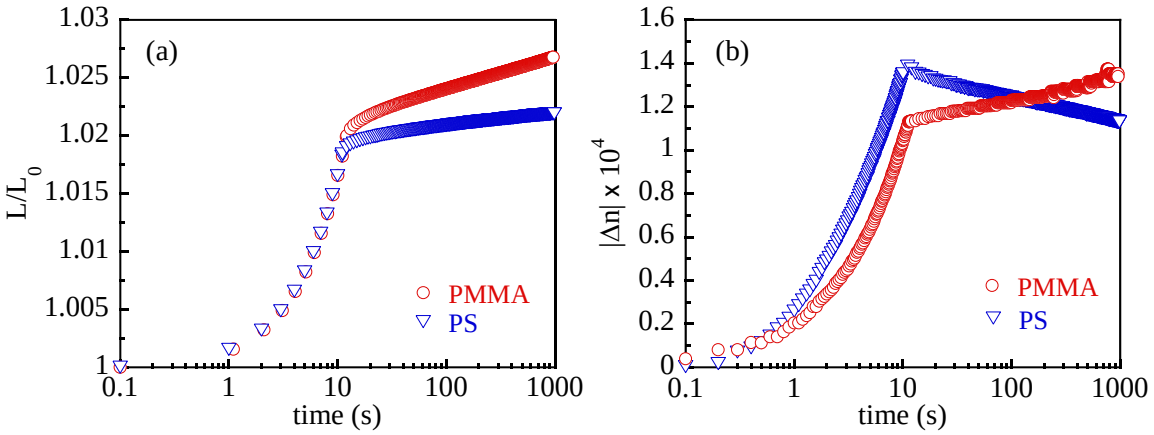

Figure 4.10 Real-time birefringence measurements during uniaxial creep experiment of PMMA and PS. The initial drawing rate was 0.1 min^{-1} and deformation was switched from uniaxial deformation to the creep mode at t = 12 s analogous to $L/L_0 = 1.02$. (a) draw ratio L/L_0 vs. time (b) absolute value of birefringence $|\Delta n|$ vs. time.

4.4 Summary

Simultaneous measurements of stress data and birefringence changes during deformation of two types of polymer glasses PS and PMMA were performed. For the first time birefringence measurements during the post-yield deformation of these two polymer glasses were carried out. The origins of birefringence at pre and post yield deformation were explained regarding the chemical structure of these two polymers. Though different stress relaxation experiments it was indicated that it is not necessarily to have a correlation between stress and birefringence data. In the case of PS the birefringence and stress data are better correlated than in PMMA where the side group has more rotational freedom and its dynamics is more de-coupled from that of backbone. By comparison of stress and birefringence relaxations between PMMA and ms-PMAA it was suggested that in presence

of higher contribution from intra-segmental component into the stress, the birefringence relaxation is taking place slowly. In short, this study was a preliminary attempt toward molecular understanding of the deformation of polymer glasses using the available experimental techniques.

CHAPTER V

INTRODCUTON TO PART B: MOLECULAR MECHANICS OF SEMICRYSTALLINE POLYMERS

After understanding the mechanics of disordered glassy state in the first part of this dissertation (Part A), in the second part (Part B), we are going to investigate mechanics of semicrystalline polymers. Semicrystalline polymers are structurally more complex than polymer glasses and accordingly it is more challenging to understand their nonlinear mechanics. In this chapter we initially present our strategy to study the mechanics of semicrystalline polymers and then briefly introduce the topics of the following three chapters that form the main body of Part B of dissertation.

5.1 Bottom-up Approach to Study Mechanics of Semicrystalline Polymers

A semicrystalline polymer, at a specific temperature, depending on the positive or negative distance from glass transition temperature (T_g) of amorphous phase, can be treated as a composite of glassy and crystalline phases (at $T < T_g$) or melt and crystalline (at $T > T_g$) phases. Because of the structural complexity of semicrystalline polymers, and incomplete understanding of the preceding studies of the molecular mechanics of glassy polymers and nonlinear rheology, study of the mechanics of these class of polymers at the molecular level remains as one of the most challenging areas in polymer physics.

Meanwhile, due to the practical importance of semicrystalline polymers especially polyolefins such as polyethylene and polypropylene, at the continuum level tremendous efforts has been paid to model the stress-strain behavior of those polymers.[130-136] These studies ignored the crucial role of the amorphous phase in delivering the required force and chain tension into the crystalline phase in order to disintegrate it, and mainly focused on modeling the stress-strain curves or characterize the changes in crystalline structure[137-142]. However, the right strategy to tackle this elusive problem, i.e. molecular mechanics of semicrystalline polymers, should be a bottom up approach that first understands the melt rheology and molecular mechanics of pure glassy phase and in the next stage by incorporating crystalline phase into the disordered phase tries to perceive the effects of crystalline phase on the mechanical performance of the resultant composite system. In this regard, study of semicrystalline polymers with higher T_g than room temperature such as polyesters; e.g. poly(l-lactic acid) (PLLA) and poly(ethylene terephthalate) (PET), could be more useful in providing suitable model polymers that are able to be quenched below T_g and produce amorphous counterparts as control samples. Another benefit with these polymers is that we are able to easily study the mechanical behavior both below and above T_g. Previous studies by Flory[143] and Peterlin[144-145] tried to understand the yielding of semicrystalline polymers by characterizing the changes of crystalline phase in presence of stress. More recent studies by Strobl[146-147] on semicrystalline polymers with high T_g treated the crystalline phase as the force-transmitting skeleton. Unlike preceding studies, the main objective of Part B is to understand the semicrystalline state as a composite structure of amorphous and crystalline phases by focusing on the imperative role of the amorphous

phase in connecting the crystalline regions to one another and providing the local stress exerted on the crystalline regions to cause yielding to occur in the crystalline phase. The importance of chain networking in the amorphous phase, and interaction of amorphous phase with crystalline phase in delivering the mechanical input into the crystalline regions are highlighted in our view.

5.2 Structure of Part B of dissertation

In Chapter VI, our molecular picture of the semicrystalline state will be rationalized based on three important mechanical experiments. Based on this molecular picture, a general framework to understand the mechanics of semicrystalline materials will be established and an innovative experiment will be designed to generate an extraordinary case where a semicrystalline polymer shows brittle behavior in uniaxial compression deformation. In Chapter VII we will specifically focus on the tensile deformation behavior of amorphous and semicrystalline Poly (lactic acid) (PLA) in order to understand the effect of presence of crystalline phase on tensile deformation of a typical polymer glass both below and above T_g. Real-time polarized optical microscope (POM) measurements during tensile deformation of semicrystalline PLA along with macroscopic mechanical experiments will reveal that crystallization has adverse effect on drawability and ductility of polymers. Depletion and/or re-arrangement of chain networking during crystallization will be proposed as the main reason of the mechanical weakness of the semicrystalline polymers and we will speculate that the effective deformation of crystalline phase is impossible in absence of a robust amorphous phase. We will testify our conjecture in Chapter VIII and propose a universal strategy to preserve the chain networking during

crystallization. It will be indicated that the semicrystalline polymer which initially was brittle or less drawable in extension turns to completely ductile and drawable material after saving the chain networking during crystallization.

CHAPTER VI

UNIVERSAL FRAMEWORK TO UNDERSTAND THE MOLECULAR MECHANICS OF SEMICRYSTALLINE POLYMERS

6.1 Introduction

Theoretically, fast quenching of a semicrystalline polymer below T_g of its amorphous phase will result in its counterpart glassy state. At a specific temperature, the main difference between two states are the structure of the chain network. In the glassy state, the chain network is inherited from chain entanglement in the melt state, while in the semicrystalline state, structure of chain network is not what is directly obtained from freezing of entanglement network. Evidently, the structure of chain network is significantly altered upon crystallization process during which polymer chains need to re-organize into the crystalline regions. Our experimental results indicate that for the identical experimental conditions during uniaxial mechanical test, the same polymer which is ductile in the glassy state shows brittle behavior in the semicrystalline state. This is the central observation that motivated us to think about the effect of crystallization on the mechanical properties of glassy polymers and study the molecular mechanics of semicrystalline polymers.

In order to study the molecular mechanics of semicrystalline polymers, we initially need to have a clear picture of the structure of these materials at the chain level. However,

there is no direct experimental technique that can visually illustrate the chain-level structure of a polymer in the semicrystalline state. On the other hand, one can always use indirect methods to speculate about the molecular structure of these materials. Therefore, in this chapter using three indirect mechanical experiments we provide a molecular picture of the semicrystalline state of polymers and based on this picture we design innovative experiments to understand the mechanics of this class of polymeric materials as a composite structure of amorphous and crystalline phases. This chapter establishes a groundwork and universal framework for further understanding of the mechanics of semicrystalline polymers in the next two chapters.

6.2 Experimental

6.2.1 Materials

Four commercial semicrystalline polymers including poly(l-lactic acid) (PLLA), poly(ethylene terephthalate) (PET), syndiotactic polystyrene (sPS) and polyamide 12 (PA 12) are used in this study. The weight average molecular weight Mw, entanglement molecular weight Me and glass transition T_g of these polymers are listed in Table 6.1. The T_g of these polymers were obtained using Discovery DSC 2500 (TA instruments) from the heating cycle when they were heated with the rate of 5 °C/min. For each sample the T_g was measured for the two cases; when the sample is heated up from fully amorphous state and also in the second heating cycle when the sample had been partially crystallized in the first cooling. In the case of PLLA and PA 12 the two values were equal, however for PET and sPS, the T_g of partially crystallized sample is slightly higher than T_g of fully amorphous

counterpart. For these polymers, i.e. PET and sPS, the T_g of fully amorphous sample is presented in the parentheses in Table 6.1.

Gel permeation chromatography GPC measurements of crystalline PLLA, PLLAc and thermally threated PLLAc, tPLLAc (the labeling will be explained in the discussion section) were carried out using THF-based GPC equipped with Wyatt Dawn Eos multi-angle laser light (MALLS) Detector and Waters Model 2414 differential refractometer concentration detector. The weight average molecular weight of PLLAc and tPLLAc was obtained to be equal to 108 kg/mol and 47 kg/mol, respectively.

Table 6.1 Molecular characteristics of various semicrystalline polymers

Polymer	Mw (kg/mol)	M_e (kg/mol)	T_g (°C)	Source
PLLA	115	3.24	60	Nature Works (Ingeo 3100HP)
PET	-	1.45	80 (77)	Eastman (7352 PET)
sPS	175	2.44	100 (93)	Idemitsu Kosan (130ZC)
PA 12	-	1.6 – 2.6	36	RTP Company (RTP 200F)

6.2.2 Sample Preparation and Experimental Protocol

6.2.2.1 Sample Preparation

In order to remove moisture from polymer pelts they were initially dried in temperature-controlled chamber (Thelco GCA Precision model 18) for few hours. For the uniaxial compression tests, cylindrical samples with the diameter and height of 5 mm were made from compression molding of resin pellets using a Carver Lab Press. The applied load during molding was equal to 9000 kg. In the case of PLLA and PET polymer resins were melted above their melting point of 190 °C and 290 °C respectively and then after

waiting for few minutes they were quickly quenched into the icy water to generate amorphous PLLA and PET. In the next stage the amorphous PLLA and PET cylinders were annealed in the temperature-controlled chamber respectively at 90-100 °C and 150-160 °C for 4 hours to prepare semicrystalline samples of PLLA and PET. Semicrystalline sPS and PA 12 samples were prepared by slow cooling from the melt state into the room temperature when melt crystallization took place during cooling process. Dog-bone samples of semicrystalline PLLA and PET with dimensions of length by width by thickness respectively equal to $10 \times 2.9 \times 1.35$ mm^3 were prepared using dog-bone shape mold and similar molding and annealing condition to that of compression pieces of these polymers.

6.2.2.2 Mechanical Measurements

Uniaxial compression tests of cylindrical samples were carried out using Instron 5969, equipped with an environmental chamber. The temperature controller for Instron has an accuracy of ±1 °C. The tests were conducted over a range of temperatures covering the glass transition temperature. Bluehill Software interfaced with Instron allows us to perform compression tests with various constant cross-head speeds V in the unit of mm/min, which were then normalized by initial height H_0 to indicate the compression rate $r = V/H_0$ (min^{-1}). Compression rate for all the measurements was set equal to 0.3 min^{-1} in order to prevent heat generation in the sample and retain isothermal condition. All cylinder-shaped specimens were well lubricated on top and bottom surface with silicone oil. Uniaxial extension of semicrystalline PLLA and PET were performed using the same Instron. Drawing rate V/L_0 where the V is the cross-head separation speed and L_0 is initial length of the sample was set to be 0.5 min^{-1}.

6.2.2.3 Wide-angle X-ray Scattering (WAXS) Measurements

Two-dimensional wide-angle X-ray scattering (WAXS) patterns were obtained with a rotating anode X-ray generator (RU 300, 12 kW, Rigaku, Woodlands, TX), which produced a beam of monochromatic Cu Kα radiation (λ = 1.54 Å). The X-ray generator operates at 40 kV and 30 mA.

6.3 Results and Discussion

As mentioned in the introduction, the central question that inspired us to study mechanics of semicrystalline polymers is this: why crystallization can have adverse effect on the ductility of a glassy amorphous polymer? Figure 6.1(a)-(b) compares the uniaxial tensile behavior of amorphous and semicrystalline PLLA and PET at the same experimental conditions of drawing speed and temperature. Freshly made (without physical aging) glassy amorphous PLLA and PET are both ductile at room temperature that is sufficiently lower than their T_g of respectively, 60 ˚C and 80 ˚C. Inducing crystalline phase by cold crystallization through annealing these polymers above their T_g, results in brittle behavior. Following we initially provide our molecular picture of the semicrystalline state in section 6.3.1 and in section 6.3.2 we predict and present experimental results showing the presence of double yielding in semicrystalline polymers, i.e. yielding of glassy phase and yielding of crystalline phase. Finally, in section 6.3.3 we design an unexpected case of brittle behavior in the uniaxial compression of semicrystalline polymers.

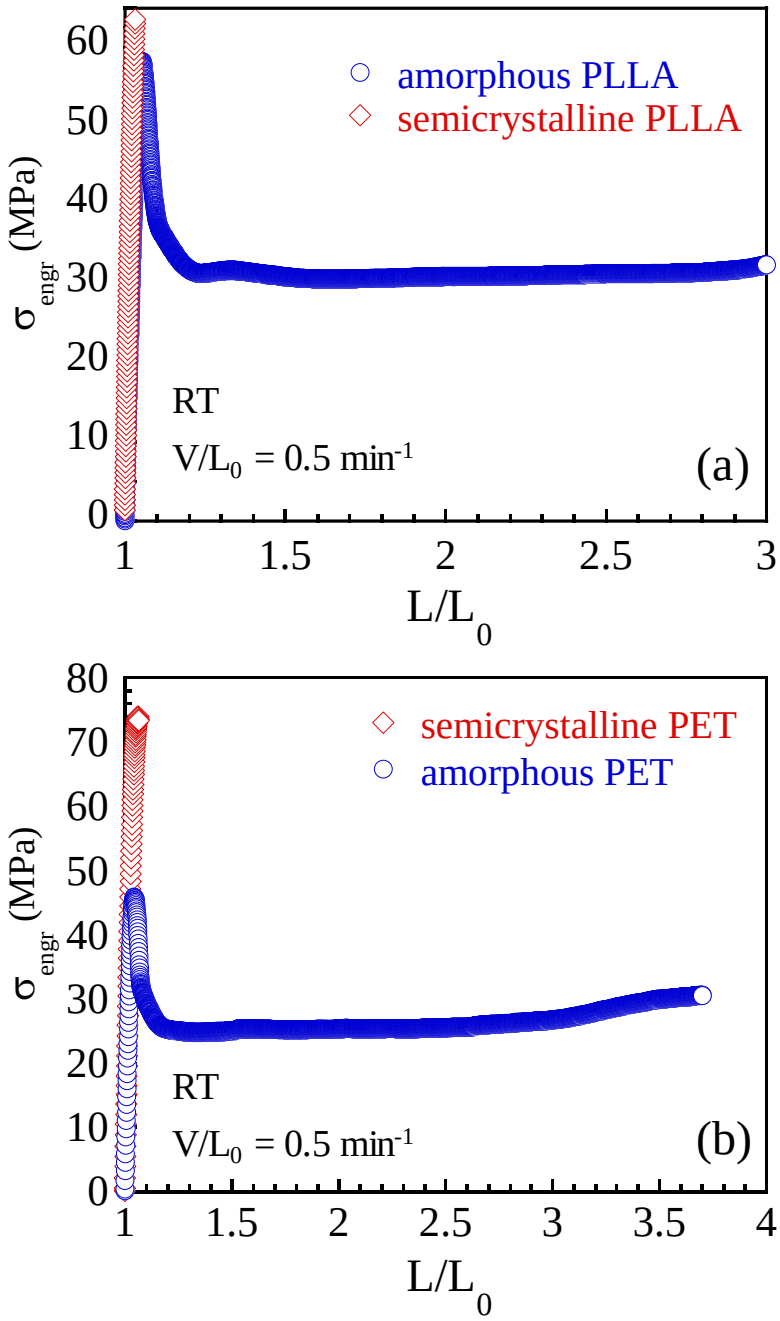

Figure 6.1 Engineering stress σ_{engr} vs draw ratio L/L_0 for uniaxial tensile deformation of semicrystalline and amorphous PLLA and PET at RT.

6.3.1 Structure of Semicrystalline vs. Glassy Amorphous Polymer

For a glassy amorphous polymer, the structure of chain network is inherited form chain entanglement by freezing polymer from melt state below T_g. While, for a semicrystalline polymer the structure of chain network is not what is obtained by freezing entanglement network. Registration of polymeric chains into the crystalline regions changes the distribution and density of chain network. On the other hand, at a specific temperature below T_g, the strength of intermolecular interactions such as Van der Waals forces should be comparable for disordered glassy and ordered crystalline phases (with slightly higher values for the crystalline phase).

Considering the semicrystalline polymer as a two-phase media of amorphous and crystalline phases, we envisage that: i) there are some chains that connect these two phases, ii) efficiency of chain network against deformation in semicrystalline polymer compared to amorphous glassy counterpart decreases, and iii) deformation initially takes place in the amorphous regions while crystalline phase mostly remains intact, therefore, the applied nominal strain is amplified in the amorphous region. Following experiments are designed to support these conjectures.

6.3.1.1 Connectors: Bridging and Tie Chains

In order to have mechanical strength and structural integrity in a semicrystalline polymer, it is necessary the amorphous and crystalline phases to be connected to each other. The schematic of Figure 6.2(c) shows the series combination of two crystalline regions and an amorphous region in between. In the amorphous phase we can identify three types of chains; free chains, tie chains and bridging chains. Free chains are the chains that are

completely in the amorphous region. Tie chains are the chains that directly connect two adjacent crystalline phases. The two ends of tie chains are located in those two crystalline regions and the middle is passing though the amorphous region. The bridging chains are chains with one end in crystalline region and the other one in the amorphous region. At temperatures below T_g, these chains through networking with the neighboring segments can always act as connectors and force transmitters. While, for temperatures above T_g these chains in order to effectively act as force transmitters the local deformation rate needs to be larger than the average relaxation rate of the part of the chains dangling in the amorphous phase. When this condition is met, the bridging chains can lock in with one another or with free chains and therefore transmit the force, otherwise, we will not have lock in effect and the chains will unrope. Figures 6.2(a) and 6.2(b) respectively, show the creep and stress relaxation behaviors of semicrystalline PLLA above T_g and at the linear region of stress-strain curve. Although stress level during creep above T_g is much larger than plateau modulus of PLLA melt G_p [45], unlike pure melt, there is a significant resistance against flow. This is indication of presence of some connector chains which cannot unrope from each other and flow during the creep experiment and those should be the tie chains. More interesting information can be deduced from stress relaxation data above T_g (Figure 6.2(b)). Obviously, for a pure melt after some time stress should relax to zero, however in the case of semicrystalline PLLA, as it is seen the stress level reaches some finite value and stays constant. The time scale in which the plateau is reached, is around 1000 s. Our measurements in the next chapter indicate that the chain relaxation time of PLLA, τ_d at this temperature (70 ˚C) is around 4000 s. Upon stop of deformation (onset of stress relaxation),

both tie and bridging chains start to relax which it shows up as the decay in stress data. After some time (1000s), the portion of the bridging chains that are in the melt state whose length is shorter than full chain length with the relaxation time around 4000 s, fully relax. Thereafter, since there is no mechanism of chain relaxation for the tie chains that are highly stretched between two adjacent crystalline regions, stress cannot further decay and stays constant at some finite value. We anticipate that the value of this finite stress should be proportional to the density of tie chains.

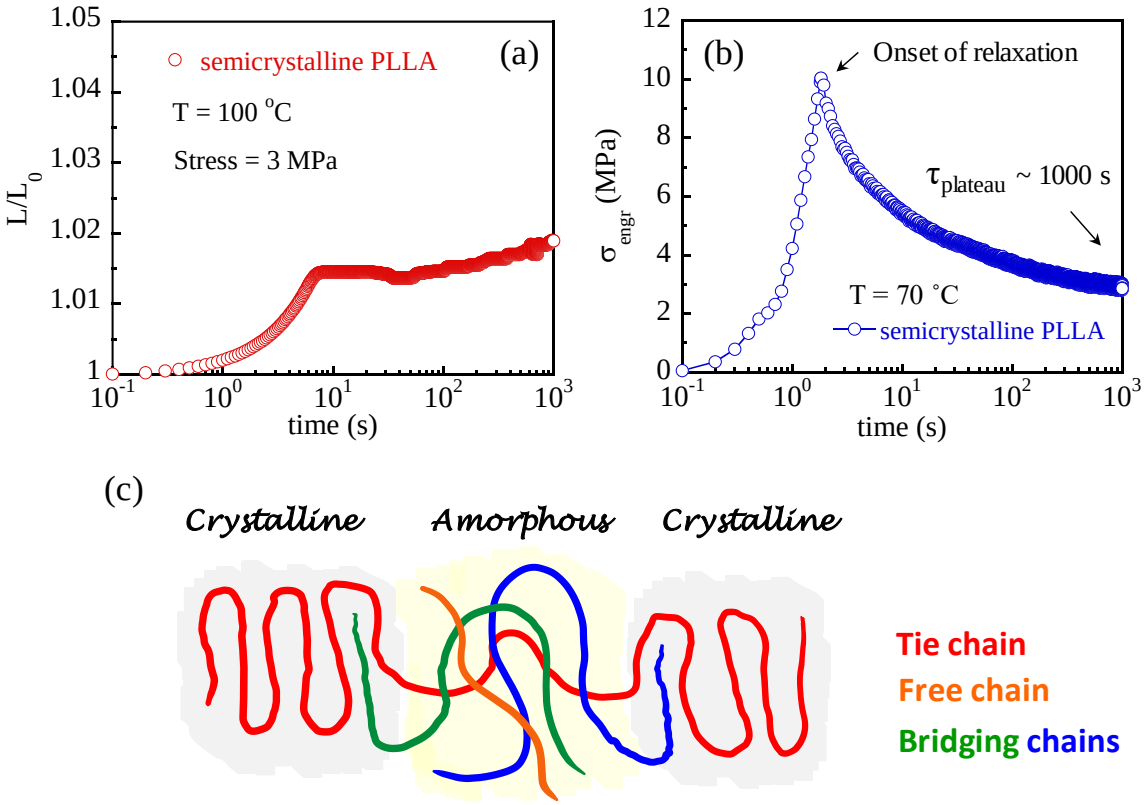

Figure 6.2 (a) draw ratio L/L0 vs time during creep of PLLAc at 100 ˚C and creep stress of 6 MPa, (b) engineering stress σ_{engr} vs time during stress relaxation of PLLAc at 70 ˚C, (c) schematic representation of interaction of amorphous (highlighted in light yellow) and

crystalline (highlighted in light gray) phases, and three different types of chains: tie, bridging and free chains.

6.3.1.2 Interruption and/or Depletion of Pre-existing Chain Network

Albeit different opinions on the origin of strain hardening at the post-yield deformation of polymer glasses[148], it is accepted that strain hardening modulus is partially indication of effectiveness of chain network in resisting against deformation[149]. Figure 6.3 compares the compression deformation of semicrystalline and amorphous PLLA. As it is seen slope of strain hardening region at the post-yield, is significantly decreased after crystallization. This is a mechanical evidence to show that the structure of chain network is altered due to crystallization and it becomes less effective to endure large deformation.

6.3.1.3 Amplification Effect

The mobility of crystalline phase is considerably lower than that of amorphous phase at both below and above T_g. Therefore, by deformation of a semicrystalline polymer (for example you can consider deformation of semicrystalline sample shown in the schematic of Figure 6.2(c) in the horizontal direction), most of the nominal deformation (the macroscopic strain $\Delta L/L_0$) is exerted on the amorphous phase. Ignoring the deformation of crystalline phase we can indicate that the local draw ratio in the amorphous phase is equal to $\lambda = 1 + (\Delta L/L_0)_{nominal}(l_c/l_a)$, where λ is local draw ratio in the amorphous phase, and l_c and l_a are respectively, the length scales of crystalline and amorphous phases.

6.3.2 Double Yielding in Deformation of Semicrystalline Polymers

As it was indicated in Figure 6.1 the semicrystalline PLLA and PET are brittle when they are extended below T_g, therefore in this section we initially start our discussion with the uniaxial compression of these polymers when they show a ductile behavior. The explanation of why the semicrystalline PLLA is brittle below T_g in extension, is presented in detail in the next chapter. Also, the reason behind why the same semicrystalline polymer which is brittle in extension could turn ductile in compression is the subject of another project which its results are not presented in this dissertation. Here we only focus on the importance of understanding a semicrystalline state as a composite structure and the crucial role of amorphous phase in exerting deformation into the crystalline phase. Figure 6.3 compares the stress σ vs compression ratio H_0/H of the cold crystallized PLLA, PLLAc and its counterpart amorphous sample PLLAa which was produced by fast quenching of PLLA melt below T_g (60 ˚C), at room temperature.

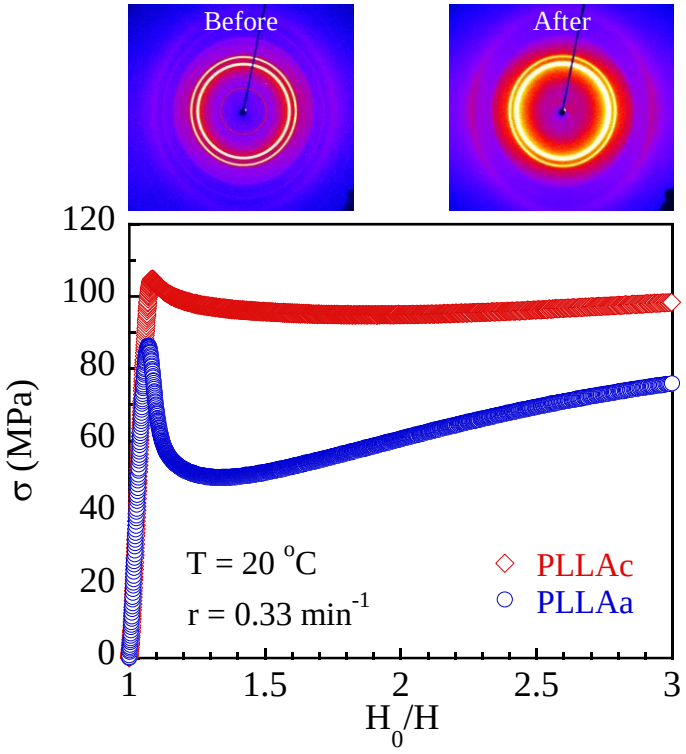

Figure 6.3 Stress σ vs compression ratio H_0/H curves for uniaxial compression of semicrystalline PLLA (PLLAc) and its amorphous counterpart PLLAa at T = 20 °C. 2D-WAXS images at left (before deformation) and right (after deformation) indicate the reduction in crystallinity at post-yield for PLLAc.

Evidently, it is seen that incorporation of crystalline phase into the amorphous one results in increase of yield stress which could be due to the rigid nature of crystalline phase. However, it is a valid question to ask that what does happen at yield point in each case (PLLAa and PLLAc)? What is/are the difference(s) in yielding of amorphous and semicrystalline polymers? According to our recent molecular model[10], yielding of a glassy polymer (polymer glass) is defined as the activation of the chain network associated with the increase in the segmental mobility and it turns out that the condition for activation of

chain network is more readily provided in the compression compared to the extension[24-25]. Considering a semicrystalline polymer as a composite structure of glassy and crystalline phases below T_g, we predict that the yielding of a semicrystalline polymer should involve two yielding, yielding of glassy phase followed by yielding of crystalline phase. Yielding of glassy phase should not be different than that of pure glassy polymer, on the other hand yielding of crystalline phase is due to destruction of the crystalline structure which itself can be combination to fragmentation and force-induced melting. Both mechanisms result in reduction of crystallinity which in the recent example is evidenced by the 2D image wide angle X-ray scattering (WAXS). Fragmentation is the mechanism of destruction of crystals which presumably does not require strong chain networking in the amorphous phase, while the force-induced melting of the crystals is a mechanism wherein the nominal deformation initially translates to the amplified chain tension in the amorphous phase, and subsequently through the bridging and tie chains is exerted into the crystalline lamellae, and pulls out the whole or portion of the chains from the crystalline lamellae and in absence of re-crystallization at $T < T_g$ results in reduction of overall crystallinity. Yielding of crystalline phase is evidenced by 2D images from WAXS, however there is no direct or indirect evidence that can unveil the yielding of glassy phase in Figure 6.3. Higher mobility and relative motion of the segments is achieved in an amorphous glassy polymer by approaching yield point[150-151], therefore for a glassy amorphous polymer yield stress can be an indicator of the strength of the intersegmental interactions. On the other hand, in an analogy with the molecular crystals[152], the strength of the crystalline phase of a polymeric material can be evaluated by the amount of cohesive energy (binding energy) which is

indication of the strength of the intermolecular interactions in the crystalline phase. Overcoming this intermolecular interaction and increasing the potential energy of the crystalline phase above its equilibrium energy state, i.e. cohesive energy, provides the conditions to destruct the crystalline structure, i.e. yielding of crystalline phase. The yield stress of glassy polymer σ_{yg} and cohesive energy density CED_c of crystalline phase (note the same dimensionality of $[MT^{-2}L^{-1}]$ for these parameters), both are decreasing functions regarding temperature (Figure 6.4). Passing T_g, σ_{yg} sharply drops to the order of plateau modulus of melt G_0, while in principle CED_c is insensitive to T_g and gradually decays and reaches its value for the melt by going beyond melting temperature T_m. Therefore, as indicated in Figure 6.4, we predict that near T_g is the temperature range where the contrast between strength of these two phases is large and that could result in apparent de-coupling in yielding of glassy and crystalline phases.

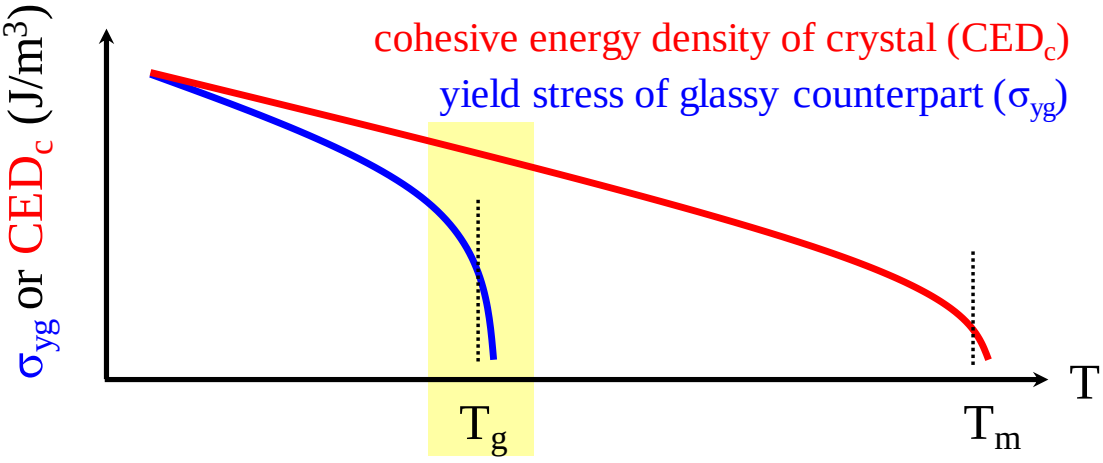

Figure 6.4 Diagram showing changes in the strength of pure glassy and pure crystalline phases in terms of yield stress (σ_{yg}) and cohesive energy density (CED_c), respectively. The

highlighted region is the temperature range that apparent de-coupling of amorphous and crystalline phases may take place.

To validate our prediction, uniaxial compression of PLLAc was done in four different temperatures and curves of σ vs H_0/H were examined in a higher magnification around the stress maximum in Figure 6.5. Interestingly as predicted, near T_g the two yielding appear as two individual peaks in the stress vs strain curves. Because of higher segmental mobility of the amorphous phase and amplification effect in deformation of this phase[45], the earlier peak has to associate with the yielding of amorphous phase and the second one should be related to the yielding of crystalline phase. In other words, in order to crystalline phase to yield it requires that initially amorphous phase to yield and develop enough chain tension so the developed high chain tension can act on the crystalline region and result in yielding of crystalline phase. At higher temperatures (Figure 6.5(d)) amorphous phase is in the melt state and does not show mechanical resistance against deformation therefore sample is compressed until the point where chain tension is high enough to start to pull-out the chains from crystal registrars. On the other hand, far below T_g, since the glassy modulus is temperature-independent and yield stress is increased by decreasing temperature, therefore, strain to yield of the glassy phase increases by lowering the temperature. Meanwhile, it is seen that the position of the second yield in Figures 6.5(b) and 6.5(c) is independent of temperature. Accordingly, at low temperatures (Figure 6.5(a)) the first yield from glassy phase which occurs at higher compression ratios merges out with the peak associated with the yield of crystalline phase and apparently, we only observe one unified but wide peak having minor strain softening.

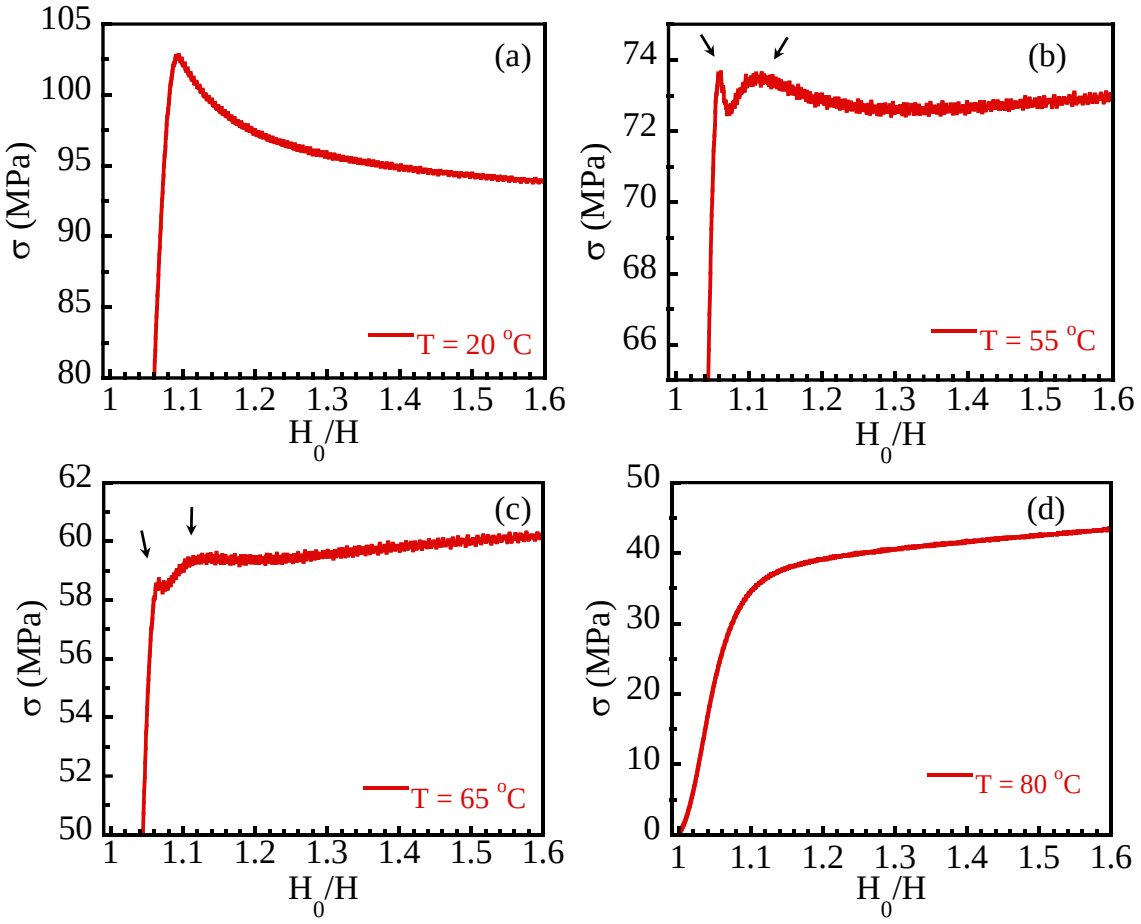

Figure 6.5 Stress σ vs compression ratio H_0/H curves for uniaxial compression of PLLAc in the vicinity of stress maximum at (a) T = 20 °C, (b) T = 55 °C (T_g – 5), (c) T = 65 °C (T_g + 5) and (d) T = 80 °C. For all the measurements compression rate was 0.33 min^{-1}. Apparent de-coupling of glassy and crystalline yields appears near T_g (indicated by arrows), while such effect is absent far above and far below T_g.

To determine whether these observations are universal, we carried out uniaxial compression of PET, Syndiotactic polystyrene (sPS) and Polyamide 12 (PA 12) at difference temperatures. Similarly, in all the cases, away from T_g an apparent yield point

with single peak is observed and close to T_g splitting of the yield points takes place. Figure 6.6(a)-(c) represents the curves of near-T_g effect for these three semicrystalline polymers.

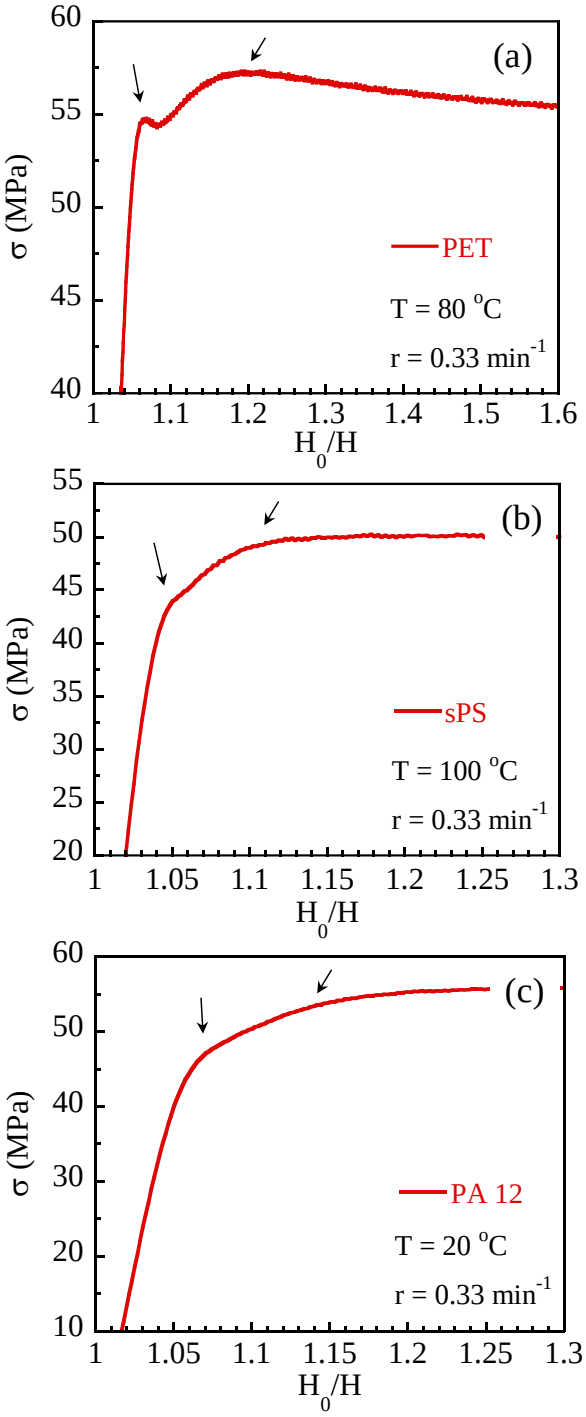

Figure 6.6 Stress σ vs compression ratio H_0/H curves for uniaxial compression of semicrystalline (a) PET (T_g = 80 °C), (b) sPS (T_g = 100 °C) and (c) PA 12 (T_g = 36 °C) in the vicinity of yield points indicating double yield, i.e. apparent de-coupling of glassy and crystalline yields (indicated by arrows).

In passing we are interested to show the presence of double yielding in the tensile deformation of semicrystalline polymers below T_g. It turns out that pre-drawing of a semicrystalline polymer above T_g makes it ductile when it is further drawn below T_g.[153] Figure 6.7 represents the engineering stress σ_{engr} vs draw ratio L/L_0 during tensile deformation of pre-drawn semicrystalline PET at T = 20 °C when it is deforming parallel to the stretching direction. Similar to the compression deformation, as it is seen pre-drawn semicrystalline PET shows two yielding points (indicated by arrows). Preceding discussions indicated the universality of double yielding phenomenon for various modes of deformation i.e. compression and extension, and different types of semicrystalline polymers, i.e. PLLA, PET, sPS and PA 12.

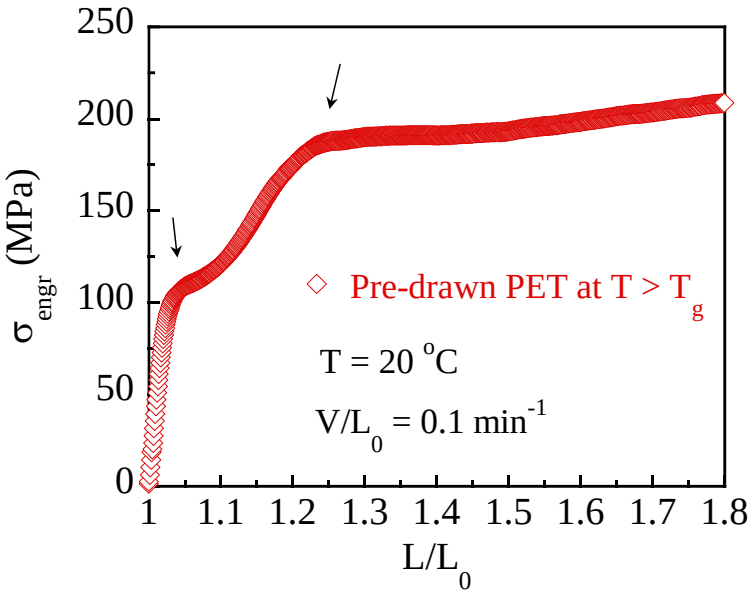

Figure 6.7 Engineering stress σ_{engr} vs draw ratio L/L_0 during tensile deformation of pre-drawn semicrystalline PET, at T = 20 °C when it is deforming parallel to the stretching direction.

6.3.3 Extraordinary Case of Brittle Response in Compression

In this section in order to reiterate the important role of tie chains and chain networking in amorphous phase, in affording the required force to yield the crystalline phase we design following experiment. Amorphous portions of the chains were selectively degraded by maintaining semicrystalline compression piece of PLLAc at high temperature ca. 140-150 °C for 100 hrs. Molecular weight M_w measurements based on gel permeation chromatography GPC indicated that after this treatment the overall molecular weight changed from 108 kg/mol to 47 kg/mol. The value of M_w after degradation is still far above entanglement molecular weight M_e of 3.24 kg/mol[45], however the response of semicrystalline polymer to the uniaxial compression changed from ductile to a brittle one

(Figure 6.8) upon this thermal treatment. This indicates that most of degradation took place in the amorphous portions of the sample. Thermal treatment resulted in degradation in amorphous phase and that phase no longer is able to yield and deliver the force to the crystalline phase. Because of non-effective chain networking in the amorphous phase, the high chain tension cannot establish and survive for long time, so chain pull out in amorphous phase takes place before that phase has the chance to exert the required force on the crystalline phase and result in yielding of the crystalline phase and that is why the WAXS images of treated semicrystalline PLLA, tPLLAc before and after compression remains unchanged. Moreover, a new amorphous cylindrical specimen for compression experiment was prepared by melting and fast quenching of thermally treated semicrystalline tPLLAc piece, which is labeled as re-processed amorphous PLLA, rpPLLAa. Conceivably, rpPLLAa shows a ductile behavior under uniaxial compression test. These set of experiments indicated that during treatment process we were able to selectively degrade the tie and bridging chains in the amorphous regions, so the chain networking in the amorphous phase is no longer effective enough to result in yielding of glassy phase and generate high chain tension and subsequently drives the crystalline phase to undergo yielding, meanwhile the overall molecular weight is high enough that rpPLLAa prepared by re-melting of treated sample, still remains ductile. It is necessary to point out that like below T_g, above T_g, those should be the highly strained amorphous chains that input the force on the crystalline regions to derive them toward yielding though force-induced melting.

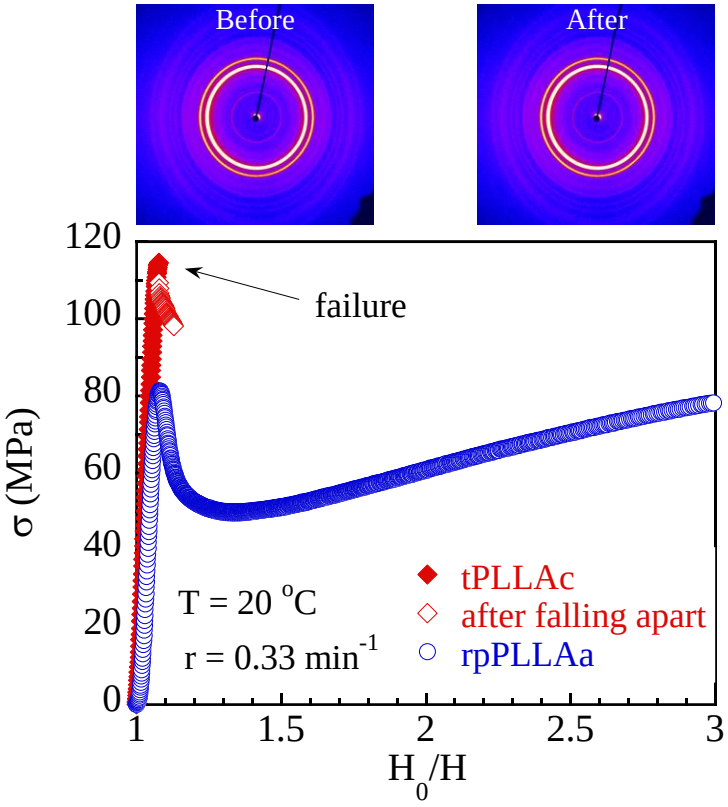

Figure 6.8 Stress σ vs compression ratio H_0/H curves for uniaxial compression of thermally treated crystalline PLLA, tPLLAc and its counterpart amorphous sample after melting and fast quenching of tPLLAc to room temperature, labeled as re-processed amorphous PLLA, rpPLLAa. Arrow shows the brittle behavior of tPLLAc. No change in 2D-WAXS image of tPLLAc before and after compression indicates that the crystalline phase is unable to yield independently in absence of effective robust amorphous phase.

6.4 Summary

Starting with the central question of "Why crystallinity has detrimental effect on ductility of polymer glasses?", we initially provided a chain level picture of the semicrystalline state based on three different mechanical experiments. Relying on our

molecular picture, in continue we studied four different semicrystalline polymers and indicated that yielding of a semicrystalline polymer below T_g involves two yielding, yielding of glassy phase and yielding of crystalline phase. Above T_g yielding of crystalline phase is the consequence of developing high chain tension in the amorphous phase. Splitting of the peaks of yielding of glassy and amorphous phases is observed in the vicinity of the glass transition temperature where the imbalance between the strength if glassy phase and coherence of crystalline phase increases. We concluded that yielding of crystalline phase is the consequence of high chain tension in the amorphous phase which below T_g it requires the preceded yielding of glassy phase. Destruction of the chain networking in the amorphous phase makes it impossible to develop surviving high chain tension in that phase and exert the required force to disintegrate the crystalline domains. In short, as Dirac states in his book of principles of quantum mechanics[154] "we must revise our idea of causality" in order to develop right foundation for theoretical description of the ongoing events. This chapter tries to represent a new perspective to study mechanics of semicrystalline polymers by paying more attention to the role of amorphous phase rather than studying the crystalline phase, isolatedly.

CHAPTER VII

WHY IS CRYSTALLINE POLY(LACTIC ACID) BRITTLE AT ROOM TEMPERATURE?

7.1 Introduction

Due to the rather poor mechanical properties, poly(lactic acid) or poly(lactide) (PLA) has yet to fulfill its promise as an advanced biodegradable non-petroleum based material to replace fossil-based polyesters such as polyethylene terephthalate (PET). In 2012 Bioplastics magazine projected the commercial annual production of PLA to reach 0.8 million tons in 2020, which still pales in comparison with PET's annual 70 million tons. Applications of PLA have been restricted to a few specialized areas such as films[155-156]and fibers[157]. Because of its low glass transition temperature T_g ~ ca. 60 ºC, PLA has low thermal resistance in its amorphous form and turns brittle rapidly upon physical aging, which occurs readily during several hours of storage at room temperature thanks to its low T_g. Upon introducing crystallization to improve thermal stability, PLA is opaque and brittle even without physical aging. Thus, until we overcome the shortcomings as related to its poor mechanical performance, low thermal resistance and lack of optical clarity, PLA would not be able to replace PET. Clear beverage bottle and coffee cup made of PLA remain an unrealistic aspiration.

Several reviews[158-161] have summarized various aspects of PLA materials, covering the synthesis,[161-164] structure,[165-168] properties,[169-173] processing,[174-182] and applications.[183-188] Despite over 27,000 publications and patents since mid-1990s, the understanding on how different internal (molecular) and external (deformation) factors affect the mechanical behavior of PLA in either amorphous or crystalline form remains highly fragmented and incoherent. This project represents our initial efforts toward the establishment of a coherent knowledge base that can guide the future development of PLA based materials toward replacement of PET.

Polymer crystallization is a common mechanism for mechanical reinforcement for class A semi-crystalline polymers whose T_g is well below room temperature, such polyethylene (PE) and polypropylene (PP). Semi-crystalline polymers with T_g well above room temperature belong to class B. PLA, PET, isotactic and syndiotactic polystyrene are in the class B. Such a classification is conveniently applied here to indicate that the subject of mechanics of PLLA can be rather different from that of PE and PP. By figuring out why at room temperature class B polymers (i.e., glassy semi-crystalline polymers) are typically brittle, we may identify means to manipulate crystallization so that the crystallization is no longer detrimental to ductility yet still present to provide adequate thermo-mechanical stability. An ultimate objective of research on PLA materials is to find ways to make ductile, clear and heat-resistant PLA materials.

In this chapter, by combining the recent understanding[189] on the essence of nonlinear rheology of entangled polymers with the phenomenological model[10] for yielding of glassy polymers, we first investigate the molecular origins of the poor mechanical characteristics

of PLA materials. We then design an effective strategy to improve overall performance, turning the same brittle, opaque, thermally unstable, PLA into a tough, clear and heat resistant material. This chapter is organized as follows. In the experimental section 7.2, we use linear viscoelastic characterization of both PDLLA (amorphous) and PLLA (crystalline) samples to obtain the packing length *p* and characteristic ratio and indicate that there should be enough chain network density to afford ductility in amorphous PLA. Section 7.3.1 presents tensile tests in several subsections. For notational simplicity, the amorphous form of PLLA, obtained by rapid thermal quench from above the melting temperature T_m, is labeled as aPLLA. In 7.3.1.1 we show that the inherently dense chain network in aPLLA is insufficient to ensure ductility at room temperature because of the fast physical-aging. The brittle-ductile transition (BDT) occurs near T_g after heavy aging, whereas the BDT can occur in a wide range of temperature depending on how rapidly PLLA is thermally quenched from its molten state. In 7.3.1.2 we show how melt stretching allows aPLLA to remain ductile against rapid aging. While freshly made aPLLA is ductile, the data in 7.3.1.3 show that PLLA with sufficient melt-crystallization destroys its ductility at room temperature in absence of significant aging. The drawability above T_g is also poor for both sufficiently melt- and cold- crystallized PLLA. Section 7.3.2 contains in situ polarized optical microscopy (POM) studies of PLLA with different levels of crystallinity. A case is made based on partially crystallized PLLA samples that brittle failure of PLLA characteristically arises from the weakness of the crystalline phase. Finally, we demonstrate in Section 7.3.4 how considerable melt stretching suppresses formation of large crystallites such as spherulites and promotes nano-crystallization nucleating from the

stretched entanglement strands in aPLLA. Such a new crystalline state makes ms-PLLA super ductile, giving rise to both optical clarity and dimensional stability at high temperatures.

7.2 Experimental

7.2.1 Materials

Sample A is an inherently amorphous PLA (PDLLA), obtained from Natureworks (Ingeo 4060D). Sample B (Natureworks, Ingeo 3100HP, MFR=24 g/10min at 210 °C and 2.16 kg), labeled as PLLA in this study, is a semi-crystalline grade of PLA with D-lactide content= 0.5%, which can crystallize in the range of 90 °C to 120 °C according to the DSC measurements given in Figure 7.1. Weight–average molecular weights M_w, relative to poly(styrene) standards, was measured by THF-based gel permeation chromatography (GPC) operated at room temperature. The M_w values of 173 kg/mol and 115 kg/mol were determined respectively for PDLLA and PLLA. In order to obtain the actual values of molecular weight for PLA, a correction factor of 0.58 has been applied by various authors.[190-193] The polydispersity index are 1.68 and 1.63 for PDLLA and PLLA respectively.

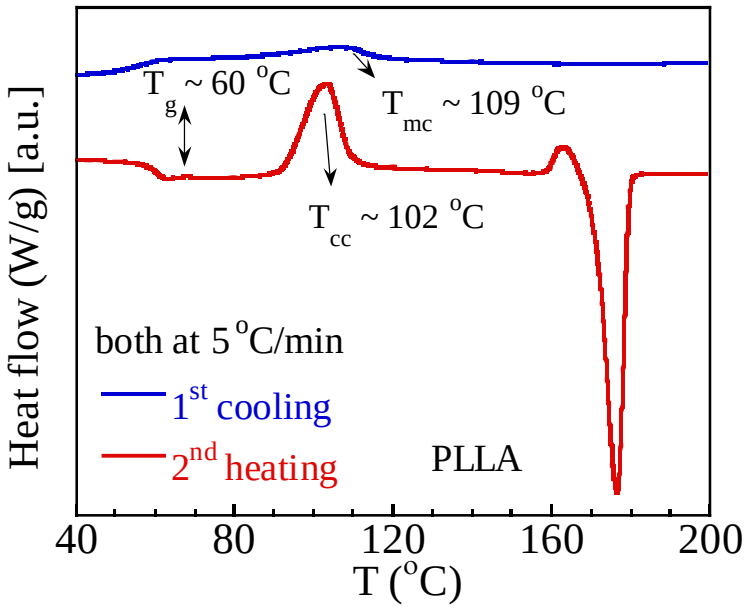

Figure 7.1 DSC scan of PLLA to reveal the melt and cold crystallization temperatures as well as glass transition temperature.

7.2.2 Apparatuses

ARES G2 (TA Instruments) was used to obtain the small amplitude oscillatory shear (SAOS) data in the frequency sweep mode of the pure PDLLA and PLLA at various temperatures from 55 to 120 °C. For PLLA, the SAOS measurement was only made at 120 °C in its molten non-crystalline state, obtained upon cooling from above T_m.

To analyze the thermal behavior of PLA samples including glass transition and melting temperatures as well as the degree of crystallinity, a differential scanning calorimter (DSC) Q200 (TA Instruments) was used. The percentage of crystallinity was evaluated by DSC,[194] relative to the reported specific enthalpy of fusion of ΔH_f^0 = 93 J/g for perfect PLLA crystal.[195] The degree of crystallinity in melt-crystallized and cold-crystallized samples were evaluated as $X = (\Delta H_m - \Delta H_{cc})/\Delta H_f^0$, where ΔH_f^0 = 93 J/g, ΔH_m is the melt enthalpy,

estimated from the curves in Figure 7.2, and ΔH_{cc} is the cold crystallization enthalpy, which is negligible. As shown in Figure 7.2, a relatively high level of crystallinity of 45% and 50% is attained in cold and melt crystallization respectively.

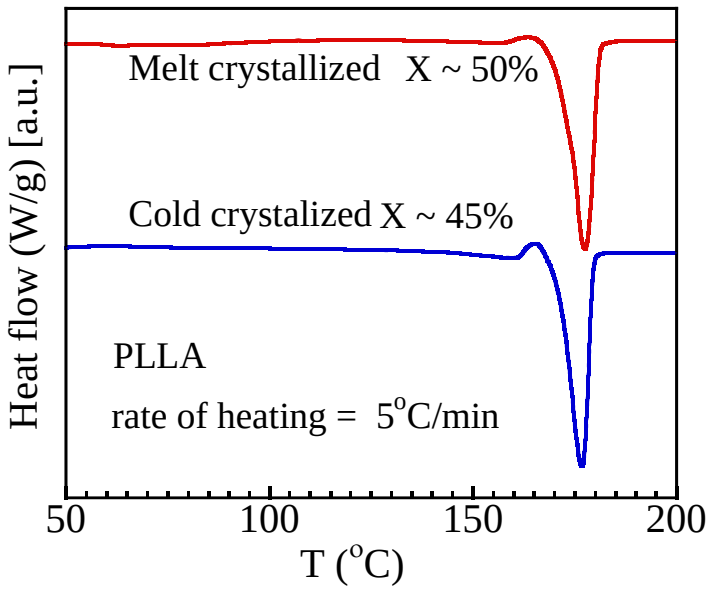

Figure 7.2 DSC scan of fully melt and cold crystallized PLLA where the percentage X of crystallinity is evaluated as $X = (\Delta H_m - \Delta H_{cc})/\Delta H_f^0$, where, $\Delta H_f^0 = 93$ J/g, ΔH_m is the melt enthalpy, estimated from the curves, and ΔH_{cc} is the cold crystallization enthalpy, which is negligible.

Two-dimensional WAXS patterns were obtained with a rotating anode X-ray generator (RU 300, 12 kW, Rigaku, Woodlands, TX), which produced a beam of monochromatic Cu Kα radiation (λ=1.54 Å). The X-ray generator operates at 40 kV and 30 mA.

Mechanical and melt-stretching tests at different temperatures were done using Instron 5969 with a home-made temperature-controlled chamber. An initial rate of V/L_0=0.5 min^{-}

[1] was used for all mechanical tests regardless of initial length L_0. For melt stretching a Hencky rate of V/L=1.67 min^{-1} was applied at 70 °C (i.e., *Wi* =122 according to the value of τ_d listed in Table 7.1) to amorphous PLLA dog-bone shaped samples. Such a high rate assures that we can elastically deform the entanglement network and achieve geometric condensation[189] effect.

A stretcher (Linham-TST350) in conjunction with polarized optical microscopy (POM) was used to study the morphological deformation of PLLA during drawing both below and above T_g. The temperature-controlled stretcher has a hot stage of dimensions 37 mm by 14 mm with a rectangular hole in the middle of 4.5 mm by 1.2 mm. The clamps move away from each other during stretching with equal speed V/2.

7.2.3 Sample Preparation

The PLLA in its amorphous state, labelled as aPLLA, is readily obtained by melting the crystalline pellets at ca. 200 ^oC and quench it into icy water to suppress crystallization that cannot take place below T_g = 60 ^oC. As shown in Section 7.3.1, such aPLLA undergoes physical aging rapidly at room temperature. To subject aPLLA to heavy aging, we anneal the freshly quenched aPLLA at 40 ^oC for several days. Such heavily aged aPLLA samples are more brittle.

The aPLLA undergoes cold crystallization upon annealing above T_g. Fully crystallized PLLA can be achieved after annealing from the amorphous state at 90-100 ^oC for four hours. Such PLLA is labeled as PLLA(fcc). Similarly, we can prepare a fully crystallized PLLA by melt crystallization, cooling from above its melting point around 200 ^oC to a

temperature range of 110-120 °C to induce large spherulites. Such PLLA is labelled as PLLA(fmc).

Dog-bone shaped PDLLA and aPLLA samples were press-molded using Carver™ Lab Press at 120 and 210 °C, respectively. The applied load for both polymers during pressing was equal to 9,000 kg. A waiting time of 3 min at 210 ^{o}C is enough to achieve a single uniform piece of molten PLLA. For PDLLA a waiting time of 5 min was applied at 120 °C. After the mentioned waiting time the PLLA-containing mold was brought out of Carver press and quenched into icy water to obtain aPLLA. Our dog-bone samples in this study have three different dimensions, with length by width by thickness equal respectively to 10×2.9×1.35, 20×9.86×1.63 and 39×3×0.6 mm^3. PLLA(fcc) samples prepared by annealing of dog-bone molded aPLLA. The sample annealing took place at 90-100 °C in a temperature-controlled chamber (Thelco GCA Precesion model 18) for a duration of 4 hours. To prepare PLLA(fmc), PLLA was brought from 210 °C to 110-120 °C by unplugging the electric heater in the Craver press to permit ambient cooling, leaving the dog-bone sample-containing mold in between the plates of the Craver press until the target temperature of 110-120 ^{o}C was reached when the heater was turned on to the new preset temperature. Four hours were allowed for the melt crystallization in this temperature range. For time-resolved POM observations, crystalline PLLA films were all made through melt-crystallization as follows. At the first stage, PLLA pellets were placed between two heat resistant polyimide sheets of 10×10 cm^2. Using a Carver press, the polyimide-sheet sandwiched PLLA was pressed under a high load of 20,000 lbs at 210 °C (considerably above T_m) for 3-5 min before unloading and immediate quenching below T_g by immersing

the sample to a bucket of water at room temperature. This procedure resulted in a large film of thickness around ca. 60 μm, from which small rectangular pieces of 13×33 mm^2 were cut, along with the sandwiching polyimide sheets. In the next stage, such a rectangular piece of aPLLA was placed on the hot stage of TST350 to be heated to 210 ^oC with a moderate rate of 20 ^oC/min to prevent detachment between PLLA and polyimide sheets. Then the sample was cooled to a target temperature of 117-120 ˚C with rate of 35 ^oC/min and kept for different durations (30-240 minutes) to arrive at the various desired morphologies, e.g., containing spatially resolvable (under POM) spherulites that are either isolated or interconnected. Finally, the rectangular piece was removed from the heater and quenched with room-temperature water, and the polyimide sheets were peeled off from both sides of the PLLA film. The typical effective dimensions of the films used for stretching under POM are 12×1.15×0.06 mm^3. Depending on the time spent at 117-120 ^oC, two types of morphologies were attainable, either relatively isolated spherulites or space-filling spherulites of considerable size. All the sample reported for their behavior under in situ POM observations were freshly prepared, i.e., physical aging was generally not allowed to take place by avoiding long duration of storage. Specifically, four films under POM study belongs to the category of partially melt crystallized PLLA (pmc-PLLA) and therefore labeled as pmc-PLLA(1)-(4). Another four films are in the category of fully melt-crystallized PLLA (fmc-PLLA), labeled as fmc-PLLA(1)-(4).

7.2.4 Characterization

Linear viscoelastic characterization is carried out to provide necessary information for melt stretching and investigation of mechanical behavior of PLLA above T_g. Based on

small-amplitude oscillatory shear (SAOS) measurements, we obtain the master curves for storage and loss moduli G' and G" of PDLLA in Figure 7.3(a) where the inset shows the temperature dependence of the relaxation dynamics, given by the William-Landel-Ferry shift factor a_T. Crystallization prevents us from obtaining similar curves for PLLA. Since PDLLA and PLLA have the similar microscopic structures and thus have[196] nearly the same glass transition temperature T_g and thus similar WLF factor a_T, we will use the SAOS information of PDLLA to estimate the terminal relaxation time $\tau_d = 1/\omega_c$ of aPLLA at all temperatures, provided that we have ω_c of PDLLA and PLLA at one common temperature whether PLLA is a melt free of crystallization. According to the DSC result in Figure 7.1, molten PLLA would not melt-crystallize at 120 ^oC during the SAOS measurements, which were made by going above T_m and subsequently lowering to 120 ^oC. In confirmation G' and G" shows crossover and terminal flow behavior in Figure 7.3(b). We have τ_d(PDLLA) to be longer than τ_d(PLLA) by a factor of 7/2.3. Thus, we infer the molecular weights of these two PLA differ by a factor of 1.45 by assuming $\tau_d \sim M_w^{3.4}$. Given that at 70 ^oC PDLLA has its terminal relaxation time τ_d around 1.33×10^4 s, and PLLA has τ_d shorter than that of PDLLA by a factor of 7/2.3 according to Figure 7.3(b), we have τ_d = 4380 s, as listed in Table 7.1.

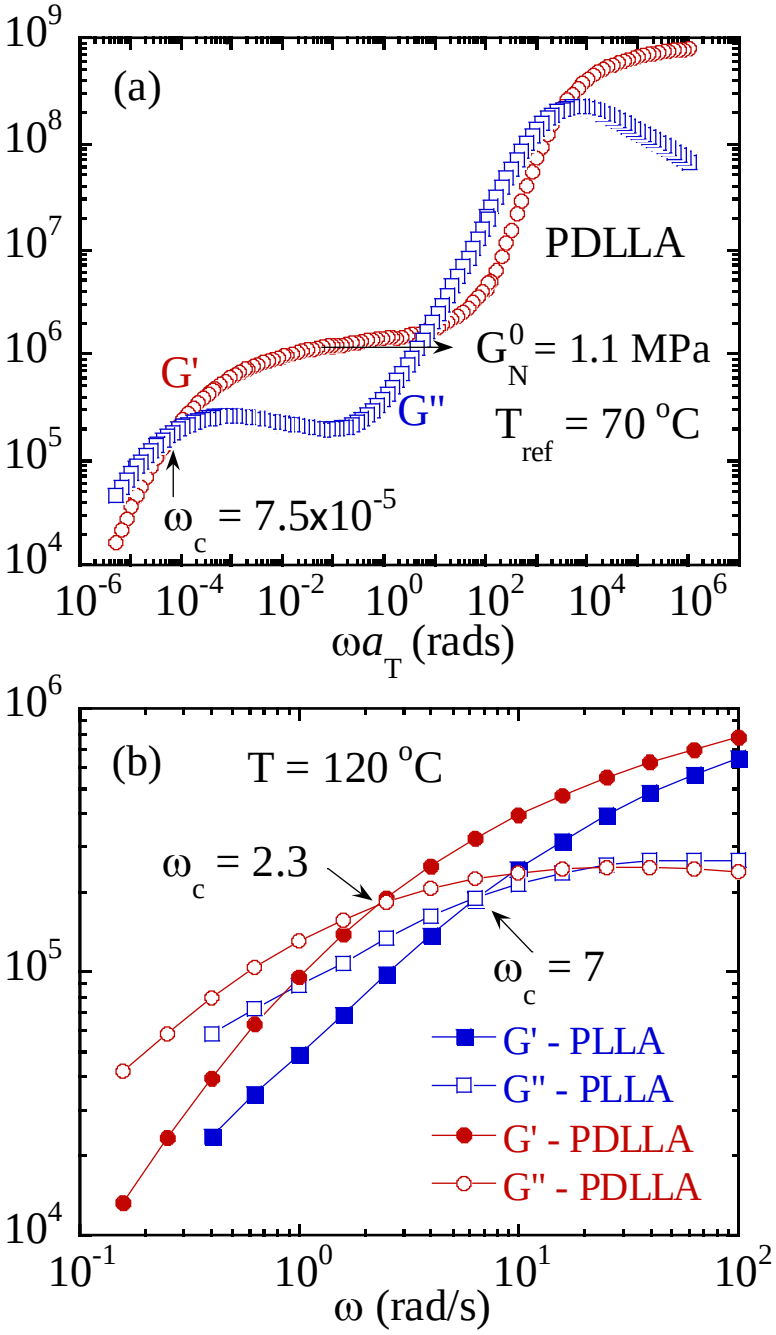

Figure 7.3 (a) Master-curves of G' and G" from small-amplitude oscillatory shear (SAOS) measurements of PDLLA at various temperatures from 55 to 120 °C. (b) SAOS of PDLLA and PLLA at T = 120 °C, revealing the crossover frequencies at 2.3 rad/s for PDLLA and 7 rad/s for PLLA.

7.2.4.1 Molecular Parameters

There have been various speculations[197-198] about why amorphous PLA is brittle at room temperature. Some invoked Wu's speculation:[199] By relating T_{BD} to the secondary relaxation temperature T_{β}. Wu correlated T_{BD} with the characteristic ratio C_{∞}. Wu's assertion based on empirical observations can be questioned as an elementary level: It is well known that BDT shifts to higher temperatures upon aging whereas the Gaussian chain conformation cannot appreciably change by annealing, i.e., a constant C_{∞} would imply a constant T_{BD} independent of the thermal history, in contradiction to the experimental observation. There are also considerable discrepancies in the literature among the various reports[197, 200-203] of the value for M_e, ranging from ca. 4 to 10.5 kg/mol. The errors likely stemmed from the fact that the melt elastic plateau behavior was often inaccessible due to the semi-crystallinity in PLA. Since both PDLLA and PLLA should have similar characteristic ratios,[204-205] they can be expected to have the similar values for packing length p and M_e. Therefore, a reliable determination of M_e from the measurement of the melt plateau modulus G_{pl} can be readily obtained from that PDLLA that is made through copolymerization of D-actic and L-actic monomers.

In any valid account for BDT of glassy polymers at least two factors must come into play:[10] (1) the robustness of the chain network whose structure, given in terms of the areal density ψ of load-bearing strands, depend on the Kuhn length $l_K \sim C_{\infty} l$ (where l is the bond length) and (2) the local minimum on the energy landscape where the polymer settles in. A most recent study reported a moderate value for the entanglement molecular weight M_e of ca. 4 kg/mol and $C_{\infty} = 6.5$ and correctly concluded[206] that the previous speculation of the

origin of brittleness at room temperature was baseless and the embrittlement arose from the fast physical aging of PLA at room temperature.

Here we employ the small amplitude oscillatory shear to obtain the storage and loss moduli G' and G" from both PDLLA and PLLA as shown in Figures 7.3(a) and 7.3(b). We can read the value of melt plateau modulus G_{pl} to be ca. 1.1 MPa, which is the value of G' at the frequency ω_{min} where G" is at its minimum. Then M_e is evaluated as $M_e = \rho RT/G_{pl}$ = 3.24 kg/mol at room temperature, where the mass density ρ = 1.25 g/cm^3 and gas constant R = 8.3 J/mol·K. According to the packing model,[207-210] there are ca. 5.5 chains[12, 39] in the pervaded volume of a Gaussian chain of entanglement molecular weight M_e, and therefore the average end-to-end distance l_{ent} of an entanglement strand is linearly related to p as

$$l_{ent} = 16.5(6^{3/2}/4\pi)p = 19.3p. \quad (1)$$

On the other hand, by definition, p is introduced as the length scale relating l_{ent} to the physical volume of an entanglement strand:

$$M_e/\rho N_a = p(l_{ent})^2. \quad (2)$$

Substituting Eq. (1) into (2), we find p = 2.26 Å and l_{ent} = 4.4 nm. Moreover, we can estimate[39]the characteristic ratio C_{ent} for a subchain of entanglement strand as $C_{ent} = (l_{ent})^2/n_e l^2$ = 6.9 where n_e is the number backbone bonds per entanglement strand, given by M_e/m_1. Finally, taking the bond length l as the average of the three bonds (OC = 1.44, CO = 1.34 and C-C = 1.54 Å)[205], i.e., l = 1.44 Å, we estimate the Kuhn length to be $l_K = (C_\infty+1)l = (C_{ent}+1)l$ = 1.14 nm. These molecular parameters (M_e, p, l_{ent}, C_{ent}, l_K) as well as the values of τ_d at several temperatures from Figures 7.3(a) and 7.3(b) are listed in Table 7.1 for the present and future references.

Table 7.1 Molecular parameters of PLA and relaxation time of PLLA (3100HP)

M_e	p	l_{ent}	C_∞	l_K	τ_d (70°C)	τ_d (76.5°C)	τ_d (81°C)
3.24 (kg/mol)	2.26 Å	4.4 nm	6.9	1.14 nm	4,380 s	438 s	119 s

7.2.4.2 Melt Stretching

According to the elementary understanding of nonlinear melt rheology,[189] we can alter the structure of the entanglement network by fast external deformation. When the applied rate is much larger than the reciprocal Rouse relaxation time, the network can be nearly affinely deformed. For example, melt stretching, i.e., uniaxial extension of entangled polymeric liquids produces geometric condensation,[189] making the areal density of entanglement strands higher in the cross-section (XY plane) transverse to the stretching Z axis. As expected, such pre-melt-deformation can greatly affect the mechanical behavior in the glassy state.[40] Based on the linear viscoelastic characteristics shown in Figure 7.3(b) for aPLLA, we carried out melt stretching 10 degrees above T_g at 70 ^oC to avoid cold crystallization (that occurs above 90 ^oC according to Figure 7.1) during thermal equilibration and subsequent melt stretching. As shown in the inserted images of wide-angle x-ray scattering (WAXS) in Figure 7.4, the melt stretched samples are free of crystallization during melt stretching. At λ_{ms} = 3.0, the ms-aPLLA remains optically transparent after stress relaxation for 300 s although WAXS image reveals induced crystallization. The induced crystallization is sufficiently rapid and acts like crosslinking so that elastic yielding via chain disentanglement is absent.

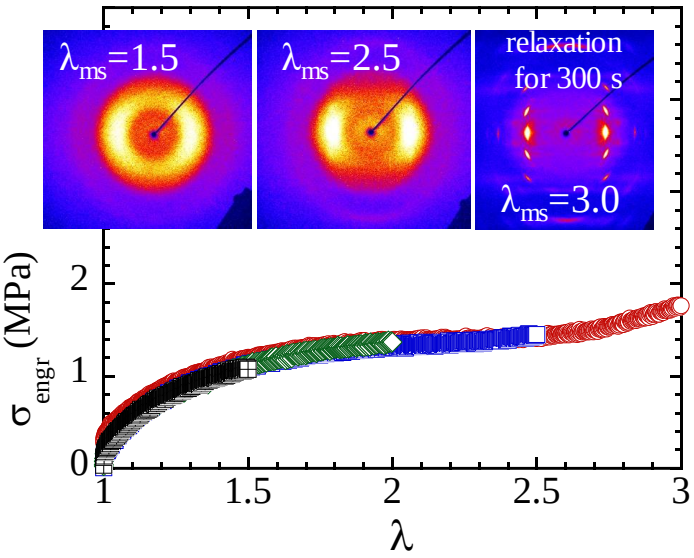

Figure 7.4 Engineering stress σ_{engr} vs stretching ratio λ from uniaxial extension of aPLLA at 70 ^{o}C where the extension rate V/L_0 = 1.67 min^{-1} and initial sample length L_0 = 10 mm. First three discrete melt stretching tests terminated at final melt stretching ratios λ_{ms} = 1.5, 2 and 2.5, followed by water spraying to cause rapid thermal quench that produces sample shrinkage and sudden buildup of the tensile stress as shown. The last melt stretching to λ_{ms} = 3 is followed by stress relaxation for 300 s to induce cold crystallization and subsequent thermal quenching to room temperature. The first two images of the 2D WAXS patterns confirm that no crystallization occurs during the melt stretching. The third WAXS image is from the sample that has experienced significant melt stretching of λ_{ms} = 3 and subsequent stress relaxation at 70 ^{o}C for 300 s.

7.3 Results and Discussions

7.3.1 Tensile Extension Tests Below and Above T_g

We first study all mechanical aspects concerning the tensile extension of aPLLA (in 7.3.1.1 and 7.3.1.2) and PLLA (in 7.3.1.3) both below and above T_g. Then we present our

speculations about the adverse effect of crystallization on ductility in 7.3.1.4 to motivate in situ POM tests. 7.3.2 is devoted to time-resolved POM observations of partial and fully crystallized PLLA during drawing both below and above T_g. Our objective here is to investigate how melt stretching and crystallization affect the ductility at different temperatures so that an effective molecular mechanism can be proposed to make PLA a strong candidate as an advanced material to replace conventional PET.

7.3.1.1 Brittle-Ductile Transition

Amorphous PLA is always brittle at room temperature if it has been stored at room temperature for many hours after thermal quenching from its molten state. Although the microscopic mechanism for fast aging of PLA remains to be identified, perhaps due to its low T_g, it is a fact that our PDLLA and PLLA quickly turn brittle, e.g., three hours after their vitrification at $T_g = 60\ ^oC$ and storage at room temperature, as shown in Figure 7.5 for aPLLA.

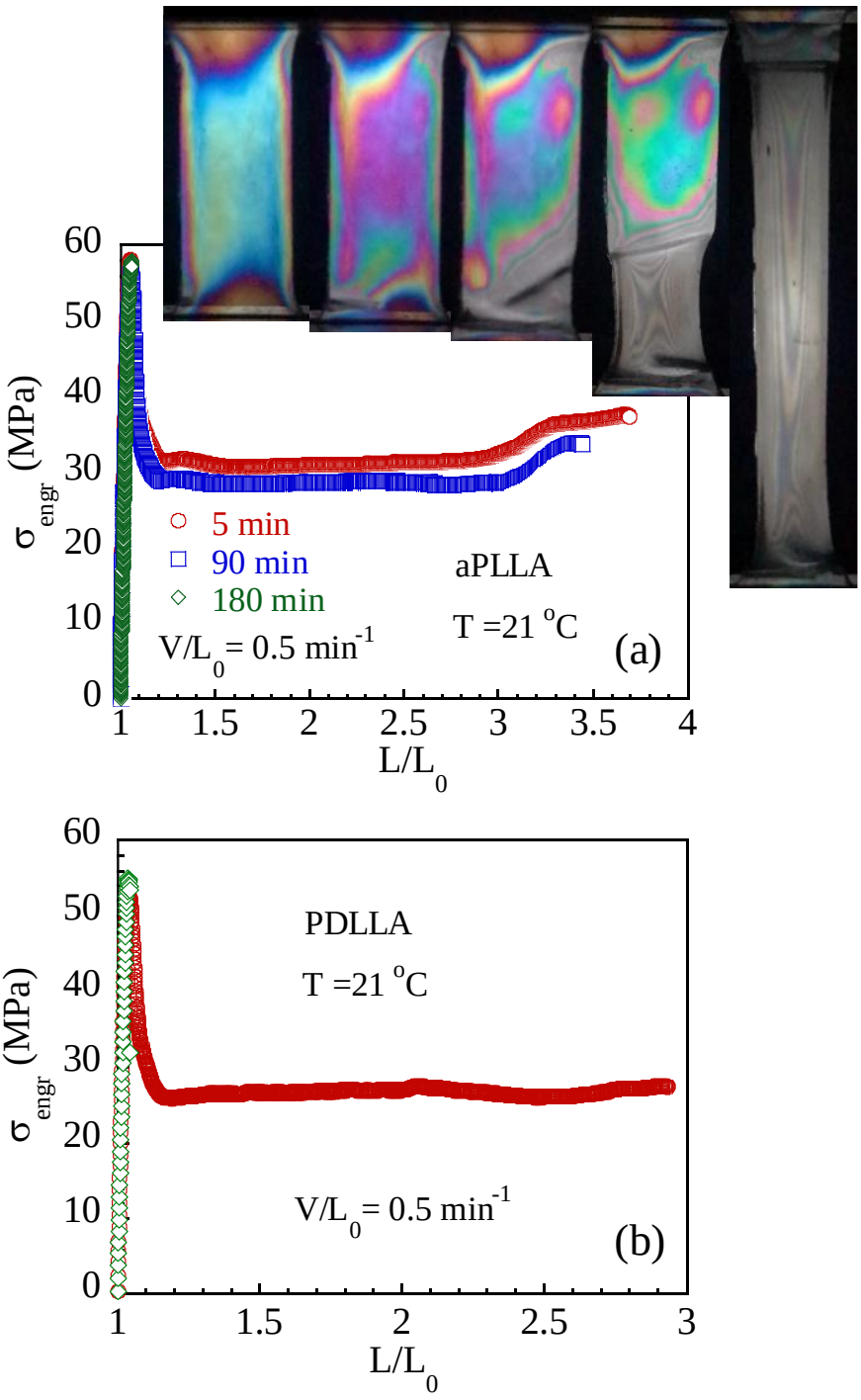

Figure 7.5 (a) Engineering stress σ_{engr} vs drawing ratio L/L_0 for aPLLA after varying amounts of storage time that results in different degrees of physical aging. The initial sample length L_0 = 20 mm, and the crosshead speed V = 10 mm/min. Images in the inset,

obtained by sandwiching the sample with crossed polarizers under white light, show the development of birefringence during cold drawing of the fresh aPLLA (5 min), where shear band and tensile strain localization are evident. (b) σ_{engr} vs L/L_0 for PDLLA, either freshly prepared or after storage at room temperature for days. Here $L_0 = 10$ and V = 5 mm/min.

Since the physical aging is so fast at room temperature, freshly made dog-bone shaped aPLLA samples were kept in the freezer (ca. -18 ^oC) to be used within a few hours. At cryogenic temperatures where the samples were brittle, the tests were repeatedly three times. Figure 7.6(a) summarizes the mechanical responses of aPLLA to uniaxial extension at various temperatures between −28 and 45 ^oC, revealing the "coordinates" of the BDT for aPLLA to be (10 ^oC, 67 MPa). After storage of the quenched aPLLA for one day, the BDT shifts to 31 ^oC, i.e., it turns brittle at room temperature. A heavily aged aPLLA that remains brittle until the temperature is within a few degrees of T_g. We omit the similar figures to Figure 7.6(a) because of the space limitation.

Analysis and interpretation of the data in Figure 7.6(a) go as follows. Given the estimated values of the packing length p and Kuhn length l_K listed in Table 7.1 we can evaluate[10] the areal density ψ of load-bearing strands (LBS) in the chain network according to an estimated average size l_{LBS} of LBS by treating LBS as a Gaussian chain with radius of gyration $l_{LBS(g)}$ and end-to-end distance l_{LBS}. Denoting the number of LBS in its own physical volume $(4\pi/3)(l_{LBS(g)})^3$ as Q, given by the ratio of this volume to its physical volume $p(l_{LBS})^2$, we consider a plane of circular area equal to $\pi(l_{LBS(g)})^2$ cutting through this volume. The number of LBS passing through the circle is given by $\psi = Q/\pi(l_{LBS(g)})^2 = (8/27)^{1/2}/pl_{LBS}$. It can be argued[10] that l_{LBS} is linearly proportional to l_K. In Ref. [10], we took

$l_{LBS} = (40/9)l_K$ as a guess, which amounts to $\psi = 0.1225/pl_K = 0.47\ nm^{-2}$. Such a calculation allows us to place the newly obtained information on the BDT of aPLLA among the available information on other glassy polymers. Adding to the literature data[211] for the tensile stress at the BDT as a function of the corresponding value of ψ, we see that aPLLA falls below the previously identified correlation,[10] as shown by the open symbols in the inset of Figure 7.6(b) that correspond to three different levels of physical aging. Such a downward deviation does not imply that aPLLA does not follow the correlation displayed by the eight other glassy polymers in Figure 7.6(b). Instead, it may be an indication of the difficulty to obtain aPLLA that is sufficiently non-aged. Physical aging allows the system to shift to a lower energy state. The deeper potential well provides stronger caging effects, corresponding to a more vitreous state. Thus, it is reasonable that a chain network adequate to bring about plasticity in a freshly quenched sample may become ineffective to drive the well-aged sample to yield and undergo ductile extension. However, we cannot rule out that PLA belongs to a different class due to its helical structure, i.e., our value for ψ is an overestimate.

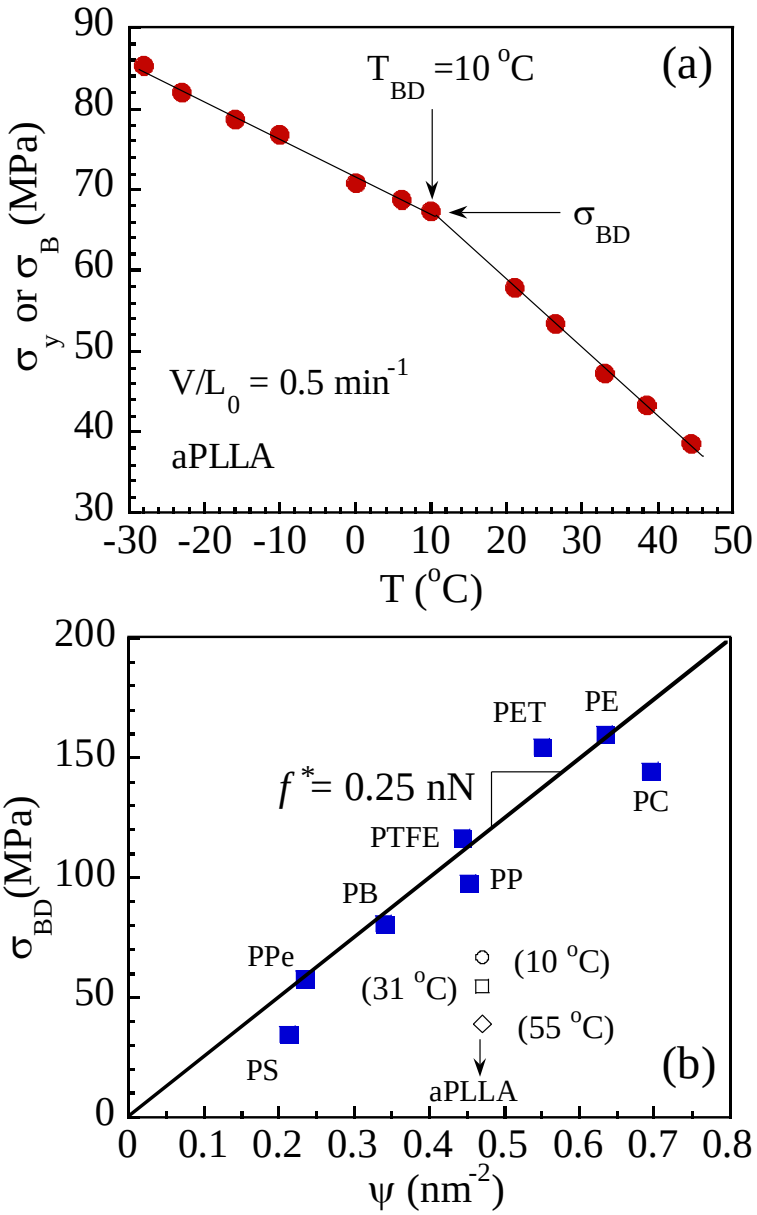

Figure 7.6 (a) Breaking stress (σ_B) and yield stress (σ_y) as a function of temperature T for aPLLA that is freshly quenched below T_g from its molten state to avoid melt-crystallization. The initial sample length L_0 = 10 mm. The kink at 10 °C reveals the location of the BDT at (10 °C, 67 MPa). (b) Tensile stress σ_{BD} at the BDT in terms of the area density ψ of the load bearing strand for nine different polymer glasses including the three

forms of aPLLA, fresh (circle), room-temperature stored (square) and heavily aged (diamond). The other eight polymers in filled squares are respectively in the order of increasing value for ψ, PS(70 ^{o}C), PPe(–60 ^{o}C), PB(–100 ^{o}C), PTFE(–196 ^{o}C), PP(–120 ^{o}C), PET (–100 ^{o}C), PE(–196 ^{o}C), bpA-PC(–140 ^{o}C), where the temperatures in the parentheses are T_{BD} of each polymer, PPe stands for poly(pentene-1), PB is 1,4-polybutadiene, and PC stands for bisphenol A polycarbonate.

7.3.1.2 Melt Stretching of aPLLA

One physical way to enhance the chain network is through adequate melt stretching. It is well known that after sufficient melt stretching brittle glassy polymers can turn ductile.[40, 212-213] For aPLLA, after melt stretching that is described in Figure 7.4, the tensile response at room temperature is much stronger along the melt-stretching direction as shown in Figure 7.7. It is important to note that the stress-strain data in Figure 7.7 were obtained after these pre-melt-deformed samples (denoted as ms-aPLLA) had been kept at room temperature for days. Therefore, ms-aPLLA is found to retain ductility despite physical aging, unlike the isotropic aPLLA studied in Figure 7.5.

Several comments are in order. First, it is worth noting that with increasing melt stretching ratio $\lambda_{ms,}$ the limiting draw ratio (L^*/L_0) at the specimen failure decreases. The product of $\lambda_{ms} = L_0/L_i$ and L^*/L_0 displays values of $(L_0/L_i)(L^*/L_0) = L^*/L_i$ = 3.1, 3.2, 3.3, 3.75 and 4.35 for λ_{ms} = 1, 1.5, 2, 2.5 and 3 respectively. The near constant L^*/L_i ~ ca. 3 up to λ_{ms}= 2 reveals the structure of the chain network. Here L_i is the initial sample length before melt stretching, and L^* is the final length at the failure of ms-PLLA. The structural failure occurs when the load bearing strand (LBS) l_{LBS} is straightened, i.e., when L^*/L_i =

l_{LBS}/l_K. Thus, l_{LBS}/l_K is ca. 3, i.e., on the average there are ca. 9 Kuhn segments per LBS. Previously, we have made a plausible estimate of $l_{LBS} = (40/9)l_K$ to correlate the breaking stress at BDT with the areal density of LBS as shown in Figure 7.6(b). Figure 7.4 indicates that the melt stretching is no longer affine beyond $\lambda_{ms} = 2$. Consequently, the ratio L^*/L_i can be expected to be greater, as is the case. Second, similar to the previous observations of the melt-stretching effects on the mechanical responses of glassy PS and PMMA, the samples quenched from melt stretching as shown in Figure 7.5 show systematically enhanced Young's modulus, increasing from 2.2 to 4.4 GPa as indicated in the inset of Figure 7.7. Correspondingly, there is increased yield stress along with considerably high overall stress levels. Third, fast melt-stretching, as described in Figure 7.4, is effective in promoting ductility in glassy polymers by producing a geometric condensation effect.[189] Upon cold drawing along the same direction as the melt stretching direction, load bearing strands can more effectively cause segmental activation because the LBS have been brought closer to one another by melt stretching. Such a recently proposed explanation[10] satisfactorily accounts for the observed effects seen in Figure 7.7.

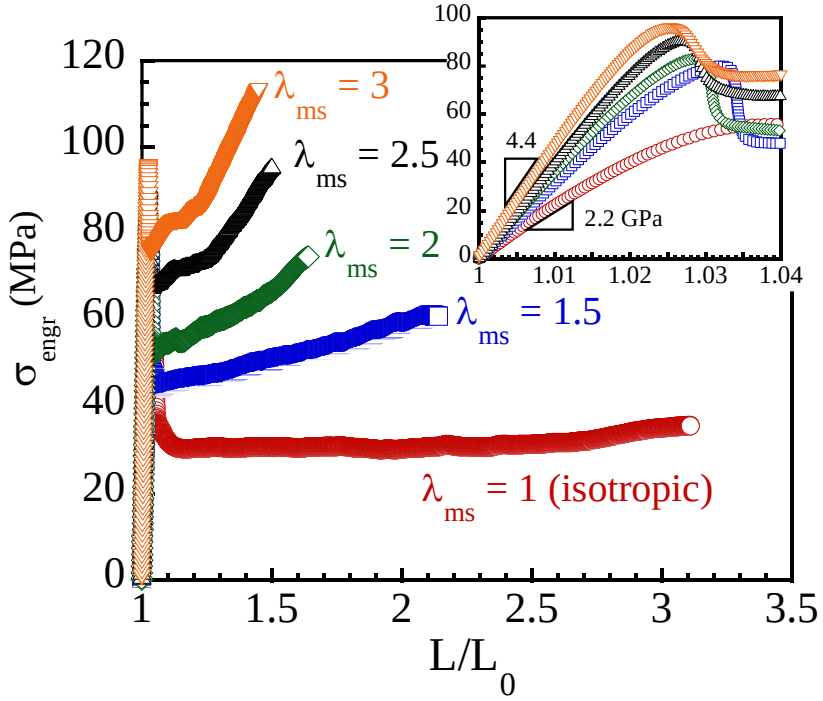

Figure 7.7 Enrgineering stress vs. draw ratio curves from uniaxial drawing of several melt-stretched aPLLA at room temperature (RT) with $V/L_0 = 0.5\ min^{-1}$, following the procedure described in Figure 7.4. In the case of $\lambda_{ms} = 3$, instead of allowing stress relaxation as indicated in Figure 7.4, the melt stretched aPLLA was immediately thermal-quenched to avoid cold crystallization. The inset shows that the Young's modulus increases markedly with λ_{ms}, from 2.2 GPa for the isotropic aPLLA to 4.4 at $\lambda_{ms} = 3$.

7.3.1.3 Lack of Ductility in Semi-crystalline PLLA

We examine crystalline PLLA obtained by either melt crystallization or cold crystallization of aPLLA. Typically, different crystalline morphologies result from the two different ways to crystallize the PLLA. The inserted images in Figure 7.8 shows the difference in the crystalline morphologies in the limit of saturated crystallization. Albeit hard to resolve in the case of cold crystallization, we assume both samples are made of

space-filling spherulites, which we label as PLLA(fmc) and PLLA(fcc), where fmc stands for fully melt-crystallized and fcc for fully cold-crystallized. If we assume the inter-spherulitic amorphous regions to be comparably narrow independent of the spherulitic size, i.e., similar in PLLA(fmc) and PLLA(fcc), the average volume fraction of such regions, $\phi_{intersph}$, is clearly very small in the melt-crystallized PLLA. As $\phi_{intersph}$ decreases with increasing spherulitic size, the drawability of PLLA is expected to deteriorate even above T_g unless there are enough tie chains to allow structural transformations of crystalline domains isotactic polypropylene is known to show such a trend.[214] In the present work, as shown in Figure 7.8, PLLAs in both crystalline forms are found to be brittle at room temperature. Above T_g, PLLA(fmc) also undergoes failure within 10 % drawing, whereas the cold-crystallized PLLA(fcc) is only slightly more drawable. It appears that the amorphous regions are not sufficiently strong and connected to the crystalline regions by tie chains to permit sufficient structural rearrangement of the crystalline domains. Strategies exist to affect the crystallization morphology[215-217] so that stronger connectivity could be established between spherulites and between lamellae, with the goal to improve mechanical properties of various semicrystalline polymers. Future work may adopt such approaches to determine whether the "self-nucleation" approach can improve ductility in well-crystallized PLLA.

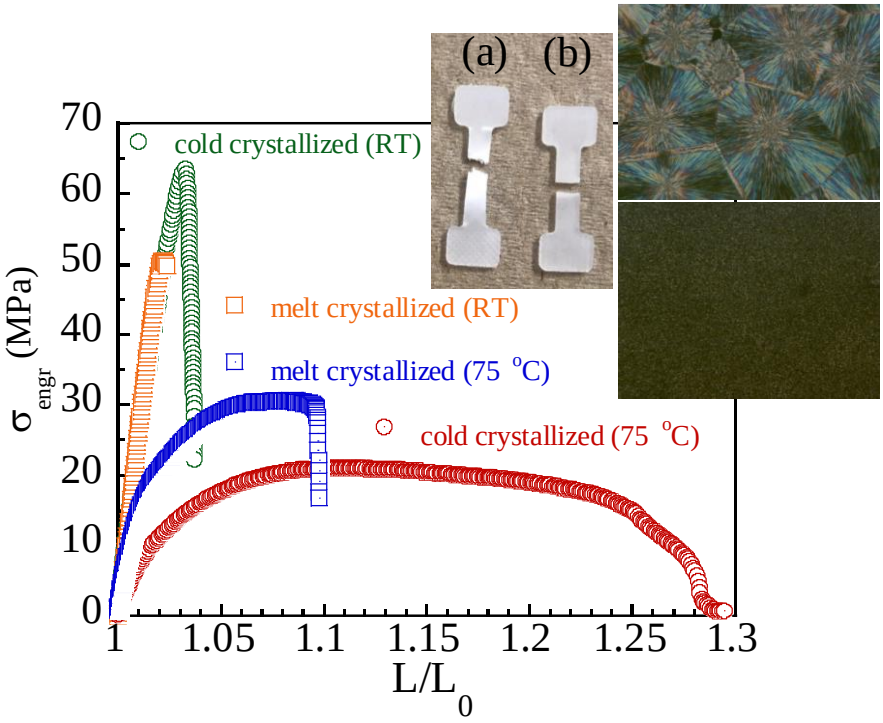

Figure 7.8 Enrgineering stress vs. draw ratio from drawing at V = 19.5 mm/min and L_0 = 39 mm of both PLLA(fmc) and PLLA(fcc) samples at room temperature and 75 °C. The inset photos show polarized-optical microscopy (POM) images of space-filled large spherulites in PLLA(fmc) and unresolvably small crystals in PLLA(fcc). A third photo in the inset shows the broken PLLA(fcc) samples with (a) at 75 °C and (b) at RT.

7.3.1.4 Effect of crystallization

As class B semi-crystalline polymers, mechanical properties of PLLA depends on temperature because the cohesive strength of the amorphous regions depends on whether they are glassy or above T_g. To characterize the ductility of PLLA, we need to figure out what determines the respective cohesive strength of the amorphous and the crystalline regions in PLLA. The cohesion of crystalline phase is related to the free energy change required to melt the crystals into the disordered state. Because there is no intermolecular

chain uncrossability in crystals, chain networking is absent. Thus, the mechanical strength of crystalline regions may be weaker than the glassy regions. As discussed below, integrity of the amorphous phase is determined by the structure of the chain network. Above T_g, the amorphous phase is a melt and its mechanical characteristics are the subject of nonlinear rheology[189]; below T_g, the mechanical behavior in the glassy state may be understood in terms of interplay between the chain network and a primary structure of intermolecular bonding arising from the vitrification.[10] To understand the adverse effect of crystallization on ductility, we present the following necessary discussions aimed to motivate additional experiments and to clarify the molecular mechanism for the loss of ductility in fully crystallized PLLA.

7.3.1.4.1 Below T_g (e.g., at room temperature)

In a semicrystalline polymer, amorphous regions exist in three places, (1) between lamellae in spherulites (i.e., intra-spherulitic), (2) at inter-spherulitic boundaries where adjacent spherulites grow to impinge on one another, and (3) in spaces where spherulites have not invaded into. The last type is present only in incompletely crystallized samples while the first two are too narrow to be spatially resolved under the standard POM observations: The intra-spherulitic (i.e., inter-lamellar) amorphous regions are typically smaller than the chain size R_g (radius of gyration), and inter-spherulitic regions are also plausibly smaller than R_g. The structure of inter-lamellar regions can be characterized by an areal density ψ_{tie} of tie chains between neighboring lamellae. When inter-spherulitic spacing is smaller than R_g, there can also be tie chains connecting adjacent spherulites.

When amorphous regions are much larger than R_g, there cannot be tie chains. The structural connectivity between crystalline and amorphous regions is controlled by "bridging chains". These bridging chains are partially embedded in the spherulites and partially dangle out into the amorphous phase to establish networking with other non-crystalline chains. Dangling chains not in network with other chains, are not bridging chains in our picture. For PLLA of sufficiently high molecular weight, chain networking (through chain uncrossability) exists in the large amorphous regions independent of the surrounding crystallization. Conceivably, full crystallization converts type (3) amorphous regions into type (2) regions. In the partially crystallized PLLA, the large amorphous regions (type (3)) can be perceived to be strong and made of a robust chain network.

According to the recent molecular model[10] for yielding and brittle-ductile transition of polymer glasses, the cohesion strength is determined by the structure of chain network that forms through intermolecular uncrossability. If the chain network undergoes structural breakdown via mutual interchain sliding at the junctions before the system gains molecular mobility to match the imposed rate of deformation, i.e., before yielding, the glassy polymer is brittle. Quite plausibly, it is easier for tie chains or bridging chains to pull out of the crystals than the process of mutual chain sliding in the disordered glassy state. Consequently, in partially crystallized PLLA, failures are expected to occur either in an intra-spherulitic manner or at spherulitic boundaries. For fully crystallized PLLA, failures can be either intra-spherulitic or inter-spherulitic. Here amorphous regions conceivably only exist in between lamellae inside spherulites and at inter-spherulitic boundaries. Such regions may contain tie chains if they are smaller than the coil size. Additionally, these

non-crystalline spaces may or may not have bridging chains. Crystallization condition may influence how the amorphous regions are constructed. PLLA would be mechanically weak if crystallization sufficiently disrupts formation of a global chain network that arises from topological entanglement via chain uncrossability.

In light of the preceding analysis, the mechanical data in Figure 7.8 may imply that there is insufficient chain networking in the amorphous regions of PLLA(fmc) and PLLA(fcc). In absence of significant structural transformation of the crystalline phase, space-filling spherulites may break up either internally or at the inter-spherulitic boundaries. In the following 7.3.2 we will carry out real-time or in situ polarized optical microscopy (POM) observations of various PLLA samples under extension to visualize how brittle and ductile responses emerge.

7.3.1.4.2 Above T_g

When spherulites fill up the space at a sufficiently high level of crystallinity, tie-chain-containing inter-spherulitic regions ensures that the system is solid like even above T_g. Conversely, at sufficiently low levels of crystallinity where inter-spherulitic regions are free of tie chains and permeating throughout the sample to form a continuous phase, the system can only behave like a melt and will creep under any amount of stress.

At temperatures above T_g but still well below T_m, before the macroscopic stress grows to a significant level, associated with high tension in tie and bridging chains, e.g., before yielding, spherulites are rigid and do not deform. Consequently, inter-spherulitic amorphous regions experience considerably higher local strains than the nominal strain. High areal densities ψ_{tie} and ψ_{bridge} of tie and bridging chains at the crystal surfaces assures

that large elastic inter-spherulitic melt deformation can take place. Drawability depends on how much such local melt deformation can take place before sufficiently large chain tension arises to cause chain pullout from spherulites. Specifically, at a given global strain, the average level of local melt deformation, on the average, is expected to be larger when spherulitic sizes are larger, corresponding to a smaller value of the volume fraction $\phi_{intersph}$ (occupied by inter-spherulitic regions). In other words, the drawability is expected to vary with the crystalline morphology as well as the degree of crystallinity. Depending the values of ψ_{tie} and ψ_{bridge}, after high melt stretching of amorphous regions between spherulites, failure may take place in one of the several ways. First, it can occur at inter-spherulitic boundaries via pullout of few tie and bridging chains from spherulites, corresponding to amorphous regions detaching from spherulites. The inter-spherulitic failure can also arise from chain disentanglement similar to that encountered in bulk melt failure[218] of various kinds. Second, there could be intra-spherulitic breakup due to either intra-lamellar failure or tie chains pulling out of lamellae, which may be labeled as inter-lamellar failure. In fact, experimental observations of such intra-spherulitic "crazing" have indeed been made in the literature: Relative to the drawing direction, both radial and tangential micro-cracks are expected and indeed found[219] to take place within a spherulite. The two types of failure take place[220] because lamellae in a spherulite orient both along and perpendicular to the drawing direction.

According to the preceding analysis, the poor drawability of either PLLA(fmc) or PLLA(fcc) shown in Figure 7.8 indicates that the slow crystallization has considerably disrupted the entanglement network present in aPLLA. In other words, in the present PLLA

ψ_{tie} and ψ_{bridge} are plausibly low, and structural failure takes place via any or a combination of the three failure "modes" listed at the end of the preceding paragraph. The crystal breakup on local scales would appear in the form of cavity or void so that the sample whitens. Photo (a) in Figure 7.8 shows a sign of such behavior. We will not elaborate on this feature and refer the reader to a recent review[221] on cavitation during ductile drawing of various semicrystalline polymers. It suffices to remark that for PLLA the crystallization has sufficiently depleted the entanglement network, making it impossible for the cavitation to stabilize – stabilization would have resulted in far better drawability than observed in Figure 7.8.

When ψ_{tie} and ψ_{bridge} are sufficiently high, it means that the crystallization did not completely disrupt the entanglement network that exists prior to the crystallization. In this limit where a robust chain network permeates throughout a semi-crystalline polymer, tensile extension may result in transformation or reconstruction of crystalline regions, involving either partial "melting" of crystals as envisioned by Flory and Yoon[222] or fragmentation of lamellae as perceived by Peterlin[144-145]. Such rearrangements of crystalline domains occur through massive chain pullout of crystals during large deformation of amorphous regions. The high drawability of linear polyethylenes and polypropylenes presumably stems from the preserved chain networking whose cohesive strength derives from the chain uncrossability. When crystallization does not destroy the entanglement network, chain pullout to result in either crystal melting or fragmentation does not lead to termination of the ductile drawing.

In summary, relative to the glassy amorphous phase, the crystalline regions may be mechanically weak and brittle whereas the cohesive strength of the non-crystalline regions is determined by the mechanical strength of the chain network. Failure of the chain network occur via chain pullout in a disordered glassy polymer when chain tension reaches a level of a fraction of one nano-Newton.[10] Because of chain alignment in the crystals, there is no interchain uncrossability as there is in amorphous state, the chain pullout force from the crystalline state can be much lower, especially when there is significant chain mobility in the crystalline phase.[223] For example, a recent AFM study[224] shows this force to be as low as 40 pN. This comparison forms the basis for our explanation for the brittle behavior of crystalline PLLA that the crystals are mechanically weaker. Here the pullout force is low for PLLA because there is evidence that considerable chain mobility also exists in the PLLA crystals.[225] Thus, while low pullout forces associated with high crystal chain mobility cannot be a favorable factor for ductility of glassy semicrystalline polymers, they permit high drawability above T_g if and only if there is sufficient chain networking, undisrupted by crystallization. Indeed, greatly reduced chain mobility in crystals, such is the case of nylons and PET,[223] may imply that the crystals are rigid and hard to be torn part before the amorphous regions lose structure integration.

7.3.2 Time Resolved Polarized-Optical Microscopy (POM) Observations During Extension

The preceding discussions motivated us to carry out in situ POM experiments and record how failure takes place during tensile extension of PLLA samples with varying crystalline characteristics. The images in Figure 7.8 indicate that the crystalline

morphology is too fine to resolve with the standard POM for the PLLA prepared with cold crystallization. Therefore, the following in situ POM studies are all based on PLLA prepared with melt-crystallization. This section is divided into two subsections to focus respectively on pmc-PLLA and fmc-PLLA samples.

7.3.2.1 Partial Crystallized PLLA

When crystallization is allowed to run its course to completion, the amorphous regions only exist at the narrow inter-spherulitic boundaries and between lamellae inside spherulites and are not spatially resolvable by the standard POM method. In order for us to resolve and determine the locations of failure during cold draw, we purposefully prepared samples that are only partially crystallized so that spherulites are "dispersed" in the amorphous matrix, amenable to characterization by the time-dependent POM observations. Using such samples, we can explore the mechanical interplay between inter-spherulitic amorphous regions and adjacent spherulites.

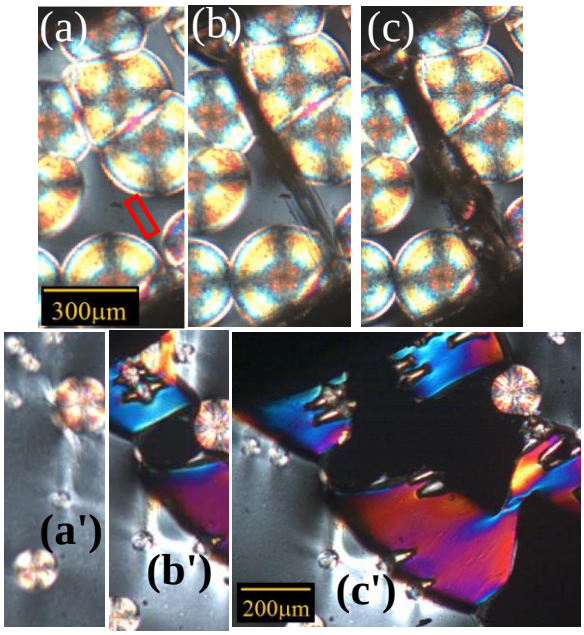

Figure 7.9 Time-resolved POM images (a)-(c) showing uniaxial drawing of pmc-PLLA(1) at room temperature at V = 3 μm/s; images (a') to (c') describe the room-temperature drawing of pmc-PLLA(2) at V = 5 μm/s.

We first apply the in situ POM method to examine the mechanical and structural responses of a glassy pmc-PLLA to cold drawing at room temperature. Figures 7.9(a)-(c) show one set of POM photos during cold drawing of a PLLA at room temperature (below T_g) that was freshly partially melt-crystallized. Image (a) shows the buildup of birefringence in the amorphous "matrix" that was initially totally dark under crossed polarizers. Failure suddenly occurs at one inter-spherulitic boundary, as shown in Figure 7.9(b). When high forces build up in tie and bridging chains, brittle failure can take place at inter-spherulitic boundaries due to chain pullout, as speculated in 7.3.1.4.1 while the amorphous region remains intact. The observed inter-spherulitic rupture can be the generic cause of brittle fracture in PLLA. Intra-spherulitic breakup took place too. Our in situ POM video shows that the localized inter-spherulitic rupture and intra-spherulitic failure allowed the sample to undergo rapid (localized) elastic recoil. This recoil produces fast tensile extension in the adjacent amorphous region, indicated by the red box, leading to crazing and the brittle-like failure. Figure 7.9(c) shows that the amorphous region was still drawing instead of complete breakup into two pieces.

In a second sample, images (a') and (b') in Figure 7.9 confirm that the amorphous region of a freshly melt-crystallized PLLA is essentially ductile. While necking takes place in the glassy, non-crystalline regions, rupture occurs at the (internal) edge and the boundary of the isolated large spherulite with the glassy matrix. Moreover, the two small spherulites

appear to be torn apart by the highly strained surroundings. The failure associated with the large spherulite left a large hole (Figure 7.9(b')) to grow toward the total breakup (Figure 7.9(c')).

At temperatures above T_g, real-time POM investigations of PLLA provide additional insights regarding the structural decohesion of such a composite like material (with spherulites acting like fillers). Here we draw PLLA samples that either contain sizeable amorphous regions among space-filling spherulites or have spherulites "dispersed" in an amorphous melt. In the first example that is fully melt-crystallized except for one large amorphous region shown in Figure 7.10(a), we confirm that spherulites usually remains attached to their amorphous surroundings during the initial extension at 76.5 ^oC. The first failure occurs at the inter-spherulitic boundary as indicated by the circle in Figure 7.10(b). At a later stage of local stretching between spherulites, when V increased from 5 μm/s to 200 μm/s, the melt starts to peel off from the spherulite and as shown in Figure 7.10(c). Since spherulites do not deform, after the inter-spherulitic rupture, the local strain rate in the amorphous "gap" is much higher than the nominal rate $\dot{\varepsilon}_n = V/L_0$: With V = 5 μm/s and L_0 = 12 mm, $\dot{\varepsilon}_n = 4.2\times10^{-4}$ s^{-1}. By analyzing the video, we estimate the local rate to be as high as $(L_0/l^*)\,\dot{\varepsilon}_n = 0.05$ s^{-1} at V = 5 mm/s. Since τ_d = 438 s at 76.5 ^oC as listed in Table 7.1, the melt extension took place at a high Weissenberg number $Wi = \dot{\varepsilon}\,\tau_d = 22 >> 1$. With V = 200 μm/s, the other "melt phase" indicated by circle 3 in Figure 7.10(c) starts to get stretched. When large tensile deformation of the entangled region results in sufficiently high tensile stress, the melt quickly detaches from the spherulite, as shown in Figure

7.10(d). Such a sharp separation is evidence that ψ_{bridge} is not sufficiently high to tear the spherulite apart: A few chain pullouts from the spherulite cannot visibly damage or transform the crystal. Alternatively, the peeling off could arise from localized tensile melt decohesion due to chain disentanglement in the bulk close to but still multiple monolayer away from the spherulitic boundary. In a second case, Figure 7.10(a') is a POM image before any internal structural failure. As the strain increases, an inter-spherulitic breakup appears as indicated by the circle in Figure 7.10(b'). Figures 7.10(c') and 10(d') show subsequent drawing at two other inter-spherulitic boundaries indicated in Figure 7.10(a'), numbered 2 and 3 respectively. According to the corresponding video, it appears that the materials were continually drawn into the stretching melt by continuously peeling off from the spherulites. Here we may suggest that ψ_{bridge} is evidently high enough to damage the integrity of the spherulites.

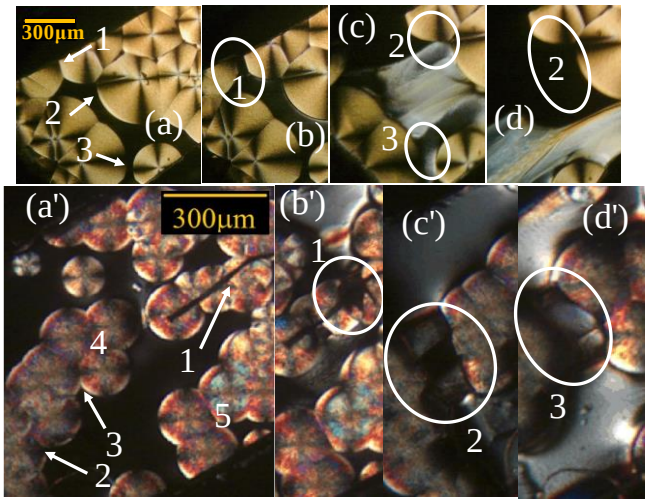

Figure 7.10 POM images at different stages of uniaxial extension at 76.5 ^{o}C: Images (a)-(d), showing pmc-PLLA(3) first ((a) and (b)) at V = 5 μm/s and subsequently ((c) and (d)) at 200 μm/s; images (a')-(d') involving pmc-PLLA(4) during drawing at V = 5 μm/s, where

five inter-spherulitic boundaries are indicated in (a') that sequentially undergo substantial melt stretching and failure as shown in (b')-(d') – the images of the inter-spherulitic separations at 4 and 5 are omitted herein.

7.3.2.2 Fully Crystallized PLLA

To illustrate the effect of full crystallization on the mechanics of PLLA, we carry out, first at room temperature, in situ POM studies of PLLA(fmc) samples where large spherulites fill up the space as shown by the image in Figure 7.8. As speculated at the end of 7.3.1.4.1, Figures 7.11(a)-(b) shows POM images how the brittle fracture occurs: the crack passed along the inter-spherulitic boundaries and on its way also cut across a spherulite. Here the amorphous regions either at inter-spherulites boundaries or between lamellae inside spherulites are too small to be spatially resolved. In terms of the concepts of areal densities ψ_{tie} and ψ_{bridge} introduced in 7.3.1.4, the images (a) and (b) in Figure 7.11 suggest that both ψ_{tie} and ψ_{bridge} are insufficiently high to prevent the observed sharp ruptures that occur both inter-spherulitically and intra-spherulitically, presumably by pullout of the few tie and bridging chains from crystal surfaces.

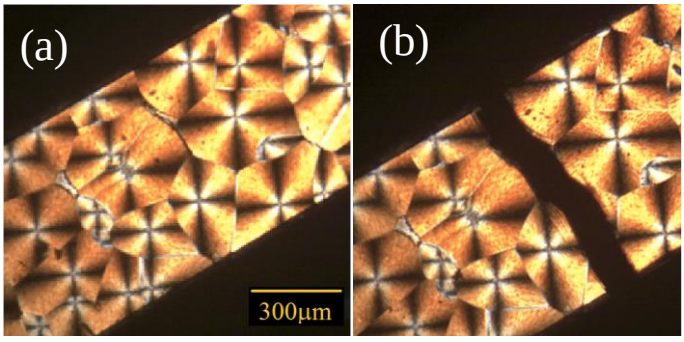

Figure 7.11 POM images (a)-(b) showing room-temperature drawing of fmc-PLLA(1) at V = 3 μm/s, before and after fracture.

The lack of drawability of PLLA(fmc) above T_g implies insufficient tie or bridge chains at inter-spherulitic boundaries and considerable spherulitic sizes. When non-deformable spherulites fill up space, they amplify the local strain field experienced by amorphous regions by roughly a factor of $1/\phi_{intersph}$. With the volume fraction of inter-spherulitic regions $\phi_{intersph} << 1$, i.e., 0.01, 5 % nominal draw ratio amounts to an average extension of amorphous regions on the order of 500 %. Since spherulitic sizes vary in space, $\phi_{intersph}$ changes locally so that $\phi_{intersph}(\mathbf{r})$ can be realistically much smaller than 0.01. Thus, melt deformation between spherulites can be remarkably high at small nominal strains. Even when the amorphous region can be regarded as an entangled melt, the melt strength can readily be exceeded at a modest nominal strain. The consequence is the observed poor drawability. Figure 7.12 contains three sets of images, showing three cases of uniaxial extension at 81 ^oC. Figure 7.12(b) shows an intra-spherulitic failure because the crystal was damaged by a small cut on the sample edge as shown in Figure 7.12(a). Images (a')-(c') in Figure 7.12 shows brittle fracture starting from the top of the image, with the crack mostly passing along the inter-spherulitic boundaries. In the third example shown in (a")-(b") of Figure 7.12, the rupture also appears to follow along the inter-spherulitic boundaries. Thus, in all cases of PLLA(fmc), the POM observations suggest that tie and bridging chains not dense enough to allow transformation of crystals by chain pullout.

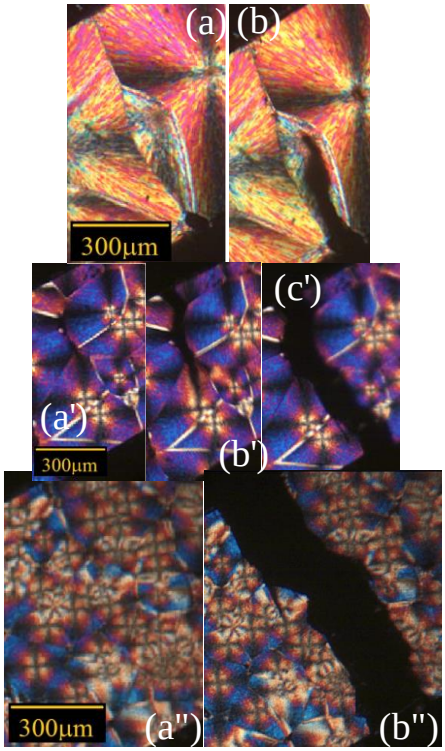

Figure 7.12 Three sets of POM images involving drawing at 81 ^{o}C of fmc-PLLA(2)-(4) at V = 5 μm/s.

7.3.3 Concluding Remarks

The peculiar adverse effects of crystallization on ductility observed by comparison between Figure 7.5 and Figure 7.8 motivated our adoption of real-time POM observations. A plausible picture emerges from the analysis of the available experimental information. Since chains pack in an ordered manner in crystals, free of networking, the crystalline phase can be mechanically weaker than the disordered amorphous state when there is enough chain entanglement. Even though there are robust chain networks in glassy amorphous regions, its mechanical connection with the surrounding crystals can be rather weak if there are few tie or bridging chains at the interface between the crystals and amorphous regions. Therefore, below T_g structural failure may readily take place along

inter-spherulitic boundaries or inside the spherulites. When a semicrystalline polymer is fully crystallized, i.e., made of space-filling spherulites, it is necessarily weak and plausibly brittle relative to the same polymer in amorphous glassy state where chain networking provides strong cohesion. Specifically, in absence of sufficient chain connectivity at the inter-spherulitic boundaries, the spherulites cannot be induced to undergo "melting". Consequently, continuous drawing causes either the spherulites to suffer intra-spherulitic fragmentation or inter-spherulitic failure. Both types were observed as shown in 7.3.2.2. In the case of inter-spherulitic failure, it is reasonable to envision that glassy chains in the amorphous region, being partially embedded in the crystalline phase, would undergo chain pullout. The pullout from lamellae has been verified using partially crystallized samples. In the well crystallized samples, another possibility is that there is little chain networking at the inter-spherulitic boundaries, either because the interstitial region is too large for inter-spherulitic tie chains to exist or there are few of such tie chains or chain entanglements have been depleted during the slow crystallization. In this case the inter-spherulitic regions would be weaker than the spherulites so that failure would be mainly located at the inter-spherulitic boundaries, as observed in 7.3.2.2.

Bridging chains are dangling chains from the peripheral of a spherulite. They cannot be mechanically effective unless they participate in chain networking in the amorphous region. When molecular weight is insufficiently large, few effective bridging chains are present at inter-spherulitic boundaries, and there may be few tie chains between lamellae inside each spherulite. The mechanical behavior of the current commercial PLLA, at room temperature and above T_g, suggests that the areal densities of tie and bridging chains are

moderate. Structural failures readily occur upon the tie and bridging chains pulling out of the crystals, manifesting in the form of both inter-spherulitic and intra-spherulitic breakup. We cannot rule out that the amorphous regions in fully crystallized PLLA are equally weak due to lack of chain entanglement. Since we are unable to spatially resolve amorphous regions in fmc-PLLA, we carried POM observations of pmc-PLLA samples both below and above T_g and revealed the structural/mechanical interplay between spherulites and surrounding amorphous regions: Inter-spherulitic failure could cause local breakdown of amorphous phase (cf. Figure 7.9(b)-(c)), and the interface between a spherulite and surrounding glassy "matrix" is weaker than the amorphous phase (cf. Figure 7.10(b)-(d)). High areal densities ψ_{tie} and ψ_{bridge} of tie and bridging chains imply that crystallization did not deplete the pre-existing chain entanglement from the molten state. Preservation of strong chain entanglement in the amorphous regions at inter-spherulitic boundaries is essential for ductility in highly crystalline polymers. In this case, as is the case for highly drawable PP and PE materials, amorphous regions may transform or reconstruct crystalline regions through massive and progressive pullout of abundant tie and bridging chains from the crystals instead of inter-spherulitic and intra-spherulitic separation, observed in PLLA. Slip along dislocation plane can also be regarded as involving ductile deformation of crystals that could take place in PP and PE[226] but not observed in our POM observations of PLLA.

7.3.4 Superior Ductility of PLA: Theoretical Design and Experimental Realization

Although melt-stretched aPLLA remains completely ductile, stable against physical aging, as indicated in 7.3.1.2, such a glassy polymer is not thermally resilient at high

temperatures above T_g as expected, e.g., at 120 ^oC, which is 60 ^oC above its T_g. Introducing crystallization in PLLA is a common approach to improve heat resistance, at the expense of poor ductility. In 7.3.1.4 and 7.3.2 we have explained why PLLA is brittle in presence of large crystals. To dramatically improve the mechanical performance of PLLA, we need the crystallization to take place on nanoscopic scales and to preserve chain entanglement.

Based on our understanding of the origin of brittleness in fully crystallized PLLA, we first contemplate a theoretical scenario to produce crystallization without disrupting the entanglement network and then explore whether such a concept would allow PLLA to exhibit superior mechanical properties. Three conditions must be met to realize the scenario. First, crystallization is readily suppressible by fast thermal quench from the molten state to below T_g. This is more realistic for class B semicrystalline polymers that can usually avoid melt crystallization with their T_g sufficiently above room temperature. Second, the amorphous polymer can avoid cold crystallization in a certain temperature range above T_g. Third, in the temperature range where cold crystallization does not take place, the overall chain relaxation time τ_d must be sufficiently long so that it is experimentally feasible to subject the melt to fast extension with a high Weissenberg number *Wi*, i.e., $Wi >> 1$. According to the established phenomenology of nonlinear polymer melt rheology,[189] an entangled melt can be highly elastically stretched at $Wi >> 1$ without significant flow.

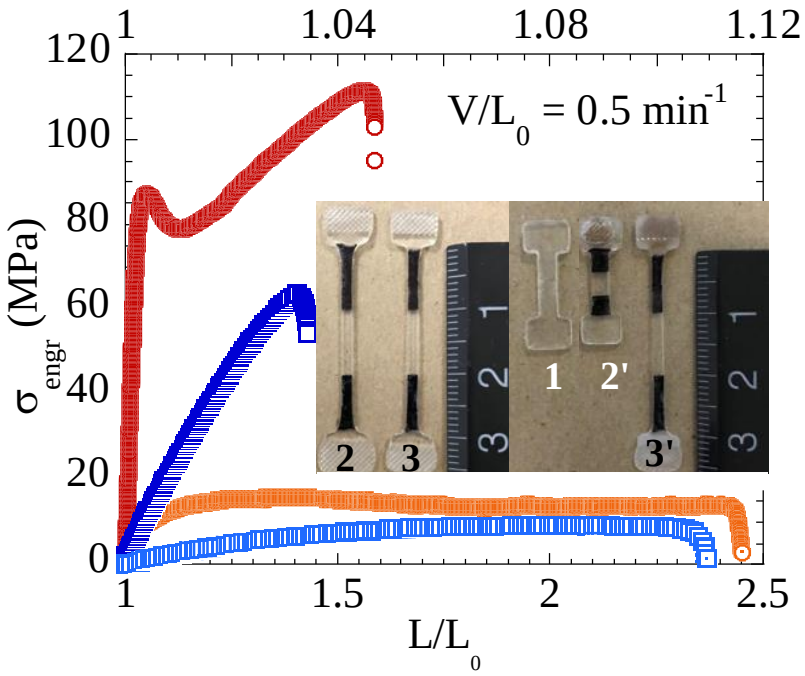

Figure 7.13 Tensile stress vs. draw ratio of the cc-ms-PLLA (circles) and isotropic aPLLA (squares) at two temperatures: room temperature (open symbols) and 100 ^{o}C (dotted symbols) where the data for aPLLA (squares) are presented using the upper X axis, ranging from 1 to 1.12. In the inset photos where the scale is in the unit of centimeter, sample 1 is an isotropic aPLLA. Melt stretching to λ_{ms} = 3 results in sample 2 (ms-aPLLA). Cold crystallization of this melt-stretched sample results in sample 3 (cc-ms-PLLA) that is as clear as sample 2. Upon subjecting sample 2 to 120 ^{o}C within a minute, the ms-aPLLA shrank back its original (pre-melt-stretching) length as shown by sample 2' in the photo. In contrast, after 1 hour of annealing at 120 ^{o}C, the cc-ms-PLLA shows indiscernible change in its length, as shown by image 3'.

Specifically, we envision the following picture. In the temperature range where the amorphous polymer does not cold crystallize the entanglement network is sufficiently fast

stretched either uniaxially or biaxially to various degrees quantified by the stretching ratio λ_{ms} (or λ_{ms1} and λ_{ms2} in the case of biaxial extension that is not explored in this paper). For a non-crystalline entangled polymer, if the melt is sufficiently stretched, the cessation of the melt stretching will result in elastic yielding due to chain disentanglement, leading to macroscopic breakup of the specimen.[189] For PLLA, upon cessation, if the chain alignment due to the fast melt stretching could induce rapid cold crystallization, the sample may avoid the elastic yielding. Assuming this is the case, we can carry out one of the two procedures as follows. We can hold the melt-stretched PLLA fixed in space to wait for the melt stretching to induce substantial cold crystallization. Alternatively, we can first rapidly quench the melt-stretched sample below T_g to preserve the melt stretching effect. We then examine whether such a melt-stretched PLLA would undergo appreciable cold-crystallization upon annealing at a suitable temperature above T_g that does not have to be the melt-stretching temperature. It turns out for the current PLLA that both protocols allow sufficiently fast cold crystallization to take place.

Specifically, Figure 7.4 shows stress vs. strain curves involving melt stretching at 70 ^oC of aPLLA to λ_{ms}=3. While aPLLA would not cold-crystallize at 70 ^oC in one hour in its isotropic state where the reptation time is long as listed in Table 7.1, after the melt stretching to λ_{ms}= 3, the aPLLA immediately starts to crystallize upon termination of the imposed stretching. More important, this directional cold crystallization could occur in a space of $3\times2^{1/2}\times l_{ent}$ ~ 19 nm if we assume that the crystallization did not remove any surviving entanglement. Here the factor of $2^{1/2}$ arises because Figure 7.4 can be interpreted to suggest that only half of the equilibrium entanglement was left. The 2D WAXS pattern

in Figure 7.4 shows the evidence of significant cold crystallization although the sample is optically clear as predicted. The transparency implies the crystal sizes are too small to strongly scatter. The melt-stretching-induced cold crystallization has made the PLLA highly heat resistant: no dimensional change was observed after annealing at 120 ^{o}C for 1 hr. The photo inset in Figure 7.13 contrasts the cold-crystalized melt-stretched PLLA (cc-ms-PLLA) with melt-stretched PDLLA. The mechanical properties of cc-ms-PLLA are also superior: At room temperature, the mechanical enhancement by melt stretching is preserved, as assessed by the comparison between Figure 7.13 and Figure 7.7. The mechanical characteristics at 100 ^{o}C are also remarkable: The Young's modulus is as high as 250 MPa. Along with the absence of any shrinkage at 120 ^{o}C, this high stiffness indicates that the sample is space-filled with nano-sizes crystals. In contrast to the stress level shown by melt stretching of aPLLA at 70 ^{o}C in Figure 7.4, the stress response of the cc-ms-PLLA at 100 ^{o}C is higher by a factor of ten. Apparently, the system behaves as if it is a heavily loaded polymer nanocomposite, with the nanocrystals acting like rigid fillers.

7.4 Summary

The key objective of this research is to explore ways to improve the mechanical performance and thermal resistance of a class of promising advanced materials, i.e., poly(lactic acid) (PLA), which is both bio-renewable and biodegradable. To achieve this, we must first understand why PLA is typically brittle in both amorphous and semicrystalline forms and then design molecular level strategies to remove the cause of poor ductility.

According to a recent molecular picture,[10] the ductility of glassy polymers is determined by the availability and ability of a robust chain network to overcome the caging effect associated with the vitrification. We attribute the brittleness of the amorphous PDLLA and aPLLA to the rapid physical aging because the chain network in such a biopolyester is shown to be of an adequate level in terms of the areal density of load-bearing strands. It is important to note that even the most ductile bisphenol-A polycarbonate is brittle at room temperature upon adequate aging. Because melt-stretching can turn brittle polystyrene completely ductile at room temperature,[40, 212-213] we show that the same physics[10] is at play and allows aPLLA to become ductile against aging. In other words, high melt stretching keeps aPLLA ductile despite ongoing physical aging. However, such melt-stretched aPPLA is not dimensionally stable at 100 ^{o}C in absence of crystallization.

Full crystallization, either by cold crystallization of a thermally quenched amorphous PLLA or melt crystallization, makes PLLA brittle at room temperature even when freshly prepared, i.e., without aging. To explain such behavior, it is necessary to understand what makes a glassy aPLLA ductile. In other words, we must first identify and evaluate the cohesive strength of a non-crystalline PLA and compare it to that of a single crystal of PLLA. Given the available phenomenology, i.e., based on the POM observations of the paritally crystallized PLLA samples, we suggest that the crystalline state is mechanically weaker than the amorphous state in PLLA. When a robust chain network is present in amorphous regions, the intermolecular chain uncrossability ensure that the glassy state can be activated. In contrast, the crystalline phase is plausibly prone to rupture because there is no chain uncrossability to suppress chain pullout from the lamellae made of parallel-packed

folded chains. The slow crystallization kinetics may have allowed a significant fraction of chain entanglement (defined by the level of mutual chain crossability) to be depleted.

We first carried out time-resolved polarized optical microscopy (POM) observations at room temperature to compare with our theoretical considerations. Specifically, we showed using melt-crystallized PLLA that highly crystallized samples are brittle as they either fracture at inter-spherulitic boundaries or suffer intra-spherulitic rupture. Thus, the in situ POM study supports the conclusion that a glassy amorphous region can be stronger than a spherulite. In the case where the PLLA is space-filled with spherulites, it tends to fail under small extension, indicating the possibilities that (a) there are insufficient tie and bridging chains between neighboring spherulites, (b) little chain networking is present in the inter-spherulitic regions (in which case the areal densities ψ_{tie} and ψ_{bridge} of tie and bridging chains are necessarily very low). We suggest that ψ_{tie} and ψ_{bridge} are low and the brittle failure occurs by pullout of the few tie and bridging chains from the crystals without transforming or reconstructing the crystalline phase. We carried out in situ POM observations of PLLA above T_g to evaluate the possibility (b).

The above-T_g POM observations suggest that there is sufficient entanglement networking in the amorphous regions to permit large tensile melt-like extension. For fully crystallized PLLA samples that are hardly drawable, our POM measurements show that the failure occurs by the amorphous regions detach from the spherulites. This implies that the existing tie and bridging chains are insufficient by pullout to convert crystals into the new amorphous phase.

In general, full melt and cold crystallization lowers ductility of PLLA below T_g. When spherulites are large and space-filling, PLLA are inevitably brittle at room temperature. By inducing nano-crystal formation through melt-stretching of amorphous PLLA, we preserve the chain uncrossability and eliminate formation of spherulites. The procedure of cold crystallization from melt-stretched PLLA produces a new form of PLLA with superior mechanical and thermal characteristics. Thus, by identifying the mechanism of poor ductility in conventional PLLA, we have uncovered a process to extremely tough, thermally stable and optically transparent PLLA, making it plausible for this important class of advanced bio-renewable and bio-degradable polymers to replace the petroleum-based polymers such as polyethylene terephthalate.

CHAPTER VIII

INDUCING NANOCRYSTALLIZATION IN SEMICRYSTALLINE POLYMERS BY ELASTIC MELT DEFORMATION

8.1 Introduction

One frontier in polymer physics is the subject of molecular mechanics of semicrystalline polymers (SCPs). Unlike other modern materials, polymeric materials are uniquely ductile. While SCPs have earned a considerable reputation as modern materials with high specific mechanical strength, a great deal of improvement could still be expected with further chain-level understanding of the physics governing the ductility of SCPs. It is well known that upon increasing either the degree of crystallinity [227] or the average size of spherulites [228] SCPs lose drawability and become brittle. Moreover, we find that glassy SCPs are typically brittle, with polypropylene (PP) being a widely known example [229-230]. Such adverse effects of crystallization on toughness has made it hard for the promising bio-based poly(L-lactic acid) (PLLA) to replace the petroleum-based polyethylene terephthalate (PET).

In our judgment, when a SCP crystallizes to form space-filling spherulites, the chain network is disrupted relative to its structure in the molten state. Specifically, lamellar crystallization depletes the interchain uncrossability constraints. For a SCP to be ductile is

for its crystalline phase to yield, i.e., to undergo plastic transformation. Spherulites in a ductile SCP must be capable of shape changes while conserving the volume during uniaxial drawing. Since spherulites, as aggregates of jammed lamellae, are rigid and can only deform through breakdown of the lamellae, there is no guarantee during drawing that such crystal melting [143] or fragmentation [144-145] can occur without localized structural failure of the underlying chain network. This is especially true when a SCP is drawn below its glass transition temperature T_g.

A great deal of recent efforts [231-236] have focused on how external deformation near and above crystallization temperature T_c induces crystallization, e.g., creating shish-kebab like crystalline morphology, most often involving isotactic PP (iPP). It is usually unclear [237] whether or not such deformation-induced crystallization result in improved mechanical properties. While pre-deformation of molten iPP has been explored to make it ductile in the glassy state [238] little is known about whether or not drawing iPP in its crystalline state can achieve comparable improvement. Our recent unpublished study shows that a much stronger iPP can be produced by exploring the effects of pre-drawing in the crystalline state.

In this chapter, we describe a different approach and perspective, aiming to identify an effective way to enhance mechanical and thermal performance for a class of SCPs, which we term class B. Class B SCPs are defined as semicrystalline polymers with higher T_g than room temperature and slow crystallization kinetics so that they can be fast thermally quenched from their molten states into a glassy state without crystallization. PET and PLLA belong to this class. Having class B SCPs in their amorphous state provides us

an opportunity to explore the possibility of having crystallization without disrupting the chain network.

We envision the following scenario to achieve considerable crystallization while preserving the integrity of the chain network. Let us consider annealing an amorphous SCP above its T_g. The annealing temperature T_{ann} can be chosen so that the SCP at T_{ann} does not undergo cold crystallization over a specific period of time t_{exp} due to lack of sufficient molecular mobility. This experimental time window is long enough for us to subject the rubbery SCP to melt deformation such as uniaxial (or biaxial) extension. It is well known [189] that melts of high molecular weight can be elastically extended to a substantial stretching ratio λ_{ms}, e.g., 3, without encountering significant chain disentanglement that would lead to structural failures of various kinds [218]. Thus, to achieve melt stretching in the elastic deformation limit, let us apply a sufficiently high extensional Hencky rate $\dot{\varepsilon}$ relative to the Rouse relaxation time $\tau_R(T_{ann})$ i.e., the Rouse-Weissenberg number $Wi_R = \dot{\varepsilon}\tau_R > 1$, so that the entanglement network is substantially melt-stretched to a stretching ratio λ_{ms} in before failure [239] of the network. Here the degree of chain orientation depends on Wi_R and λ_{ms}. If sufficient molecular orientation is produced by the melt stretching, it is plausible that in presence of the significant chain alignment cold crystallization would immediately take place on the length scale of the network mesh size.

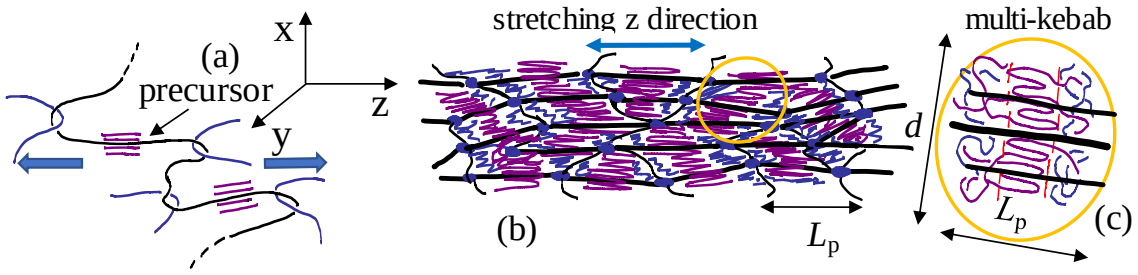

Figure 8.1 (a) Elastic stretching of a chain network to create precursors, i.e., highly aligned entanglement strands for cold crystallization at temperature (T_g<) T_{ann} where cold crystallization would not occur in absence of the melt stretching. (b) Upon full crystallization, a web of connected kebab confined within the network mesh size, leaving the network intact. The stretched meshes define the cylinder-shaped clusters with diameter d and height L_p. (c) The characteristic dimension of the crystals, L_p, is defined by the size of the stretched mesh whereas the lateral dimension d depends the regularity of the chain network.

Specifically, as shown Figure 8.1(a), we foresee a rapid emergence of precursors for nanocrystallization associated with the highly stretched strands in the entanglement network. The crystal sizes can be expected to be nanoscopic for several reasons. First, the density of nucleation sites should be as high as defined by the mesh size, which can be taken as the entanglement spacing for simplicity. Second, upon crystallization that acts like crosslinking, the chain network locks up so that no disentanglement due to the high chain retraction force could take place. Consequently, no strands can escape from the interchain uncrossability constraint, thus limiting the available strands per nucleation site for crystallization. More explicitly, as sketched in Figure 8.1(b), it is reasonable to propose a specific morphology, involving a network of connected small lamellae, where each lamella may be in the shape of short cylinders of diameter d and height L_p, as shown in Figure 8.1(c).

8.2 Experimental

8.2.1 Materials

Two commercial semi-crystalline polymers, poly(l-lactic acid) (PLLA) and poly(ethylene terephthalate) (PET) were used in this study. The weight average molecular weight M_w, entanglement molecular weight M_e and glass transition T_g of these polymers are listed in Table 8.1.

Table 8.1 Molecular characteristics of studied semi-crystalline polymers

Polymer	Mw (kg/mol)	M_e (kg/mol)	T_g (°C)	T_m (°C)	Source
PLLA	115	3.24	60	175	Nature Works (Ingeo 3100HP)
PET	-	1.45	80	250	Eastman (7352 PET)

8.2.2 Sample Preparation

In order to remove moisture from PLLA and PET, the resins were initially dried in temperature-controlled chamber (Thelco GCA Precision, model 18) for several hours. For the uniaxial tensile tests and melt-stretching, dog-bone samples were made from compression molding of the resins using a Carver Press. The applied load during molding was equal to 9000 kg. PLLA and PET resins were first heated above their respective melting points of 210 °C and 290 °C and then, after minutes, were quickly quenched into icy water to obtain amorphous PLLA and PET. In order to have the crystalline states, amorphous PLLA and PET samples were annealed in the temperature-controlled chamber respectively at 90-100 °C and 150-160 °C for 4 hours.

8.2.3 Experimental Procedures

8.2.3.1 Mechanical Tests

Uniaxial tensile tests of either dog-bone shaped or stripe like samples (cut from the middle part of melt-stretched samples), were carried out using Instron 5969, equipped with a temperature-controlled chamber. The temperature controller for Instron has an accuracy of ±1 °C. Uniaxial extensional tests were conducted with various constant cross-head speeds V, corresponding to an initial drawing rate V/L_0, where L_0 is the initial specimen length. Drawing rate V/L_0 for the mechanical measurements, presented in Figure 8.7 and Figure 8.10, was set equal to 0.5 min^{-1}.

8.2.3.2 Melt Stretching

The same Instron was used to perform melt stretching and step-strain tests. For these experiments, the Instron was programed using Bluehill software to apply a constant Hencky rate $\dot{\varepsilon}$, i.e. keeping constant V/L where the L is instantaneous length during stretching. Two types of dog-bone shape samples with the sizes of 10 × 1.5 × 3 mm^3 and 35 × 2 × 8 mm^3 (length × thickness × width) were used. Melt-stretching of amorphous PLLA and PET was carried out at Hencky rate $\dot{\varepsilon} = V/L = 0.028\ s^{-1}$ and T = 70 ˚C and 0.056 s^{-1} and 85 ˚C respectively. For PLLA, this corresponds to *Wi* = 118 s^{-1}, where the Weissenberg number *Wi* is a product of (V/L) and the terminal relaxation time τ = 4380 s [45]. Figures 8.2(a)-(c) indicate the melt stretching behavior of these samples. In the case of PLLA it was found that after physical aging the onset of upturn in the mechanical stress data, indicative of strain-induced crystallization takes place at a lower stretching ratio, as shown in Figure 8.2(b). Acceleration of cold crystallization after sufficient aging, has been

reported for other polymers such as isotactic polybutene-1. [240] The cold-crystallization from annealing of pre-melt-stretched PLLA, presented in Figure 8.3 and Figure 8.6, involved freshly prepared, non-aged PLLA. In contrast, the in situ WAXD measurements in Figure 8.5 was based on an aged PLLA. For PLLA, physical aging readily occurs during storage at room temperature for several hours. The effect of melt-stretching was preserved by immediate thermal quenching to room temperature by spraying icy water onto the specimen at the end of the melt-stretching.

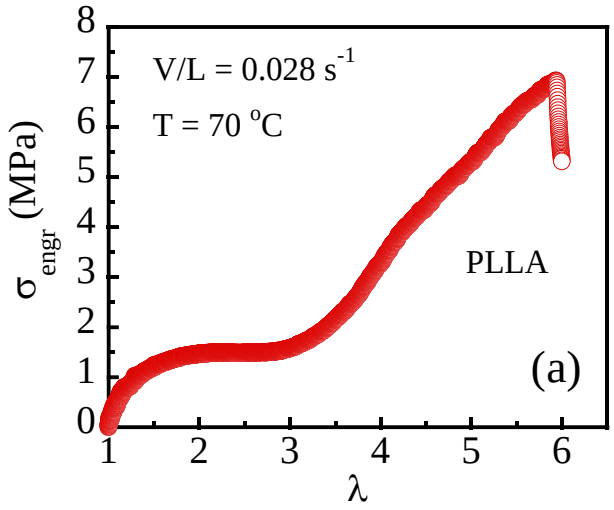
V/L = 0.028 s-1
T = 70 °C
PLLA
(a)
σ engr (MPa)
λ

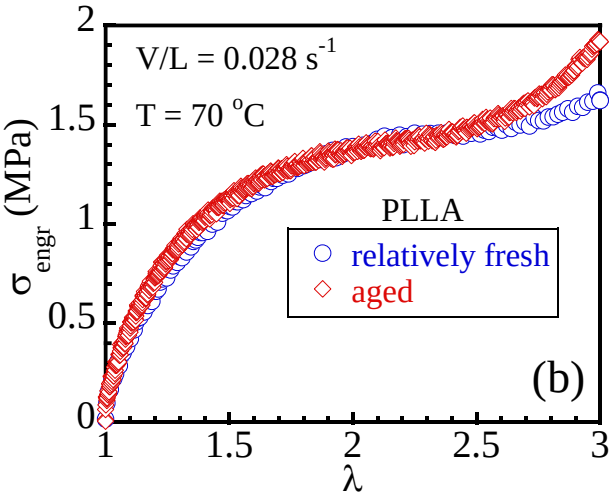
V/L = 0.028 s-1
T = 70 °C
PLLA
relatively fresh
aged
(b)
σ engr (MPa)
λ

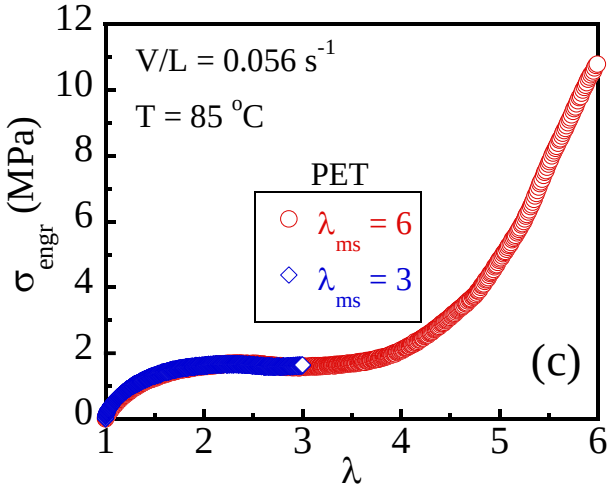
V/L = 0.056 s-1
T = 85 °C
PET
λ ms = 6
λ ms = 3
(c)
σ engr (MPa)
λ

Figure 8.2 Engineering stress σ_{engr} vs stretching ratio $\lambda = L/L_0$ during melt-stretching of (a) freshly-prepared amorphous PLLA until it fails at a high stretching ratio (b) freshly prepared and aged amorphous PLLA until $\lambda_{ms} = 3$ and (c) amorphous PET to λ_{ms} of 3 and 6.

8.2.3.3 Custom-Built Annealing Device (Heater)

A custom-built heater [48, 241] was employed to achieve quick annealing of pre-melt-stretched amorphous PLLA and PET. The procedure is as follows. First, a specimen is mounted onto the Instron at room temperature. Before annealing the Instron reads zero tensile stress. The heater is made of two hot metal plates with a narrow gap and is preset to a given temperature, e.g., 70 ˚C for PLLA and 100 ˚C for PET. To start the annealing test, we first began to record the stress using Instron which read zero. Then the specimen was brought into the hot narrow gap. Figure 8.3(b) represents the stress data during annealing of a pre-melt-stretched PLLA and shows that the heater was introduced to heat up the specimen at t = ca. 20 s.

8.2.3.4 Atomic Force Microscope Measurements

The samples were microtomed in the direction parallel to the stretching direction to generate a smooth surface. The measurements were done in a non-calibrated PF-QNM mode (peak force tapping - quantitative nanomechanical mapping) using a Dimesion Icon (Bruker-Nano, USA) equipped with a heating stage. ScanAsyst fluid + cantilever (Bruker-Nano) with a nominal spring constant of 0.7 N/m and a nominal tip radius of 2 nm were used. The image modification and analysis was done by NanoScope Analysis (Bruker-Nano).

8.2.3.5 Scattering Studies

Ex situ (after crystallization and stretching) x-ray scattering measurements were preformed using lab-scale wide-angle x-ray scattering (WAXD) apparatus or synchrotron radiation in both modes of WAXD and small-angle (SAXS). Real-time WAXD and SAXS measurements along with temperature and/or stress during annealing or stretching, were carried out using the in situ synchrotron radiation. The details of the x-ray sources are as follows:

Lab-scale WAXD apparatus: rotating anode X-ray generator (RU 300, 12 kW, Rigaku, Woodlands, TX), which produces a beam of monochromatic Cu Kα radiation (λ = 1.54 Å). For this device the X-ray generator operates at 40 kV 134 and 30 mA.

WAXD and SAXS synchrotron radiation were carried out in BL19U (λ = 1.03 Å) beamline in the Shanghai Synchrotron Radiation Facility (SSRF). Pilatus 200K and Pilatus 1M detector was used to collect 2D WAXD and SAXS patterns respectively with 0.1s and 5s exposure time. The corresponding sample-to detector distances calibrated for WAXD and SAXS were 74 and 2100 mm, respectively. A homemade apparatus was used in this work, which was equipped with a hot air blower to achieve a uniform heating environment of the sample with the accuracy of roughly ±0.5 ^{o}C. Two temperature probes were set in the heating/stretching chamber to realize the real-time detection of the temperature of the environment where the sample is located.

8.3 Results and discussion

In this chapter, based on PLLA and PET, we set out to present a successful demonstration of such nanocrystallization as foreseen from the preceding theoretical

considerations. Two protocols are available to achieve such scale-controlled, network-preserved cold crystallization. In both scenarios, a class B SCP in its amorphous state is brought above its T_g at T_{ann} and subjected to melt stretching. Beyond a threshold of stretching ratio λ^*, cold-crystallization appears to take place, judging from the stress vs. strain curve, as described in the experimental section. In the first protocol, the melt extension is terminated before reaching λ^* to commence the stress relaxation in anticipation that cold crystallization could be induced by the melt stretching. As shown in Figure 8.3(a), the tensile stress is found to decline until it turns negative as the crystallizing specimen increases its length because of the directional crystallization. Such a new PLLA is optically transparent, suggesting that the crystal sizes are well below the wavelength of visible light. To confirm crystallization, ex situ wide-angle-X-ray diffraction (WAXD) measurements are carried out to show as the inset in Figure 8.3(a) that there is indeed oriented crystallization. Hereafter we shall refer to this new crystalline state of PLLA as nc-PLLA.

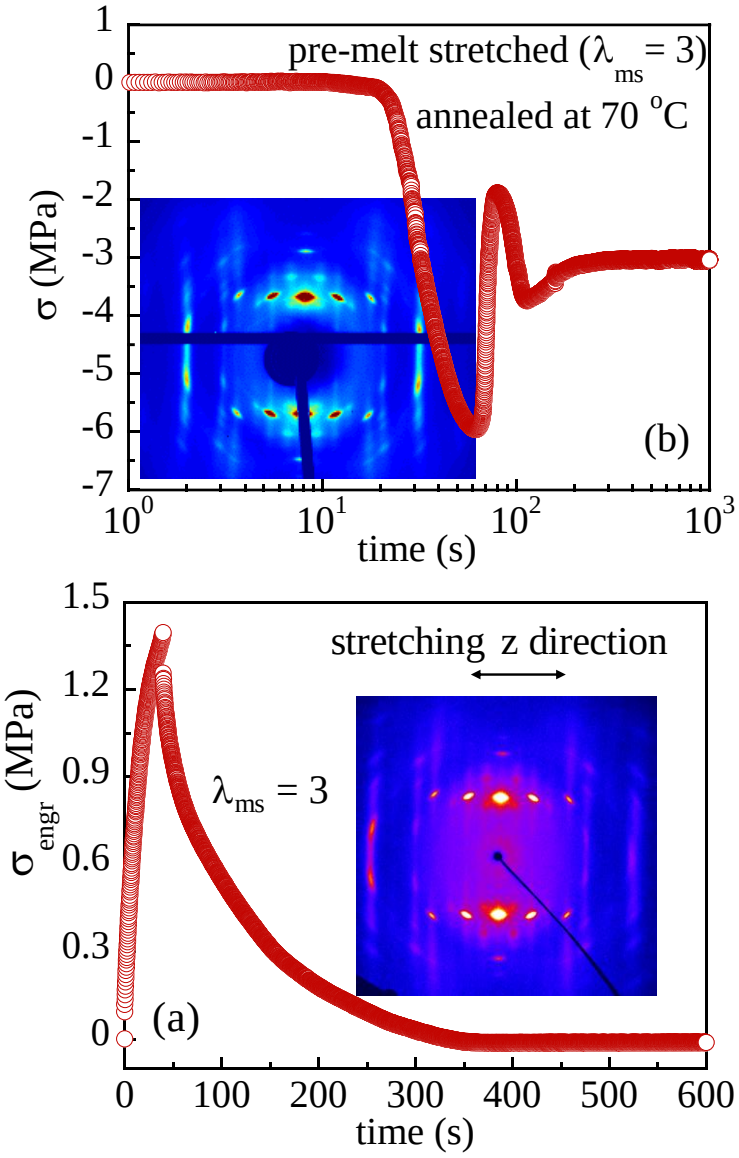

Figure 8.3 (a) Stress growth upon stepwise melt extension of PLLA at T = 70 °C, barely ten degrees above T_g at Hencky rate $\dot{\varepsilon} = 0.027\ s^{-1}$ and stress relaxation at $\lambda_{ms} = 3$. The inset photo is ex situ WAXD characterization of the sample at the end of the stress relaxation. (b) Stress reading upon annealing at 70 °C of a pre-melt-stretched PLLA, obtained according to the conditions described in (a). The inset photo is ex situ WAXD characterization of the sample at the end of the annealing.

Based on class B SCPs as PLLA and PET, it is straightforward to carry out melt-stretching at T_{ann} ($> T_g$) to a stretching ratio of λ_{ms} as described in the preceding paragraph and preserve the resulting chain orientation by rapid thermal quenching to room temperature. The pre-deformed polymer glasses remain amorphous in storage at room temperature. When it is heated to a temperature $T_2 > T_g$, cold crystallization may be induced by holding the pre-stretched specimen fixed between two clamps of an Instron tester. For the detailed description of this second protocol, see the experimental section. The protocol affords us the additional control over the condition for the induced nanocrystallization by choosing T_2 different from T_{ann}. Upon thermal equilibration at $T_2 > T_g$, the stretched chains become mobile so that the following two competing processes take place. Since T_2 is chosen to be well below the equilibrium crystallization temperature T_c, it is thermodynamically favorable for the system to cold-crystallize. At a given T_2, the crystallization kinetics depends on the degree of chain orientation and strand mobility. Independently, the intrachain retraction forces due to the pre-melt-stretching tend to make each chain retract toward its equilibrium coiled state. In absence of any crystallization, elastic breakup could occur due to localized chain disentanglement [239]. If this disentanglement would prevail, there may not be sufficient chain orientation to induce anisotropic crystallization. To avoid such elastic yielding, T_2 can be chosen just several degrees above T_g. Figure 8.3(b) shows the annealing process in terms of the measured stress: The pre-melt stretched PLLA starts to heat up at t = 20 s, and the thermal expansion causes the specimen to bend to generate negative stress. As the temperature rises above T_g at t = 60 s, the specimen begins to contract, correspondingly the stress starts to increase but

is still negative. The emergence of nanocrystallization prevents the elastic recoil so that the specimen remains bent. The explanation is confirmed by the ex situ WAXD pattern given in the inset of Figure 8.3(b). Since the new state of the PLLA is transparent before and after the annealing, we are able to confirm 30% increase in the birefringence in the nc-PLLA relative to the pre-melt-stretched amorphous PLLA.

To verify the molecular mechanism for the nanocrystallization, depicted in Figure 8.1(a)-(b), atomic force microscopic (AFM) measurements were carried out. The AFM image in Figure 8.4 of the nc-PLLA is obtained from the protocol described in Figure 8.3(b) and shows a spatial feature that could be identified with nano-sized lamellae depicted in Figure 8.1(b)-(c), with L_p = 15 nm and d varying from one to three in the unit of L_p.

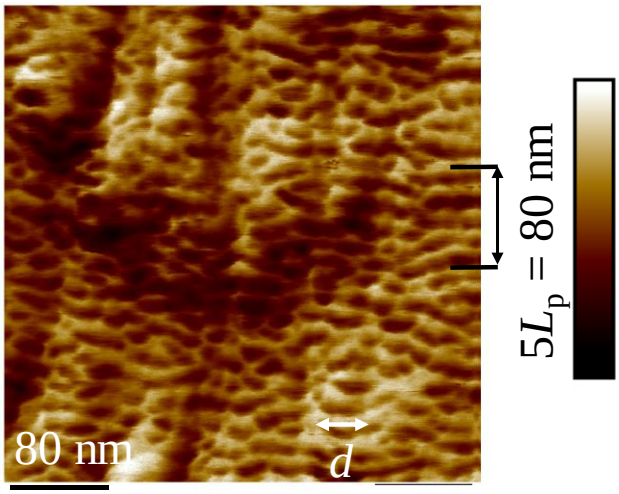

Figure 8.4 AFM image of the annealed pre-melt-stretched PLLA, revealing a unique morphology of the crystalline phase, consisting a family of "cylinders", separated by the lighter (softer) regions. The image was taken at 80 ^{o}C, showing the Derjaguin-Muller-Toporov modulus in an arbitrary unit (a.u.). The cylinders are vertically (along the direction

of stretching) separated by an average distance L_p = ca. 15 nm, with an average height shorter than 15 nm and diameter d varying from one to a few of L_p.

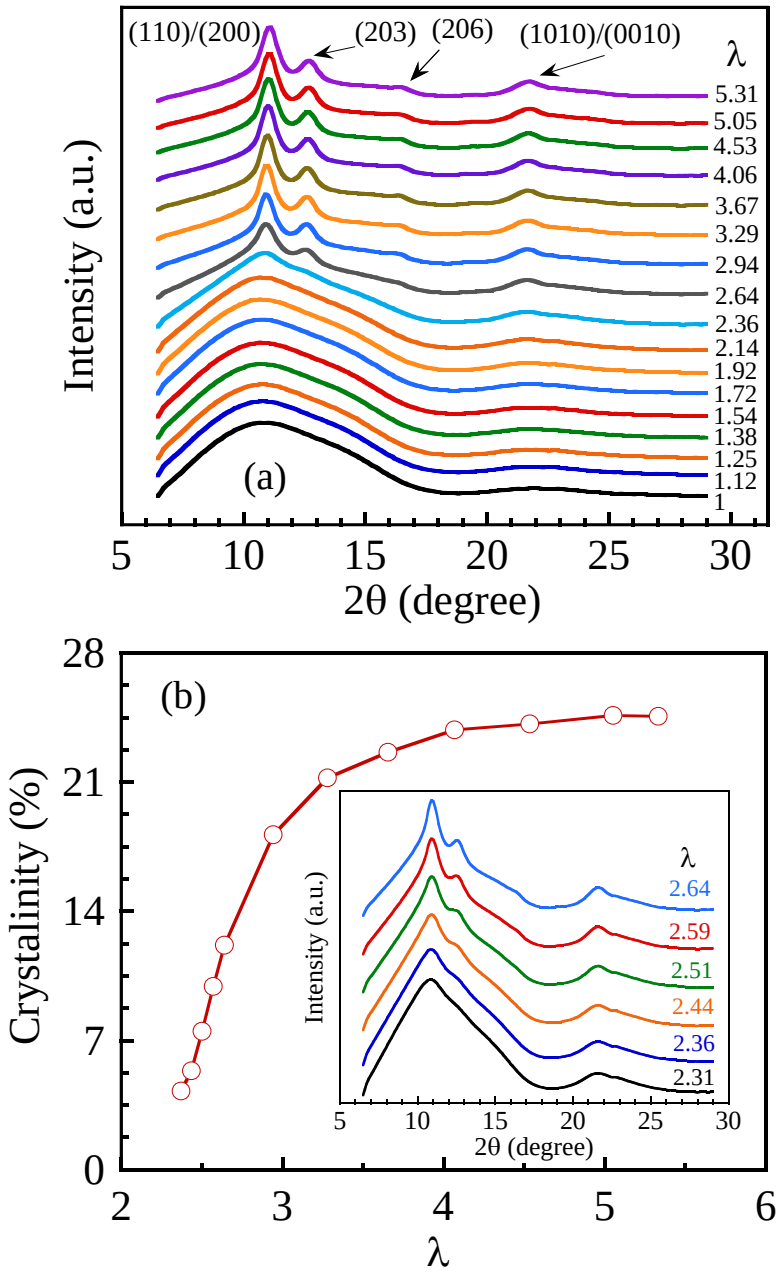

Figure 8.5 (a) Time-resolved WAXD measurements during uniaxial melt stretching of PLLA at 70 ^{o}C and Hencky rate $\dot{\varepsilon}$ = 0.027 s^{-1} up to λ = 5.5, revealing a series of characteristic structural information. (b) Degree of crystallinity as a function of the

stretching ratio λ. The inset shows the abrupt emergence of crystallization over a narrow range of λ.

To firmly establish such an approach to create a new state of crystallization in certain SCPs, we can perform in situ X-ray scattering in both wide-angle (WAXD) and small-angle (SAXS) modes. At 70 ^{o}C, according to the differential scanning calorimetry, the well-aged PLLA in its amorphous state would not undergo any discernible crystallization in half an hour. However, crystallization can be induced during melt stretching according to Figure 8.2. Time-resolved WAXD measurements are carried out to show in Figure 8.5 (a)-(b) that measurable crystallization indeed starts to emerge around $\lambda = 2.5$, which is also signified by the rise of the tensile stress in Figure 8.2 in the Experimental section. The degree of crystallinity grows sharply from $\lambda = 2.5$ to 3.5, reaching 25% during the melt stretching at Hencky rate = 0.027 s^{-1}, as indicated in Figure 8.5(b). At a rate ten times slower, the saturation crystallinity is over 30% according to our in situ measurements, which are omitted to save space.

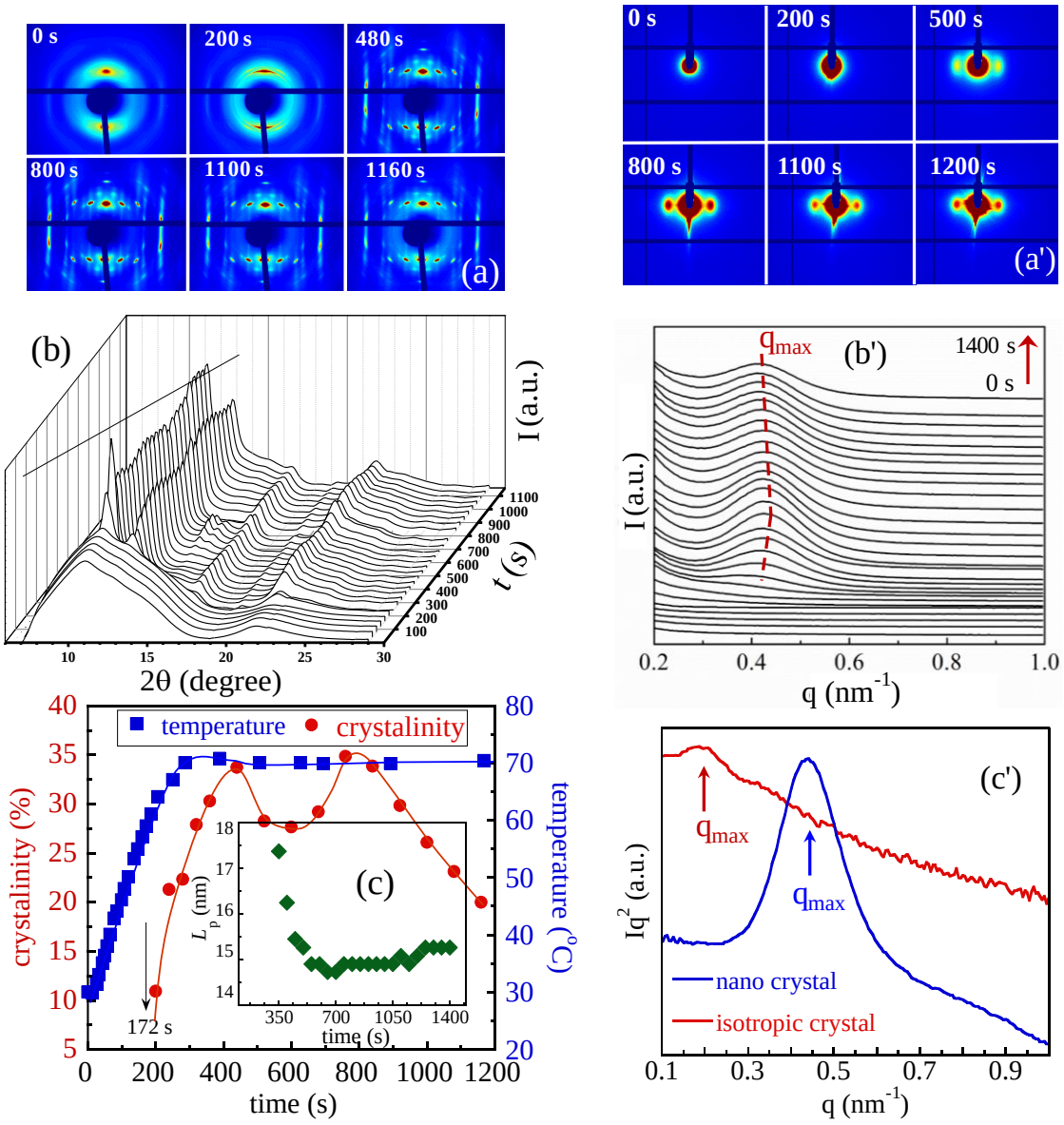

Figure 8.6 Time-resolved 2D patterns of (a) WAXD and (a') SAXS at different times during annealing at 70 °C of a pre-melt-stretched PLLA. Temporal evolutions of (b) WAXD intensity profiles along the equatorial direction and (b') SAXS intensity profiles along the meridional direction. (c) Emergent crystallinity (left Y axis) and temperature profile (right Y axis) as a function of time, with the inset showing the SAXS measurement of the long period L_p, obtained from (b'). (c') Calibrated SAXS intensities in terms of Iq^2 (Lorentz

correction) [242] to reveal a change in the long period L_p from the equilibrium value of 30 nm to 15 nm.

Time-resolved WAXD and SAXS capability also permits us to detect the formation of the cold crystallization during annealing of pre-melt-stretched SCPs. Specifically, during the annealing, which is described in Figure 8.3(b) for PLLA, both WAXD and SAXS measurements are carried out as a function of time. Figure 8.6(a) and (a') show the respective WAXD and SAXS patterns at the various times. Figure 8.6(b) and (b') present the characteristic q dependence of the scattering intensities at both wide and small angles as a function of time. As indicated in Figure 8.6(c), the chain-orientation-induced cold crystallization becomes discernible as the pre-melt-stretched PLLA heats up across T_g = 60 ^oC at 172 s. The crystallinity shoots up to ca. 35%, as shown by the circles in Figure 8.6(c), followed by a drop and rise before a further decrease of the crystallinity beyond t = 800 s. Clearly, the crystallization and melting have alternated, where the melting is plausibly driven by the persistent chain tension produced by the pre-melt-stretching. Tracing the peak positions of the SAXS intensity in Figure 8.6(b'), we can also determine the long period $L_p = 2\pi/q_{max}$ as a function of the annealing time and find in the inset of Figure 8.6(c) that L_p locks onto a value around 15 nm. It is important to note that this value agrees well with the average separation of the kebabs along the drawing direction, as shown in Figure 8.4.

It is interesting to discuss the meaning of L_p revealed by the SAXS measurements in the context of Figure 8.1(b) and Figure 8.4. According to our sketch, the crystalline structure should have a period about λ_{ms} times the mesh size of the entanglement network.

If the mesh size can be taken as the equilibrium entanglement spacing [45] l_{ent0} = ca. 4.4 nm, L_p should be at least 13.2 nm. According to the AFM and SAXS measurements, L_p = 15 nm in support of the basic idea (cf. Figure 1) that has guided us to create the new crystalline state. The AFM image also shows $d > L_p$, implying that the lamellae are not restricted by the lateral mesh size. If it is restricted to the mesh width of $l_{ent0}/(\lambda_{ms})^{1/2} \sim 2.5$ nm, we would have observed $d \sim 2.5$ nm, instead of > 15 nm. The lateral lamellar growth is determined by the irregularities of the chain network. Therefore, the lateral dimensions are also bounded. According to Figure 8.4, the lamellae could be cylindrical with the diameter, typically no greater than three times L_p, i.e., d varying from L_p to $3L_p$.

For SCPs that have higher T_g than room temperature and slow crystallization kinetics, we can bypass crystallization and prepare them in their amorphous form in order to achieve nanocrystallization. Such crystallization preserves the structural integrity of the chain network and therefore could make these SCPs super tough and strong. We have verified that the same protocols that permit the creation of nc-PLLA described in Figure 8.3 through Figure 8.6 apply to PET. See section 8.3.1, for similar phenomenology involving PET. Specifically, Figure 8.7 compares the stress vs. strain curves of two crystalline PLLA, one cold crystallized PLLA in absence of any pre-deformation and the nc-PLLA. The contrast is sharp: PLLA is brittle at room temperature (RT) and hardly drawable above T_g, and the nc-PLLA is superbly tough at room temperature and remarkably strong even above T_g. Finally, it is worth mentioning that the transparent nc-PLLA shows outstanding thermal stability, e.g., able to retain its dimension at 120 ^oC (well above T_g) for over 30 min,

suggesting that the nano-sized crystals are space filling and jammed up, as shown in Figure 8.1(b).

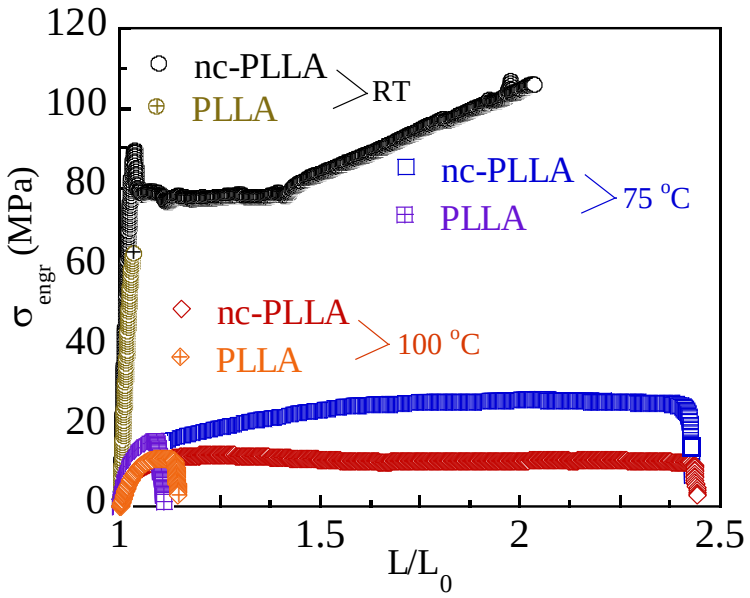

Figure 8.7 Engineering stress vs. draw ratio during uniaxial extension along the same direction as melt stretching with $V/L_0 = 0.5\ min^{-1}$, at room temperature as well as 75 and 100 °C, for the nc-PLLA produced using the method described in Figure 8.3(a) as well as the untreated PLLA (symbols containing plus sign). L_0 = 30 and 35 mm respectively for PLLA and nc-PLLA specimens.

8.3.1 Universality of Our Method (case of PET)

Figure 8.8 represents the ex situ WAXD and SAXS data of nano-crystalline PET (nc-PET), resulting from annealing of the pre-melt-stretched PET Similar to the case of nc-PLLA, the directional crystallinity can be inferenced from the 2D WAXD pattern. From the SAXS intensity profile along the stretching direction, the long period L_p of nc-PET can be estimated equal to $2\pi/q_{max}$ = 7.5 nm. This value is lower than the reported value of 8 to 14 nm for the isotopic semi-crystalline PET in the literature [243]. The large difference in L_p

of nc-PLLA (15 nm) and nc-PET (7.5 nm) reflects a difference in the mesh size of the chain network.

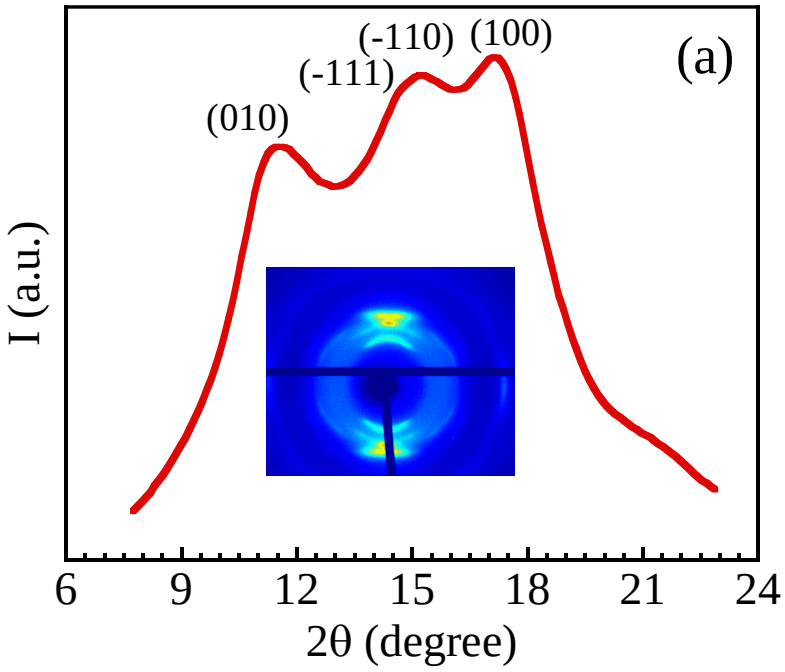

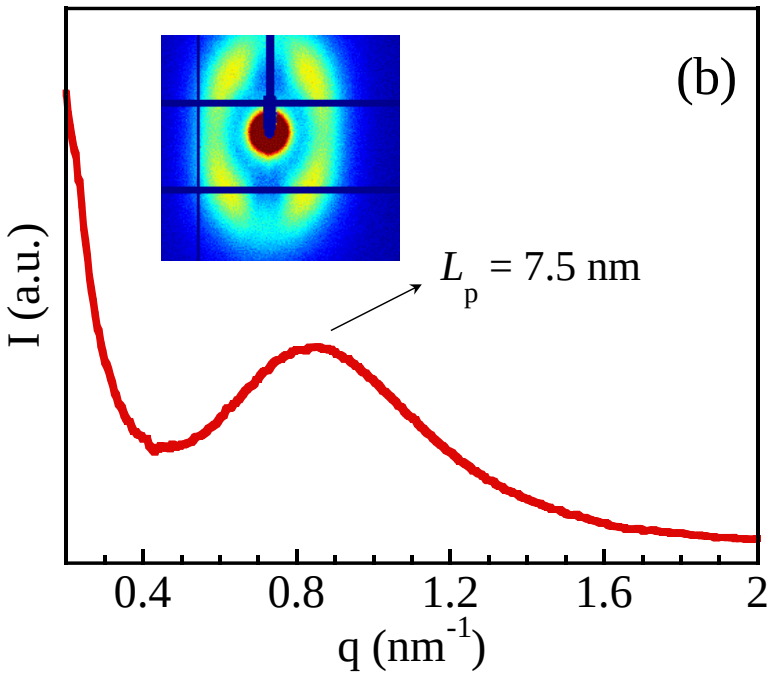

Figure 8.8 X-ray scattering intensity profiles along with corresponding 2D patterns as inset images of nano-crystalline PET: (a) WAXD data and (b) SAXS data. Stretching direction is horizontal.

To acquire more detailed information regarding the cold crystallization of pre-melt-stretched PET, in situ WAXD and SAXS measurements were also carried out during annealing of the sample at 100 ˚C. Figures 8.9(a)-(b) present the 2D WAXD and SAXS patterns along with crystallinity development and long-period evolution over the time span of 1400 s.

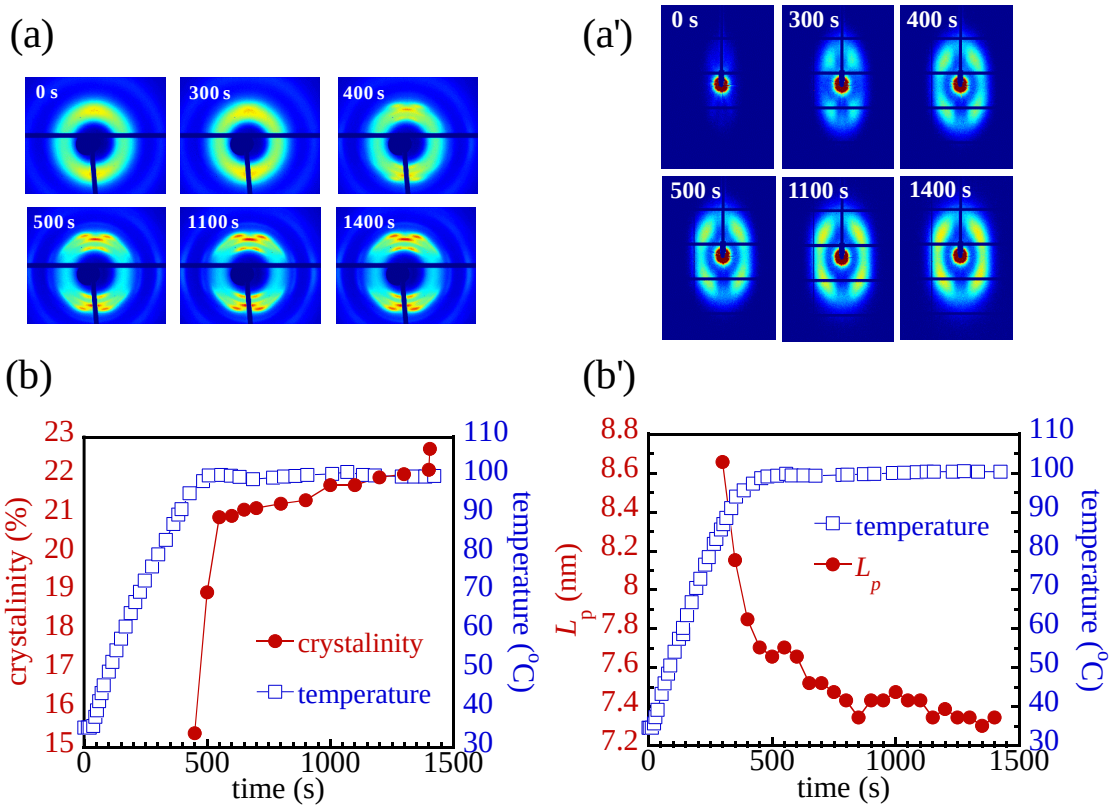

Figure 8.9 In situ x-ray scattering measurements during annealing of pre-melt-stretched PET in terms of (a) 2D WAXD pattern, (a') 2D SAXS pattern, (b) crystallinity increase,

(b') evolution of the long period L_p, where the temperature rise as a function of time is given in terms of the squares.

Mechanical properties in terms of uniaxial tensile deformation of nc-PET at room temperature is shown in Figure 8.10 in comparison to the isotropic semi-crystalline PET. The characteristic is similar to that presented in Figure 8.7 for nc-PLLA.

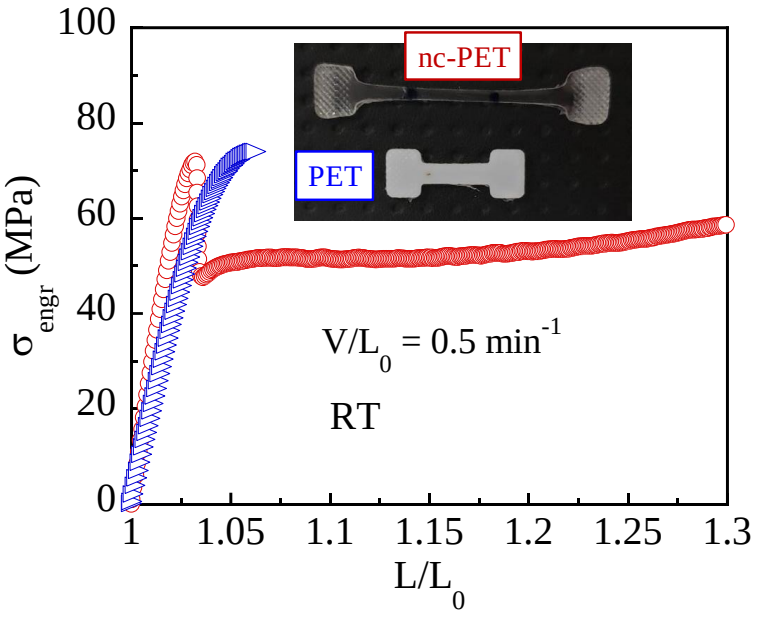

Figure 8.10 Engineering stress σ_{engr} vs draw ratio L/L_0 from uniaxial tensile test of crystalline PET and nc-PET at room temperature (RT). The inset image contrasts the appearance of two types of semi-crystalline PET; opaque semi-crystalline PET vs. transparent nano-crystalline PET.

8.4 Summary

In summary, we have identified effective ways to produce a new nano-crystalline state through cold crystallization of melt-stretched PLLA and PET while preserving the chain network arising from the interchain uncrossability. Specifically, the new morphology is a

connected web of kebabs (lamellae), grouped into clusters of cylindrical shape with various diameters. The new crystalline phase, made of these clusters, is space filling, providing desirable heat resistance and is superbly ductile and optically transparent, presenting itself as a promising next-generation polymeric materials.

CHAPTER IX

SUMMARY

Chain entanglement is the most important physical concept that governs the mechanical properties of polymers at the disordered melt state (polymer rheology). In the melt state, the non-bonded interactions, e.g. Van der Waals forces, do not have significant impact on the mechanical, i.e. rheological, properties. However, molecular interactions play an important role in determining mechanical properties in the solid state which is achieved through vitrification for an amorphous polymer, and crystallization/vitrification for a semicrystalline polymer. Unlike amorphous glassy polymers that the entanglement network is frozen by lowering the temperature below T_g, for a semicrystalline polymer, in addition to emergence of the molecular interactions, the structure of chain network is evidently altered through re-organization of the polymer chains into the crystalline regions. Therefore, understanding the mechanics of semicrystalline polymers is more challenging task than study of the mechanics of polymer glasses which itself is more arduous subject compared to polymer rheology.

This dissertation, through a hierarchical approach, offers a chain-level understanding of the mechanics of these two class of polymeric materials; glassy and semicrystalline polymers. We firstly study the molecular mechanics of glassy polymers in Part A, and then

in Part B, we focus on the more challenging problem of the molecular mechanics of semicrystalline polymers. In both parts several different polymers are studied in order to show the universality of the discussions. Specifically, in Part B we picked semicrystalline polymers that they are available in both semicrystalline and glassy amorphous states. This provides us the ability to study the mechanics of a semicrystalline polymer by refence to its mechanics in the glassy amorphous state. Accordingly, we can set apart the additional effects from the change in the structure of the chain network, on the mechanical properties of polymers. Chapter I and Chapter V are general introductions to respectively, Part A and Part B, where in each part three independent but comprehensive projects have been carried out. Following paragraphs recapitulate those projects.

Chapter II: this chapter presents many experimental results in order to motivate and advance our understanding on crazing during tensile deformation of glassy polymers. Ample data are presented to show that crazing is an activated process and therefore takes time to emerge. For example, ductile polymers can also show crazing prior to yielding as demonstrated with bisphenol A polycarbonate and PMMA at elevated temperatures. As an integral part of the investigation, we show that crazing can emerge in absence of any ongoing deformation, i.e., taking place not during extension but after termination of the extension. More remarkably, glassy polymers such as polystyrene and amorphous PLA can undergo macroscopic fracture without any ongoing extension after a rapid step extension that first results in massive crazing. Moreover, we investigate several ways to either suppress or promote craze formation. Specifically, it is shown that a craze-free ductile PLA turns brittle and develops crazing upon physical aging or the incorporation of "solvent".

Conversely, adequate pre-melt-stretching is found to prevent physical aging from causing crazing and brittle fracture. Crazing perhaps reveals the existence of structural and dynamic heterogeneity that can be more severe in one glassy polymer than another. For example, PMMA hardly shows crazing before brittle fracture at room temperature in contrast to PS. Through a theoretical refrainment to our previous Hybrid Molecular Model we indicated that all the glassy polymers of linear flexible chains show comparable characteristics in terms of the underlying chain network and accordingly at the present, no theoretical description is available to predict which polymer is more prone to crazing.

Chapter III: contrasting the conventional rubber-toughening mechanism, we show that the new PMMA based rubber-toughened nanocomposite (PMMA-rt/nc) achieves the desired rubber-toughening through molecular level interactions between the glassy PMMA chains and the nano-sized rubbery domains. PMMA-rt/nc, as an inverted polymer nanocomposite, is found to be sufficiently rigid to be treated as a polymer glass, yet ready to undergo plastic deformation like a ductile polymer glass. In parallel, we study high-impact polystyrene (HIPS) and acrylonitrile-butadiene-styrene (ABS) to elucidate the conventional rubber-toughening mechanism. Unlike PMMA-rt/nc, HIPS and ABS cannot undergo yielding and plastic deformation at room temperature. The delayed brittle fracture in HIPS and ABS is accomplished through crazing-initiated rubbery cavitation, manifested in the form of whitening of the specimen at the point of apparent yielding. Further experiments show that HIPS and ABS can be made to avoid crazing and consequently whitening as well as the brittle fracture when they have undergone adequate pre-melt stretching that can enhance the chain networks in the glassy polymer matrix. The evidence

of plastic deformation in the pre-melt-stretched HIPS and ABS comes from the fact that such specimens, unlike to the untreated counterparts, undergo contraction of their transverse dimensions during the extension. In contrast, the untreated HIPS and ABS keep their transverse dimensions fixed during room-temperature uniaxial drawing until the point of fracture.

Chapter IV: is an experimental attempt to get molecular level insights about the deformation of polymer glasses using in situ birefringence measurements. For the first time birefringence values of PS and PMMA during post-yield deformation at room temperature are measured. It is found that post-yield deformation of PS and PMMA include conformational changes at the chain level and therefore birefringence values of these polymers in the glassy state at the post-yield, have similar sign to their values in the melt state. Stress relaxation experiments indicate that there is no direct correlation between stress relaxation and birefringence relaxation. In the case of PS which the dynamic of side group is highly coupled with that of backbone the rate of birefringence relaxation is faster than that of stress relaxation, while PMMA because of having an additional rotational freedom in the side group has faster stress relaxation than birefringence relaxation. It is suggested that in presence of higher contribution from intra-segmental component into the stress, the birefringence relaxation takes place slowly. The results also suggest that the segmental mobility at the strain hardening region increases.

Chapter VI: we initially rationalize our molecular picture of the semicrystalline state using three mechanical experiments performed on poly(l-lactic acid). In the next stage, different semicrystalline polymers including poly(l-lactic acid), poly(ethylene

terephthalate), syndiotactic polystyrene and polyamide 12 are studied in terms of their mechanical responses to the uniaxial compression deformation. Apparent decoupling of yielding of amorphous and crystalline phases are identified as separate peaks in the stress strain curve in the vicinity of the glass transition temperature. The same feature is also observed for the uniaxial extension of pre-drawn semicrystalline poly(ethylene terephthalate). It is indicated that in absence of a strong amorphous phase the semicrystalline polymer is unable to yield and undergo plastic deformation and it fails in a brittle manner in the uniaxial compression. Treating a semicrystalline polymer as a composite of amorphous and crystalline phases, putting emphasis on the crucial role of the amorphous phase in acting as the connectors between crystalline domains and indicating that the yielding of amorphous phase is a prerequisite for yielding of the crystalline phase, we offer a new framework toward better understanding of the mechanical properties of semicrystalline polymers at the molecular level.

Chapter VII: using time-resolved polarized-optical-microscopy (POM) we have investigated how and why crystallization tends to cause deterioration of ductility in semicrystalline PLLA. Specifically, the POM study supports the idea that polymer crystals (spherulitic in form in the case of PLLA) are mechanically weaker than glassy non-crystalline domains whose cohesive strength stems from the chain networking due to intermolecular uncrossability.

Chapter VIII: based on two widely studied semicrystalline polymers, poly (L-lactic acid) (PLLA) and polyethylene terephthalate (PET) of high glass transition temperature T_g, this chapter shows that these brittle materials can be made to be super tough, heat

resistant and optically clear by creating nano kebab (lamellar) crystals while preserving the entanglement network. Atomic force microscopic images confirm the perceived nano-crystallization. Time-resolved X-ray scattering/diffraction measurements reveal the emergence of cold crystallization during either stress relaxation from large stepwise melt-stretching of PLLA and PET or annealing of pre-melt-stretched PLLA and PET above T_g. Mechanical tests show that the polymers in this new state are superbly tough and strong even well above T_g, e.g., above 100 ^oC.

COPYRIGHT NOTICES

BIBLOGRAPHY

1. Brown, H.; Argon, A.; Cohen, R.; Gebizlioglu, O.; Kramer, E., New mechanism for craze toughening of glassy polymers. *Macromolecules* 1989, 22 (2), 1002-1004.
2. Bucknall, C., Role of surface chain mobility in crazing. *Polymer* 2012, 53 (21), 4778-4786.
3. Kramer, E. J.; Berger, L. L., Fundamental processes of craze growth and fracture. In *Crazing in Polymers Vol. 2*, Springer: 1990; pp 1-68.
4. Argon, A. S.; Hannoosh, J. G., Initiation of crazes in polystyrene. *Philosophical Magazine* 1977, 36 (5), 1195-1216.
5. Kausch-Blecken von Schmeling, H.; Williams, J., Polymer fracture. *Encyclopedia of Polymer Science and Technology* 2002, 1-65.
6. Gent, A., Hypothetical mechanism of crazing in glassy plastics. *Journal of Materials Science* 1970, 5 (11), 925-932.
7. Vincent, P., The tough-brittle transition in thermoplastics. *Polymer* 1960, 1, 425-444.
8. Bowden, P., The yield behaviour of glassy polymers. In *The physics of glassy polymers*, Springer: 1973; pp 279-339.
9. Van Melick, H.; Govaert, L.; Meijer, H., Prediction of brittle-to-ductile transitions in polystyrene. *Polymer* 2003, 44 (2), 457-465.
10. Wang, S.-Q.; Cheng, S.; Lin, P.; Li, X., A phenomenological molecular model for yielding and brittle-ductile transition of polymer glasses. *The Journal of chemical physics* 2014, 141 (9), 094905.
11. Wang, S.-Q.; Cheng, S., Experiments-inspired molecular modeling of yielding and failure of polymer glasses under large deformation. *Taylor & Francis*: 2016.

12. Wang, S.-Q., On chain statistics and entanglement of flexible linear polymer melts. *Macromolecules* 2007, 40 (24), 8684-8694.

13. Ludwik, P., Die Bedeutung des Gleit-und Reißwiderstandes für die Werkstoffprüfung. *Z. des Verein. deutscher Ingenieure* 1927, 71, 1532-1538.

14. Davidenkov, N. N.; Wittman, F., *Phys. Tech. Znst. (USSR)* 1937, 4, 300.

15. Orowan, E., Fracture and strength of solids. *Rep. Prog. Phys.* 1949, 12 (1), 185.

16. Ward, I. M.; Sweeney, J., *Mechanical properties of solid polymers*, 3rd. *John Wiley & Sons, Ltd.:* Chichester, UK, 2012.

17. van Melick, H. G. H.; Govaert, L. E.; Meijer, H. E. H., Localisation phenomena in glassy polymers: influence of thermal and mechanical history. *Polymer* 2003, 44 (12), 3579-3591.

18. Haward, R. N., *The physics of glassy polymers*. Springer Science & Business Media: 2012.

19. Roth, C. B., *Polymer Glasses*. CRC Press: 2016.

20. Argon, A. S., *The physics of deformation and fracture of polymers*. 2013.

21. Eyring, H., Viscosity, Plasticity, and Diffusion as Examples of Absolute Reaction Rates. *J. Chem. Phys.* 1936, 4 (4), 283-291.

22. Chen, K.; Schweizer, K. S., Stress-enhanced mobility and dynamic yielding in polymer glasses. *Europhys. Lett.* 2007, 79 (2), 26006.

23. Chen, K.; Schweizer, K. S., Theory of Yielding, Strain Softening, and Steady Plastic Flow in Polymer Glasses under Constant Strain Rate Deformation. *Macromolecules* 2011, 44 (10), 3988-4000.

24. Liu, J.; Lin, P.; Cheng, S.; Wang, W.; Mays, J. W.; Wang, S.-Q., Polystyrene Glasses under Compression: Ductile and Brittle Responses. *ACS Macro Lett.* 2015, 4 (10), 1072-1076.

25. Liu, J.; Zhao, Z.; Wang, W.; Mays, J. W.; Wang, S. Q., Brittle-ductile transition in uniaxial compression of polymer glasses. *Journal of Polymer Science Part B: Polymer Physics* 2019.

26. Goldstein, M., Viscous Liquids and the Glass Transition: A Potential Energy Barrier Picture. *The Journal of Chemical Physics* 1969, 51 (9), 3728-3739.

27. Stillinger, F. H., A Topographic View of Supercooled Liquids and Glass Formation. *Science* 1995, 267 (5206), 1935-1939.

28. Debenedetti, P. G.; Stillinger, F. H., Supercooled liquids and the glass transition. *Nature* 2001, 410 (6825), 259-267.

29. Andreas, H., Exploring the potential energy landscape of glass-forming systems: from inherent structures via metabasins to macroscopic transport. *J. Phys.: Condens. Matter* 2008, 20 (37), 373101.

30. Donald, A. M., Crazing. In *The Physics of Glassy Polymers*, Haward, R. N.; Young, R. J., Eds. Springer Netherlands: Dordrecht, 1997; pp 295-341.

31. Deblieck, R. A. C.; van Beek, D. J. M.; Remerie, K.; Ward, I. M., Failure mechanisms in polyolefines: The role of crazing, shear yielding and the entanglement network. *Polymer* 2011, 52 (14), 2979-2990.

32. Bartczak, Z., Effect of chain entanglements on plastic deformation behavior of linear polyethylene. *Macromolecules* 2005, 38 (18), 7702-7713.

33. Pawlak, A.; Galeski, A., Plastic deformation of crystalline polymers: the role of cavitation and crystal plasticity. *Macromolecules* 2005, 38 (23), 9688-9697.

34. Ranganathan, R.; Kumar, V.; Brayton, A. L.; Kröger, M.; Rutledge, G. C., Atomistic Modeling of Plastic Deformation in Semicrystalline Polyethylene: Role of Interphase Topology, Entanglements, and Chain Dynamics. *Macromolecules* 2020.

35. Bucknall, C. B., New criterion for craze initiation. *Polymer* 2007, 48 (4), 1030-1041.

36. Argon, A. S., Craze initiation in glassy polymers - Revisited. *Polymer* 2011, *52* (10), 2319-2327.

37. Wang, S. Q.; Cheng, S. W., Experiments-inspired molecular modeling of yielding and failure of polymer glasses under large deformation, Chapter 12. Polymer Glasses, Roth, C., Ed. *CRC Press:* 2016; pp 395-423.

38. Matsushige, K.; Radcliffe, S. V.; Baer, E., The pressure and temperature effects on brittle-to-ductile transition in PS and PMMA. *J. Appl. Polym. Sci.* 1976, 20 (7), 1853-1866.

39. Fetters, L.; Lohse, D.; Richter, D.; Witten, T.; Zirkel, A., Connection between polymer molecular weight, density, chain dimensions, and melt viscoelastic properties. *Macromolecules* 1994, 27 (17), 4639-4647.

40. Zartman, G. D.; Cheng, S.; Li, X.; Lin, F.; Becker, M. L.; Wang, S.-Q., How melt-stretching affects mechanical behavior of polymer glasses. *Macromolecules* 2012, 45 (16), 6719-6732.

41. Zhao, Y.; Liu, J.; Li, X.; Lu, Y.; Wang, S.-Q., How and Why Polymer Glasses Lose Their Ductility Due to Plasticizers. *Macromolecules* 2017, 50 (5), 2024-2032.

42. Chung, Y. G.; Lacks, D. J., Sheared polymer glass and the question of mechanical rejuvenation. *The Journal of chemical physics* 2012, 136 (12), 124907.

43. Argon, A., Craze initiation in glassy polymers–Revisited. *Polymer* 2011, 52 (10), 2319-2327.

44. Li, X.; Wang, S.-Q., Mapping Brittle and Ductile Behaviors of Polymeric Glasses under Large Extension. *ACS Macro Lett.* 2015, 4 (10), 1110-1113.

45. Razavi, M.; Wang, S.-Q., Why Is Crystalline Poly (lactic acid) Brittle at Room Temperature? *Macromolecules* 2019, 52 (14), 5429-5441.

46. Donald, A. M.; Kramer, E. J., Effect of strain history on craze microstructure. *Polymer* 1982, 23 (3), 457-460.

47. Legrand, D. G., Yielding, crazing, and fracture of polymers. II. Studies of the retraction of crazed and drawn films. *J. Appl. Polym. Sci.* 1972, 16 (6), 1367-1376.

48. Cheng, S.; Wang, S.-Q., Elastic yielding after cold drawing of ductile polymer glasses. *Macromolecules* 2014, 47 (11), 3661-3671.

49. Cheng, S.; Wang, S.-Q., Elastic yielding in cold drawn polymer glasses well below the glass transition temperature. *Physical review letters* 2013, 110 (6), 065506.

50. Ender, D.; Andrews, R., Cold drawing of glassy polystyrene under dead load. *Journal of Applied Physics* 1965, 36 (10), 3057-3062.

51. Tanabe, Y.; Kanetsuna, H., Structure of oriented polystyrene monofilaments and its relationship to brittle-to-ductile transition. *J. Appl. Polym. Sci.* 1978, 22 (6), 1619-1630.

52. Beardmore, P.; Rabinowitz, S. d., Craze formation and growth in anisotropic polymers. *Journal of Materials Science* 1975, 10 (10), 1763-1770.

53. Harris, J.; Ward, I., Crazing behaviour in oriented poly (ethylene terephthalate). *Journal of Materials Science* 1970, 5 (7), 573-579.

54. Bernier, G.; Kambour, R., The Role of Organic Agents in the Stress Crazing and Cracking of Poly (2, 6-dimethyl-1, 4-phenylene oixde). *Macromolecules* 1968, 1 (5), 393-400.

55. Kambour, R.; Romagosa, E.; Gruner, C., Swelling, crazing, and cracking of an aromatic copolyether-sulfone in organic media. *Macromolecules* 1972, 5 (4), 335-340.

56. Kambour, R. P.; Gruner, C.; Romagosa, E. d., Solvent crazing of "dry" polystyrene and "dry" crazing of plasticized polystyrene. *Journal of Polymer Science: Polymer Physics Edition* 1973, 11 (10), 1879-1890.

57. Cheng, S.; Johnson, L.; Wang, S.-Q., Crazing and strain localization of polycarbonate glass in creep. *Polymer* 2013, 54 (13), 3363-3369.

58. Razavi, M.; Huang, D.; Liu, S.; Guo, H.; Wang, S.-Q., Examining an Alternative Molecular Mechanism To Toughen Glassy Polymers. *Macromolecules* 2020, 53, 323-333.

59. Bucknall, C.; Smith, R., Stress-whitening in high-impact polystyrenes. *Polymer* 1965, 6 (8), 437-446.

60. Haward, R. N., The physics of glassy polymers. *Springer Science & Business Media*: 2012, Page 315.

61. Argon, A. S., Role of heterogeneities in crazing of glassy polymers. *Pure Appl. Chem.* 1975, 43 (1-2), 247-272.

62. Starr, F. W.; Douglas, J. F.; Sastry, S., The relationship of dynamical heterogeneity to the Adam-Gibbs and random first-order transition theories of glass formation. *Journal of Chemical Physics* 2013, 138 (12), 12A541.

63. Bucknall, C. B., Toughened plastics. *Springer:* 1977.

64. Merz, E.; Claver, G.; Baer, M., Studies on heterogeneous polymeric systems. *Journal of Polymer Science* 1956, 22 (101), 325-341.

65. Bucknall, C., Rubber toughening. The Physics of Glassy Polymers, *Springer:* 1997; pp 363-412.

66. Pearson, R. A.; Yee, A. F., Influence of particle size and particle size distribution on toughening mechanisms in rubber-modified epoxies. *Journal of materials science* 1991, 26 (14), 3828-3844.

67. Smit, R.; Brekelmans, W.; Meijer, H., Predictive modelling of the properties and toughness of polymeric materials Part II Effect of microstructural properties on the macroscopic response of rubber-modified polymers. *Journal of materials science* 2000, 35 (11), 2869-2879.

68. Bubeck, R.; Buckley, D.; Kramer, E.; Brown, H., Modes of deformation in rubber-modified thermoplastics during tensile impact. *Journal of materials science* 1991, 26 (23), 6249-6259.

69. Guo, H.; Sonnati, M. O.; Post, R. L.; Vietti, D. E., Acrylic film and acrylic backsheet prepared therefrom. *United States Patent Application*: 2012.

70. Guo, H. Multi-stage polymer composition and films made therefrom. *United States Patent Application* 2019.

71. Frank, B.; Gast, A. P.; Russell, T. P.; Brown, H. R.; Hawker, C., Polymer mobility in thin films. *Macromolecules* 1996, 29 (20), 6531-6534.

72. Roth, C. B.; Dutcher, J. R., Glass transition and chain mobility in thin polymer films. *Journal of Electroanalytical Chemistry* 2005, 584 (1), 13-22.

73. Jones, R., The dynamics of thin polymer films. *Current opinion in colloid & interface science* 1999, 4 (2), 153-158.

74. Inoue, R.; Kanaya, T.; Nishida, K.; Tsukushi, I.; Telling, M.; Gabrys, B.; Tyagi, M.; Soles, C.; Wu, W.-l., Glass transition and molecular mobility in polymer thin films. *Physical Review E* 2009, 80 (3), 031802.

75. Forrest, J.; Dalnoki-Veress, K., Sub-glass-transition temperature interface formation between an immiscible glass rubber pair. *Journal of Polymer Science Part B: Polymer Physics* 2001, 39 (21), 2664-2670.

76. Baglay, R. R.; Roth, C. B., Local glass transition temperature $T_g(z)$ of polystyrene next to different polymers: Hard vs. soft confinement. *The Journal of chemical physics* 2017, 146 (20), 203307.

77. Tito, N. B.; Lipson, J. E.; Milner, S. T., Lattice model of mobility at interfaces: free surfaces, substrates, and bilayers. *Soft Matter* 2013, 9 (39), 9403-9413.

78. Rauscher, P. M.; Pye, J. E.; Baglay, R. R.; Roth, C. B., Effect of adjacent rubbery layers on the physical aging of glassy polymers. *Macromolecules* 2013, 46 (24), 9806-9817.

79. Siqueira, D. F.; Schubert, D.; Erb, V.; Stamm, M.; Amato, J., Interface thickness of the incompatible polymer system PS/PnBMA as measured by neutron reflectometry and ellipsometry. *Colloid and Polymer Science* 1995, 273 (11), 1041-1048.

80. Hailan Guo, S. Z., Robert Martin, Flexible acrylic resin. *The Dow Chemical Company* 2016.

81. Sperling, L. H., Polymeric multicomponent materials: an introduction. *Wiley-Interscience:* 1997.

82. Aranguren, M. I.; Mora, E.; DeGroot Jr, J. V.; Macosko, C. W., Effect of reinforcing fillers on the rheology of polymer melts. *Journal of Rheology* 1992, 36 (6), 1165-1182.

83. Jouault, N.; Vallat, P.; Dalmas, F.; Said, S.; Jestin, J.; Boué, F., Well-dispersed fractal aggregates as filler in polymer− silica nanocomposites: long-range effects in rheology. *Macromolecules* 2009, 42 (6), 2031-2040.

84. Shim, S. E.; Isayev, A. I., Rheology and structure of precipitated silica and poly (dimethyl siloxane) system. *Rheologica acta* 2004, 43 (2), 127-136.

85. Adams, J. L.; Graessley, W. W.; Register, R. A., Rheology and the microphase separation transition in styrene-isoprene block copolymers. *Macromolecules* 1994, 27 (21), 6026-6032.

86. Bates, F. S., Block copolymers near the microphase separation transition. 2. Linear dynamic mechanical properties. *Macromolecules* 1984, 17 (12), 2607-2613.

87. Rosedale, J.; Bates, F. S., Rheology of ordered and disordered symmetric poly (ethylenepropylene)-poly (ethylethylene) diblock copolymers. *Macromolecules* 1990, 23 (8), 2329-2338.

88. Colby, R. H., Block copolymer dynamics. *Current Opinion in Colloid & Interface Science* 1996, 1 (4), 454-465.

89. Veenstra, H.; Hoogvliet, R. M.; Norder, B.; De Boer, A. P., Microphase separation and rheology of a semicrystalline poly (ether-ester) multiblock copolymer. *Journal of Polymer Science Part B: Polymer Physics* 1998, 36 (11), 1795-1804.

90. Donald, A. M.; Kramer, E. J., Plastic deformation mechanisms in poly (acrylonitrile-butadiene styrene)[ABS]. *Journal of Materials Science* 1982, 17 (6), 1765-1772.

91. Okamoto, Y.; Miyagi, H.; Mitsui, S., New cavitation mechanism of rubber dispersed polystyrene. *Macromolecules* 1993, 26 (24), 6547-6551.

92. Correa, C.; De Sousa, J., Rubber particle size and cavitation process in high impact polystyrene blends. *Journal of materials science* 1997, 32 (24), 6539-6547.

93. Bucknall, C., Quantitative approaches to particle cavitation, shear yielding, and crazing in rubber-toughened polymers. *Journal of Polymer Science Part B: Polymer Physics* 2007, 45 (12), 1399-1409.

94. Socrate, S.; Boyce, M.; Lazzeri, A., A micromechanical model for multiple crazing in high impact polystyrene. *Mechanics of Materials* 2001, 33 (3), 155-175.

95. Mark, J. E., Physical properties of polymers handbook. *Springer:* 2007; Vol. 1076.

96. Hsiao, C.; Sauer, J., On crazing of linear high polymers. *Journal of Applied Physics* 1950, 21 (11), 1071-1083.

97. Tanabe, Y.; Kanetsuna, H., Brittle-to-ductile transition based upon amorphous orientation of polystyrene monofilaments. *Journal of Applied Polymer Science* 1978, 22 (9), 2707-2711.

98. Wang, S.-Q., Nonlinear polymer rheology. *Wiley Online Library:* 2018.

99. Li, X.; Liu, J.; Liu, Z.; Tsige, M.; Wang, S.-Q., Illustrating the molecular origin of mechanical stress in ductile deformation of polymer glasses. *Physical review letters* 2018, 120 (7), 077801.

100. Hoy, R. S.; Robbins, M. O., Strain hardening of polymer glasses: Effect of entanglement density, temperature, and rate. *Journal of Polymer Science Part B: Polymer Physics* 2006, 44 (24), 3487-3500.

101. Hoy, R. S.; Robbins, M. O., Strain hardening in polymer glasses: limitations of network models. *Physical review letters* 2007, 99 (11), 117801.

102. Liu, Z.; Li, X.; Zheng, Y.; Wang, S.-Q.; Tsige, M., Chain network: key to the ductile behavior of polymer glasses. *Macromolecules* 2018, 51 (5), 1666-1673.

103. Hong, S.; Chang, C.; Stein, R., Effect of internal field on the birefringence of polyethylene crystals and on the anisotropy of polymer chains. I. Birefringence effects. *Journal of Polymer Science: Polymer Physics Edition* 1975, 13 (7), 1447-1459.

104. Smith, R. P., Anisotropy of Polarizability of Polymeric Chains. *The Journal of Chemical Physics* 1966, 44 (7), 2543-2547.

105. Saiz, E.; Rainde, E., Dipole moments and birefringence of polymers. *Prentice-Hall, Englewood Cliffs*, NJ: 1992.

106. Sun, H.; Ntetsikas, K.; Avgeropoulos, A.; Wang, S.-Q., Breakdown of time–temperature equivalence in startup uniaxial extension of entangled polymer melts. *Macromolecules* 2013, 46 (10), 4151-4159.

107. Sun, H.; Liu, G.; Ntetsikas, K.; Avgeropoulos, A.; Wang, S.-Q., Rheology of Entangled Polymers Not Far above Glass Transition Temperature: Transient Elasticity and Intersegmental Viscous Stress. *Macromolecules* 2014, 47 (16), 5839-5850.

108. Janeschitz-Kriegl, H., Polymer melt rheology and flow birefringence. *Springer Science & Business Media*: 2012; Vol. 6.

109. Zhu, X.; Wang, S.-Q., Mechanisms for different failure modes in startup uniaxial extension: Tensile (rupture-like) failure and necking. *Journal of Rheology* 2013, 57 (1), 223-248.

110. Wang, Y.; Wang, S.-Q., Rupture in rapid uniaxial extension of linear entangled melts. *Rheologica acta* 2010, 49 (11-12), 1179-1185.

111. Rudd, J.; Andrews, R., Photoelastic properties of polystyrene in the glassy state. III. Styrene derivatives and copolymers. *Journal of Applied Physics* 1960, 31 (5), 818-826.

112. Read, B. In Dynamic birefringence of poly (methyl methacrylate), *Journal of Polymer Science Part C: Polymer Symposia*, Wiley Online Library: 1967; pp 1887-1902.

113. Sampson, R. C., A stress-optic law for photoelastic analysis of orthotropic composites. *Experimental Mechanics* 1970, 10 (5), 210-215.

114. Ramesh, K., Experimental stress analysis. *National Programme on Technology Enhanced Learning* 2011.

115. Wang, S.-Q. How Melt-Stretching Affects Mechanical Behavior of Polymer Glasses. http://ideaexchange.uakron.edu/polymerscience_ideas/586/.

116. Venerus, D. C.; Zhu, S.-H.; Öttinger, H. C., Stress and birefringence measurements during the uniaxial elongation of polystyrene melts. *Journal of Rheology* 1999, 43 (3), 795-813.

117. Sørensen, B. E., A revised Michel-Lévy interference colour chart based on first-principles calculations. *European Journal of Mineralogy* 2013, 25 (1), 5-10.

118. Takahashi, S.; Saito, H., Conformational change of phenyl ring side group during stress relaxation in glassy poly (styrene-co-acrylonitrile). *Macromolecules* 2004, 37 (3), 1062-1066.

119. Tagaya, A.; Ohkita, H.; Harada, T.; Ishibashi, K.; Koike, Y., Zero-birefringence optical polymers. *Macromolecules* 2006, 39 (8), 3019-3023.

120. Shafiee, H.; Tagaya, A.; Koike, Y., Mechanism of generation of photoelastic birefringence in methacrylate polymers for optical devices. *Journal of Polymer Science Part B: Polymer Physics* 2010, 48 (19), 2029-2037.

121. Isayev, A., Orientation development in the injection molding of amorphous polymers. *Polymer Engineering & Science* 1983, 23 (5), 271-284.

122. Razavi, M.; Cheng, S.; Huang, D.; Zhang, S.; Wang, S.-Q., Crazing and yielding in glassy polymers of high molecular weight. *Polymer* 2020, 122445.

123. De Focatiis, D. S.; Buckley, C. P., Prediction of frozen-in birefringence in oriented glassy polymers using a molecularly aware constitutive model allowing for finite molecular extensibility. *Macromolecules* 2011, 44 (8), 3085-3095.

124. Bennin, T.; Ricci, J.; Ediger, M., Enhanced Segmental Dynamics of Poly (lactic acid) Glasses during Constant Strain Rate Deformation. *Macromolecules* 2019, 52 (17), 6428-6437.

125. Ricci, J.; Bennin, T.; Ediger, M., Direct Comparison of Probe Reorientation and Linear Mechanical Measurements of Segmental Dynamics in Glassy Poly (methyl methacrylate). *Macromolecules* 2018, 51 (19), 7785-7793.

126. L. J. Fetters, D. J. L., R. H. Colby, Chain dimensions and entanglment spacing. 2007.

127. Chen, K.; Schweizer, K. S., Suppressed segmental relaxation as the origin of strain hardening in polymer glasses. *Physical review letters* 2009, 102 (3), 038301.

128. Rottler, J., Molecular mobility in driven monomeric and polymeric glasses. *Physical Review E* 2018, 98 (1), 010501.

129. Liu, J.; Lin, P.; Li, X.; Wang, S.-Q., Nonlinear stress relaxation behavior of ductile polymer glasses from large extension and compression. *Polymer* 2015, 81, 129-139.

130. Patlazhan, S.; Remond, Y., Structural mechanics of semicrystalline polymers prior to the yield point: a review. *Journal of Materials Science* 2012, 47 (19), 6749-6767.

131. Van Dommelen, J. v.; Parks, D.; Boyce, M.; Brekelmans, W.; Baaijens, F., Micromechanical modeling of the elasto-viscoplastic behavior of semi-crystalline polymers. *Journal of the Mechanics and Physics of Solids* 2003, 51 (3), 519-541.

132. Drozdov, A.; Klitkou, R.; Christiansen, J. d., Cyclic viscoplasticity of semicrystalline polymers with finite deformations. *Mechanics of Materials* 2013, 56, 53-64.

133. Jeridi, M.; Laiarinandrasana, L.; Sai, K., Comparative study of continuum damage mechanics and Mechanics of Porous Media based on multi-mechanism model on Polyamide 6 semi-crystalline polymer. *International Journal of Solids and Structures* 2015, 53, 12-27.

134. Gueguen, O.; Ahzi, S.; Makradi, A.; Belouettar, S., A new three-phase model to estimate the effective elastic properties of semi-crystalline polymers: application to PET. *Mechanics of Materials* 2010, 42 (1), 1-10.

135. Nikolov, S.; Doghri, I.; Pierard, O.; Zealouk, L.; Goldberg, A., Multi-scale constitutive modeling of the small deformations of semi-crystalline polymers. *Journal of the Mechanics and Physics of Solids* 2002, 50 (11), 2275-2302.

136. Sedighiamiri, A.; Van Erp, T.; Peters, G.; Govaert, L.; Van Dommelen, J., Micromechanical modeling of the elastic properties of semicrystalline polymers: A three-phase approach. *Journal of Polymer Science Part B: Polymer Physics* 2010, 48 (20), 2173-2184.

137. Schneider, K., Investigation of structural changes in semi-crystalline polymers during deformation by synchrotron X-ray scattering. *Journal of Polymer Science Part B: Polymer Physics* 2010, 48 (14), 1574-1586.

138. Schneider, K.; Trabelsi, S.; Zafeiropoulos, N.; Davies, R.; Riekel, C.; Stamm, M. In The study of cavitation in HDPE using time resolved synchrotron X-ray scattering during tensile deformation, *Macromolecular symposia*, Wiley Online Library: 2006; pp 241-248.

139. Stoclet, G.; Lefebvre, J. M.; Yeniad, B.; du Sart, G. G.; De Vos, S., On the strain-induced structural evolution of Poly (ethylene-2, 5-furanoate) upon uniaxial stretching: An in-situ SAXS-WAXS study. *Polymer* 2018, 134, 227-241.

140. Thomas, C.; Seguela, R.; Detrez, F.; Miri, V.; Vanmansart, C., Plastic deformation of spherulitic semi-crystalline polymers: An in situ AFM study of polybutene under tensile drawing. *Polymer* 2009, 50 (15), 3714-3723.

141. Liu, L.-Z.; Hsiao, B. S.; Fu, B. X.; Ran, S.; Toki, S.; Chu, B.; Tsou, A. H.; Agarwal, P. K., Structure Changes during Uniaxial Deformation of Ethylene-Based Semicrystalline Ethylene− Propylene Copolymer. 1. SAXS Study. *Macromolecules* 2003, 36 (6), 1920-1929.

142. Mao, Y.; Bucknall, D. G.; Kriegel, R. M., Simultaneous WAXS/SAXS study on semi-crystalline Poly (ethylene furanoate) under uniaxial stretching. *Polymer* 2018, 143, 228-236.

143. Flory, P. J., Molecular morphology in semicrystalline polymers. *Nature* 1978, 272 (5650), 226-229.

144. Peterlin, A., Molecular model of drawing polyethylene and polypropylene. *Journal of materials science* 1971, 6 (6), 490-508.

145. Peterlin, A., Drawing and extrusion of semi-crystalline polymers. *Colloid and polymer science* 1987, 265 (5), 357-382.

146. Hong, K.; Rastogi, A.; Strobl, G., A model treating tensile deformation of semicrystalline polymers: quasi-static stress− strain relationship and viscous stress determined for a sample of polyethylene. *Macromolecules* 2004, 37 (26), 10165-10173.

147. Hong, K.; Rastogi, A.; Strobl, G., Model treatment of tensile deformation of semicrystalline polymers: static elastic moduli and creep parameters derived for a sample of polyethylene. *Macromolecules* 2004, 37 (26), 10174-10179.

148. Kramer, E. J., Open questions in the physics of deformation of polymer glasses. *Journal of Polymer Science Part B: Polymer Physics* 2005, 43 (23), 3369-3371.

149. Van Melick, H.; Govaert, L.; Meijer, H., On the origin of strain hardening in glassy polymers. *Polymer* 2003, 44 (8), 2493-2502.

150. Razavi, M.; Cheng, S.; Huang, D.; Zhang, S.; Wang, S.-Q., Crazing and yielding in glassy polymers of high molecular weight. *Polymer* 2020, 122445.

151. Lee, H.-N.; Paeng, K.; Swallen, S. F.; Ediger, M., Direct measurement of molecular mobility in actively deformed polymer glasses. *Science* 2009, 323 (5911), 231-234.

152. Rohrer, G. S., Structure and bonding in crystalline materials. *Cambridge University Press:* 2001.

153. Smith, T.; Razavi, M.; Wang, S., Improving ductility of glassy semicrystalline polymers by pre-deformation. *Bulletin of the American Physical Society* 2020.

154. Dirac, P. A. M., The principles of quantum mechanics. *Oxford university press*: 1981.

155. Siracusa, V.; Rocculi, P.; Romani, S.; Dalla Rosa, M., Biodegradable polymers for food packaging: a review. *Trends in Food Science & Technology* 2008, 19 (12), 634-643.

156. Sinclair, R., The case for polylactic acid as a commodity packaging plastic. *Journal of Macromolecular Science, Part A: Pure and Applied Chemistry* 1996, 33 (5), 585-597.

157. Dugan, J. S., Novel properties of PLA fibers. *International Nonwovens Journal* 2001, (3), 1558925001OS-01000308.

158. Saeidlou, S.; Huneault, M. A.; Li, H.; Park, C. B., Poly (lactic acid) crystallization. *Progress in Polymer Science* 2012, 37 (12), 1657-1677.

159. Farah, S.; Anderson, D. G.; Langer, R., Physical and mechanical properties of PLA, and their functions in widespread applications—A comprehensive review. *Advanced drug delivery reviews* 2016, 107, 367-392.

160. Liu, G.; Zhang, X.; Wang, D., Tailoring Crystallization: Towards High-Performance Poly (lactic acid). *Advanced Materials* 2014, 26 (40), 6905-6911.

161. Drumright, R. E.; Gruber, P. R.; Henton, D. E., Polylactic acid technology. *Advanced materials* 2000, 12 (23), 1841-1846.

162. Lasprilla, A. J.; Martinez, G. A.; Lunelli, B. H.; Jardini, A. L.; Maciel Filho, R., Poly-lactic acid synthesis for application in biomedical devices—A review. *Biotechnology advances* 2012, 30 (1), 321-328.

163. Mehta, R.; Kumar, V.; Bhunia, H.; Upadhyay, S., Synthesis of poly (lactic acid): a review. *Journal of Macromolecular Science, Part C: Polymer Reviews* 2005, 45 (4), 325-349.

164. Ovitt, T. M.; Coates, G. W., Stereoselective ring-opening polymerization of meso-lactide: synthesis of syndiotactic poly (lactic acid). *Journal of the American Chemical Society* 1999, 121 (16), 4072-4073.

165. Kang, S.; Hsu, S. L.; Stidham, H. D.; Smith, P. B.; Leugers, M. A.; Yang, X., A spectroscopic analysis of poly (lactic acid) structure. *Macromolecules* 2001, 34 (13), 4542-4548.

166. Tabi, T.; Sajó, I.; Szabó, F.; Luyt, A.; Kovács, J., Crystalline structure of annealed polylactic acid and its relation to processing. *Express Polymer Letters* 2010, 4 (10).

167. Drieskens, M.; Peeters, R.; Mullens, J.; Franco, D.; Lemstra, P. J.; Hristova-Bogaerds, D. G., Structure versus properties relationship of poly (lactic acid). I. Effect of crystallinity on barrier properties. *Journal of Polymer Science Part B: Polymer Physics* 2009, 47 (22), 2247-2258.

168. Tsuji, H.; Horii, F.; Nakagawa, M.; Ikada, Y.; Odani, H.; Kitamaru, R., Stereocomplex formation between enantiomeric poly (lactic acid) s. 7. Phase structure of the stereocomplex crystallized from a dilute acetonitrile solution as studied by high-resolution solid-state carbon-13 NMR spectroscopy. *Macromolecules* 1992, 25 (16), 4114-4118.

169. Martin, O.; Averous, L., Poly (lactic acid): plasticization and properties of biodegradable multiphase systems. *Polymer* 2001, 42 (14), 6209-6219.

170. Petersson, L.; Kvien, I.; Oksman, K., Structure and thermal properties of poly (lactic acid)/cellulose whiskers nanocomposite materials. *Composites Science and Technology* 2007, 67 (11-12), 2535-2544.

171. Ajioka, M.; Enomoto, K.; Suzuki, K.; Yamaguchi, A., Basic properties of polylactic acid produced by the direct condensation polymerization of lactic acid. *Bulletin of the Chemical Society of Japan* 1995, 68 (8), 2125-2131.

172. Perego, G.; Cella, G. D.; Bastioli, C., Effect of molecular weight and crystallinity on poly (lactic acid) mechanical properties. *Journal of Applied Polymer Science* 1996, 59 (1), 37-43.

173. Carrasco, F.; Pagès, P.; Gámez-Pérez, J.; Santana, O.; Maspoch, M. L., Processing of poly (lactic acid): Characterization of chemical structure, thermal stability and mechanical properties. *Polymer Degradation and stability* 2010, 95 (2), 116-125.

174. Stoclet, G.; Lefebvre, J.; Séguéla, R.; Vanmansart, C., In-situ SAXS study of the plastic deformation behavior of polylactide upon cold-drawing. *Polymer* 2014, 55 (7), 1817-1828.

175. Stoclet, G.; Seguela, R.; Lefebvre, J.; Elkoun, S.; Vanmansart, C., Strain-induced molecular ordering in polylactide upon uniaxial stretching. *Macromolecules* 2010, 43 (3), 1488-1498.

176. Stoclet, G.; Séguéla, R.; Lefebvre, J.; Li, S.; Vert, M., Thermal and strain-induced chain ordering in lactic acid stereocopolymers: influence of the composition in stereomers. *Macromolecules* 2011, 44 (12), 4961-4969.

177. Stoclet, G.; Seguela, R.; Lefebvre, J.-M.; Rochas, C., New insights on the strain-induced mesophase of poly (d, l-lactide): in situ WAXS and DSC study of the thermo-mechanical stability. *Macromolecules* 2010, 43 (17), 7228-7237.

178. Stoclet, G.; Seguela, R.; Vanmansart, C.; Rochas, C.; Lefebvre, J.-M., WAXS study of the structural reorganization of semi-crystalline polylactide under tensile drawing. *Polymer* 2012, 53 (2), 519-528.

179. Iannace, S.; Maffezzoli, A.; Leo, G.; Nicolais, L., Influence of crystal and amorphous phase morphology on hydrolytic degradation of PLLA subjected to different processing conditions. *Polymer* 2001, 42 (8), 3799-3807.

180. Ouagne, P.; Bizet, L.; Baley, C.; Bréard, J., Analysis of the film-stacking processing parameters for PLLA/flax fiber biocomposites. *Journal of Composite Materials* 2010, 44 (10), 1201-1215.

181. Taubner, V.; Shishoo, R., Influence of processing parameters on the degradation of poly (L-lactide) during extrusion. *Journal of applied polymer science* 2001, 79 (12), 2128-2135.

182. Weir, N.; Buchanan, F.; Orr, J.; Farrar, D.; Boyd, A., Processing, annealing and sterilisation of poly-L-lactide. *Biomaterials* 2004, 25 (18), 3939-3949.

183. Auras, R. A.; Lim, L.-T.; Selke, S. E.; Tsuji, H., *Poly (lactic acid): synthesis, structures, properties, processing, and applications*. John Wiley & Sons: 2011; Vol. 10.

184. Lunt, J., Large-scale production, properties and commercial applications of polylactic acid polymers. *Polymer degradation and stability* 1998, 59 (1-3), 145-152.

185. Castro-Aguirre, E.; Iñiguez-Franco, F.; Samsudin, H.; Fang, X.; Auras, R., Poly (lactic acid)—Mass production, processing, industrial applications, and end of life. *Advanced Drug Delivery Reviews* 2016, 107, 333-366.

186. Aghjeh, M. R.; Nazari, M.; Khonakdar, H. A.; Jafari, S. H.; Wagenknecht, U.; Heinrich, G., In depth analysis of micro-mechanism of mechanical property alternations in PLA/EVA/clay nanocomposites: a combined theoretical and experimental approach. *Materials & Design* 2015, *88*, 1277-1289.

187. Aghjeh, M. R.; Asadi, V.; Mehdijabbar, P.; Khonakdar, H. A.; Jafari, S. H., Application of linear rheology in determination of nanoclay localization in PLA/EVA/Clay nanocomposites: Correlation with microstructure and thermal properties. *Composites Part B: Engineering* 2016, *86*, 273-284.

188. Aghjeh, M. R.; Kazerouni, Y.; Otadi, M.; Khonakdar, H. A.; Jafari, S. H.; Ebadi-Dehaghani, H.; Mousavi, S. H., A combined experimental and theoretical approach to quantitative assessment of microstructure in PLA/PP/organo-clay nanocomposites; wide-angle x-ray scattering and rheological analysis. *Composites Part B: Engineering* 2017.

189. Wang, S.-Q., Nonlinear Polymer Rheology: Macroscopic phenomenology and Molecular foundation. *Wiley: Hoboken, NJ*, 2018.

190. Jalabert, M.; Fraschini, C.; Prud'Homme, R. E., Synthesis and characterization of poly (L-lactide) s and poly (D-lactide) s of controlled molecular weight. *Journal of Polymer Science Part A: Polymer Chemistry* 2007, 45 (10), 1944-1955.

191. Ma, H.; Okuda, J., Kinetics and mechanism of L-lactide polymerization by rare earth metal silylamido complexes: effect of alcohol addition. *Macromolecules* 2005, 38 (7), 2665-2673.

192. Spassky, N.; Simic, V.; Montaudo, M. S.; Hubert-Pfalzgraf, L. G., Inter-and intramolecular ester exchange reactions in the ring-opening polymerization of (D, L)-lactide using lanthanide alkoxide initiators. *Macromolecular Chemistry and Physics* 2000, 201 (17), 2432-2440.

193. Kowalski, A.; Duda, A.; Penczek, S., Polymerization of L, L-lactide initiated by aluminum isopropoxide trimer or tetramer. *Macromolecules* 1998, 31 (7), 2114-2122.

194. Kong, Y.; Hay, J., The measurement of the crystallinity of polymers by DSC. *Polymer* 2002, 43 (14), 3873-3878.

195. Fischer, E.; Sterzel, H. J.; Wegner, G., Investigation of the structure of solution grown crystals of lactide copolymers by means of chemical reactions. *Kolloid-Zeitschrift und Zeitschrift für Polymere* 1973, 251 (11), 980-990.

196. Zuza, E.; Ugartemendia, J. M.; Lopez, A.; Meaurio, E.; Lejardi, A.; Sarasua, J.-R., Glass transition behavior and dynamic fragility in polylactides containing mobile and rigid amorphous fractions. *Polymer* 2008, 49 (20), 4427-4432.

197. Grijpma, D.; Penning, J.; Pennings, A., Chain entanglement, mechanical properties and drawability of poly (lactide). *Colloid & Polymer Science* 1994, 272 (9), 1068-1081.

198. Tsuji, H.; Ikada, Y., Properties and morphologies of poly (L-lactide): 1. Annealing condition effects on properties and morphologies of poly (L-lactide). *Polymer* 1995, 36 (14), 2709-2716.

199. Wu, S., Secondary relaxation, brittle–ductile transition temperature, and chain structure. *J. Appl. Polym. Sci.* 1992, 46 (4), 619-624.

200. Ren, J.; Urakawa, O.; Adachi, K., Dielectric and viscoelastic studies of segmental and normal mode relaxations in undiluted poly (d, l-lactic acid). *Macromolecules* 2003, 36 (1), 210-219.

201. Dorgan, J. R.; Janzen, J.; Clayton, M. P.; Hait, S. B.; Knauss, D. M., Melt rheology of variable L-content poly (lactic acid). *Journal of Rheology* 2005, 49 (3), 607-619.

202. Dorgan, J. R.; Williams, J. S.; Lewis, D. N., Melt rheology of poly (lactic acid): Entanglement and chain architecture effects. *Journal of rheology* 1999, 43 (5), 1141-1155.
203. Cooper-White, J. J.; Mackay, M. E., Rheological properties of poly (lactides). Effect of molecular weight and temperature on the viscoelasticity of poly (l-lactic acid). *Journal of Polymer Science Part B: Polymer Physics* 1999, 37 (15), 1803-1814.
204. Tonelli, A. E.; Flory, P. J., The configurational statistics of random poly (lactic acid) chains. I. Experimental results. *Macromolecules* 1969, 2 (3), 225-227.
205. Brant, D. A.; Tonelli, A. E.; Flory, P. J., The configurational statistics of random poly (lactic acid) chains. II. Theory. *Macromolecules* 1969, 2 (3), 228-235.
206. Dorgan, J. R.; Janzen, J.; Clayton, M. P.; Hait, S. B.; Knauss, D. M., Melt rheology of variable L-content poly(lactic acid). *J. Rheol.* 2005, 49 (3), 607-619.
207. Rault, J., Conjecture on the distance between entanglements in polymer melts. *Comptes rendus de l academie des sciences serie ii* 1985, 300 (10), 433-436.
208. Heymans, N., Diffuse versus point entanglements—homopolymers and blends. *Journal of materials science* 1986, 21 (6), 1919-1926.
209. Lin, Y., Number of entanglement strands per cubed tube diameter, a fundamental aspect of topological universality in polymer viscoelasticity. *Macromolecules* 1987, 20 (12), 3080-3083.
210. Kavassalis, T. A.; Noolandi, J., New view of entanglements in dense polymer systems. *Phys. Rev. Lett.* 1987, 59 (23), 2674.
211. Wang, S. Q.; Cheng, S. W., *Polymer Glasses*. edited by C. Roth, CRC Press: 2016.
212. Gruenwald, G., *Modern Plastics* 1960, 38, 137.
213. Ender, D. H.; Andrews, R. D., Cold Drawing of Glassy Polystyrene under Dead Load. *J. Appl. Phys.* 1965, 36 (10), 3057-3062.
214. Ehrenstein, G. W., Polymeric materials: structure, properties, applications. *Carl Hanser Verlag GmbH Co KG*: 2012.
215. Gurarslan, A.; Joijode, A. S.; Tonelli, A. E., Polymers coalesced from their cyclodextrin inclusion complexes: What can they tell us about the morphology of melt-crystallized polymers? *J. Polym. Sci., Part B: Polym. Phys.* 2012, 50 (12), 813-823.

216. Joijode, A. S.; Hawkins, K.; Tonelli, A. E., Improving Poly (ethylene terephthalate) Through Self-nucleation. *Macromol. Mater. Eng.* 2013, 298 (11), 1190-1200.

217. Gurarslan, A.; Joijode, A.; Shen, J.; Narayanan, G.; Antony, G.; Li, S.; Caydamli, Y.; Tonelli, A., Reorganizing Polymer Chains with Cyclodextrins. *Polymers* 2017, 9 (12), 673.

218. Zhu, X.; Wang, S.-Q., Mechanisms for different failure modes in startup uniaxial extension: Tensile (rupture-like) failure and necking. *J. Rheol.* 2012, 57 (1), 223-248.

219. Nitta, K.-H.; Takayanagi, M., Direct observation of the deformation of isolated huge spherulites in isotactic polypropylene. *Journal of materials science* 2003, 38 (24), 4889-4894.

220. Men, Y.; Rieger, J.; Homeyer, J., Synchrotron ultrasmall-angle X-ray scattering studies on tensile deformation of poly (1-butene). *Macromolecules* 2004, 37 (25), 9481-9488.

221. Lu, Y.; Men, Y., Cavitation-Induced Stress Whitening in Semi-Crystalline Polymers. *Macromol. Mater. Eng.* 2018, 303 (11), 1800203.

222. Flory, P. J.; Yoon, D. Y., Molecular morphology in semi-crystalline polymers. *Nature* 1978, 272 (5650), 226-229.

223. Hu, W. G.; Schmidt-Rohr, K., Polymer ultradrawability: the crucial role of α-relaxation chain mobility in the crystallites. *Acta Polym.* 1999, 50 (8), 271-285.

224. Liu, K.; Song, Y.; Feng, W.; Liu, N.; Zhang, W.; Zhang, X., Extracting a single polyethylene oxide chain from a single crystal by a combination of atomic force microscopy imaging and single-molecule force spectroscopy: toward the investigation of molecular interactions in their condensed states. *J. Am. Chem. Soc.* 2011, 133 (10), 3226-3229.

225. Chen, W.; Reichert, D.; Miyoshi, T., Helical jump motions of poly (l-Lactic Acid) chains in the α phase as revealed by solid-state NMR. *The Journal of Physical Chemistry B* 2015, 119 (12), 4552-4563.

226. Gerrits, N.; Young, R., Texture development in uniaxially drawn polyethylene tape. *Journal of materials science* 1991, 26 (8), 2137-2142.

227. Mandelkern, L.; Smith, F. L.; Failla, M.; Kennedy, M. A.; Peacock, A. J., The brittle-ductile transition in linear polyethylene. *J. Polym. Sci. Pt. B-Polym. Phys.* 1993, 31 (4), 491-493.

228. Ehrenstein, G.; Theriault, R. P., Polymeric Materials: Structure, Properties. Applications. *Hanser. Cincinnati* 2001.

229. Van der Wal, A.; Mulder, J.; Thijs, H.; Gaymans, R., Fracture of polypropylene: 1. The effect of molecular weight and temperature at low and high test speed. *Polymer* 1998, 39 (22), 5467-5475.

230. van der Wal, A.; Mulder, J. J.; Gaymans, R. J., Fracture of polypropylene: 2. The effect of crystallinity. *Polymer* 1998, 39 (22), 5477-5481.

231. Kumaraswamy, G.; Verma, R. K.; Kornfield, J. A.; Yeh, F.; Hsiao, B. S., Shear-enhanced crystallization in isotactic polypropylene. In-situ synchrotron SAXS and WAXD. *Macromolecules* 2004, 37 (24), 9005-9017.

232. Somani, R. H.; Yang, L.; Zhu, L.; Hsiao, B. S., Flow-induced shish-kebab precursor structures in entangled polymer melts. *Polymer* 2005, 46 (20), 8587-8623.

233. Elmoumni, A.; Winter, H. H., Large strain requirements for shear-induced crystallization of isotactic polypropylene. *Rheologica acta* 2006, 45 (6), 793-801.

234. Hamad, F. G.; Colby, R. H.; Milner, S. T., Onset of Flow-Induced Crystallization Kinetics of Highly Isotactic Polypropylene. *Macromolecules* 2015, 48 (11), 3725-3738.

235. Nazari, B.; Tran, H.; Beauregard, B.; Flynn-Hepford, M.; Harrell, D.; Milner, S. T.; Colby, R. H., Two distinct morphologies for semicrystalline isotactic polypropylene crystallized after shear flow. *Macromolecules* 2018, 51 (13), 4750-4761.

236. Cui, K.; Ma, Z.; Tian, N.; Su, F.; Liu, D.; Li, L., Multiscale and multistep ordering of flow-induced nucleation of polymers. *Chemical reviews* 2018, 118 (4), 1840-1886.

237. Okada, K.; Tanaka, Y.; Masunaga, H.; Hikosaka, M., 3D structure of nano-oriented crystals of poly (ethylene terephthalate) formed by elongational crystallization from the melt. *Polym. J.* 2018, 50 (2), 167-176.

238. Zhu, Y. H.; Okui, N.; Tanaka, T.; Umemoto, S.; Sakai, T., Low-temperature properties of hard elastic polypropylene fibers. *Polymer* 1991, 32 (14), 2588-2593.

239. Wang, Y.; Boukany, P.; Wang, S.-Q.; Wang, X., Elastic breakup in uniaxial extension of entangled polymer melts. *Phys. Rev. Lett.* 2007, 99 (23), 237801.

240. Stolte, I.; Androsch, R.; Di Lorenzo, M. L.; Schick, C., Effect of aging the glass of isotactic polybutene-1 on form II nucleation and cold crystallization. *The Journal of Physical Chemistry B* 2013, 117 (48), 15196-15203.

241. Zhao, Z.; Zhao, X.; Liu, J.; Wang, W.; Mays, J.; Wang, S.-Q., Characterizing effects of fast melt deformation on entangled polymers in their glassy state. *The Journal of Chemical Physics* 2019, 151 (12), 124906.

242. He, B. B., Two-dimensional X-ray diffraction. *Wiley Online Library*: 2009; Vol. 2.

243. Baldenegro-Perez, L. A.; Navarro-Rodriguez, D.; Medellin-Rodriguez, F. J.; Hsiao, B.; Avila-Orta, C. A.; Sics, I., Molecular weight and crystallization temperature effects on poly (ethylene terephthalate)(PET) homopolymers, an isothermal crystallization analysis. *Polymers* 2014, 6 (2), 583-600.